Arnold Schwarzenegger
Governor

URBAN SURFACE MODIFICATION AS A POTENTIAL OZONE AIR-QUALITY IMPROVEMENT STRATEGY IN CALIFORNIA

PHASE TWO: FINE-RESOLUTION METEOROLOGICAL AND PHOTOCHEMICAL MODELING OF URBAN HEAT ISLANDS

PIER FINAL PROJECT REPORT

Prepared For:
California Energy Commission
Public Interest Energy Research Program

Prepared By:
Altostratus Inc.

August 2009
CEC-500-2009-071

Prepared By:
Altostratus Inc.
Haider Taha
Martinez, California
Commission Contract No. 500-02-004

Prepared For:
Public Interest Energy Research (PIER)
California Energy Commission

Marla Mueller
Contract Manager

Linda Spiegel
Program Area Lead
Energy-Related Environmental Research

Kenneth Koyama
Office Manager
Energy Systems Research

Martha Krebs, Ph.D.
PIER Director

Thom Kelly, Ph.D.
Deputy Director
ENERGY RESEARCH & DEVELOPMENT DIVISION

Melissa Jones
Executive Director

Acknowledgements and Disclaimers

The California Energy Commission’s (Energy Commission’s)Public Interest Energy Research (PIER) Program supported this work.

Acknowledgements are due project managers Nicole Davis (Global Environmental Research), Marla Mueller (Energy Commission/CIEE), and Kelly Birkinshaw (Energy Commission). The project advisory committee (PAC) and others listed below are acknowledged for having provided data or general guidance: Phil Martien, Bay Area Air Quality Management District (BAAQMD); Kathy Diehl, U.S. Environmental Protection Agency – San Francisco (Region 9); Ash Lashgari and Aileen McCauley, California Air Resources Board; Charles Anderson and Janice Lam, Sacramento Metropolitan Air Quality Management District; and Steve Burian, University of Utah.

The author acknowledges the U.S. Environmental Protection Agency for the original DA-SM2-U model. Environ Inc. is acknowledged for the CAMx photochemical model and the National Center for Atmospheric Research (NCAR) is acknowledged for the MM5 modeling system. These models were subsequently modified, updated, and applied in specific context in this study at Altostratus Inc. New models and data were also developed based on these and other systems.

Please cite this report as follows:

Taha, Haider (Altostratus Inc.). 2009. *Urban Surface Modification as a Potential Ozone Air-Quality Improvement Strategy in California—Phase Two: Fine-Resolution Meteorological and Photochemical Modeling of Urban Heat Islands*. California Energy Commission, PIER Energy-Related Environmental Research. CEC-500-2009-071.

Preface

The Public Interest Energy Research (PIER) Program supports public interest energy research and development that will help improve the quality of life in California by bringing environmentally safe, affordable, and reliable energy services and products to the marketplace.

The PIER Program, managed by the California Energy Commission (Energy Commission), conducts public interest research, development, and demonstration (RD&D) projects to benefit California.

The PIER Program strives to conduct the most promising public interest energy research by partnering with RD&D entities, including individuals, businesses, utilities, and public or private research institutions.

PIER funding efforts are focused on the following RD&D program areas:

- Buildings End-Use Energy Efficiency
- Energy Innovations Small Grants
- Energy-Related Environmental Research
- Energy Systems Integration
- Environmentally Preferred Advanced Generation
- Industrial/Agricultural/Water End-Use Energy Efficiency
- Renewable Energy Technologies
- Transportation

Urban Surface Modification as a Potential Ozone Air-Quality Improvement Strategy in California — Phase Two: Fine-Resolution Meteorological and Photochemical Modeling of Urban Heat Islands is the final report for the Urban Heat Island Modeling project (Contract Number 500-02-004) conducted by Altostratus Inc. The information from this project contributes to PIER's Energy-Related Environmental Research Program.

For more information about the PIER Program, please visit the Energy Commission's website at www.energy.ca.gov/pier or contact the Energy Commission at 916-654-5164.

Table of Contents

List of Figures

List of Tables

Abstract

Many California air districts seek to reduce ozone pollution. Because higher air temperatures increase ozone production and electricity use, research has focused on reducing air temperatures in urban heat islands—areas that produce and retain more heat than rural communities.

For this study, researchers developed, updated, and applied a fine-resolution, urban meteorological model to drive fine-resolution photochemical simulations for two California regions, to evaluate the air temperature and ozone effects of urban infrastructure and vegetation surface modifications in those regions. The new model improves simulation of fine-resolution meteorological and air-pollutant fields in the air layer beneath the mean height of buildings and vegetation.

Building on Phase 1 modeling, Phase 2 identified larger localized impacts on meteorology and ozone and captured new phenomena of interest to urban air quality researchers. Model results show that modifying urban surfaces is very effective for large areas, but that modifying smaller areas may have positive and negative effects. This reemphasizes the need to develop an optimal, region-specific surface modification mix. The simulations suggest that while increased urban reflectivity is relatively more effective than increased canopy cover locally, the regional and downwind effects can be relatively more uniform.

Keywords: Air quality, albedo, canopy cover, fine-resolution modeling, mesoscale modeling, meso-urban modeling, ozone, photochemical modeling, surface modifications, urban heat island

Executive Summary

Introduction

Regulators use photochemical air-quality modeling to plan and implement strategies that improve air quality and help achieve ozone attainment status. Researchers run photochemical models to determine how air pollution forms, builds up, and disperses under various emissions and meteorological scenarios. The Clean Air Act requires that ozone non-attainment areas, especially those designated as serious or higher, develop ozone-reduction plans. These state implementation plans must include strategies that are quantifiable and enforceable.

Heat islands are urban areas that generate, absorb, and retain more heat than rural areas because of the buildings, roads, and other urban structures. For many areas in California with severe air quality problems, heat island mitigation strategies—which reduce heat (and therefore, ozone production) by modifying surfaces in the urban environment—could be useful in reaching ozone attainment and reducing energy demand (by reducing the need for cooling). However, emissions reductions from these strategies cannot be measured directly. Instead, decision makers rely on computer models to predict benefits; therefore large uncertainties exist in the quantification of benefits and cost-effectiveness. Because of these uncertainties, surface-modification strategies, such as changing the albedo (reflectance) of rooftops, have not been included to the extent possible in these plans. Improving and tailoring the meteorological and photochemical models for fine-resolution applications could provide a better understanding and increased acceptance of heat island mitigation strategies.

As with many other strategies, surface modifications can cause not only net decreases in ozone, but also net increases as well. The optimal mix of region-specific ozone-reduction strategies will differ from one region to another and will depend on local emissions, meteorology, unique weather episodes, topography, air flow patterns, and other factors. As a result, modeling of those potential impacts is crucial to understanding the benefits of surface modification strategies in a variety of situations and environments.

Purpose

This project sought to improve the resolution and accuracy of meteorological and photochemical modeling and develop a fine-resolution air-quality modeling capability for California. Such an improvement should increase confidence in model performance when used to evaluate the energy, emissions, and air-quality effects of surface modifications at individual city blocks or neighborhood levels. An improved meteorological-photochemical modeling system will help support decision-making processes related to heat island control through implementation of surface-modification activities.

Project Objectives

This study explored and evaluated the ability of surface modifications (on roofs, paved surfaces, and increasing vegetation) in urban areas for improving ozone air quality in California. The improved models and data were applied to urban areas in California to better evaluate the potential of heat island control strategies, such as increased urban albedo (that is, surface reflectivity, such as that from roofs and pavements) and increased urban canopy cover (from trees), on local air quality. Two regions were modeled in Phase 2. The main objective of this phase was to develop and update new models and implement a method and new data techniques that could be used for a detailed evaluation of surface modifications' impacts on heat islands, energy use, emissions, and air quality.

This work built on Phase 1 by developing new models and further improving the resolution of the simulations for the urban canopy layer—the urban air layer beneath the mean height of buildings. (The report detailing the Phase 1 work is *Urban Surface Modification as a Potential Ozone Air Quality Improvement in California: Phase One: Initial Mesoscale Modeling*, and it is available at www.energy.ca.gov/pier/project_reports/CEC-500-2005-128.html.) The urban canopy layer is particularly important because it contains the bulk of the population and air-pollutant emissions, and it is where initial chemical reactions that produce smog occur. The resulting meteorological model, urbanized MM5 (uMM5), incorporates all updates, modifications, and improvements performed over the span of this project. The uMM5 model provides the driving meteorological fields used in the fine-resolution photochemical simulations that examine the behavior of air pollution.

A secondary objective was to apply the new method, models, data, and techniques to two of California's urban areas: the greater Sacramento area and a small domain in the Orange-Riverside counties area of Los Angeles. The photochemical episodes modeled here are July 29 through August 4, 2000, for Central California (CCOS-2000) and August 3 through August 7, 1997, for Southern California (SCOS-97).

Project Outcomes

The improved urbanized model (uMM5) can capture small-scale phenomena that are not typically detectable in mesoscale modeling. These include, for example, cool islands (when cities are cooler than suburbs), heat islands, flow convergence associated with heat-island circulation, flow divergence at the leading edge of urban areas, and the slower wind over them (due to drag and roughness). Convergence occurs when air flows onto an area, increasing pressure, and divergence occurs when air flows out of that area. Both states affect pollution formation and transport, so it is important to include them in the modeling.

The improved model can also simulate in more detail the vertical profiles of various components of turbulent kinetic energy generation and dissipation and their relation to vertical shape factors of buildings, vegetation, and other obstacles. In short, it can simulate how air moves around and in relation to objects in its path—crucial information for analyzing pollution formation and movement. More important, the improved meteorological-photochemical model combination shows larger changes in ozone than the previous model for localized areas.

Overall, the simulations suggest that heat-island control strategies can be very effective when modifying the albedo of surfaces or increasing vegetative cover over large areas, however, limited-area control may have both positive and negative effects, sometimes on the same order of magnitude, although at different times and locations. Limited-area urban heat island control can produce local improvements in air quality but achieve mixed results further downwind. The latter situation arises because of changes in air mixing, height of the boundary layer (the bottom layer of the troposphere in contact with the earth's surface), wind speed (which can flush pollutants), and wind flow's interaction with the basin's topography. Thus, this modeling sheds light on some aspects of the "threshold" effect identified in Phase 1 and suggests that for urban heat island control to be effective, a larger area (not only a small portion of the basin) should be modified. Modifying larger areas produces significant positive air quality impacts and, at the fine resolutions studied here, are larger than those reported from the Phase 1 mesoscale modeling (which models resolutions ranging from a few kilometers to tens of kilometers in the horizontal and tens to hundreds of meters in the vertical).

Sacramento

The model results show that changing surface materials' reflectivity (albedo) and increasing vegetation (canopy cover) can affect air temperature significantly during the day but have little or no effect at night. The resulting cooler air can be transported downwind and affect areas beyond the modified urban regions. In the Sacramento area, air temperature can be reduced by up to 2.5°C to 3°C. The fine-resolution photochemical simulations showed peak ozone concentrations were consistently located downwind of downtown Sacramento. For the simulated days, concentrations were decreased by up to 16–26 parts per billion in the high-albedo scenario and by up to 15–19 parts per billion in the increased-canopy scenario. Some more extreme changes are also seen in one or two instances. These occur at a few spots in the domain, typically affecting areas 1–2 square kilometers or slightly larger. These large reductions were captured by the model because of its fine-resolution simulation capabilities. The fine-resolution simulations are useful for "zooming into" the coarse-grid ozone-change fields to detect and capture the fine-resolution details that are important for analysis, urban surface albedo and canopy cover modification, and planning at neighborhood scales.

Urban heat island control was found to lower ozone concentrations over the larger areas in the domain. Spatially averaged ozone concentration decreases of 5–14 parts per billion were found in the high-albedo scenario (where albedo was increased) and 5–10 parts per billion were found in the increased canopy scenario. These values are more representative of the regional impacts in Sacramento than the extremes discussed above.

Analysis of the 8-hour average ozone shows that, except for one instance, the impact of urban heat island control in all locations and all days is a decrease in the 8-hour ozone averages. The relative reduction factor analysis shows that the daily maximum 8-hour average in the Sacramento area can be decreased by between 4 percent and 14 percent across the episode days, with the largest impacts seen on July 31 and August 1. Although the effects of increased albedo are generally larger than those of increased canopy cover, the difference is not particularly big and, in some cases, increased canopy cover is more effective. This difference is noticeable at monitor locations close to the downtown area.

Orange-Riverside

A similar analysis was performed for a small domain across the Orange and Riverside counties in the Los Angeles area. The fine-resolution base-case meteorological simulations captured the general flow pattern and temperature regimes across the eastern and western basins of the domain, which are separated by the Santa Ana mountains. The simulations also detect urban heat islands. The base-case photochemical simulations of Orange-Riverside domain showed that the peak concentrations occur downwind of the coastal area, in the mountain range and eastern basin as expected, but that some higher concentrations on August 5 also entered the domain from the Los Angeles area. The simulated peaks were 113 parts per billion on August 5 and 97 parts per billion on August 6. High concentrations in coastal areas of the domain ranged up to 82 parts per billion on August 5 and up to 85 parts per billion on August 6.

In terms of urban heat island-control impacts, the effects are less clear in the Orange-Riverside domain relative to Sacramento because of the mountains' blocking effect and the modified area's small size. The largest air-temperature reductions in both the increased-albedo and increased-canopy-cover scenarios can reach up to 3°C. Ozone impacts can also be significant despite the mixed signal. In terms of the maximum 8-hour average ozone, the simulations suggest that the dominant effect is a decrease in concentrations. The relative reduction factor analysis (which compares the average concentration of the modeled peak ozone before urban surface modifications to the average concentration of the modeled peak ozone after they were implemented) shows that the daily maximum 8-hour average can be decreased by between 3 percent and 10 percent across the episode days in Irvine and up to 3 percent in the Tustin area. The largest effects were seen during the main days of the episode at both locations. The eastern basin, on the other hand, saw some decreases (but also increases) in concentrations on the same order of magnitude. However, the eastern half (and basin) of the Orange-Riverside domain is not populated.

Conclusions

This study successfully developed new fine-resolution models, specific input parameters, and data designed for evaluating and measuring the impacts of heat-island control surface modifications on meteorology and air quality, including their potential use in evaluating regulatory implications. The application of the models to two California domains was successfully completed, and the simulation results suggest beneficial meteorological and air quality impacts from large-area implementation of urban surface modification but mixed results with limited-area (neighborhood) control. In the Sacramento area, potential reductions reach up to 3°C in air temperature and 5–14 parts per billion in ozone. In the Orange-Riverside domain, the ozone reductions range from 4–10 parts per billion. These ozone reductions (reported here for both domains) are averaged over portions of the respective domains. In addition, larger ozone reductions in both locations were also obtained but in more limited areas and during shorter time intervals. The results reemphasize the need for developing region-specific scenarios to identify an optimal mix of infrastructure and vegetation surface modifications that will maximize the local net benefits.

Results from Phase 2 modeling are generally in line with the larger-scale modeling results of Phase 1 after accounting for differences in resolution. The simulations suggest that while increased urban albedo is relatively more effective than increased canopy cover locally, the regional and downwind effects can be relatively more uniform across these two scenarios.

Recommendations

A number of useful follow-up research tasks could be conducted to further the acceptance of heat-island control as a potential ozone air-quality improvement strategy. Recommended future work and issues to address include the following:

- Evaluating the effectiveness of surface modification strategies under various seasonal and multi-episodic conditions.
- Modeling the effects of these strategies in whole domains in Southern and Central California, rather than the limited-area control that was tested for Orange-Riverside.
- Modeling site-specific, market-based changes in albedo and canopy cover on a neighborhood-by-neighborhood basis, rather than using maximum feasible values or idealized scenarios that may represent the best possible outcomes but that are less likely to be achieved.
- Including the variability of biogenic emission rates in very fine-resolution domain simulations and their response to changing meteorology.
- Evaluating the effects of these strategies under conditions of future urbanization that consider likely growth trends and future-year emission inventories (with planned emission caps in place).
- Evaluating the potential benefits of these strategies and related variations under scenarios of climate change for California.
- Developing additional fine-resolution characterization of urban areas in California, such as the San Francisco Bay Area, Los Angeles Basin, and Fresno/Bakersfield.

Benefits to California

This work provides two benefits: (1) a new-generation, improved modeling capability that can be used to evaluate potential impacts of heat-island control strategies in California (as well as other applications that require fine-resolution modeling capabilities), and (2) the actual savings in cooling energy, reductions in emissions, and improved air quality that could be achieved if heat-island control strategies were to be implemented in California's urban areas.

The modeling system that was further developed in this effort is being considered by a number of California air districts for modeling heat island control strategies for State Implementation Plan planning. The improvements in data, methods, and techniques used in these models have increased their ability to more accurately determine the energy and environmental impacts of potential mitigation strategies.

In addition, this work became an integral part of a national effort, led by the U.S. Environmental Protection Agency, to improve community modeling systems and related urban data for researchers and regulators in air emissions, dispersion, and air quality modeling.

Technical Summary

The first phase of this study, completed in 2004, developed models and data for California-specific applications and a framework for modeling and analyzing the potential air-quality impacts of surface modifications, that is, heat island control. Two strategies of interest—increased urban albedo and canopy (tree and shrub) cover—were evaluated at the mesoscale. In the second phase, summarized in this report, these strategies were further evaluated at finer resolutions using a new generation meso-urban meteorological model in conjunction with fine-resolution photochemical simulations. Throughout this report, the term *mesoscale* is used to refer to resolutions ranging from a few kilometers to tens of kilometers in the horizontal and tens to hundreds of meters in the vertical. The term *meso-urban,* as it relates to the urbanized MM5 (uMM5) setup in this study, refers to resolutions of 1 kilometer (km) in the horizontal and a few meters in the vertical.

The California Energy Commission supported this study to explore and evaluate the use of surface modifications to improve ozone air quality in California, *in addition to their energy savings*. As with many other control strategies, the modification of surface properties in urban areas can cause both net decreases and increases in ozone. The task, thus, is to develop strategies that are tailored specifically to regions of interest (region-specific) in that they would have overall beneficial impacts while minimizing negative effects. The best mix of such strategies (to maximize the net ozone reductions) will differ from one region to another and will depend on factors such as local emissions, meteorology, episodic conditions, topography, and flow regimes. Thus ideally, the variability in all forcing mechanisms should be considered and specific modeling studies should be designed to quantify such local potential impacts and, by extension, the results are region-specific and non-transferable to other areas.

From a regulatory perspective, photochemical air-quality modeling is an important tool and a cornerstone component in the planning process to ultimately implement strategies that target ozone attainment status. The Clean Air Act requires that non-attainment areas, especially those designated as *serious* or higher (for ozone), use photochemical grid models to study the potential impacts of proposed control strategies and/or demonstrate attainment, using designated field-intensive periods or historical air-quality episodes, for example, those with high observed ozone concentrations. The modeling episodes selected in both phases of this study were chosen to be compatible with those used by regulatory agencies in California. The photochemical episodes modeled here are August 3 through August 7, 1997, for Southern California (SCOS-97) and July 29 through August 4, 2000, for Central California (CCOS-2000). The meteorological modeling episodes in this study include an additional two days of model spin-up prior to the start of the photochemical episodes.

The Southern California August 1997 episode resulted in the Los Angeles Basin's second highest annual maximum observed ozone concentration of 187 parts per billion (ppb) in the Riverside-Rubidoux area. The episode occurred during typical ozone-conducive conditions, such as the presence of a high-pressure system, stagnation, small pressure gradients across the basin, high air temperatures, large solar radiation input (actinic flux), and capping inversions (inhibited mixing). Wind transport during the episode was moderate, and onshore flow was generally weak as a result of the above conditions. Beginning August 6 of that episode, a coastal eddy developed and continued into August 7. This provided a mechanism for southerly transport of pollutants to the north and northeast of the Basin, as well as into the Santa-Clarita and Antelope Valley regions, where near-peak concentrations were also observed on August 6.

Peak inland temperatures in Southern California during that episode were frequently higher than 38°C, and the highest temperature of 45°C in the Los Angeles Basin was observed in Riverside on August 5. The mesoscale temperature, wind, and pressure gradients were relatively consistent from August 3 through 6, but changed later because of the eddy development on August 7. The peak observed ozone concentrations in the Basin are summarized in Table ES-1 (extracted from the Phase 1 report).

Table ES-1. Observed peak ozone in Southern California

Date in 1997	Observed peak	General location of observed peak
August 4	140 ppb	Central San Bernardino Mountains
August 5	187 ppb	Rubidoux
August 6	170 ppb	Central San Bernardino Mountains
August 7	150 ppb	Central San Bernardino Mountains

The Central California July-August 2000 episode, especially on the primary days considered here (July 31 through August 2), was characterized by strong inversions, as evidenced by a high 500-millibar (mb) geopotential height and high 850-mb temperatures typical of subsidence motion. It was also typical of the conditions conducive to ozone build-up, for example, the Pacific high-pressure system and its extension over California preventing cyclonic systems from passing though the area. The result of such conditions is typically a stagnant air mass that is poorly mixed. In all days of the episode, high ozone was observed in Livermore and transport from the San Francisco Bay Area was strong; to the southeast (San Joaquin Valley) on some days and to the northeast (Sacramento) on others. On July 31, flow through the Bay Area affected regions in Fresno and Bakersfield but had no direct impact on Sacramento. The flow arriving Sacramento on that day passed further north of the Bay Area. On August 1, the flow went through the Bay Area and thus produced the higher ozone in Sacramento. The peak observed ozone concentrations in Central California are summarized in Table ES-2 (which is also taken from the Phase 1 report).

Table ES-2. Observed peak ozone in Central California

Date in 2000	Observed peak	General location of observed peak
July 31	126 ppb	Livermore
August 1	133 ppb	Sacramento
August 2	151 ppb	San Joaquin (Edison)

As discussed in Phase 1 report, the goal of urban-surface modification strategies, such as those proposed here, is to help lower ozone concentrations in California cities directly (by reducing cooling electricity use) and indirectly (by affecting meteorology-dependent emissions and photochemistry). The anticipated effects from surface modifications such as increased albedo and canopy cover arise because of the relatively lower surface temperatures (slower rates of warming) of the modified surfaces. These in turn cause changes in air temperatures, area-emission rates of ozone precursors, cooling electricity use and related emissions from power plants, and rates of photochemical production of ozone. Benefits would accrue through (1) lower air temperatures that would reduce cooling electricity needs (thus reducing power plant emissions), (2) reduced meteorology-dependent emissions from anthropogenic sources (such as mobile sources, off-road vehicles, evaporative and diurnal losses, and refueling operations) and biogenic sources (such as vegetation and soil), and (3) reduced rates of tropospheric and ground-level ozone formation and/or accumulation.

On the other hand, the adverse impacts of these strategies (that is, potential ozone increases) can arise from a combination of conditions that allows this pollutant to accumulate. Chemistry aside, these include reduced dilution and mixing caused by slower winds and decreased planetary boundary-layer (PBL) heights. However, shallower polluted boundary layers in urban areas that are nitrogen oxide (NO_X)-rich can sometimes have the opposite effect (and as the NO_X/volatile organic compound [VOC] ratio changes in space and time). The atmospheric photochemical system producing ozone is nonlinear, which further complicates those conditions conducive to ozone formation and accumulation. Thus, the proposed surface modification strategies can result in increased ozone depending on local conditions. For each region, the relative levels of benefits and adverse effects also change based on the level of surface modifications. For example, in coastal regions and/or areas with flow obstruction (basins, mountain ranges), there seems to be a region-specific threshold or range for such modifications beyond which any further increases in surface modifications tend to produce smaller net benefits and possibly adverse effects as well. Because of such issues and the existence of competing non-linear effects, region-by-region and multi-episodic assessments and modeling may be needed to identify such regional thresholds and the optimal mix of surface modification strategies for each region.

Phase 2 of this study builds upon Phase 1 by further improving the resolution of the simulations in computational domains of interest, such as the urban canopy layer (UCL). This goal is achieved by introducing and further developing a new-generation fine-resolution meteorological (meso-urban) models and using them to drive fine-resolution photochemical simulations. While resolutions can be set as fine as needed, in this application the horizontal resolutions were 1 kilometer (km) and in the vertical they were on the order of 3 meters (m) near the ground. Figure ES-1 depicts the horizontal modeling domains; those shown with a black background are the mesoscale domains of Phase 1, whereas the small green rectangles delineate the additional fine-resolution meso-urban modeling grids introduced in Phase 2. In this report, only Sacramento and a portion of the Los Angeles (Orange-Riverside counties) grids are discussed and analyzed. Figure ES-2 shows a schematic representation of the fine-resolution vertical structure of the model within the UCL and compares it to the vertical structure used in typical mesoscale modeling.

The purpose of developing and using fine-resolution meso-urban and photochemical models is to evaluate in more detail the relevant dynamics, thermodynamics, physics, and photochemistry within the urban canopy layer. This layer is of interest, obviously, because this is where the bulk of the population is found, where most emissions are initially injected, and where initial chemical reactions producing smog occur. Thus, in theory at least, improving the modeling of the urban atmospheric environment within the canopy layer is critical to better assess environmental and air pollution/health impacts, as well as for more accurate regulatory air-quality planning.

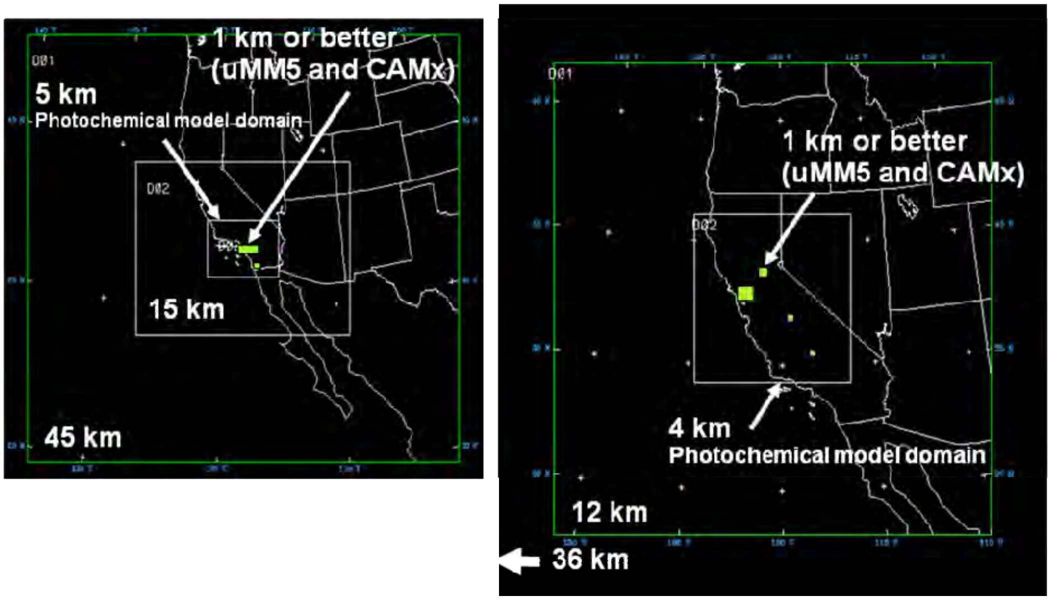

Figure ES-1. Modeling domains for phases 1 and 2 of the study (for Southern California, left, and Central California, right). Black background shows mesoscale meteorological modeling domains. The "mesoscale" photochemical modeling grids of Phase 1 (as also used by regulatory agencies) is shown as 5 km and 4 km grids, respectively. Green rectangles show meso-urban (uMM5) and fine-resolution Comprehensive Air Quality Model with Extensions (CAMx) modeling grids added in Phase 2.

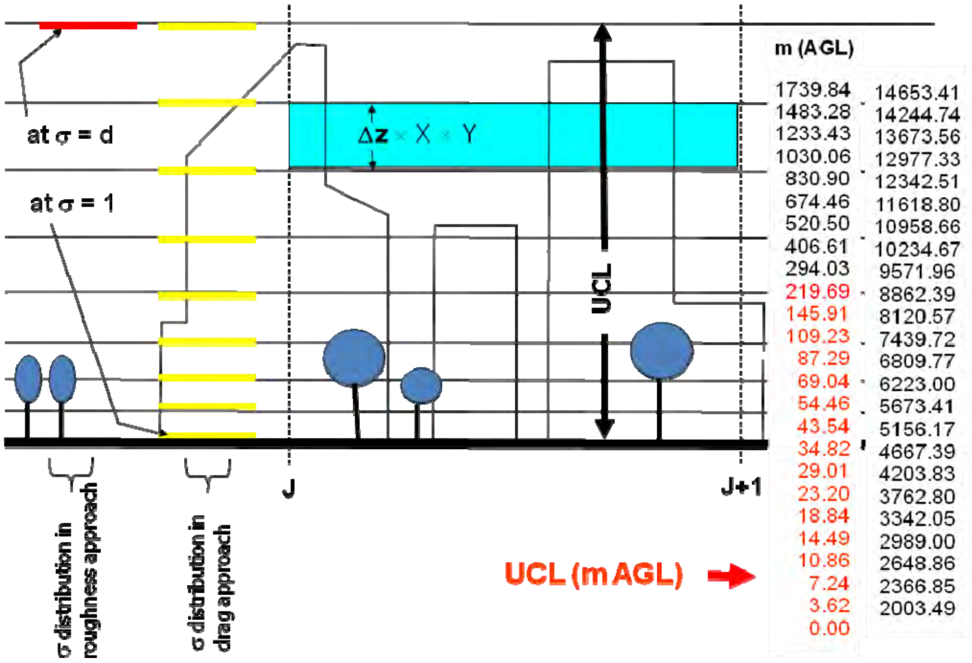

Figure ES-2. Schematic representation of fine-resolution meso-urban and mesoscale model vertical structures. The red line represents a typical first atmospheric level in roughness-based mesoscale models (for example, at displacement height, d), whereas the yellow lines, starting at the actual surface, indicate several additional vertical layers in the uMM5 for the same interval. The numbers at right show the heights (m, above ground level [AGL]) used in this modeling study, with the red entries being within the canopy layer.

Thus, the main goal of Phase 2 is two-fold: (1) to update and improve a meso-urban fine-resolution meteorological model (uMM5) for providing the driving meteorological fields to a fine-resolution photochemical model, and (2) to develop the corresponding region-specific fine-resolution input data and model parameters input that such new-generation models require. A related objective is to apply the new model, parameterization, and data to one region in California to demonstrate the model's effectiveness and its diagnosis of the potential impacts of surface modifications (urban heat island [UHI] control) on meteorology and air quality. In this report, the Sacramento area was selected for model application and discussion of results. In addition, a portion of the Los Angeles area, in Orange-Riverside counties was also evaluated. The uMM5 was initially based on the DA-SM2-U model (Dupont et al. 2004; Otte et al. 2004).

Both objectives were successfully met in Phase 2. A meso-urban model is now configured and available for use in California air-quality studies and a detailed morphological database for Sacramento (as a first prototype) is available as well. Some of the model and data improvements tackled in this study include (1) the generation of fine-resolution three-dimensional (3-D) morphology that is specific to Sacramento and Orange-Riverside (O-R) counties , (2) development of new techniques to derive and ingest morphology into the uMM5, (3) improved computational aspects for drag and roughness in the model, (4) development of a mapping technique for generating morphology in areas where no 3-D/geometrical information exists, (5) modifications of drag coefficients of buildings and vegetation, and (6) initiation of a nested (two-way feedback) version of the currently stand-alone uMM5. The fine-resolution, meso-urban meteorological fields were used in driving fine-resolution photochemical simulations (using fine-resolution grids in the CAMx photochemical model). This application is the first time that these types of models have been applied to studying the effects of *surface perturbations* on meteorology and air quality in California.

The development and use of fine-resolution meso-urban meteorological and corresponding fine-resolution photochemical models is critical because, in theory at least, such fine-resolution modeling capabilities and data are useful not only in enabling fine-resolution photochemical air-quality modeling but also in developing fine-resolution, four-dimensional emission inventories that should ultimately improve the process of air-quality modeling and demonstration for a variety of strategies. Such modeling capabilities are also useful for actual planning and implementation since they allow for detailed evaluation of meteorological and air-quality impacts at a neighborhood scale or on a block-by-block basis, if needed.

In addition to all meteorological, emissions, and surface initial and boundary conditions that are typically needed in mesoscale meteorological and air photochemical modeling, meso-urban models, such as the uMM5 used here, require an additional set of specific input parameters, such as detailed 3-D morphology. Those required by the uMM5 are listed in Table ES-3. These two- and three-dimensional arrays of parameters were developed in this study for the two domains discussed above using a combination of sources and an alternate, low-cost method (Figure ES-3) instead of the more typical sources of data, such as LIDAR, that are very expensive. The alternate methods rely in part on using remote-sensed morphology data, such as from Google's Earth Pro facility. Thus, a number of parameters were developed at 1 m (Δz) vertical intervals (height) and for several wind approach directions (such as N, NNE, NE, ENE, E) through the top of the canopy layer, that is, about 140–160 m above ground level (AGL) in the Sacramento and O-R domains. Once these parameters were developed (gridded over a domain of interest), an attempt was made to correlate them to region-specific Land Use and Land Cover (LULC) classification schemes. The mapping was then used as an extrapolation template to generate morphology and related data in urban areas where no three-dimensional morphological information exists. In Phase 2, Sacramento- and O-R-specific LULC were identified and used for mapping correlation and extrapolation.

Table ES-3. Fine-resolution 2- and 3-dimensional morphological parameters needed by the uMM5

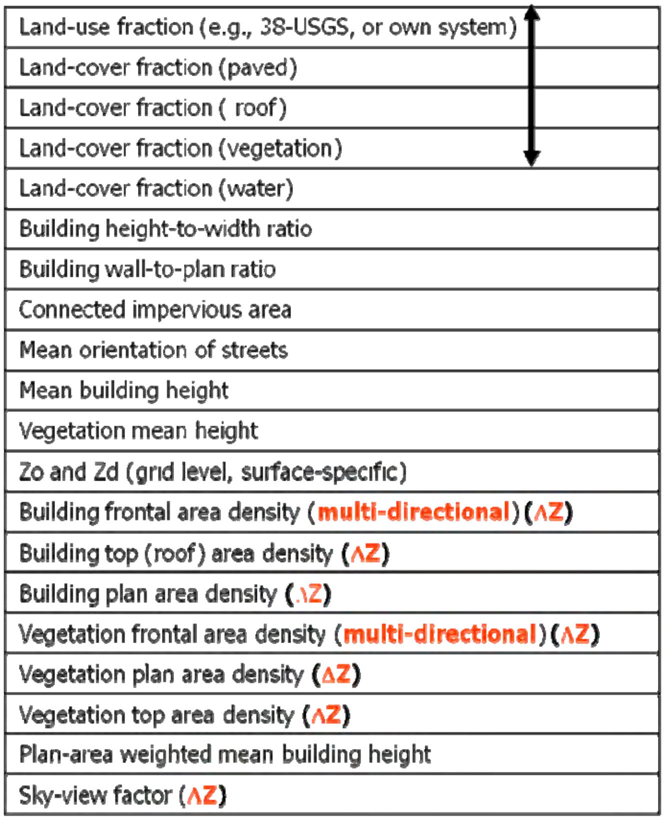

Land-use fraction (e.g., 38-USGS, or own system)
Land-cover fraction (paved)
Land-cover fraction (roof)
Land-cover fraction (vegetation)
Land-cover fraction (water)
Building height-to-width ratio
Building wall-to-plan ratio
Connected impervious area
Mean orientation of streets
Mean building height
Vegetation mean height
Zo and Zd (grid level, surface-specific)
Building frontal area density (**multi-directional**) (**ΔZ**)
Building top (roof) area density (**ΔZ**)
Building plan area density (**ΔZ**)
Vegetation frontal area density (**multi-directional**) (**ΔZ**)
Vegetation plan area density (**ΔZ**)
Vegetation top area density (**ΔZ**)
Plan-area weighted mean building height
Sky-view factor (**ΔZ**)

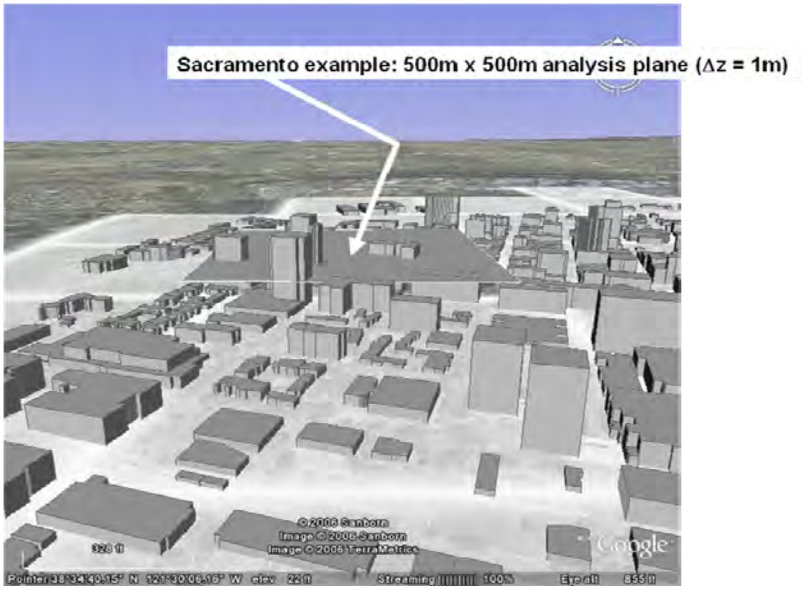

Sacramento example: 500m x 500m analysis plane (Δz = 1m)

Figure ES-3. An analysis plane used to compute the parameters from Table ES-3 at each 1-m vertical interval

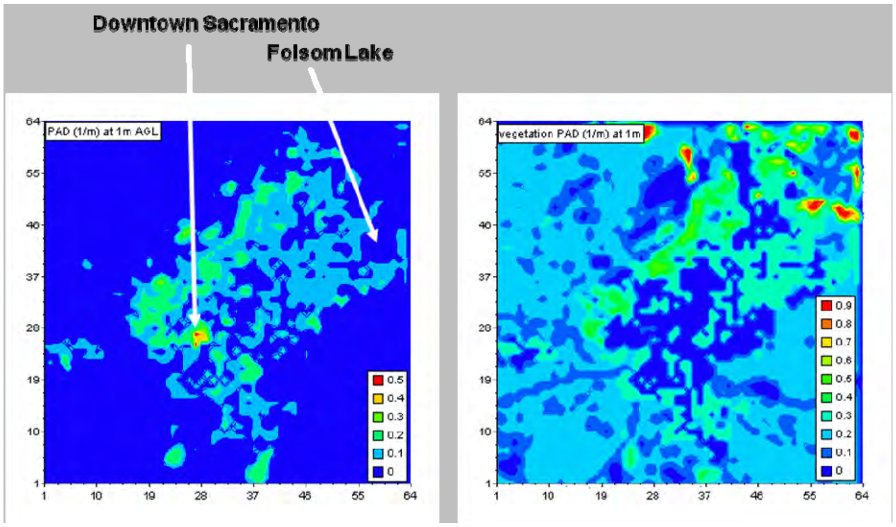

Figure ES-4. Plan area density (PAD) function (m2m-3) for the Sacramento uMM5 domain. The example shows cross sections at 1 m AGL for buildings (left) and vegetation canopy (right).

Figure ES-4 shows an example of a domain-wide morphological characterization of Sacramento resulting from the techniques developed in this study and in conjunction with land-use and land-cover information. The new definition of the urban areas (boundaries seen in Figure ES-4) is more up-to-date than a definition based on other, older, and less-resolved data sources and shows Sacramento's recent growth.

Following the stages of model set-up and configuration, and development of all needed input parameters, a base-case meteorological and photochemical scenario was developed for each domain. A brief performance evaluation exercise was also carried out (a detailed performance evaluation was conducted in Phase 1). This was then followed by the simulation of two perturbation scenarios per domain. One scenario assumes high-albedo increases and the other involves increased canopy cover. Below, modeling results for Sacramento are discussed first, followed by those for the O-R domain. The meteorology discussion focuses on temperature, whereas the photochemistry discussion focuses on the ozone concentrations field.

Sacramento

The meso-urban simulations of the base-case scenario in the Sacramento region (Sacramento uMM5 domain) produce a generally repetitive diurnal profile whereby a UHI starts small (~1°C) at 1500 local sidereal time (LST), grows to about 2°C–4°C by 1800 LST, peaks around 2100 LST (at up to 6°C), then begins to decrease so that it is at 2°C–3°C (up to 5°C) by 0000 LST, and continues to get smaller until, between 0900 and 1200 LST of the next day, there is no UHI during early morning hours and then the urban area becomes 1°C–2°C cooler than the surrounds by mid-morning to mid-day. Finally at around 1500 LST of the next day, the UHI appears again (1°C), and the cycle is repeated through the episode. The temperature field and magnitudes of the UHI are different from day to day, but the aforementioned profile is relatively typical. The meso-urban model is able to capture fine-resolution meteorological phenomena of interest that were not reproducible with mesoscale simulations in Phase 1. For example, and as seen in Figure ES-5, the model captures a well-defined 5°C UHI at 0000 LST August 1 and a cool island at 1200 LST (up to 2°C cooler than surrounds) on August 2, the latter due to shadowing, thermal mass, and canyon effects in the urban areas. For a visual reference of the aerial extent of these heat and cool islands, compare the temperature fields in Figure ES-5 with urbanization extent shown in Figure ES-4.

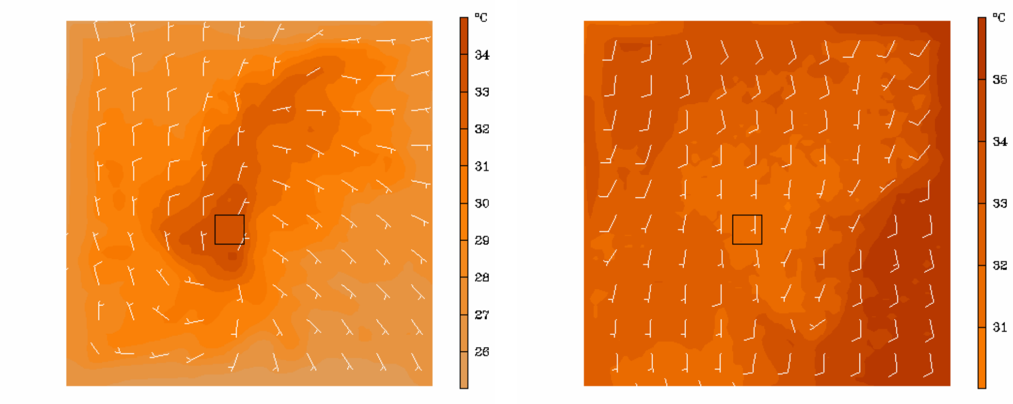

Figure ES-5. Left: uMM5-simulated urban heat island of 5ºC at 0000 LST August 1. Right: A uMM5-simulated cool island of 2ºC at 1200 LST August 2 in the Sacramento area. The inscribed square shows the relative location of Downtown Sacramento.

The simulations also capture the fine-resolution divergence/convergence features of the flow that were also not detectable in Phase 1 mesoscale modeling, as well as the slower wind over urban areas (due to drag and roughness). For example, the urban-area winds can be slower by 2–3 meters per second (ms^{-1}) compared to upwind or surrounding areas during the early morning hours.

The uMM5 model's ability to simulate the fine-resolution vertical profiles of meteorological fields (for example, in the UCL) is improved over that of the mesoscale model. Figure ES-6 shows an example of simulated turbulent kinetic energy (TKE) budget terms at 1400 LST August 1 in an arbitrary location in Sacramento (this location is a residential-commercial area with a canopy-layer top at 18 m AGL). In the figure, production terms are positive, and dissipation terms are negative, and the hour at 1400 LST was chosen because it generally represents the warmer part of the day (and unstable conditions). The vertical profiles of shear and buoyancy production of TKE, as well as other terms, follow the vertical changes in obstacles' shapes. For example, in this case, the profiles of building frontal area density (FAD) and that shear production of TKE generally peaks at or slightly higher than the elevation where an abrupt decrease in FAD exists (critical FAD level), which generally represents the top of most buildings in the grid cell being examined. Similarly, buoyant production of TKE also generally follows the vertical FAD profiles of buildings and vegetation and increases from the surface up to the critical FAD level and then remains roughly constant throughout the rest of the UCL. The accelerated cascade dissipation term of TKE also is largest at and slightly above the critical FAD level. But while buoyancy is sustained above the critical FAD level, the accelerated cascade term decreases with height as FAD decreases.

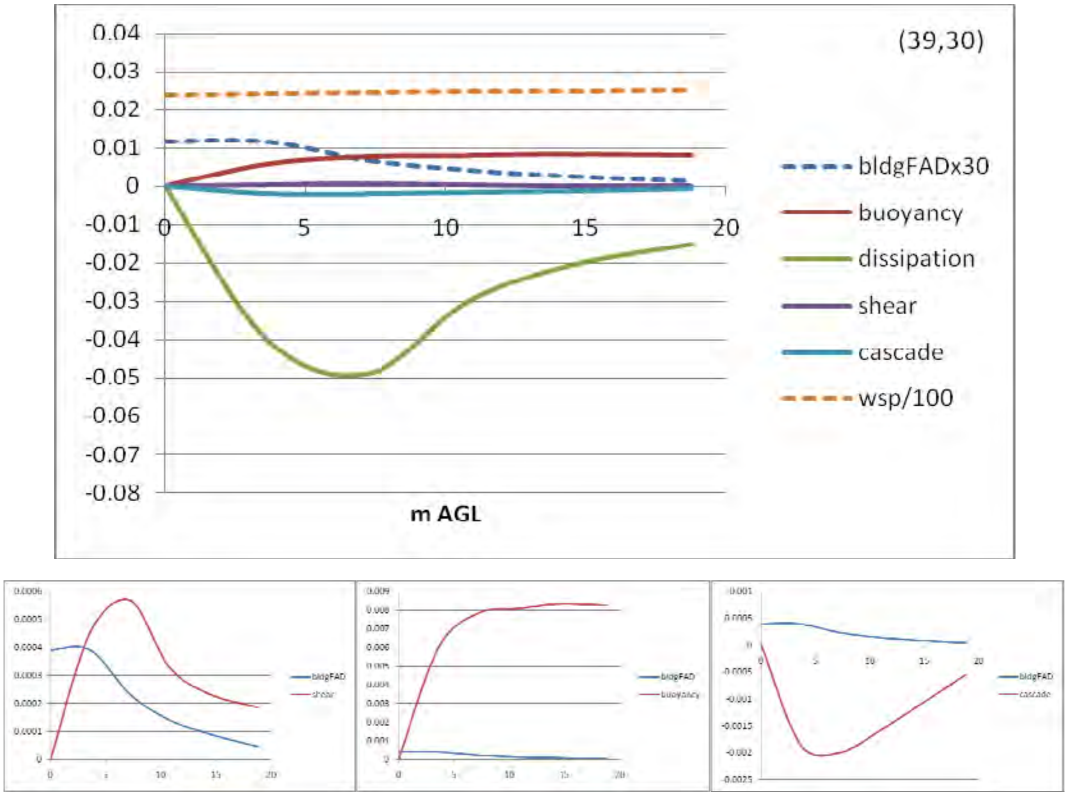

Shear Buoyancy Cascade

Figure ES-6. TKE budget components for location 39,30 in Sacramento modeling domain at 1400 LST.

The simulated vertical profiles of temperature within the UCL (not shown) capture the effects of land-cover variations within the domain. For example, the simulations show that an area with vegetation canopy cover can be up to 2°C cooler than other, less vegetated areas. The simulated heat fluxes in the UCL indicate Bowen ratios $\beta > 20$, $\beta \sim 3.5$, and $\beta \sim 1.3$, respectively, for high-rise, residential, and forested areas in Sacramento. These ratios are generally consistent with observed and documented values in such land covers (for example, Oke 1978).

The base-case simulations of the Sacramento 1-km photochemical modeling domain (which roughly corresponds to the uMM5 grid) show the peak concentrations consistently downwind of the downtown area, which is expected as a result of transport and chemistry time scales. The high ozone is displaced to the southeast of the domain on July 31, to the east on August 1, and to the northeast on August 2 (Figure ES-7 shows the latter). The 1-km domain's peaks are respectively 96, 117, and 101 ppb on those three days and are relatively more accurate (closer to observations in this domain) than those obtained from the coarse simulations of Phase 1. A brief model performance evaluation exercise shows that both paired and unpaired accuracies of the peak meet the U.S. Environmental Protection Agency (U.S. EPA) recommended performance benchmarks. However while the model captures reasonably well the downwind elevated concentrations, its performance is relatively poorer in capturing the observed concentrations near and downwind of the downtown area (mid-domain region) where it underestimates the local peaks. Figure ES-7 shows, as an example, the simulated ozone concentrations field at 1400 LST on August 2, when the simulated peak was 101 ppb, and as time series at three monitors of interest in the eastern portion of the domain for July 31 through August 2.

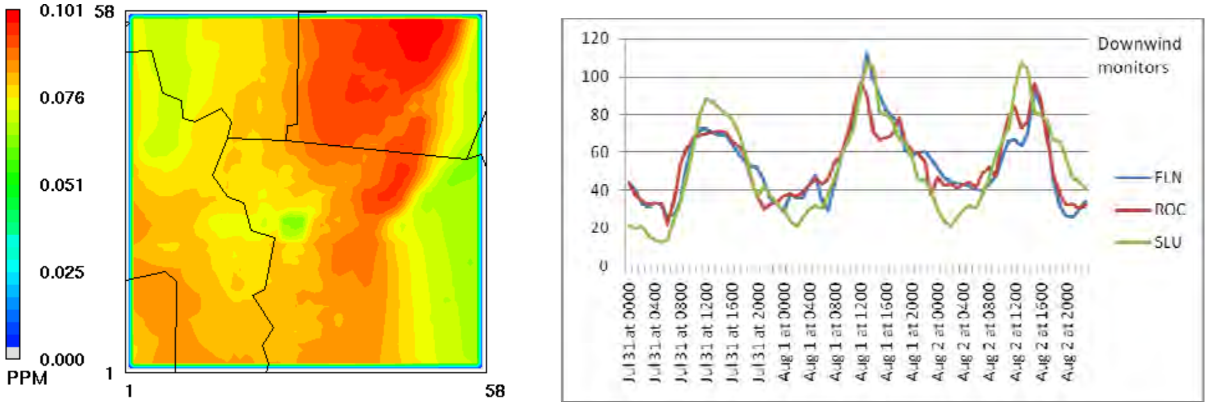

Figure ES-7. Left: Simulated ozone concentration field (ppm) at 1400 on August 2 in the Sacramento 1-km domain. Right: Simulated ozone (ppb) at three monitors in the domain for three days of interest (July 31 through August 2). Monitor locations: Folsom/Natoma (FLN), Rocklin (ROC), and Sloughhouse (SLU).

For the perturbation scenarios, model results show that during nighttime hours increased surface albedo and canopy cover have no effects, but that during the day, they have a significant impact on air temperature. In addition, they show that the “cooler” air can be advected downwind and thus can also affect areas beyond the modified urban regions (for example, where surface albedo or canopy cover was increased). In the Sacramento uMM5 domain, air temperature can be reduced (in the increased-albedo scenario) by up to 2.5°C at 1100 LST July 31, 2°C at 1200 LST August 1, and 3°C at 1300 LST August 2. The associated reductions in surface temperature are up to 7°C at 1100 LST July 31, 10°C at 1200 LST August 1, and 7°C at 1300 LST August 2. The increase in canopy cover has generally a similar effect on air and surface temperatures as increased albedo but with lower magnitudes. In this scenario, the largest reductions in air temperature reach up to 1.5°C, 1.5°C, and 2.5°C respectively at 1100 LST July 31, 1300 LST August 1, and 1300 LST August 2. The associated (time-coincident) reductions in surface temperature are 4°C at 1100 LST July 31, 5.5°C at 1300 LST August 1, and 4°C at 1300 LST August 2.

In terms of air quality impacts, the simulations indicate that during the episode days of interest, concentrations can be decreased by up to 16–26 ppb in the high-albedo scenario and by up to

15–19 ppb in the increased-canopy scenario. These occur in relatively small areas in the domain, typically 1–2 square kilometers (km^2) or slightly larger. Some more extreme changes (30s of ppb) are also seen in one or two instances. Such large reductions are captured by the model because of the fine resolution simulation capabilities relative to coarser and more convectional simulations, for example, those in Phase 1, where the perturbations were averaged over larger areas. Therefore, fine-resolution simulations are a useful tool in "zooming into" the coarse-grid simulated fields to detect and capture the fine-resolution details that are important for analysis and planning (such as urban planning and State Implementation Plan (SIP) credit modeling). Bearing in mind the difference in resolution, the results from the Phase 2 simulations generally agree with the coarse-model results from Phase 1.

The more interesting aspect of air-quality changes is the impact that UHI control has on lowering the pollution concentrations over the larger areas in the domain. Decreases of 5–14 ppb in the high-albedo scenario and 5–10 ppb in the increased canopy scenario are more representative of the sub-regional impacts of these strategies in Sacramento. On one day of the episode, some negative impacts also occurred upwind (to the west) of the areas experiencing decreased concentrations. The increases can reach up to 11 ppb in the high-albedo scenario and up to 5 ppb in the increased-canopy scenario. However, the area affected by increased concentrations is much smaller than that affected by decreased concentrations, and the increases are short-lived.

In general, the modeling suggests that the effects of changes in canopy cover (as assumed in this modeling approach) are similar to or smaller than those of increased urban albedo. At the times and locations of the simulated daily ozone peaks, albedo increase is 20 percent to 100 percent more effective than increased canopy cover in terms of impacts on the peak concentrations when paired in space and time. However, if only pairing in space is considered, that is, at the peak's location but regardless of the *time*, then both strategies can have a similar effectiveness. The simulations also suggest that while these strategies can have different local impacts (mid domain and in urbanized areas), their effects become more similar downwind of urban Sacramento in some cases.

Figure ES-8 shows an example of the relative impacts of increased albedo and canopy cover on ozone concentrations at a selected downwind location, in this case, where the simulated peak concentration on August 1 occurred. While the high-albedo scenario can decrease the local peak by up to 22 ppb, the increase in canopy cover decreases it by up to 15 ppb.

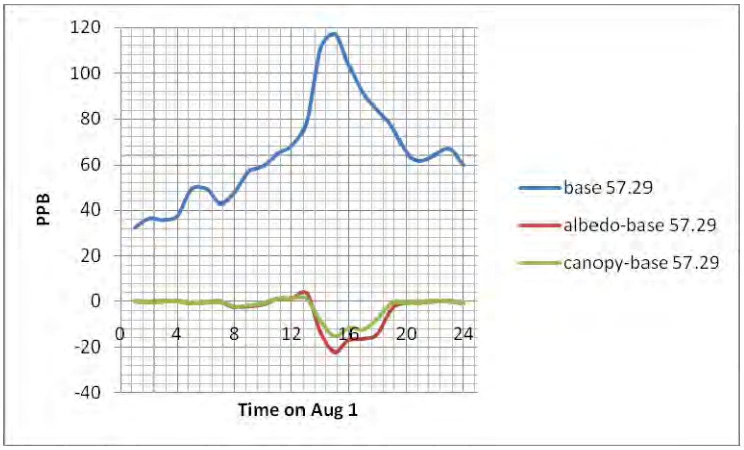

Figure ES-8. August 1, simulated peak = 117 ppb at location 57,29 (bottom of figure: changes in ozone concentration from UHI control; blue=base, red=albedo increase, green=canopy cover increase).

Analysis of the 8-hour average ozone shows that except for one instance at the Rocklin monitor location, the UHI control in all locations and days resulted in a decrease in the daily maximum 8-hour average. The relative reduction factor (RRF) analysis shows that the daily maximum 8-hour average can be decreased by anywhere between 4 percent and 14 percent across the episode days, with the largest impacts seen on July 31 and August 1. While the effects of increased albedo are generally larger than those of increased canopy cover, the difference is not particularly big and, in some cases, increased canopy cover is more effective. The latter situation is noticeable closer to the downtown area. Figure ES-9 exemplifies this discussion for a monitor location at Folsom/Natoma (FLN), in the eastern part of the domain.

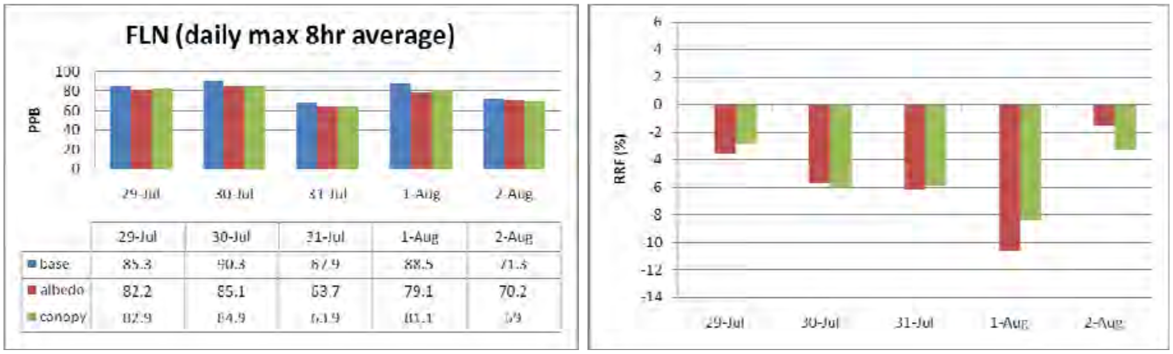

	29-Jul	30-Jul	31-Jul	1-Aug	2-Aug
🟦 base	85.3	90.3	67.9	88.5	71.3
🟥 albedo	82.2	85.1	63.7	79.1	70.2
🟩 canopy	82.9	84.9	63.9	81.1	69

Figure ES-9. Left: Simulated daily maximum 8-hour average ozone at Folsom/Natoma (FLN) monitor location. Right: Reduction (%) in daily maximum as RRF.

Orange-Riverside

The base-case simulations of the O-R domain capture the relatively uniform temperature field across the domain during nighttime and early morning hours, with a weak gradient between the coastal area (west) and the inland area (east). During the late morning, inland areas (eastern half of the domain) warm up faster than the western half. The coastal areas can be 6°C cooler (or more) than the far inland areas beyond the Santa Ana Mountains. Some urban areas are warmer than others, for example the Garden Grove/Orange and Irvine areas can be about 6°C warmer than at the coastal town of Newport Beach. However, it is not clear how much of this is a result of heat island versus simply inland heating of the cool sea breeze during that part of the day. It is likely that a larger part is caused by the latter effect. However, these urban areas do develop distinguishable UHI of 2°C–3°C in the afternoon and evening hours. At about 2100 LST, a UHI of 1°C–2°C persists in the western basin—that is, in the Orange-Irvine area.

The model's ability to simulate the fine-resolution vertical profiles of meteorological fields of interest (such as TKE components, temperature, and heat fluxes) was also evaluated at several locations in O-R, as was done for the Sacramento simulations. That discussion will not be repeated here. While the magnitudes are different from one location to another, the profiles exhibit a relatively similar behavior. The temperature profiles also reflect the effects of land-cover differences in the region (such as varying vegetation fractions) and the corresponding heat flux profiles show negative sensible and positive latent heat fluxes near the surface (both contributing to cooling) in vegetated areas but postive through the UCL in the less-vegetated regions. The land cover differences contributs to some vegetated areas in O-R being up to 4°C cooler than less-vegetated regions.

The base-case photochemical simulations show that the peak concentrations are downwind of the coastal area, in the mountain range and eastern basin as expected, but that some higher concentrations on August 5 also enter the domain from the northwest—that is, from the land portion of the coarse grid covering the Los Angeles area. The simulations produce a peak of 113 ppb on August 5 and 97 ppb on August 6 (see Figure ES-10 showing the simulated temperature and wind fields, as well as the ozone peak). The domain-wide high concentrations are found at mid- and eastern domain, across the Orange-Riverside border and just east of the Santa Ana Mountains (SAM). High concentrations in coastal areas of the domain range from 50 to 80 ppb on both days of interest (up to 82 ppb on August 5 and 85 ppb on August 6).

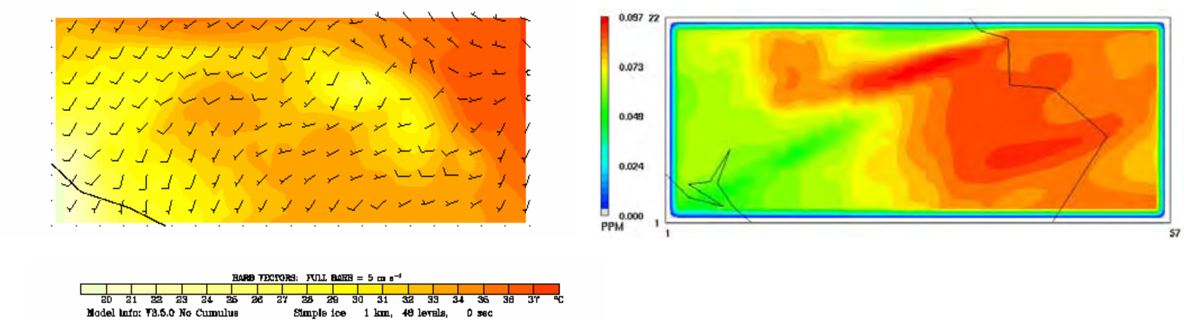

Figure ES-10. Simulated air temperature and wind fields (left) and ozone concentrations (right) at 1200 LST August 6 (time of simulated peak ozone in O-R on that day)

Scenarios of surface perturbations, similar to those discussed above for Sacramento, were also evaluated in the O-R domain. As with the Sacramento results, the O-R simulations show that during nighttime hours surface modifications have minimal or no effect on air temperature. After sunrise, the temperature difference (cooling effect) appears. The largest air-temperature reductions in the increased-albedo scenario can reach up to 2.5°C–3°C at 1500 LST August 5 and 2°C–2.5°C at 1100 LST August 6. In terms of time-coincident surface temperature changes, the high-albedo scenario can cause reductions of up to 5°C 1500 LST on August 5 and 6°C at 1100 LST August 6.

The increase in canopy cover has the same general impact on air and surface temperatures but at relatively lower magnitudes than the high-albedo scenario. The largest reductions in air temperature reach up to 3°C and 1.5°C, respectively, at 1500 LST August 5 and 1400 LST August 6. The corresponding (time-coincident) reductions in surface temperature are 4°C at 1500 LST August 5 and 4.5°C at 1400 LST August 6. Figure ES-11 shows, for example, the change in surface temperature in the O-R domain (right side of figure) as a result of increased surface albedo in the urbanized areas, that is, proportional to building FAD shown in the left side of the figure.

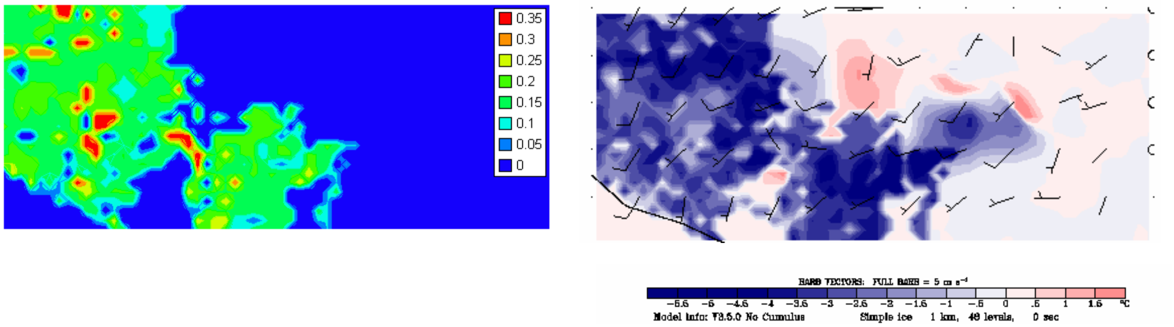

Figure ES-11. Left: Building FAD function (m2m-3) at 1 m AGL for the O-R domain. Right: Surface temperature decrease, as an example, at 1100 LST August 6.

The air-quality (ozone concentrations) response to UHI control in O-R was then evaluated in a similar fashion. Unlike in Sacramento, the signal in O-R is relatively noisy, and there appears to be both increases and decreases in concentrations that can be on the same order of magnitude, although at different locations and times. The simulations suggest that the larger decreases in daytime concentrations tend to occur in the western basin (urbanized areas of Orange, Tustin, Irvine, Newport Beach, Mission Viejo, and other cities) and that the larger increases tend to occur in the eastern basin, beyond the Santa Ana Mountain range, in non-urbanized areas. The dominant effect in the urban area is a decrease in ozone, whereas the dominant effect in the eastern non-urban domain is an increase in ozone. Thus, limited-area UHI control, such as in this hypothetical situation and peculiar O-R domain, can produce *local* improvements in air quality but cause negative impacts further downwind or in a different air basin. This is a result of changes in mixing, boundary-layer height, wind speed (flushing of pollutants), and their interaction with the basin's topography—in this case, the blocking effect of the eastern mountain range. In UHI control scenarios, the weakened westerly wind component of the sea breeze contributes to increased downwind concentrations and peaks. Therefore, this modeling situation can shed some light on one version of the "threshold" effect, or levels at which control begins to have negative effects, as identified in Phase 1. This also suggests that for UHI control to be effective, a larger area (not only a small portion of the basin) should be modified.

The *local* changes in concentrations (that is, in the modified urban areas of the western basin) follow the more typical patterns seen in simulating UHI control in other regions, including Sacramento. That is, the decreases in ozone tend to occur mostly during the daytime, whereas some increases in concentrations can occur earlier in the evening or early morning hours. In the Irvine area of the O-R domain, for example, the largest concentration decreases are between 6 and 10 ppb during daytime and the largest increases between 4 and 7 ppb, occurring in the evening. In the Tustin area, the largest daytime decreases range from 3 to 6 ppb, whereas the largest increases reach up to 4 ppb at night.

In terms of the maximum 8-hour average ozone, the O-R simulations suggest that the dominant effect is a decrease in concentrations. The 8-hour RRF analysis, as seen in Figure ES-12, shows that the daily maximum 8-hour average can be decreased by between 3 percent and 10 percent across the episode days in Irvine and up to 3 percent in the Tustin area. The largest impacts are seen during the main days of the episode (August 5 and 6) at both locations.

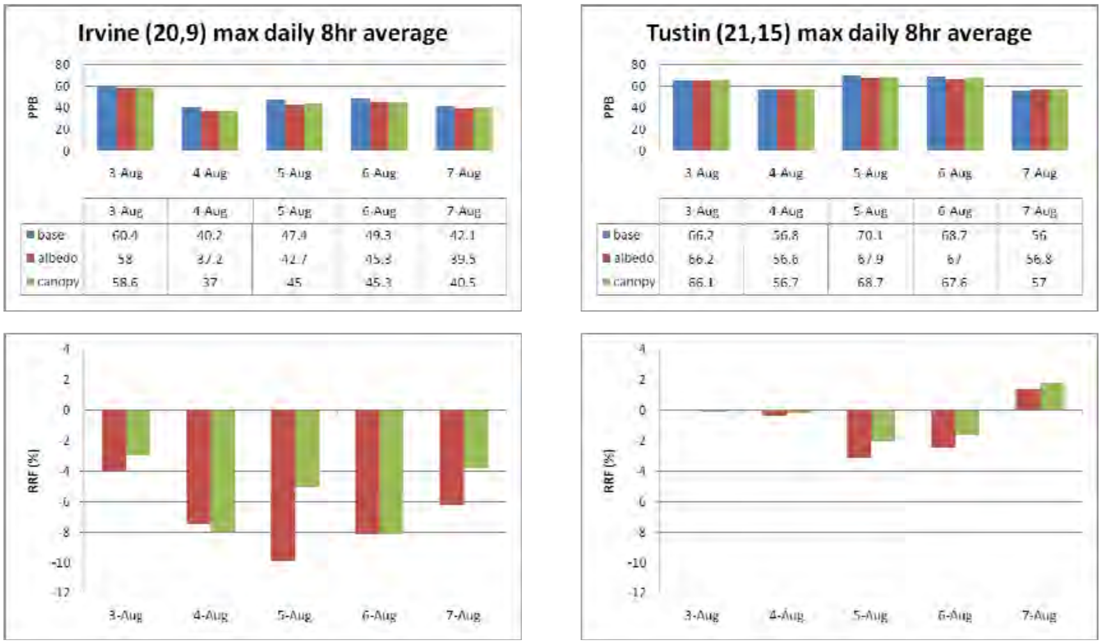

Figure ES-12. Daily maximum 8-hour average ozone (simulated) and potential RRF as a result of increasing surface albedo (red) and canopy cover (green) at two locations in the O-R modeling domain.

1.0 Introduction and Background

1.1. Phase 1 Summary

The general overarching objective of this modeling study was to evaluate the potential meteorological and ozone air-quality impacts of surface modifications in California. Such strategies, also known as “urban heat island control,” include a range of technologies, but this study focused on two of them: (1) increased urban surface albedo, and (2) urban reforestation (also known as increased canopy cover). While any region will benefit from implementing such strategies, this and earlier modeling studies suggest that the larger metropolitan areas will achieve the most benefits and largest impacts. This is likely because larger areas have more potential for surface modification. Thus, the modeling in Phase 1 focused on four large areas: (1) the Sacramento valley, (2) the San Francisco Bay Area, (3) North and South San Joaquin (Fresno and Bakersfield), and (4) Southern California (the Los Angeles Basin and San Diego).

Phase 1 of the study consisted of mesoscale meteorological, emissions, and photochemical modeling, with a focus on the four regions identified above. The finest grid resolutions in that first phase were 4–5 kilometers (km) in the horizontal and 20–50 meters (m) in the vertical, within the canopy layer. A number of model modifications (Taha 2005) were implemented to improve the model’s applicability to and accuracy in urban heat island (UHI)-control modeling. However, no explicit urban canopy parameterizations (UCP) were used beyond fine-resolution characterization of the urban areas and related scenarios of surface modifications.

In general, the baseline meteorological and photochemical simulations in Phase 1 reproduced the observed fields (for example, temperature, winds, and ozone concentration fields) reasonably well. Their spatial distributions (such as locations of peak temperatures and regional ozone highs) were also reasonably well reproduced. The mesoscale simulations captured the observed peak temperatures in several regions of the domains and indicated that urban areas can be about 3°C (up to 6°C) warmer than their immediate surrounds during the daytime. The simulated wind flow patterns were also reasonably comparable to the observations, both in the southern and central domains.

In Southern California, the simulations replicate the influence of a high-pressure system on August 5 and the development of a coastal eddy on the August 6 that caused southerly transport into Ventura County and Santa Clarita/Antelope Valley (which in turn displaced the location of that day’s peak) as qualitatively seen in Figure 1.1 (compare the top left and right figures for flow conditions offshore and south of Los Angeles). In Central California, the simulations captured the coupling (transport) and disconnection between the San Francisco Bay Area and Sacramento Valley on certain days (Figure 1.2).

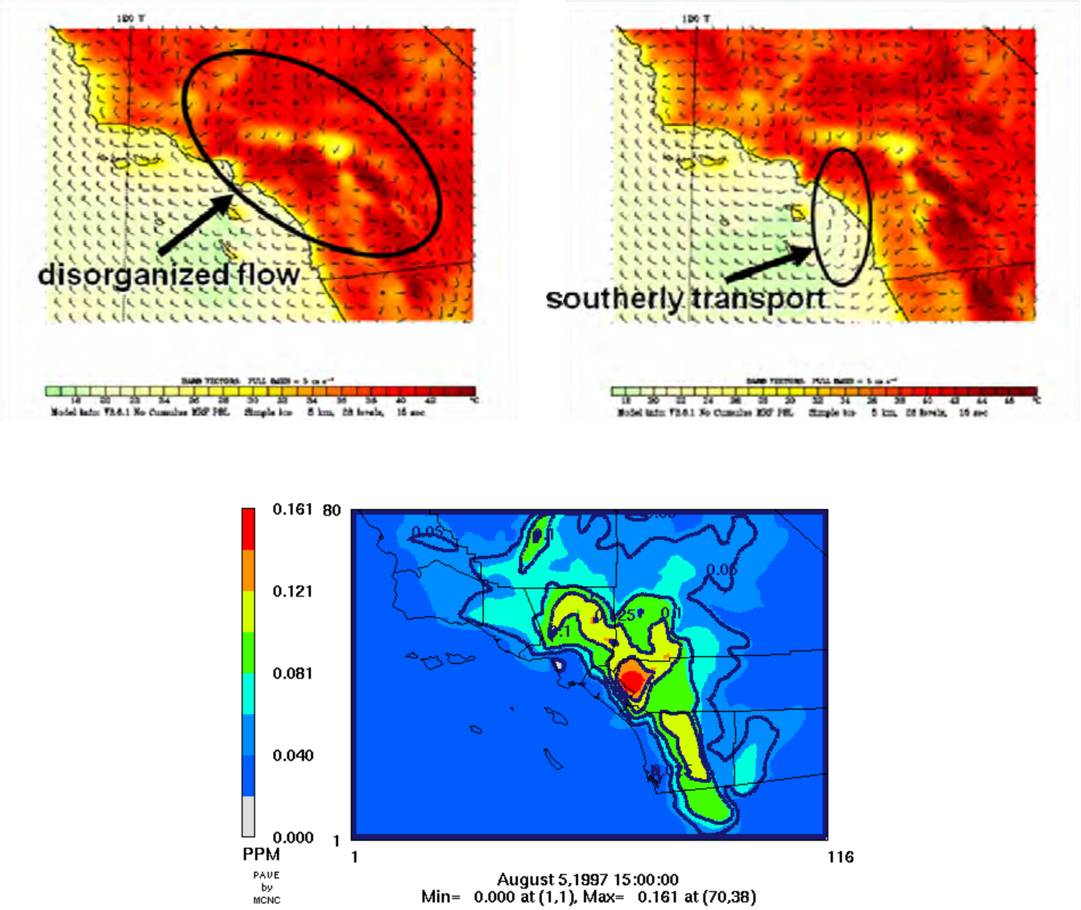

Figure 1.1. Top: Simulated temperature and wind fields at 1400 LST on August 5 (top left) and August 6 (top right) 1997, at σ = 0.999, for Southern California. Bottom: Simulated peak ozone on August 5.

During the early stages of Phase 1, a number of base-case scenarios was developed for each of the Central and Southern California domains, and extensive model performance evaluation was performed, both for meteorological and photochemical simulations. The statistical analysis showed that the photochemical model performance was comparable to that in simulations performed for and reported by regulatory agencies in California. Generally, model performance in this study is uneven, that is, not uniform across sub-domains or episode days, but it is better than in regulatory modeling—for example, in zones 3 and 4 in Central California (at left in Figure 1.3) and Zone 4 in Southern California (Figure 1.3, right). Zone 4 is of interest because it is a downwind location where the peak ozone concentrations were observed. In addition, the episodic model performance for Central California is generally better than for Southern California. And, while model performance in this study may be reasonable enough for the purpose of evaluating the potential meteorological and air-quality impacts of heat island control, it may require further refinements in future modeling efforts before results can be used in developing regulatory guidelines or policy recommendations that are implementation-specific for each region.

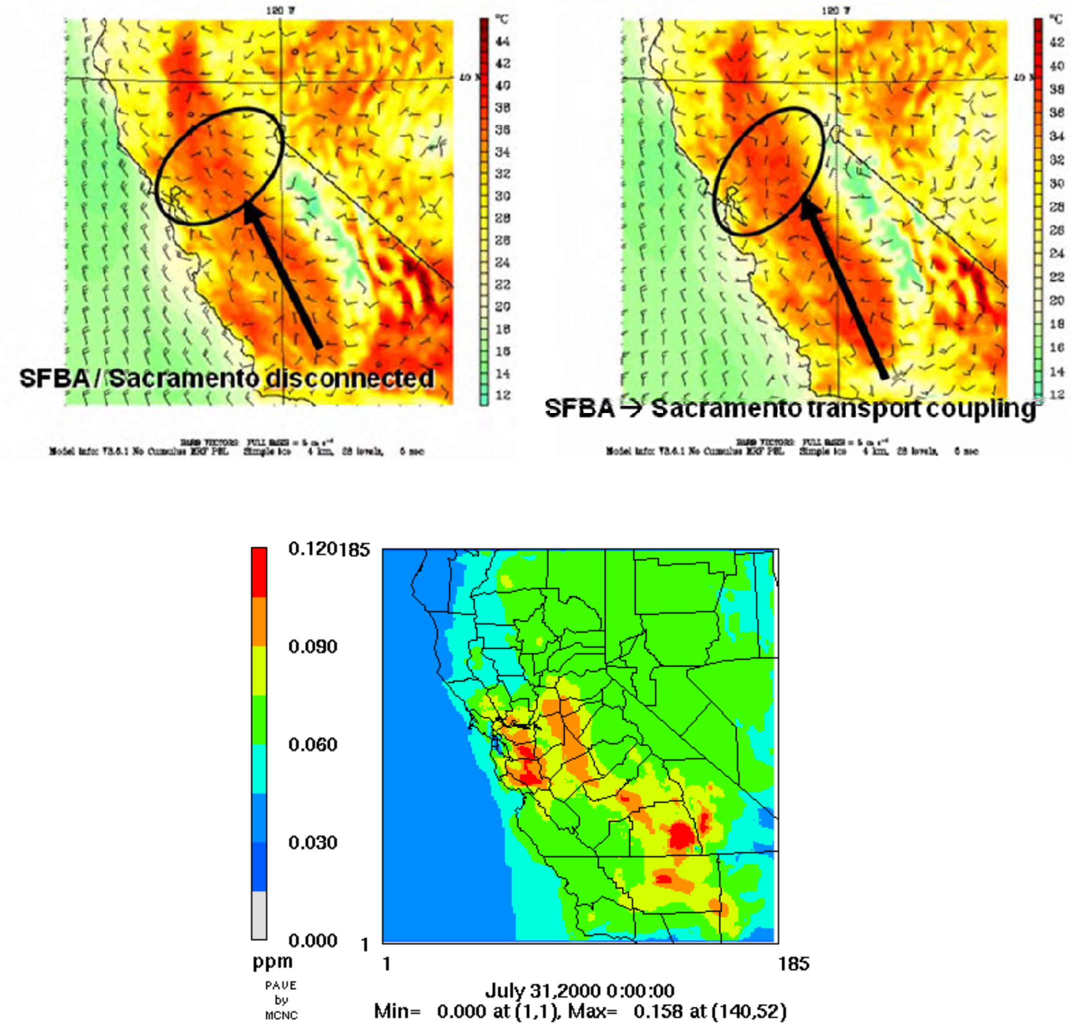

Figure 1.2. Top: Simulated temperature and winds at 1600 PST on July 31 (top left) and August 1 (top right) 2000, at $\sigma = 0.999$, for Central California. Bottom: Simulated peak ozone on July 31.

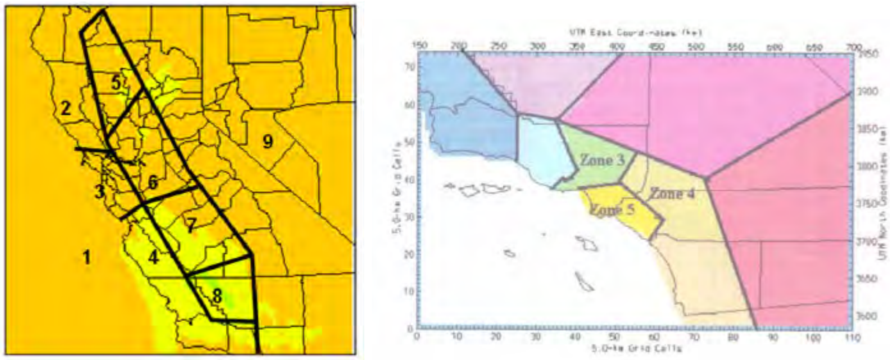

Figure 1.3. Model performance evaluation sub-domains in Central (left) and Southern (right) California, based on the California Air Resources Board (ARB) and Air Quality Management Districts

In support of this modeling effort, a detailed land use and land cover (LULC) characterization methodology (based on the United States Geological Survey [USGS] 200-m LULC) was developed in Phase 1. This was done to improve the specification of the lower boundary conditions in the modeling domains and also to develop more accurate and realistic scenarios for potential urban surface modifications in each region. The characterization was performed at 200 m so as to improve the resolution of the various potential scenarios for increasing surface albedo of different roofs, pavements, and built-up surfaces, and for increasing vegetative cover. The Phase 1 report details the derivation of UHI control scenarios and addresses the effects of increased urban albedo and canopy cover. It also details the potential negative effects of increased ultraviolet (UV) albedo (as part of increased-albedo strategies) and the effects of potential increases in biogenic hydrocarbons (isoprene and terpenes) that could result from increased canopy cover. Taha (2005) shows that both issues are non-problematic because UV albedo of reflective materials can generally be lower than that of non-reflective materials (or unchanged in most cases) and that carefully selected vegetation species introduce little or zero additional hydrocarbon emissions.

As a result of increased surface albedo and vegetative cover, the heating rates of modified surfaces are smaller relative to those of non-modified surfaces. A host of meteorological perturbations follows, but the most noticeable changes are seen as relatively lower surface and air temperatures. Changes in air temperature are the targeted effects of interest in this application, since decreased temperatures also helps reduce cooling electricity use, emissions of VOCs (an ozone precursor), and photochemical reaction rates in one dominant mechanism producing tropospheric ozone, peroxyacetyl nitrate (PAN) chemistry.

Snapshot results from Phase 1 are shown in Figure 1.4, which is an example of the simulated changes (differences from base case conditions) in 2 m air temperature as a result of “implementing” surface-modification strategies. The base-case wind vector field (at 10 m) is superimposed on the temperature-change field in each domain. The figure shows that as the level of surface modifications increases, the changes (e.g., decreases) in air temperature become larger, as evidenced by going from case 01 (moderate increases in vegetative cover) to case 22 (simultaneous larger increases in surface albedo and vegetative cover). But while the decrease in air temperature continues to grow larger with increased surface modifications, the photochemical simulations suggest that the *net* ozone air quality improvements may not always continue to increase beyond a certain threshold. This is because the impacts of perturbations in other meteorological fields become important as well, such as the decrease in planetary boundary layer (PBL) height and reduction in wind speed—both of which can lead to locally increased ozone concentrations. This aspect was discussed in the Phase 1 report and will be revisited later in section 4.1.2 of this report.

The spatial distribution of changes in meteorological fields, such as temperature, follow closely the geographical distribution of surface modifications. Thus, where surface modifications are larger, the impacts on air temperature in the affected areas and immediately downwind of them are greater. The perturbed meteorological fields, resulting because of surface modifications, were used to (1) compute and update emission rates (in particular, the emissions of biogenic hydrocarbons from existing vegetation), and (2) provide the meteorological fields needed to drive the photochemical simulations, that is, in solving the model’s photochemical reactions and transport, advection, deposition, diffusion terms, and other factors. Overall, there was a large spatiotemporal variation in the impacts on ozone concentrations. In general, the regional peaks in all Central California regions decreased as a result of implementing these strategies. However, in Southern California the domain peak could increase or decrease on August 5 in some scenarios, but it always decreased on August 6.

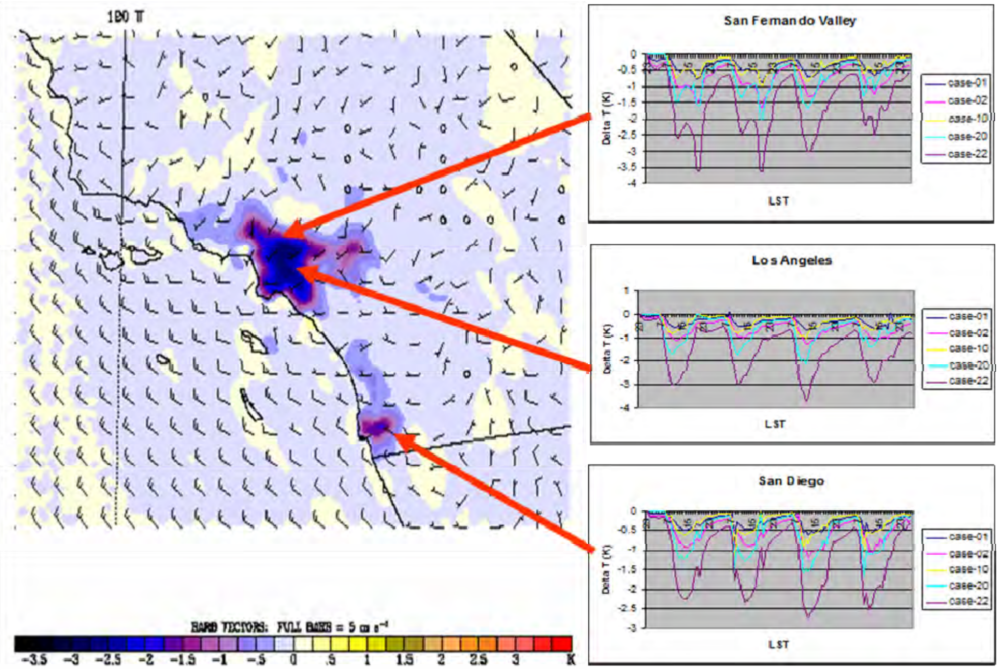

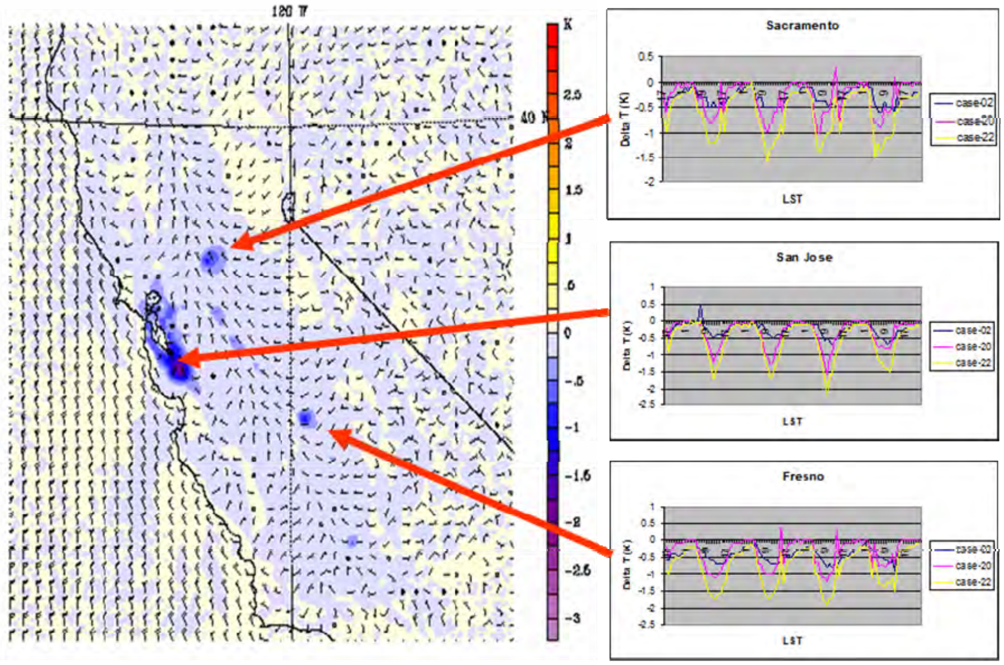

Figure 1.4. Change in air temperature in Southern California (top) and Central California (bottom) as a result of increased urban albedo and canopy cover (examples at 1300 LST on August 4 and 1200 LST on July 31, respectively). The insets at right show time-series of differences for all five days of the episode and at selected locations. Cases 01: Small increases in vegetation, 02: Larger increases in vegetation, 10: Small increases in albedo, 20: Larger increases in albedo, and 22: Combined larger increases in albedo and vegetation cover.

In terms of air-quality impacts, the effects of UHI control seem to be significant. In Figure 1.5 the changes in three indices are given for a number of scenarios (cases 01 through 22 as defined earlier in Figure 1.4) in Southern California. In this particular example, each of the three indices is averaged over all *urban* grid cells in Southern California. The indices shown are the daily 1-hour maximum, daily maximum 8-hour average, and 24-hour average. The decreases in ozone concentrations (as indicated by these indices) become larger as the level of surface modifications becomes more aggressive, up to case 20. The averaged changes are significant in terms of absolute concentrations. However, beyond case 20 (e.g., case 22), the net decreases in ozone concentrations become relatively smaller, possibly because a threshold of surface modifications level has been reached, as discussed above.

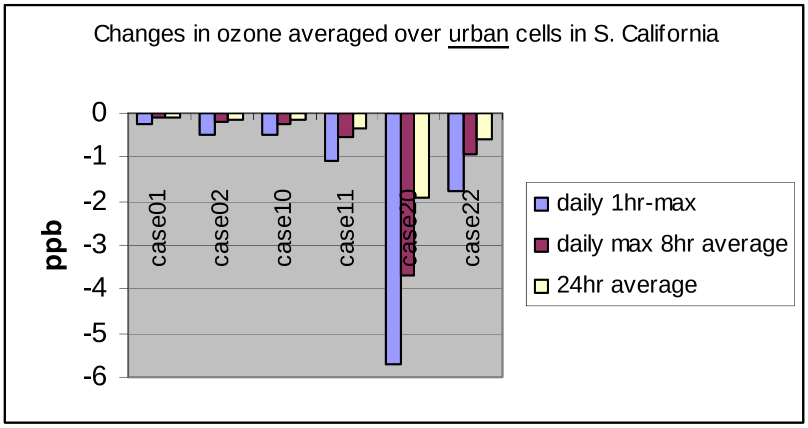

Figure 1.5. Changes in ground-level ozone in Southern California for several control scenarios

An example of results for Central California is Figure 1.6, where changes in regional *peak* concentrations are shown for four regions and three days of the episode. The changes in the peaks in the San Francisco Bay Area, Sacramento, and the north and south San Joaquin Valley are shown for case 20—a case with a large increase in albedo. As with Southern California, the effects of UHI control are significant.

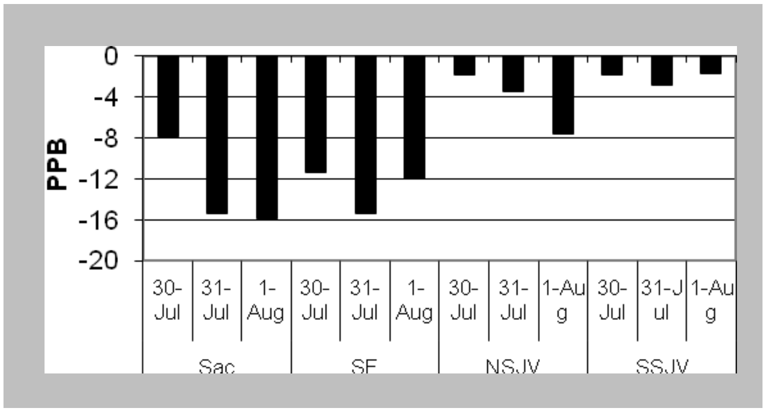

Figure 1.6. Changes in regional peak ozone for a case with large albedo increases

In summary, the Phase 1 modeling and simulation work suggests that implementing surface-modification strategies in California would benefit the state in terms of ozone air quality. Overall, there would be net improvements in several key indicators. This report recommends that these strategies be considered as an additional means to complement other emission control venues, to help reach and/or maintain attainment in the future. This presents regulators with a potential additional control strategy to consider among a menu of conventional and non-conventional strategies already being considered or implemented. However, the main drawback in evaluating the potential impacts of heat-island control is that the large-scale effects (both positive and negative) can currently be demonstrated solely through numerical modeling and that the observable, quantifiable, and repeatable effects will not be easy to document for quite some time to come. The use of numerical modeling in this case, as with any other strategy, carries an inherent risk that should be accounted for. In other words, there is risk in beginning to implement this strategy for the *sole purpose of improving air quality* although this strategy's energy benefits have already been established). Thus, there may be pitfalls that regulators need to carefully consider when beginning related planning, evaluation, and implementation processes.

Phase 1 also identified a number of follow-up items to address, among them was the issue of fine-resolution meso-urban modeling capability and related fine-resolution data development. This was taken up in Phase 2 of the study, as summarized in this report. Here, the term *mesocale* is used to refer to resolutions ranging from a few kilometers to tens of kilometers in the horizontal and tens to hundreds of meters in the vertical. The term *meso-urban* refers to resolutions tackled by the new model in *this* application, that is, 1 km in the horizontal and a few meters in the vertical.

1.2. Study Purpose — Phase 2

Following the *mesoscale* evaluation of control impacts (of surface modifications) in Phase 1, the main objective in Phase 2 was to build upon that framework and develop a methodology for more detailed modeling and analysis, for example, at the resolution of neighborhoods or city blocks. To perform this, a meso-urban meteorological model (uMM5) was updated, modified, and adapted to UHI-mitigation study and applied to two domains in California.

The second phase of the study is a UCP, fine-resolution (urbanized) meteorological and photochemical modeling stage that builds on earlier efforts, e.g., Taha (1999); Taha and Bornstein (1999); Taha (2005); Dupont et al. (2004); and Otte et al. (2004). This effort significantly modified and updated the models, creating a new and improved version that is particularly adapted for UHI-mitigation modeling studies. The uMM5 is now being considered by the U.S. Environmental Protection Agency (U.S. EPA) as one of several models in its effort to develop a nationwide community fine-resolution urban modeling system and data portal (Ching 2007). It also is being considered by a number of air districts for potential use in their State Implementation Plan (SIP) modeling of heat island control strategies. Some aspects and formulations in the uMM5, and in the original DA-SM2-U of Dupont et al. (2004), might also serve as a basis for urbanizing the WRF model (Chen et al. 2007).

The *main* goal in Phase 2 was to develop and update new models and implement a methodology and new simulations and data techniques that can be used for detailed evaluation of surface modifications' impacts on heat islands, energy use, emissions, and air quality. A *secondary* goal was to apply the new methodology, models, data, and techniques developed to one California region, and the greater Sacramento valley was selected for this application. In this report, an additional region called Orange-Riverside (O-R) is also presented.

1.3. General Background

1.3.1. Energy and Urban Climate

Urban climates, energy, emissions, and air quality are interrelated through a number of pathways and feedback mechanisms. Energy conversion and use can contribute to creating specific urban-climate phenomena, such as heat islands, via increased anthropogenic heating of ambient air by equipment, air conditioners, cooling towers, motor vehicle air conditioners, and other heat sources, such as industrial facilities, refineries, processing plants, and power plants. Typical values of anthropogenic heat flux density in residential areas are on the order of 10–20 watts per square meter (W m^{-2}) and in dense urban cores are in the range of 50–100 W m^{-2} (Taha 1997a). Flux densities larger than 100 W m^{-2} are thought to occur at certain times in extremely dense urban cores, such as Lower Manhattan (about 120–150 W m^{-2}). In Japan, flux densities of up to 500 W m^{-2} have been reported, although this is highly uncommon. By comparison, the maximum incoming solar radiation flux density at *street* level on a cloudless summer day can range from 800 to 1000 W m^{-2} around solar noon. While anthropogenic heating is only one of several heat-island causative mechanisms, and is relatively small, it can be significant in areas where such sources are highly concentrated. Energy use and conversion also result in increased emissions of air pollutants, such as carbon dioxide (CO_2), nitrogen oxides (NO_X), volatile organic compounds (VOC), and water vapor, and can enhance local greenhouse effects. Increased emissions of aerosols can also affect the concentration of condensation nuclei and possibly convective cloud formation over and downwind of urban areas.

In turn, the local climate directly affects energy use; for example, in heating, ventilating, and air conditioning (HVAC), transport and air-conditioning, industrial processes, and so on. In buildings, relatively more cooling and less heating is generally needed when heat islands are present. In addition, HVAC system efficiencies depend to a certain extent on ambient air temperature and therefore are affected by urban climates, even if by small amounts.

The abundance of high thermal-capacity materials in urban areas—for example concrete, brick, stone, pavements, asphalt, steel, and so on—causes urban areas to store relatively more heat than rural surrounds. Many of these materials also have high thermal conductivities, therefore, further increasing heat fluxes and storage into the medium. Urban regions also typically have a larger surface area exposed to the sun per ground area than do rural regions. This is called the envelope-to-ground area ratio, and rural areas tend to have ratios close to 1, residential neighborhoods, on the order of 2–3.and in urban cores, the ratio reaches about 5 or higher. In areas like Manhattan, the ratio can easily reach 10 or more. The combination of these two factors (increased thermal capacity and envelope-to-ground ratio) leads to solar radiation being captured and stored more efficiently in urban areas, thus contributing to heat islands. In addition, the smaller sky-view factor (SVF) in urban areas, relative to that in open surrounds, helps create a canopy-layer heat island, especially during nighttime. This arises because radiative cooling of urban surfaces (and canopy-layer air) to the sky is hindered by the obstructions (e.g., in walls and structures). As a result, a heat island can be created due to the differential in cooling rates between urban areas and rural surrounds. The same mechanism is at work during daytime, that is, the SVF effect, but its relative contribution is smaller than at night. In addition, the reverse effect can also occur, for example, shading in urban canyons and the competing effect of decreased effective albedo.

The albedo of building materials, pavements, and other urban structures is generally similar to or lower than that of vegetation or barren land (which is abundant in rural areas). But in some cases, the reverse is true—that is, albedo of urban surfaces can be higher than that of the rural surrounds. For example, low-altitude aircraft measurements over the Los Angeles Basin (Taha 1997b) have shown that urban albedo in some parts can reach up to 0.20 when the rural, more vegetated surroundings have an albedo of 0.15. In general, a heat island can arise when *effective* urban albedo is lower than that of the rural surrounding areas. Thus, in addition to the fact that many urban surfaces (such as roofs, walls, pavements, streets, structures, and others) can have low albedos individually, urban areas also create a lower *effective* albedo, collectively.

As a result of relatively smaller vegetative cover in urban areas, the partitioning of incoming solar radiation into sensible and latent heat fluxes is altered. Therefore, in urban areas, the Bowen ratio (β) (the ratio of sensible to latent heat fluxes) is larger, and this ultimately results in higher air temperatures. In rural areas or suburbs where there is typically more vegetation, evaporation, and evaporative cooling (assuming that a minimum of watering is done), β is smaller, and that can help keep air temperatures relatively lower. Typical values for β are around 4 or 5 in vegetated urban areas and about 0.8 to 1.5 in vegetative canopies. By comparison, β is in the neighborhood of 0.1 for oceans, and in the tropical forests it is about 0.2.

1.3.2. Meteorology and Air Quality

Several modeling studies in the past (Taha 1999; Taha et al. 1999; Sailor 1993; and Taha 1996,1997b) have suggested that urban environmental control strategies, that is, increased surface albedo and canopy cover, can reduce surface and air temperatures in areas where such surface modifications are most concentrated. The main local impacts of interest from relatively lower ambient temperatures include the following, in descending order:

1. A reduction in temperature-dependent rates of certain photochemical reactions.
2. A decrease in temperature-dependent biogenic hydrocarbon emissions from existing vegetation.
3. A decrease in evaporative losses of organic compounds from mobile and stationary sources.
4. A decreased need for cooling energy, generating capacity, and, ultimately, emissions from power plants.
5. Decreases from on-road and off-road mobile source emissions.

Thus, generally speaking, increased urban surface albedo and vegetative cover have the potential to reduce ozone formation. However, cooling an urban area via such strategies can also cause adverse effects on ozone air quality because inhibited mixing and changes in the wind field can increase ozone concentrations in certain areas and under certain conditions. As Phase 1 modeling has shown, there can exist a certain regional threshold beyond which the net improvement in air becomes relatively smaller, even though temperature continues to decrease past that threshold (Taha 2005).

Gabersek and Taha (1996) and Taha (1996,1997a,b) show that these strategies may be an effective way of reducing urban air temperatures in various regions of the United States (for example, by up to 5°C in summer in areas such as the Los Angeles Basin), thus helping to reduce exposure to ozone. Taha et al. (2000) show that the effects in three U.S. regions tend to be generally positive but that negative, unwanted effects still occur. That study showed that Sacramento, California, would benefit more from these strategies than Salt Lake City, Utah, or Baton Rouge, Louisiana. In the latter two regions, the peak ozone concentration did not change as a result of surface modification, whereas in Sacramento, a peak of 139 parts per billion (ppb) was decreased by 9 ppb. Area-wide indices in all three regions decreased in general. Taha (2003c) performed an extensive meteorological-photochemical modeling study of the Houston-Galveston, Texas, region to assess the potential impacts of surface modifications. Although that study was inconclusive, due to outstanding issues with model performance and quantification of the resulting signal, it showed that the impacts (both positive and negative) can be significant and that further work must be done to improve model performance and more accurately quantify the potential benefits of these strategies.

A number of studies also have examined the role of meteorology in tropospheric and ground-level ozone formation, scavenging, transport, and accumulation. These studies, in general, show a positive correlation between ozone concentrations and temperature. A warmer environment is generally more conducive to ozone formation and accumulation mainly because of temperature impact on peroxyacetly nitrate (PAN) chemistry (increased breakup of PAN), accompanying stagnation (reduced venting and transport), high solar radiation input (actinic flux), and other factors, but it is the mix of conditions—that is, meteorology and emissions—that determines the ultimate outcome in a specific region under specific conditions.

Several studies also provide correlations between some measures of air temperature and ozone concentrations. For example, Jones et al. (1989) correlated the number of days with ozone exceedances above 120 ppb with near-surface air temperature above 30°C in selected urban areas. For Houston, Washington D.C., and New York, Wakim (1989) also developed such correlations. In Atlanta, Georgia, Cardelino and Chameides (1990) showed a significant correlation between temperature and ozone levels, based on ambient data. They suggested, as is discussed in this report, that temperature is not the only factor in smog production; that is, that higher air temperatures do not always guarantee that ozone concentrations will be higher than during days with relatively lower temperatures. Using the carbon bond (CB-IV) mechanism as implemented in the optional mechanisms-IV (OZIPM4) model, Hogo and Gery (1988) show that the effect of increased air temperature on maximum ozone concentrations is significant, regardless of whether only chemistry effects are accounted for or both chemistry and emission effects are included. The chemistry effect (mainly the effect of PAN chemistry) alone would increase maximum ozone concentrations by 2.8 ppb/°C, whereas the combined chemistry and emission effects would increase it by 5.3 ppb/°C (the correlations are valid in the temperature range of 18°C to 34°C).

The U.S. EPA estimates that an increase in air temperature of 4°C in the New York region could cause an increase of 4% in ozone concentrations (Smith and Tirpak 1989). A study by Morris et al. (1989) found that in California, ozone concentrations could increase by 20% or 30 ppb (150 to

180 ppb) during high-ozone days in August as a result of a 4°C increase in air temperature and that the number of days in August with ozone higher than 120 ppb could increase by 30%. There can also be a decrease in ozone concentrations under certain conditions, e.g., up to 2.5%. In the San Joaquin Valley (Fresno and Bakersfield) the increase reached about 5 ppb in daily maximum ozone. In areas farther away from anthropogenic emission sources, such as near the Sierra-Nevada, only little changes occurred in ozone.

2.0 Methodology and Approach

2.1. Meteorological Models

2.1.1. uMM5

While Phase 1 of the study used only mesoscale models, the second phase used a combination of standard and urbanized (meso-urban) versions of the Pennsylvania State University/National Center for Atmospheric Research (PSU/NCAR) MM5 model. The standard MM5 is described in a number of sources, such as Dudhia (1993), and briefly in Section 2.1.2. The modified input and surface characterization methodology used in the mesoscale model are discussed in Taha (2005). The urbanized (UCP) EPA MM5 is discussed in Dupont et al. (2004) and Otte et al. (2004). The uMM5, an Altostratus-modified version of this model, is described in Taha (2005). Its features are only very briefly highlighted here.

The uMM5, further developed in this study, is based on the DA-SM2-U model (Dupont et al. 2004), with the objective of simulating fine-resolution, canopy-layer meteorological fields, such as those hundreds of meters in the horizontal and a few meters in the vertical. To achieve this goal, and to accommodate the fine resolutions involved, the mesoscale model formulation is modified such that additional source/sink terms are added to the conservation relations to more accurately represent phenomena at sub-grid scales and within the canopy layer. The newer parameterizations, described in Dupont et al. (2004), Martilli et al. (2002), Otte et al. (2004), and Taha (2005) involve the following:

1. **Momentum equations**: Addition of two source/sink terms for momentum (1,2); one for a better representation of the effects of horizontal surfaces of buildings and structures (roughness-based) and the other due to vertical surfaces (pressure and drag-based) of buildings and vegetation:

$$\frac{\partial \rho u_i}{\partial t} = F_{g(ui)} + \underbrace{F_{ui}^{j}}_{1} + \underbrace{\sum_{j} D_{ui}^{j}}_{2} \qquad (1)$$

2. **Liquid water potential temperature (thermal equation)**: Addition of two sink/source terms (3,4). The first is a source term, due to sensible heat flux from roofs and vegetation canopies, whereas the second term is anthropogenic heat flux:

$$\frac{\partial \rho \theta_L}{\partial t} = F_{g(\theta L)} + \underbrace{H_j}_{3} + \underbrace{Q_f}_{4} \qquad (2)$$

3. **Moisture equation**: Source terms (5) within the canopy (in addition to ground-level sources). These are for: 1) evapotranspiration from the canopy, and 2) evaporation of building- and vegetation-intercepted water:

$$\frac{\partial \rho q}{\partial t} = F_{g(q)} + \underbrace{S_j}_{5} \qquad (3)$$

4. **Turbulent Kinetic Energy (TKE) equation**: Addition of source/sink terms (6,7,8,9) to account for the effects of building and vegetation on the flow field. The effect of horizontal building surfaces is accounted for via shear production (6), whereas effects of sensible heat fluxes from building and vegetation surfaces are accounted for via buoyant production of TKE (7). Other effects of obstacles, e.g., buildings, are accounted for via a wake production term (8) and an additional dissipation (accelerated cascade) term (9):

$$\frac{\partial E}{\partial t} = \frac{\partial u_i E}{\partial x_i} + \left\{ k_m \left[\left(\frac{\partial u}{\partial z}\right)^2 + \left(\frac{\partial v}{\partial z}\right)^2 \right] S_{air} + \underbrace{F_E^{bui}}_{6} \right\} + \left\{ \frac{g}{\theta_v} \langle w\theta_v \rangle + \underbrace{H_E}_{7} \right\}$$

$$- \frac{1}{\rho}\frac{\partial\left(\rho\langle wE\rangle\right)}{\partial z} - \varepsilon + \underbrace{\sum_j w_E^j}_{8} - \underbrace{\sum_j D_E^j}_{9} \qquad (4)$$

5. **Radiative energy balance**: Includes additional computations of effective canyon albedo and sky-view factor and their impacts on surface-atmosphere radiative exchange.

6. **Detailed soil model:** Based on SM2 (3-D) of Dupont et al. (2004), which is an extension of the Interactions between Soil-Biosphere-Atmosphere (ISBA) soil model of Noilhan and Planton (1989). This model, while very extensive, is not discussed here since it was not modified in this study. The reader is referred to Dupont et al. (2004) for a detailed discussion of the soil model.

In equations 1–4, all symbols retain their conventional meteorological meaning and F_g is the general forcing term in each relation, i.e., the form before inclusion of terms 1 through 9. The uMM5's drag-force-based calculations are carried out whenever canopies, vertical structures, or surfaces exist in a computational grid cell. For areas where no such obstacles exist, the model reverts to an approach essentially similar to the standard roughness-length formulation of mesoscale models, but allows for finer resolutions by computing the transfer coefficients for momentum and heat for each surface type and then averaging up the corresponding fluxes to the model grid. Thus, even without the drag-force approach improvements, the roughness approach in the uMM5 is *still* more spatially resolved than in the standard MM5, where the surface-transfer coefficients are calculated at the grid-cell level only.

Some of the terms above are parameterized as follows, per Martilli et al. (2002). The source terms for momentum due to friction on horizontal surfaces and due to drag from vertical surfaces are parameterized as follows:

$$F_{ui}(k) = \frac{\rho(k)}{V_{ai}(k)} \cdot \frac{A_{hj} \cdot A_{Tj} \cdot \left(u_j^*\right)^2 u_i(k)}{\left\{\left(u_x(k)\right)^2 + \left(u_y(k)\right)^2\right\}^{0.5}} \qquad (5)$$

$$D_{ui}^{j}(k) = -\rho(k) \cdot C_{dj} \cdot A_{fj}(k) \cdot u_i(k) \left\{ \left(u_x(k)\right)^2 + \left(u_y(k)\right)^2 \right\}^{0.5} \qquad (6)$$

where, A_h and A_T are, respectively, cover and top-area density (TAD), V is volume, and u_x=u, u_y=v.

The modified conservation relations, as briefly discussed above, are more suitable for finer-resolution simulations than otherwise possible with the roughness-length-based formulation that is typical of mesoscale models. Because of this added capability, it is possible to now simulate more accurately the fine-resolution meteorological fields within the canopy layer. Thus it is possible to increase the number of *useful* vertical levels in the model. Figure 2.1 shows a diagrammatic comparison between the vertical level structures of a roughness-based approach (e.g., regular MM5) versus a drag-force approach (e.g., uMM5) as used here, based on Dupont et al. (2004). In addition, the figure also gives the actual heights (in meters, above ground level [AGL]) as used in the present simulations of the Sacramento and O-R domains. Of course, those vertical levels can be made finer and more resolved if needed.

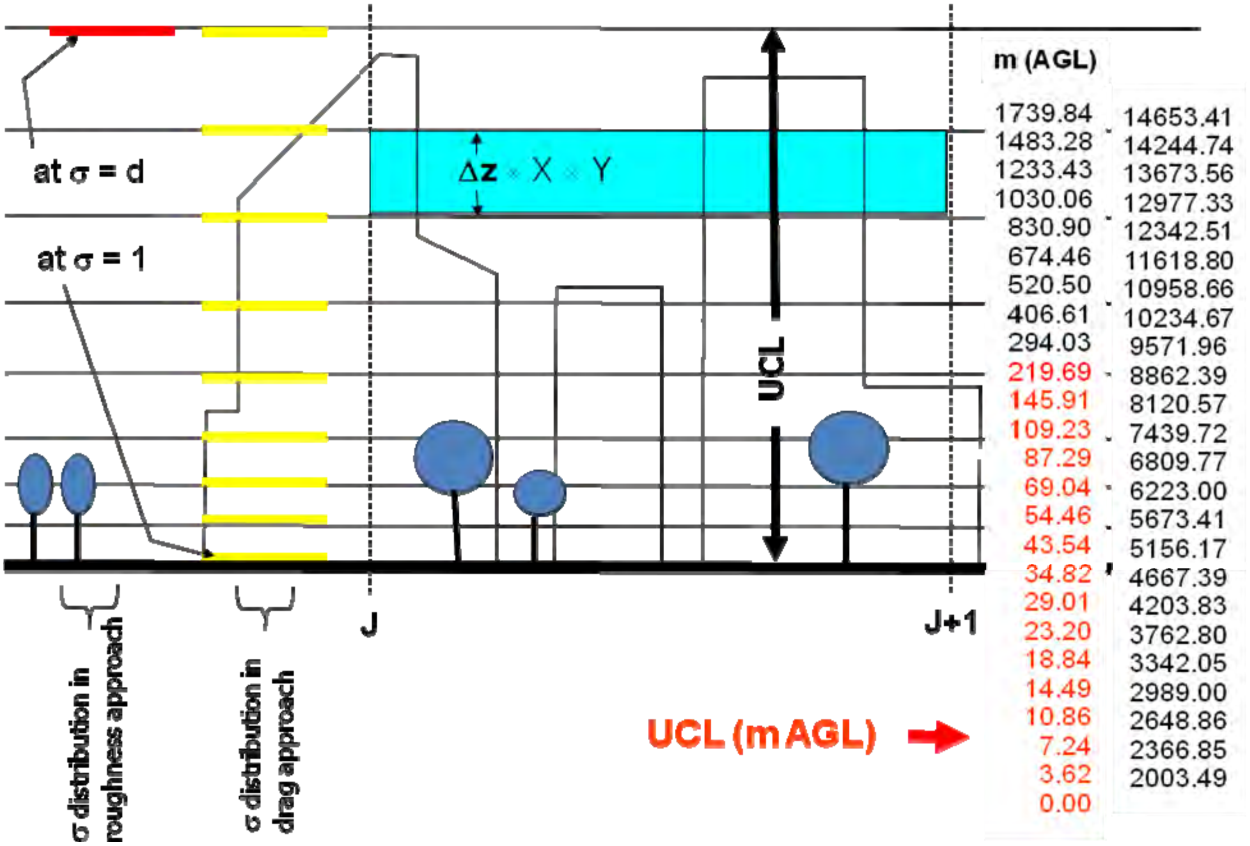

Figure 2.1. Schematic representation of fine-resolution meso-urban and mesoscale model vertical structures. The red line represents a typical first atmospheric level in roughness-based mesoscale models (e.g., at displacement height, d), whereas the yellow lines, starting at the actual surface, indicate several additional vertical layers in the uMM5 for the same interval. The numbers at right show the heights (m, AGL) used in this modeling study, with the red entries being within the canopy layer.

Several aspects of the model were further improved and implemented or, at least, tested and evaluated. The model's ability to ingest and process the new types of information, site-specific morphology, and three-dimensional parameters was improved. Instead of LULC-based surface characterization, as is typically done in mesoscale models, the uMM5 incorporates externally computed and accurately developed surface properties fields, such as three-dimensional morphology or surface physical properties. The LULC-*independent* input is typically derived from remote-sensed data and region-specific field surveys. The model can also accommodate and incorporate modified UCP and morphology data, for example based on Google's Earth Pro geometrical data. The modifications to the input data and the model were designed to render the system more appropriate for UHI mitigation studies. The capability of developing various surface modification scenarios was incorporated into the system. The model's structure and code were also modified to allow for nested-grid, two-way-feedback simulations, unlike in the original DA-SM2-U, which was a standalone model run off-line with output downscaled from the coarser grids of the model.

Other modifications were implemented to further improve the model's fine-resolution site-specificity and computational accuracy. For example, drag coefficients for vegetation and buildings were assumed constant in the original versions of the model. These were modified to account for the spatially varying geometrical properties and shape factors of buildings (and vegetation). Of course, this is useful only where suitable information is available in the input data (geometrical characterization detail). In addition, computations of various parameters were modified to account for multiple wind approach directions at each model grid cell. Calculations of wind speed and TKE were modified so as to account for the morphology parameters (frontal area density [FAD], top area density [TAD], and plan area density [PAD]) corresponding to each direction. Similarly, computation of roughness length at the grid-cell level, where needed, was also modified to account for various wind directions, by using the appropriate functional form (FAD) for each approach direction.

Finally, two aspects of relevance to UHI-control strategies were also modified. The computation of effective albedo and related calculation of radiative extinction in urban canyons were improved by accounting for urban canyon orientation at finer resolutions than in the original model, where average canyon orientation was used. The effects of canopy cover (and increases thereof) were also improved via accounting for watering schedules, which can be important in hot-weather locations like California.

2.1.2. MM5

The mesoscale model used in simulating the coarse-grid domains in this study is the PSU/NCAR MM5 (Dudhia 1993; Grell et al. 1994). It is one of the more widely used mesoscale models in conjunction with photochemical regulatory modeling (e.g., Tesche et al. 2001; Seaman and Stauffer 1996; and Seaman et al. 1997). For simulating the potential impacts of urban surface modification strategies, the MM5 was used by Taha (2003 a,b,c) and in Phase 1 by Taha (2005).

The MM5 is an Eulerian, three-dimensional grid, non-hydrostatic, primitive-equation prognostic model. The basis of the model is the three-dimensional prognostic equations for wind (u,v,w), temperature, perturbation pressure, and water vapor mixing ratio. It uses a sigma-altitude (sigma-z) terrain-following vertical coordinate system and allows for multiple nesting. The sigma levels are defined according to a hydrostatic reference state and are time-independent (invariant) during the course of the simulation. The model allows for moving nests as well as turning on and off selected nests during the simulation. There can be one-way nesting or two-way feedback, and various smoothing methods are available.

For sub-grid scale parameterizations of turbulent fluxes, the model allows for a number of different (local and non-local) PBL schemes such Eta and Gayno-Seaman, Medium Range Forecast (MRF) (Hong and Pan 1996), fine-resolution Blackadar (Zhang and Anthes 1982), and Mellor-Yamada (Burk and Thompson 1989). The model has a number of physics, microphysics, and convection options. Microphysics options include stable precipitation parameterizations, such as warm rain (Hsie and Anthes 1984), ice physics (Dudhia 1993), ice and graupel (Tao and Simpson 1993), and the Schultz and Reisner schemes (Schultz 1995; Reisner et al. 1998). The uMM5 (discussed above) is currently implemented (hard-coded) mostly in the Gayno_Seaman (GS) PBL scheme.

The model also has a number of cumulus parameterization schemes, such as ; Grell et al. (1994); Kain and Fritsch (1993); Grell et al. (1991); and Betts and Miller (1986). It allows for coupling land-surface models, such as PM and OSU/NOAH (Pan and Mahrt 1987; Chen and Dudhia 2000). The MM5 has four-dimensional data assimilation (FDDA) capabilities (Stauffer and Seaman 1990) for both analyses and observational (station, point) nudging. Use of FDDA can in certain cases improve the model performance, especially over longer simulation time frames, depending on the actual conditions being simulated.

The model's grid is based on the Arakawa-B stagger configuration, where scalars are defined at the center of the grid and velocity variables are allocated at the corners. In the vertical, all variables are defined at half-sigma levels except for the vertical component of velocity, which is defined at the full sigma levels. Typical minimum horizontal grid resolution is on the order of 500 m (although in theory, the model can be run at smaller grid spacing). In the vertical, resolution is variable, and the grid is stretched (for example: a few meters thick near the ground to hundreds of meters thick near model top). Of course, both horizontal and vertical resolutions can be significantly improved by modifying the sub-grid-scale parameterization.

Model initialization is based on integrated divergence removal. Initial and boundary-condition data are typically specified from large-scale (synoptic) three-dimensional analyses and usually applied at the outermost grids of the coarse domains. Example analyses are those from the National Centers for Environmental Prediction/NCAR Reanalysis Project (NNRP) and global data assimilation system (GDAS) and are available from the NCAR archives and other sources. The model's top boundary conditions are those of a radiative or rigid layer and at the surface, those of prognostic surface temperature, constant or varying water surface temperature, and a constant-flux surface layer (fluxes based on similarity theory). At the lateral boundaries, time-dependent in/outflow (relaxation) conditions are assumed. The model produces comprehensive forecast variables (e.g., wind field, temperature, water vapor, cloud rain and ice, boundary-layer fluxes and variables, perturbation pressure, and others), and a host of derived quantities.

2.2. Photochemical Model

This study uses the Comprehensive Air Quality Model with Extensions (CAMx) (Yarwood et al. 1996). The CAMx is an Eulerian, three-dimensional grid, photochemical model that allows simulation and assessment of "one atmosphere," i.e., ozone (gaseous) and particulate matter air pollution. This state-of-science model is modular in structure, which facilitates updates, modifications, and integration of user-developed algorithms and routines. In addition, the model allows for a number of coordinate systems (map projections) and for nested configurations to provide detail and efficiency in simulating larger domains. More recent versions incorporate additional improvements in treatment of ozone and particulate matter. At its core, CAMx uses a continuity equation (advection-diffusion equation) closed by k-theory for both horizontal and vertical advection, transport, and diffusion. As with other similar photochemical models, such as UAM-V and CMAQ, CAMx solves the advection-diffusion equation and accounts for emissions (sources), dispersion/transport, chemical transformations, and removal (sinks). The typical pollutant continuity equation for a species "i" is:

$$\frac{\partial C_i}{\partial t} = -\nabla_h \bullet \overrightarrow{V}_h C_i + \left[\frac{\partial C_i e}{\partial z} - C_i \frac{\partial}{\partial z}\left(\frac{\partial h}{\partial t}\right)\right] + \nabla \bullet \rho K \nabla\left(\frac{C_i}{\rho}\right) + \left\langle\frac{\partial C_i}{\partial t}\right\rangle_{emi} + \left\langle\frac{\partial C_i}{\partial t}\right\rangle_{rem} + \left\langle\frac{\partial C_i}{\partial t}\right\rangle_{chem} \tag{7}$$

where C is concentration, V is wind vector (the subscript "h" indicates horizontal component), e is vertical entrainment rate, z is height, h is layer-interface height, K is diffusivity, ρ is density, and the subscript for the last three terms indicate emission (source), removal (sink), and chemistry (e.g., reactions, transformations). In CAMx, this equation is solved numerically using a time-splitting (operator splitting) method to evaluate the various terms separately and then their combined contributions. Advection solution is split into vertical, N-S, and E-W in a mass consistent fashion. The chemistry term of the above equation can be solved with different chemical and lumping mechanisms, such as CB-IV or the SAPRC(99). Finally, both dry and wet deposition (scavenging) can be accounted for in CAMx.

The model grid is based on the Arakawa-C stagger configuration. In the horizontal, scalars and concentrations are located at cell center to represent cell-averaged conditions, whereas wind vector is carried at the edges (cell interfaces) and the u- and v- components are staggered with respect to each other. The meteorological fields are passed from the meteorological model (e.g., MM5 or uMM5) to CAMx into this grid configuration. In the vertical, scalars are situated at cell center (halfway between layer interfaces) except for vertical entrainment rate and vertical diffusivities that are at the layer interfaces.

CAMx also has useful features, such as the following:

1. A flexible two-way nesting and feedback structure and the ability to turn on or off selected nested grids during the course of model integration, which facilitates the more efficient use of computing resources.

2. The availability of versions of the CB-IV and the SAPRC chemical mechanisms that provide alternate methods of VOC lumping in surrogate species.
3. Options for standard or fast chemical kinetics solvers which can provide significant model speedup where needed.
4. Plume-in grid simulation capabilities to handle the details of point-source plumes, such as NOx plumes, within the grid until the plume has dispersed well enough for accurate representation within the model grid structure.
5. Ozone source apportionment technology (OSAT) which is a CAMx feature that allows to track the source regions and/or source categories contributing to resulting ozone concentrations at specific (user-selected) grid cells.
6. Process analysis (PA) capabilities whereby the results can be evaluated in terms of model formulation and the relative role of various terms and processes (such as process rates for advection, diffusion, chemistry, deposition, and others) in the conservation relations or provide reaction-rate data for all chemical mechanisms in selected grid cells.
7. An advanced photolysis model (NCAR's Tropospheric Ultraviolet & Visible Radiation [TUV] radiative transfer and photolysis model) that allows modification of photolysis rates to account for changes in albedo, ozone column, zenith angle, elevation, and other factors, and an option to adjust these rates for the impacts of clouds based on the Regional Acid Deposition Model (RADM) (Cheng et al. 1987).

2.3. Emission Inventories

Episodic emission inventories used in both phases of this study were discussed in the Phase 1 report and will not be repeated here. While both CB-IV and SAPRC99-speciated inventories were obtained, the study so far has used only the CB-IV inventories for reasons related to use and application permissions. One new aspect to mention in this discussion of emissions is that the gridded emission rates were downscaled from the coarse-grid domains (4 km in the Central California Ozone Study [CCOS] and 5 km in the Southern California Ozone Study [SCOS]) to the finer-resolution modeling grids of the nested 1 km photochemical model (corresponding to the uMM5 meteorological grid). Figure 2.2 shows an example of fine-resolution emissions generated for the Sacramento 1 km domain from interpolating (downscaling) the 4 km emission inventories of the mother domain. The figure shows a snapshot of emissions of anthropogenic nitric oxide (NO) at 1200 LST on July 31, as an example (in this case, the resolution is improved from 4 km to 1 km—that is, 16 times)

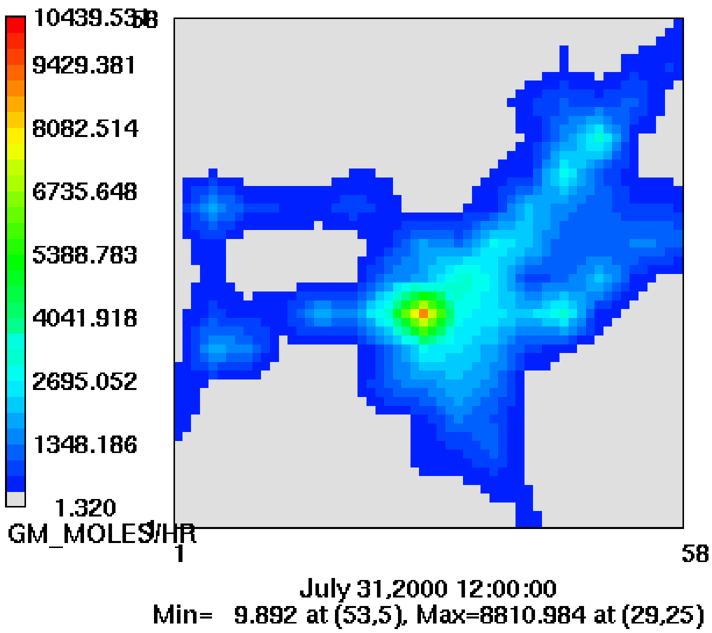

Figure 2.2. Example of fine-resolution emissions generated for the Sacramento 1 km domain from interpolating (downscaling) the 4 km emission inventories in this area. The figure shows a snapshot of emissions of anthropogenic NO at 1200 LST July 31. The high emission rates at the center of the domain are from the Downtown Sacramento area.

2.4. Urban Canopy Parameterizations (UCP) and Morphology Data Generation and Application

2.4.1. UCP Data Development

As discussed in Section 2.1.1, the uMM5 is based on modified conservation relations, in this case, based on the drag-force approach to momentum equations and related TKE, heat, moisture, and other parameterizations (Martilli et al. 2002; Dupont et al. 2004; Taha 2007). The additional sink/source terms incorporated in equations 1–4 are volumetrically scaled via a number of three-dimensional morphological or UCP parameters. For the uMM5, the needed set parameters (these are in addition to all input needed by the standard MM5) are summarized in Table 2.1.

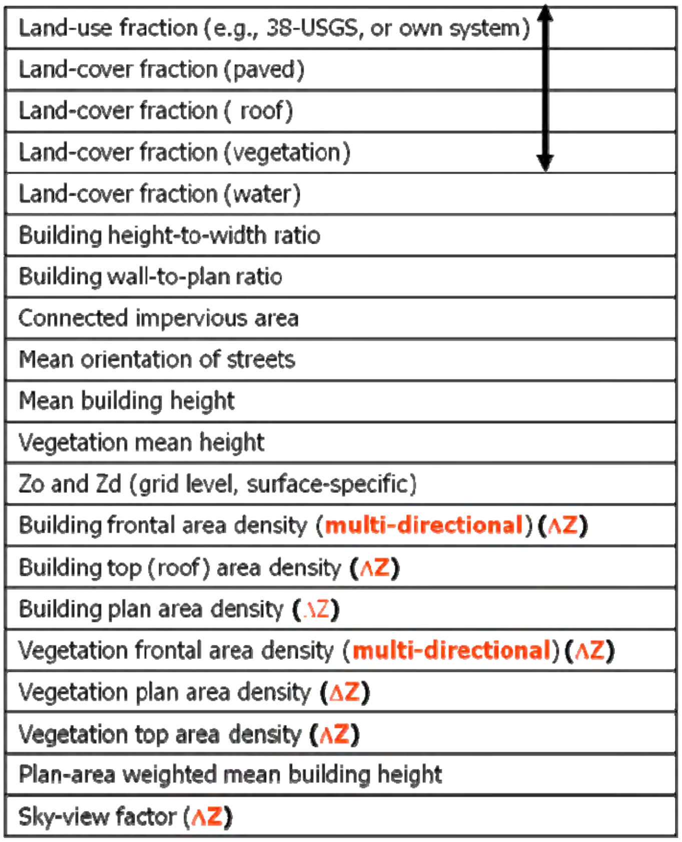

Land-use fraction (e.g., 38-USGS, or own system)
Land-cover fraction (paved)
Land-cover fraction (roof)
Land-cover fraction (vegetation)
Land-cover fraction (water)
Building height-to-width ratio
Building wall-to-plan ratio
Connected impervious area
Mean orientation of streets
Mean building height
Vegetation mean height
Zo and Zd (grid level, surface-specific)
Building frontal area density (**multi-directional**) (**ΔZ**)
Building top (roof) area density (**ΔZ**)
Building plan area density (**ΔZ**)
Vegetation frontal area density (**multi-directional**) (**ΔZ**)
Vegetation plan area density (**ΔZ**)
Vegetation top area density (**ΔZ**)
Plan-area weighted mean building height
Sky-view factor (**ΔZ**)

Table 2.1. uMM5 morphology input parameters. All are gridded at the model's resolution. (Δz) indicates specification at 1-m interval in the vertical throughout the canopy layer depth, (multi-directional) indicates specification at different wind approach directions.

While these terms are self-explanatory, equations 8–17 below provide some additional definitions. In Table 2.1, parameters that are labeled "multi-directional" are those that need to be characterized for various wind approach directions. Those that have a "Δz" label need to be characterized as vertical profiles at selected intervals, e.g., in this study at a 1 m interval in the vertical through the top of the canopy layer. Therefore, some parameters, such as FAD (for buildings and for vegetation), need to be characterized at every vertical interval *and* at several wind approach directions, e.g., N, NNE, NE, ENE, and E.

Once these parameters were developed in a gridded fashion for a domain of interest, an attempt was made to correlate them to a region-specific LULC classification scheme. If successful, such mapping could then serve as an extrapolation template to urban areas where no three-dimensional morphological information exists. In this modeling phase, the LULC template is shown in Table 2.3 (discussed later), which is applicable to the Sacramento and O-R regions.

The parameters in Table 2.1 are simply defined as the following:

1. Mean building height weighted by building plan area, defined as*:*

$$\bar{h}_{AW} = \frac{\sum_{i=1}^{N} A_i h_i}{\sum_{i=1}^{N} A_i} \qquad (8)$$

where A_i is the footprint area of building *i* and h_i is the height of the building.

2. Wall-to-plan area ratio (W2P) is defined as:

$$\lambda_W = \frac{A_W}{A_T} \qquad (9)$$

where A_W is the total surface area of the walls, and A_T is the area of the grid cell.

3. Building height-to-width ratio, H2W (λ_S) is calculated for any two buildings as:

$$\lambda_S = 0.5\frac{[H_1 + H_2]}{D} \qquad (10)$$

where H_1 and H_2 are the heights of two buildings along wind direction, and D is the average horizontal distance between them. Once the above parameters are known, they can be used in approximating the sky view factor. This is useful in scaling surface albedo to estimate effective urban albedo.

4. Plan area density is derived from:

$$A_p(z) = \frac{\frac{1}{\Delta z}\int_{z-\frac{1}{2}\Delta z}^{z+\frac{1}{2}\Delta z} A_P(z')dz'}{A_T \Delta z} \qquad (11)$$

where, $A_p(z')$ is the plan area of roughness elements at height z', A_T is area of the grid cell, and Δz is the height increment used in the calculation, e.g., 1 m.

5. Top area density within a height increment Δz can be approximated by the difference between the plan areas at two heights. Thus, the top area density function ($A_t(z)$) can then be defined as the top plan area of roughness elements per height increment Δz divided by the volume of the height increment:

$$A_t(z) = \frac{A_p\left(z - \frac{\Delta z}{2}\right) - A_p\left(z + \frac{\Delta z}{2}\right)}{A_T \Delta z} \qquad (12)$$

where A_T and A_p are as defined above. When top area density function is integrated from ground level to the top of the canopy, a new parameter λ_P is defined (this will be used later in equation (16) in roughness-length calculations):

$$\lambda_P = \int_0^{h_c} A_t(z')dz' \qquad (13)$$

6. Frontal area density (FAD)

$$A_f(z,\theta) = \frac{A(\theta)}{A_T \Delta z} \qquad (14)$$

where A(θ) is the area of roughness elements projected into the plane normal to the approaching wind direction (θ) within a height increment (Δz). This calculation can be done for any wind direction, but to minimize data, it is typically done for representative wind approach directions, e.g., N, NNE, NE, ENE, E, ESE, SE, and SSE (assuming opposite directions are similar). A related parameter is frontal area index, which is defined as the total area (A) projected into the wind approach direction (θ) (of all roughness elements) divided by the cell area (in this case) (to be used in equation (17) for roughness-length calculations):

$$\lambda_f\ (\theta) = \frac{A}{A_T} \qquad (15)$$

7. Finally, displacement height and roughness length (Z_d and Z_o) depend on computation of above listed parameters. There are several approaches to computing displacement height and roughness length, and each has its merits and disadvantages (Grimmond and Oke 1999). Here, a formula by Macdonald et al. (1998) is proposed since it is independent of u* (which would have required additional calculations based on knowledge of vertical wind profile at each location of interest, e.g., grid point):

$$\frac{z_d}{z_H} = 1 + \alpha^{-\lambda_p}\left(\lambda_p - 1\right) \qquad (16)$$

$$\frac{z_o}{z_H} = \left(1 - \frac{z_d}{z_H}\right)\exp\left\{-\left(0.5\beta\frac{C_D}{k^2}\left(1 - \frac{z_d}{z_H}\right)\lambda_f\right)^{-0.5}\right\} \qquad (17)$$

where Z_H is height, α is an empirical coefficient, C_D is a drag coefficient, k is the von Kármán constant, and β is a correction factor for the drag coefficient. Macdonald et al. (1998) recommended for staggered arrays of cubes that $\alpha \approx 4.43$ and $\beta \approx 1.0$. These values were also used by Grimmond and Oke (1999). In equation (17), the drag coefficient C_D is set at 1.2 and λ_f and λ_p are as computed in equations (15) and (13), respectively.

For the specific needs of the uMM5 in this application to *California*, there exist little data sources that can readily provide the UCP parameter inputs, e.g., those listed in Table 2.1. There is a significant national effort led by Burian et al. (2003) that has established morphological data for a number of metropolitan areas in the United States based mainly on use of LIDAR remote-sensed data. However, for California, Burian and co-workers developed only limited morphological data, e.g., for Los Angeles they characterized an area only about 3 × 3 km (as seen in Figure 2.3). From the National Statistics Building Database (NSBD), they also characterized a portion of San Francisco and Oakland (not shown). However, for the scale and special needs of this application there was no single appropriate data source that could be used to readily derive the UCP input. Therefore, an alternate approach was developed for this project and used, as explained next.

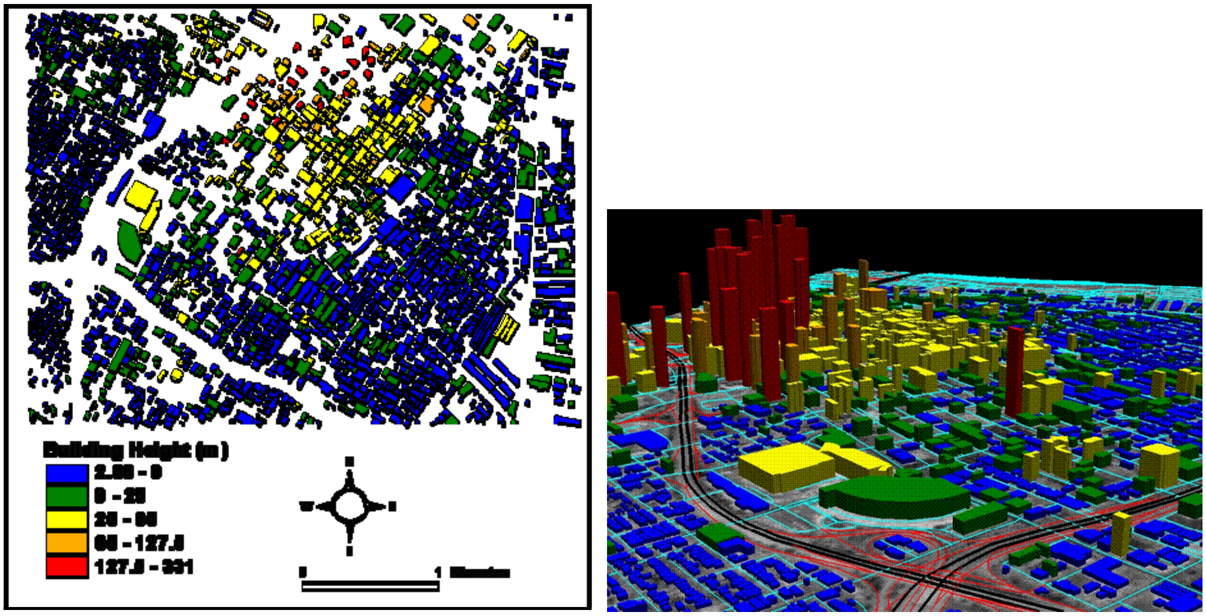

Figure 2.3. Geographical extent of existing morphological characterization of the Los Angeles area . Also see: www.civil.utah.edu/~burian/Research//UrbanData/UrbanDatabases.htm.
(Source: Burian et al. 2003).

During the initial stages of Phase 2, a number of land use and land cover (LULC) and urban data sources were examined from the point of view of generating and deriving the three-dimensional morphological parameters needed by the uMM5. The data sources included: (1) EarthData (www.earthdata.com), (2) i-cubed (www.i3.com), (3) Urban Data Solutions (www.u-data.com), (4) Vexcel (www.vexcel.com), and (5) Google's Earth Pro (Professional).

In addition, some other LULC data sources were considered, such as those of (1) the California Department of Forestry and Fire Protection, (2) the California Resources Agency, (3) the California Department of Water Resources, (4) the Southern California Association of Governments (SCAG), and (5) the Association of Bay Area Governments (ABAG). Considering the direct relevance to deriving three-dimensional urban geometrical characterization as well as the cost of data acquisition and level of processing involved, it was decided to use Earth Pro data as an optimal solution.

The methodology was first developed in this study and is a first of its kind as a simple alternative to exclusively LIDAR data. It involves a number of steps to characterize a region's morphology based on Earth Pro data. The first step involves accurately overlaying the uMM5 modeling grid (or any other model's grid) on the Earth Pro imagery and three-dimensional building information (an example shown in Figure 2.4**,** at the top of the figure). For this purpose, the latitude and longitude of the model's grid is carefully matched to Earth Pro's coordinates to ensure correct geographical collocation between the two. Thus each model's grid cell becomes an analysis plane (see the bottom of the figure). In this application, the analysis cells or planes were set at 500 × 500 m for the Sacramento and O-R uMM5 domains. Each cell then has a corresponding horizontal plane (of the same dimensions) whose altitude can be controlled by the user, as shown at the bottom of Figure 2.4. The plane can be moved in the vertical direction at any desired interval, here 1 m. The plane does not actually need to move at 1-m intervals, only when there is a change in the vertical profile function being derived, but the data is developed at and fed into the model at 1-m vertical intervals. The model ingests up to 300 levels (300 m AGL in areas with very tall buildings) of vertical function profiles such as building and vegetation canopy FAD, PAD, and TAD functions.

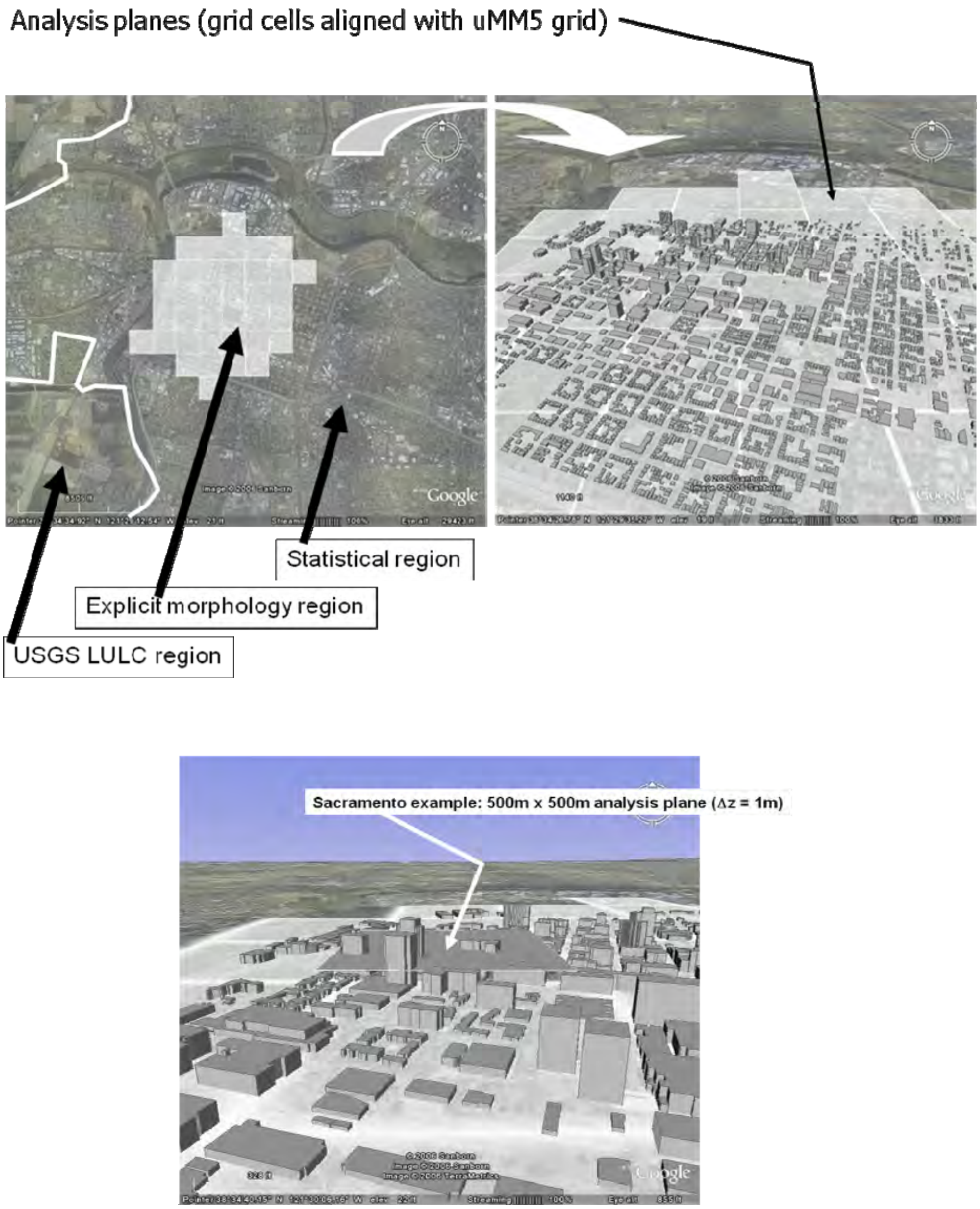

Figure 2.4. Aspects of using Earth Pro to derive three-dimensional morphology data for uMM5

At each vertical interval Δz of the plane's displacement (defining a computational volume X × Y × Δz, highlighted in blue in Figure 2.1) all parameters of interest are computed, such as FAD, PAD, and TAD for buildings and canopy cover. Those that require characterization at various wind approach directions are also computed by rotating the analysis plane so that the surfaces of interest (e.g., walls, canopy) face the wind approach direction of interest and facilitate the morphology calculations.

Other relevant characterizations and quantifications are also performed simultaneously while computing the PAD, FAD, and TAD functions as above. These include estimating (1) the fractions of roofs and pavements in each uMM5 grid cell or analysis plane that could potentially be available for surface albedo modification, and (2) the ground-level surface area and land-function that could be targeted for increased canopy cover. Land-use and land-cover identification is also carried out at this stage, as well as the derivation of other parameters not directly related to PAD, TAD, or FAD functions.

Although Earth Pro is very accurate in characterizing building geometry, one drawback of its use in characterizing *vegetation* canopy (aside from fractional cover and density) is that it lacks vertical profile information for vegetation. As a result, vertical functions related to vegetation, such as FAD, PAD, and TAD, are derived from a combination of sources, for example, idealized statistical correlations with LULC and canopy information from other studies and locations (e.g., Burian et al. 2003). Another drawback of using Earth Pro in such calculations is that it is a very tedious process that cannot be automated easily. Additionally, the three-dimensional geometrical data is not available for whole regions everywhere, only for relatively smaller selected sub-domains (selected by Google). To address these deficiencies, some method of morphological data extrapolation is needed. Thus the UCP surface characterization (the uMM5 morphological parameter input) in this second phase of the study involves four general "layers" or analysis domains (these are shown for Sacramento, as an example, in the top left part of Figure 2.4), as follows:

1. **Areas where three-dimensional urban geometry data is available.** This is the actual portion of a domain where there exists three-dimensional building and/or canopy information (it is labeled "explicit morphology region" in the figure). In these sub-domains, morphology parameters and functions are derived directly (explicitly) from observable features and properties, following the methodology discussed above. In addition to building geometry, the gridded LULC in this type of analysis domain is classified visually (tediously, yet accurately) and a new system was developed based on this analysis (see the LULC list in Table 2.3).

2. **Urban areas (urban land-use) where three-dimensional urban geometry is not available (statistical region).** These are other sub-domains where there is no three-dimensional building or morphological information but still have urban LULC (e.g., new urban areas or areas too large to cover with detailed geometrical characterization). In such sub-domains, three-dimensional morphology parameters are developed based on a statistical approach, where correlations are developed between morphology characteristics and fine-resolution LULC or land function (as listed in Table 2.3).

3. **Areas where urban and rural land-use information of interest is available, but there is no land-cover or morphology information.** In such areas, a fine-resolution LULC characterization (such as a 200 m USGS LULC characterization) is performed for the remainder of the analysis domain and used to override the model's default input (e.g., in this case, the default MM5 input). In such sub-domains the LULC is identified visually according to the 38/39-USGS LULC classification scheme, as summarized in Table 2.2.

4. Areas where only coarse USGS LULC data is available. The default USGS classification scheme is used for a coarse-domain (non.uMM5) characterization.

Table 2.2. USGS LULC classification scheme

Level I	Level II	Level III	Level IV
Urban or Built-Up (1000)	Residential (1100)	Single Family Residential (1110)	High Density Single Family Residential (1111)
			Low Density Single Family Residential (1112)
		Multi-Family Residential (1120)	Mixed Multi-Family Residential (1121)
			Duplexes, Triplexes, and 2/3 unit Condos (1122)
			Low-Rise Apartments, Condos, Townhouses (1123)
			Medium-Rise Apartments and Condos (1124)
			High-Rise Apartments and Condos (1125)
		Mobile Homes and Trailer Parks (1130)	Trailer Parks - High Density (1131)
			Trailer Parks - Low Density (1132)
		Mixed Residential (1140)	
		Rural Residential (1150)	Rural Residential High Density (1151)
			Rural Residential Low Density (1152)
	Commercial and Services (1200)	General Office Use (1210)	Low- to Medium-Rise Major Office (1211)
			High-Rise Major Office (1212)
			Skyscrapers (1213)
		Retail Stores and Commercial Services (1220)	Regional Shopping Center (1221)
			Retail Centers (1222)
			Modern Strip Development (1223)
			Older Strip Development (1224)
		Other Commercial (1230)	Commercial Storage (1231)
			Commercial Recreation (1232)
			Hotels and Motels (1233)
			Attended Pay Public Parking (1234)
		Public Facilities (1240)	Government Offices (1241)
			Police and Sheriff Stations (1242)
			Fire Stations (1243)
			Major Medical Health Care (1244)
			Religious Facilities (1245)
			Other Public Facilities (1246)
			Non-Attended Public Parking (1247)
		Special Use Facilities (1250)	Correctional Facilities (1251)
			Special Care Facilities (1252)
			Other Special Facilities (1253)
		Educational Institutions (1260)	Pre-Schools/Day Care Centers (1261)
			Elementary Schools (1262)
			Junior High Schools (1263)
			Senior High Schools (1264)
			Colleges and Universities (1265)
			Trade Schools (1266)

Table 2.2. (continued)

Level I	Level II	Level III	Level IV
		Military Installations (1270)	Military Base (Built-Up Areas) (1271) Vacant Military Area (1272) Military Air Field (1273)
	Industrial (1300)	Light Industrial (1310)	Manufacturing, Assembly, and Industrial (1311) Motion Picture and Television Studios (1312) Packing Houses and Grain Elevators (1313) Research and Development (1314)
		Heavy Industrial (1320)	Manufacturing (1321) Petroleum Refining and Processing (1322) Open Storage (1323) Major Metal Processing (1324) Chemical Processing (1325)
		Extraction (1330)	Mineral Extraction - Other than Oil and Gas (1331) Mineral Extraction - Oil and Gas (1332)
		Wholesaling and Warehousing (1340)	
	Transportation, Communication, and Utilities (1400)	Transportation (1410)	Airports (1411) Railroads (1412) Freeways and Major Roads (1413) Park and Ride Lots (1414) Bus Terminals and Yards (1415) Truck Terminals (1416) Harbor Facilities (1417) Navigation Aids (1418)
		Communication Facilities (1420)	
		Utility Facilities (1430)	Electrical Power Facilities (1431) Solid Waste Disposal Facilities (1432) Liquid Waste Disposal Facilities (1433) Water Storage Facilities (1434) Natural Gas and Petroleum Facilities (1435) Water Transfer Facilities (1436) Improved Flood Waterways and Structures (1437) Mixed Wind Energy Generation (1438)
		Maintenance Yards (1440) Mixed Transportation (1450)	
		Mixed Transportation and Utility (1460)	
	Mixed Commercial and Industrial (1500)		
	Mixed Urban (1600)		
	Under Construction (1700)		
	Open Space and Recreation (1800)	Golf Courses (1810)	
		Local Parks and Recreation (1820)	Parks (1821)

Table 2.2. (continued)

Level I	Level II	Level III	Level IV
		Regional Parks and Recreation (1830)	
		Cemeteries (1840)	
		Wildlife Preserves and Sanctuaries (1850)	
		Specimen Gardens and Arboreta (1860)	
		Beach Parks (1870)	
		Other Open Space and Recreation (1880)	
	Urban Vacant (1900)		
Agriculture (2000)	Cropland and Improved Pasture Land (2100)	Irrigated Cropland and Improved Pasture (2110)	
		Non-Irrigated Cropland and Improved Pasture (2120)	
	Orchards and Vineyards (2200)		
	Nurseries (2300)		
	Dairy and Intensive Livestock (2400)		
	Poultry Operations (2500)		
	Other Agriculture (2600)		
	Horse Ranches (2700)		
Vacant (3000)	Vacant Undifferentiated (3100)		
	Abandoned Orchards and Vineyards (3200)		
	Vacant with Limited Improvements (3300)		
	Beaches (Vacant) (3400)		
Water (4000)	Water, Undifferentiated (4100)		
	Harbor Water Facilities (4200)		
	Marina Water Facilities (4300)		
	Water Within a Military Installation (4400)		
	Area of Inundation (4500)		
No Data (0)			

Several LULC classification systems or schemes (public and private/specific) exist in this modeling application; however, because of specific model input requirements, a hybrid classification system was developed, in part based on USGS Level II categories and in part based on region-specific observations from Earth Pro (i.e., for the Sacramento and O-R domains). The categorization also serves the purpose of extrapolating UCP data to regions with no three-dimensional urban information, as discussed above. The classification scheme is listed in Table 2.3. Appendix A contains aerial snapshots illustrating each type of LULC class identified in Table 2.3, and Appendix B contains a comparison of the building characteristics.

Table 2.3. Study-specific LULC based on Earth Pro analysis of Sacramento and O-R domains

11	Residential
111	High-density
1111	Detached
11111	Single-Family
11112	Multi-Family
1112	Attached
11121	Single-Family
11122	Multi-Family
112	Low-density
1121	Detached
11211	Single-Family
11212	Multi-Family
1122	Attached
11221	Single-Family
11222	Multi-Family
113	High-rise/multi-family
114	Condominiums
115	Mixed residential (single/multi – attached/detached)
116	High-density, mobile homes/parks
12	Commercial
121	Low-rise commercial building; low-rise malls and strip malls
122	High-rise commercial; high-rise offices
13	Industrial
14	Transportation and utility, Airports, Highways
15	Mixed commercial and industrial
16	Mixed urban
161	Mixed commercial and residential
162	Mixed residential and transportation (highways)
163	Mixed green/open spaces and transportation (highways)
164	Mixed residential and recreation
165	Mixed residential and high-rise commercial
17	Other urban
18	Open space and/or recreation
19	Services
20	Downtown core
21	Urban high-rise
22	Academic and educational
23	Health services and hospitals
24	Sports
25	Other facilities, military, storage
31	Green / open areas / gold courses / vineyards and hills
99	Water, beaches, channels

Note: *High-rise* is defined here as five stories or taller.

A combination of the above approaches and data sources was used in completely characterizing the LULC and morphology of the Sacramento and O-R uMM5 modeling domains. Some examples of the resulting parameters and profiles are given below. Figure 2.5 shows the vertical profiles for PAD, FAD, and TAD functions in the *downtown* area of Sacramento, as an example, derived directly and explicitly from a region where three-dimensional morphological data is available (see Figure 2.4, where the white polygons delineate this area). For compactness, these vertical profiles were averaged for presentation in these figures (i.e., averaged per LULC type in downtown Sacramento).

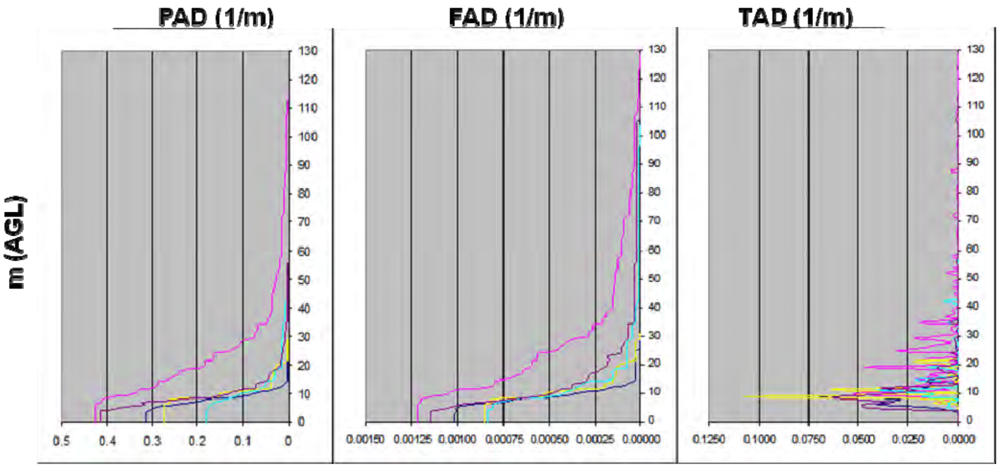

Figure 2.5. Example per-LULC vertical profile averages in Downtown Sacramento (representative of that area only). Red: commercial, Brown: mixed, Light blue: industrial/commercial, Blue: residential, Yellow: industrial.

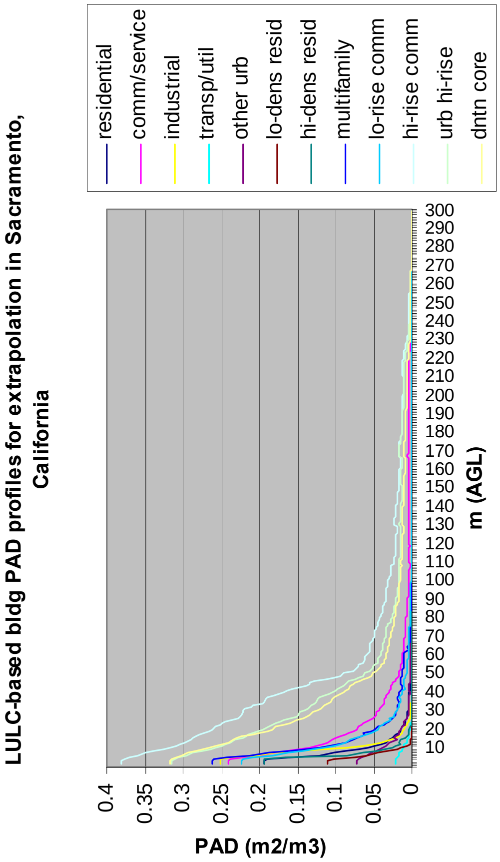

Figure 2.6. Building PAD profiles as a basis for extrapolation in non-UCP regions of the Greater Sacramento Valley area. PAD is then used in computing other parameters such as FAD, TAD, H2W, W2P, mean building height statistics, and SVF

While Figure 2.5 shows the vertical profiles pertaining to the area where three-dimensional morphology data is available, Figure 2.6 shows the profiles (for example, PAD) used for LULC-based extrapolation to areas where no three-dimensional morphology information is available in the greater Sacramento area. Following that, Figure 2.7 shows the vertical profiles for buildings and vegetation canopy that are used for extrapolation in the O-R domain.

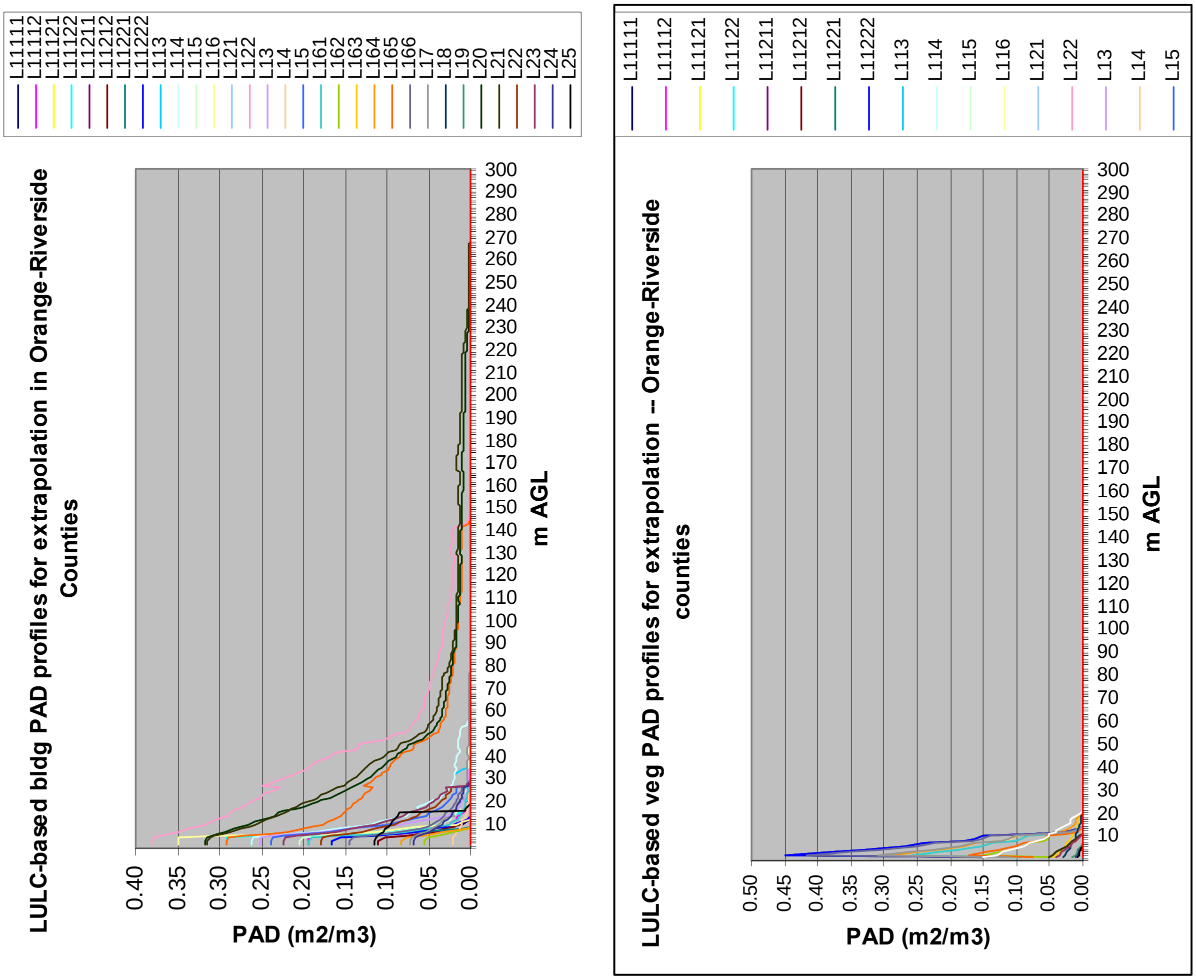

Figure 2.7. Building PAD (left) and vegetation PAD (right) profiles as a basis for extrapolation in non-UCP regions of the Orange-Riverside modeling domain. PAD is then used in computing other parameters such as FAD, TAD, H2W, W2P, mean building height statistics, and SVF. For LULC key (L### in the legend at top of figure), refer to Table 2.3).

The vertical characterization of the modeling domain within the UCL was thus completed for both the Sacramento and O-R uMM5 domains (the modeling domain selection is discussed later). In Figures 2.8 through 2.22 various aspects of this characterization exercise are shown, as examples. First, in Figure 2.8a the Sacramento uMM5 modeling domain is shown against the Google Earth Pro background and Figure 2.8b shows the urban area definition in Sacramento per USGS classification system that is a default input into the regular MM5. Note that the latter was *not* used in this study (instead, the morphology input was used to characterize the uMM5 domain) but is shown here to contrast the default urban outline used in conventional mesoscale modeling, versus the new outline as developed from the morphology work in this study (as seen in Figure 2.9, for example). The larger size of Sacramento in the latter compared to the former, older USGS LULC characterization of the area, is noticeable. Figures 2.9 through 2.14 show cross sections through PAD and FAD functions (for buildings and vegetation) at three arbitrary vertical levels to show how they vary with height in the Sacramento region. The FAD functions displayed in the figures are averaged over wind approach directions. The same type of information and sequence is shown again in Figures 2.15 through 2.22 but for the O-R modeling domain.

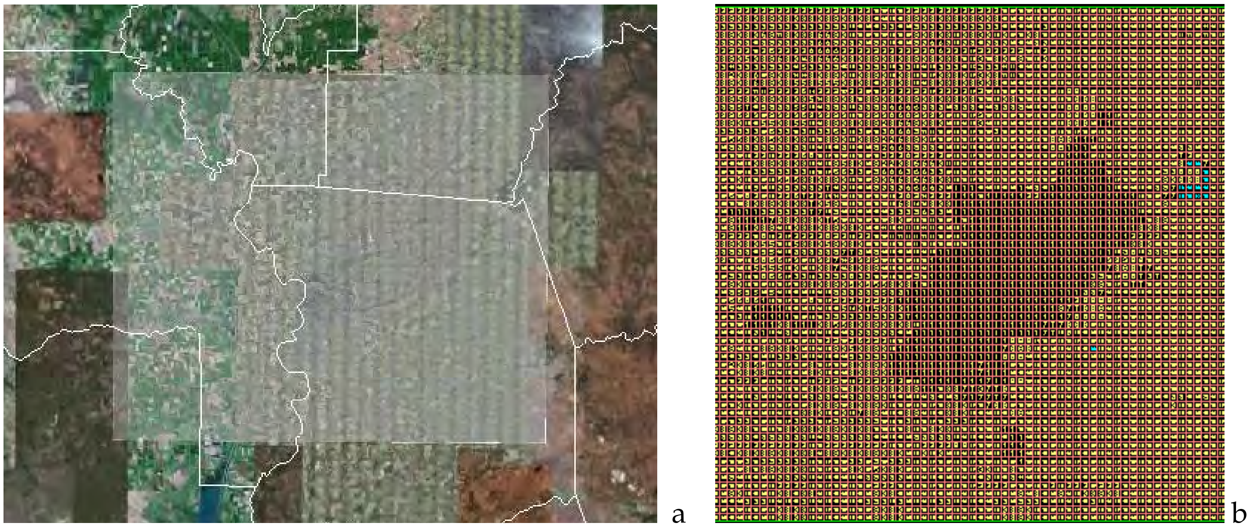

Figure 2.8. (a) Sacramento uMM5 domain overlaid on the Earth Pro background, (b) older outline of urban Sacramento per regular MM5 model input (based on USGS LULC classification scheme). Compare figure (b) with newer outline of urban areas in figure 2.9 based on morphology characterization work.

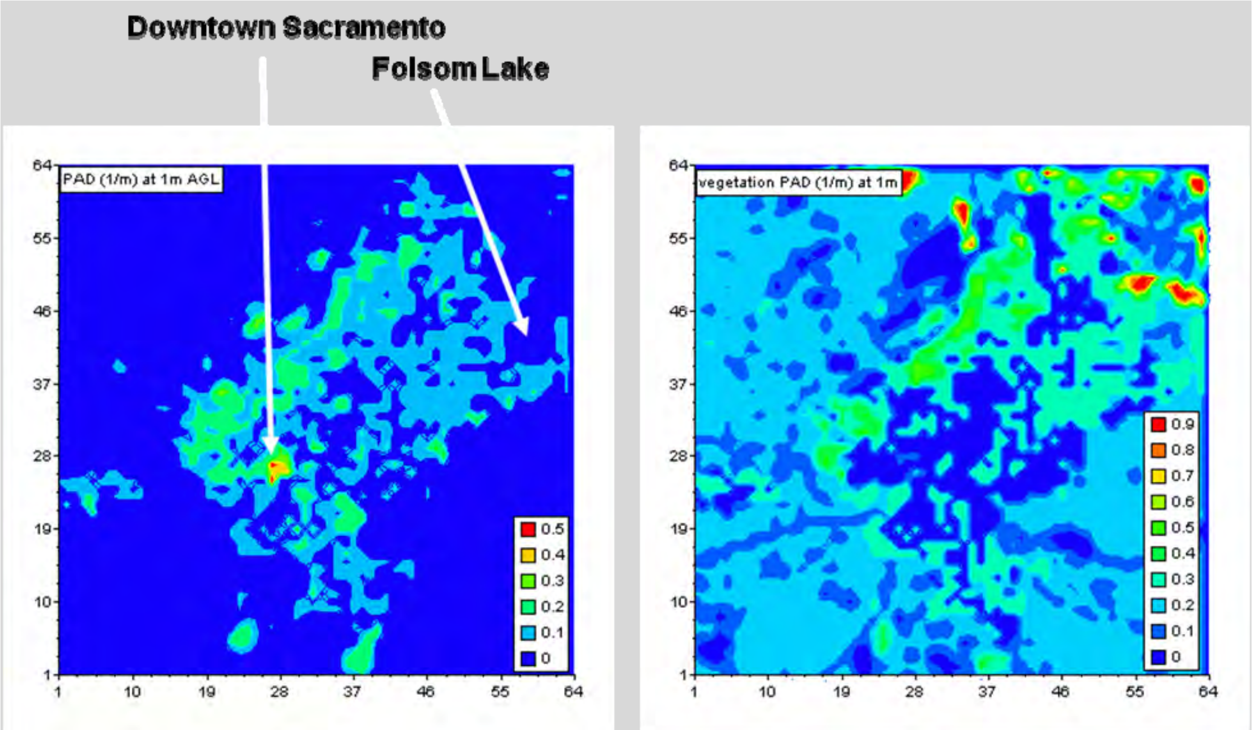

Figure 2.9. PAD function (m^2m^{-3}) for Sacramento uMM5 grid. Cross section at 1 m AGL for buildings (left) and vegetation canopy (right).

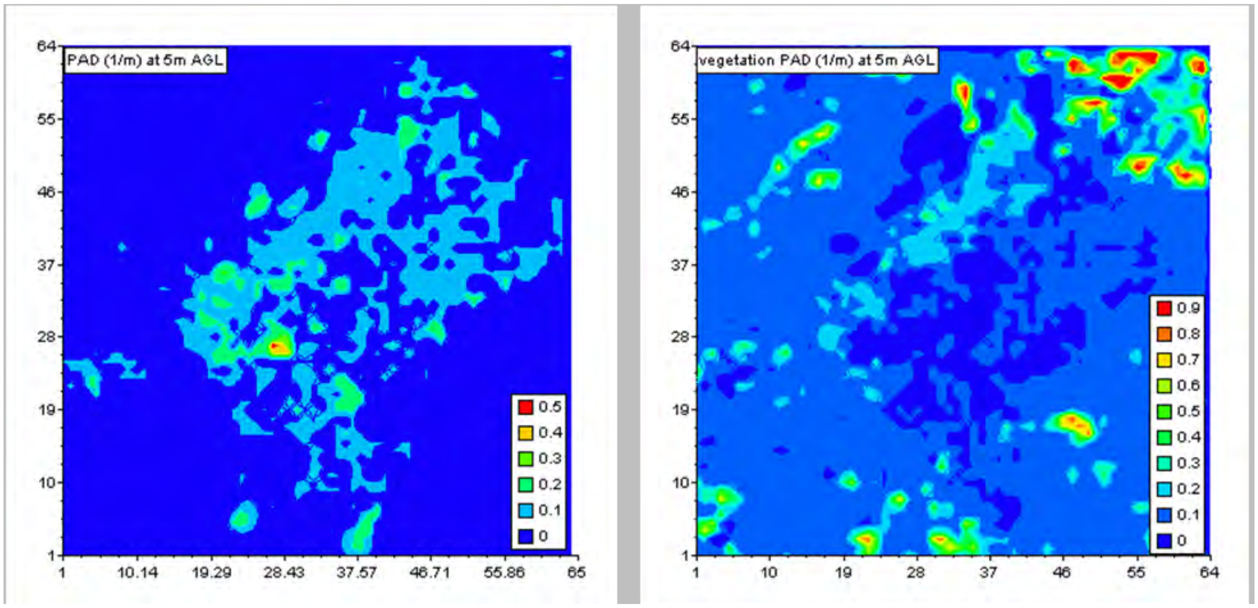

Figure 2.10. PAD function (m^2m^{-3}) for Sacramento uMM5 grid. Cross section at 5 m AGL for buildings (left) and vegetation canopy (right).

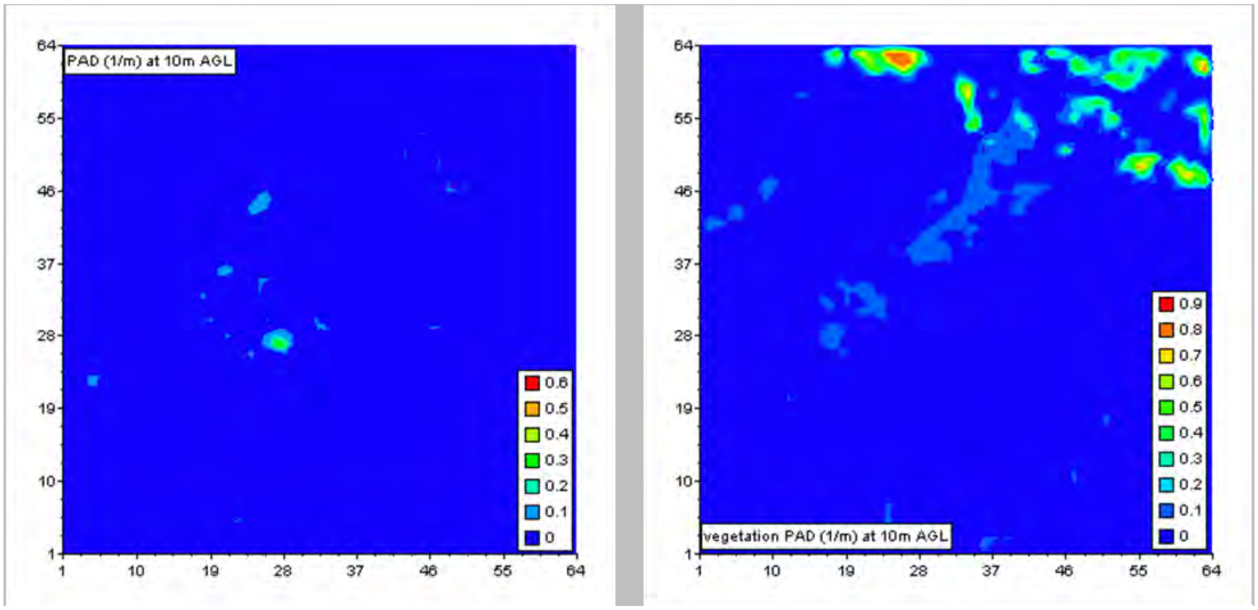

Figure 2.11. PAD function (m^2m^{-3}) for Sacramento uMM5 grid. Cross section at 10 m AGL for buildings (left) and vegetation canopy (right).

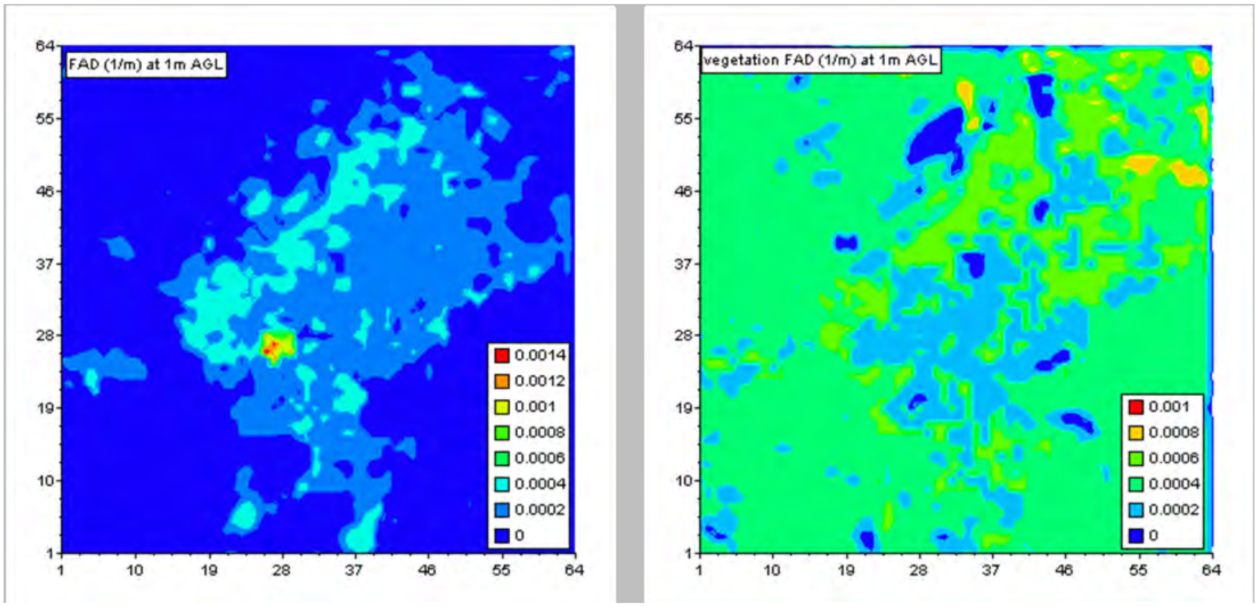

Figure 2.12. FAD function (m^2m^{-3}) for Sacramento uMM5 grid. Cross section at 1 m AGL for buildings (left) and vegetation canopy (right).

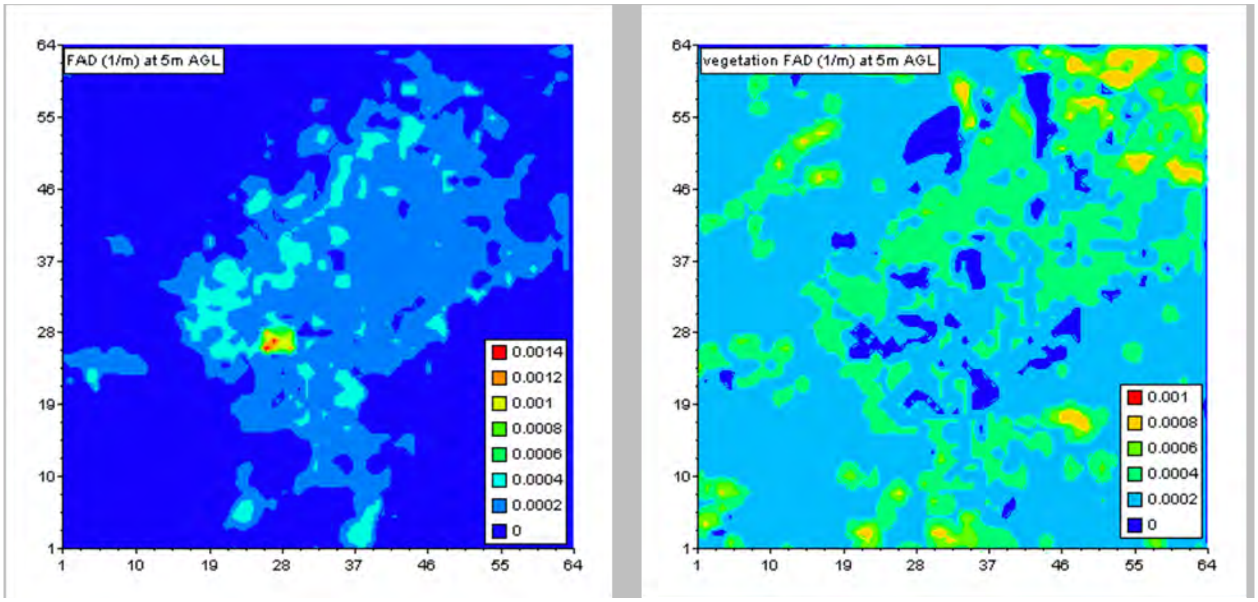

Figure 2.13. FAD function (m^2m^{-3}) for Sacramento uMM5 grid. Cross section at 5 m AGL for buildings (left) and vegetation canopy (right).

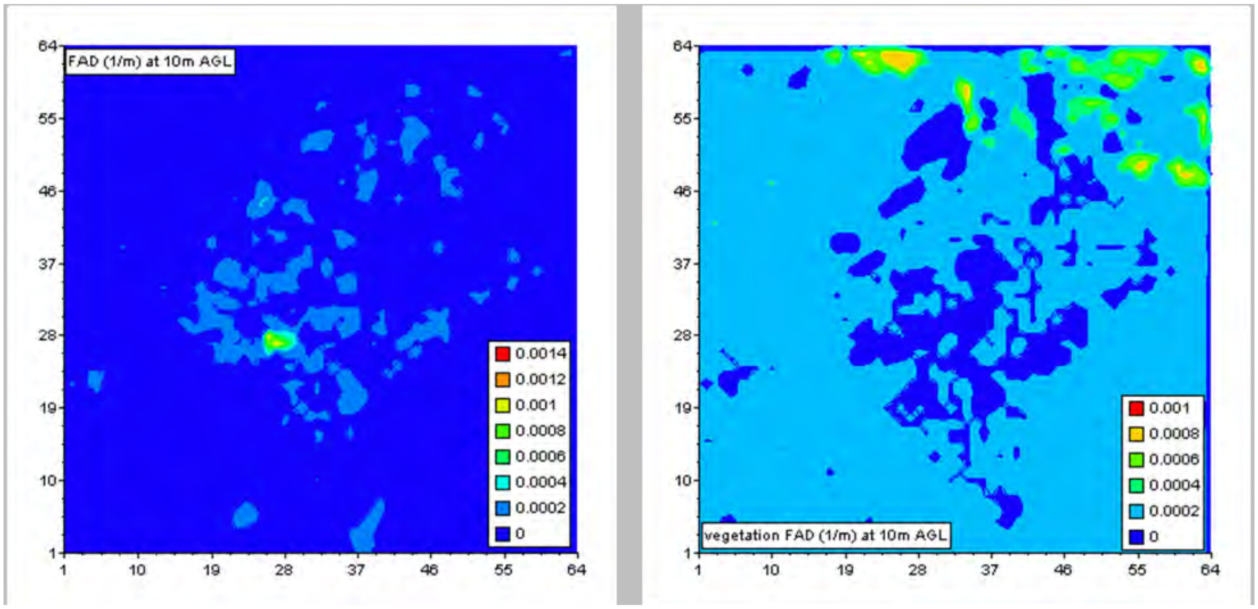

Figure 2.14. FAD function (m^2m^{-3}) for Sacramento uMM5 grid. Cross section at 10 m AGL for buildings (left) and vegetation canopy (right).

Figure 2.15a shows the O-R uMM5 modeling domain is against the Google Earth Pro background for Southern California and Figure 2.15b shows the urban area definition in O-R based on the USGS classification system default input into the regular MM5. Again, note that this LULC data was *not* used in this study (instead, the morphology input was used to characterize the uMM5 domain) but is shown here to contrast the default urban outline used in conventional mesoscale modeling versus the new outline as developed from the morphology work in this study (in Figures 2.16 for example). Figures 2.16 through 2.22 show cross sections through PAD and FAD functions (for buildings and vegetation) at three arbitrary levels to demonstrate how they vary with height in the O-R modeling domain region.

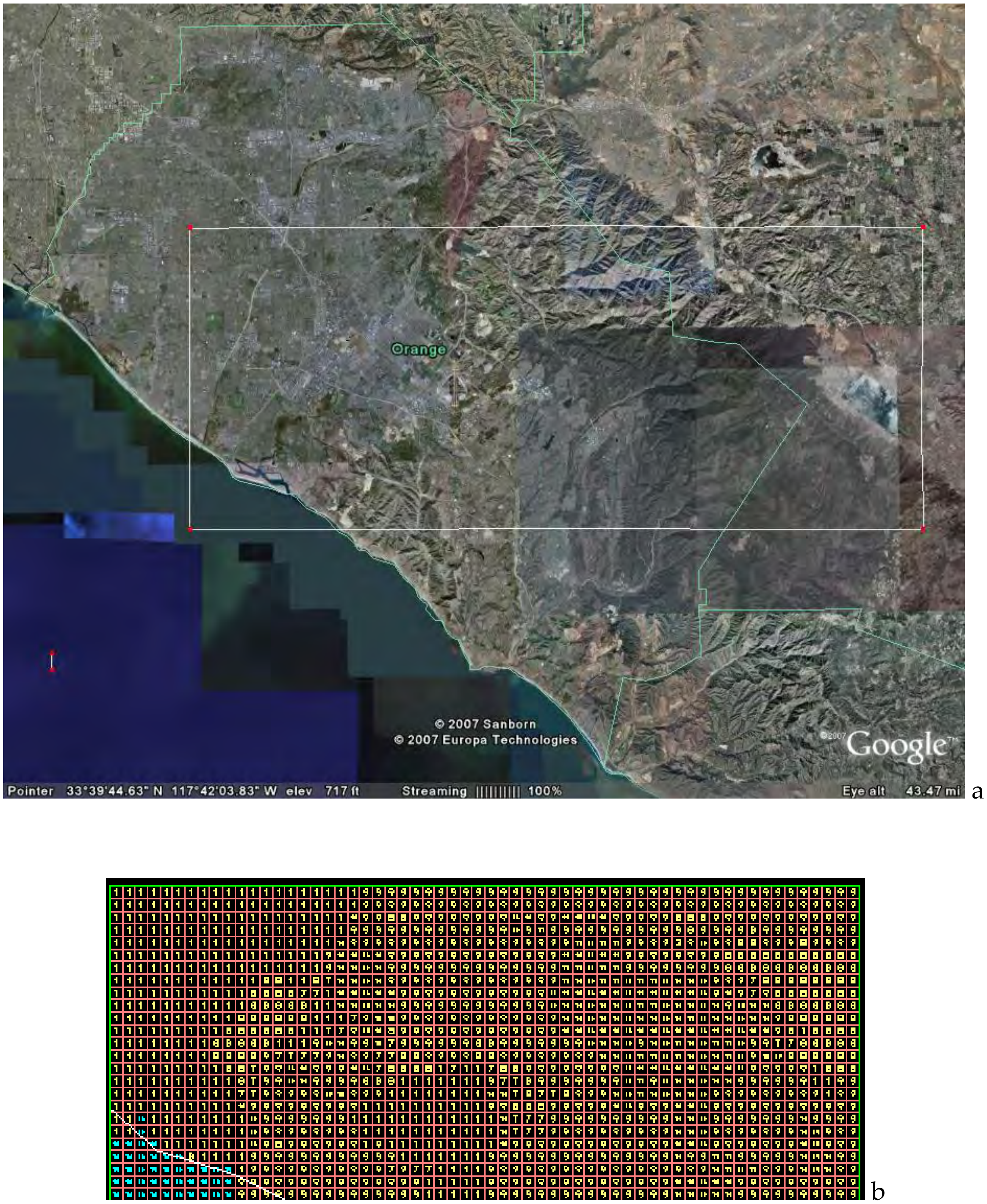

Figure 2.15. (a) O-R uMM5 modeling domain overlaid on Earth Pro background of the Southern California coast, (b) older outline of urban area per regular MM5 model input (based on USGS LULC classification scheme)

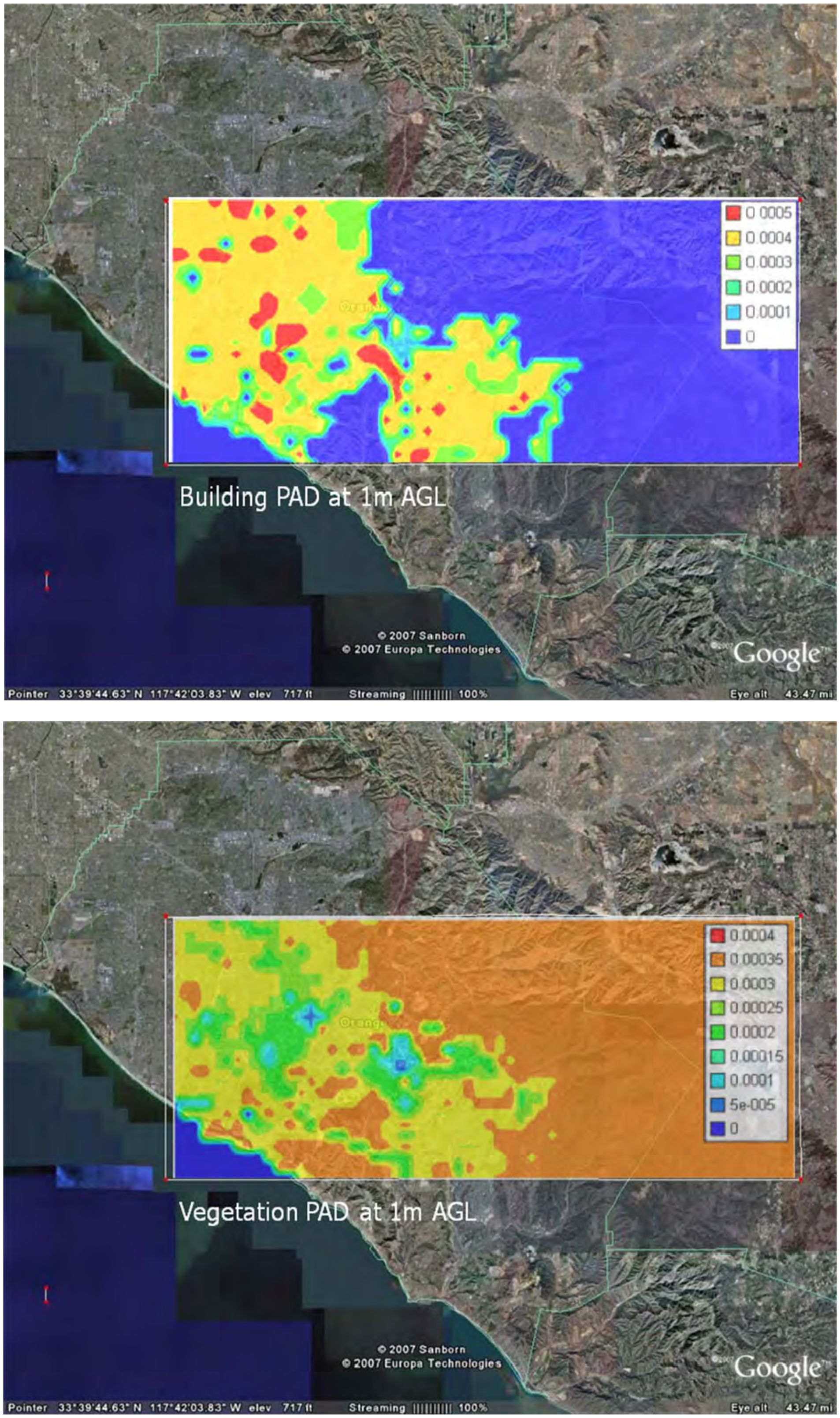

Figure 2.16. Top: building PAD at 1 m AGL; Bottom: vegetation PAD at 1 m AGL in the uMM5 modeling domain (highlighted) in the Orange–Riverside (O-R) counties in Southern California

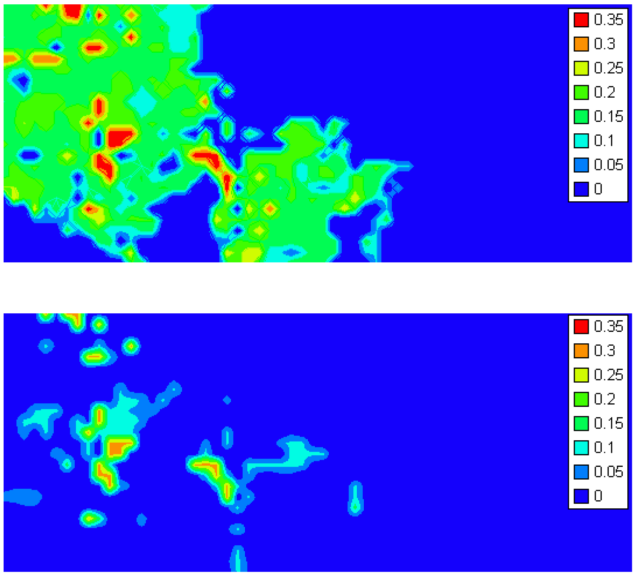

Figure 2.17. Building PAD at 1 m (top) and 10 m (bottom) in O-R modeling domain

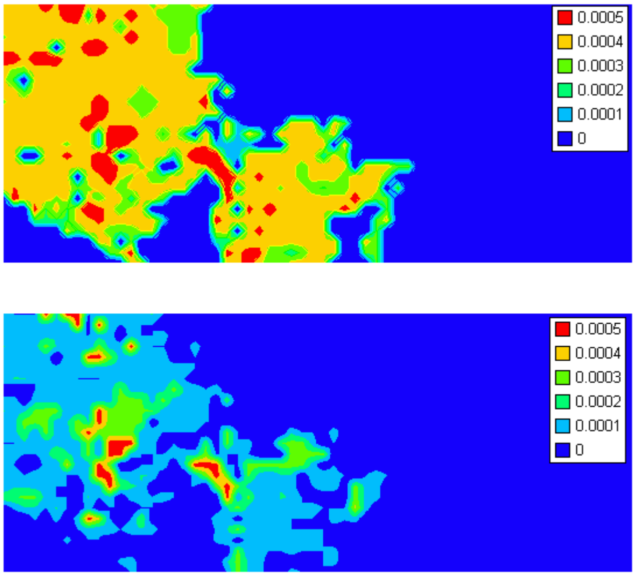

Figure 2.18. Building FAD at 1 m (top) 10 m (bottom) in O-R modeling domain

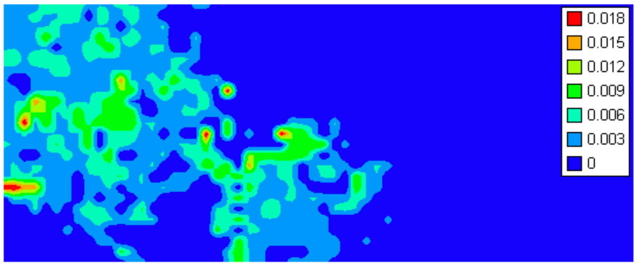

Figure 2.19. Building TAD at 10 m in O-R modeling domain

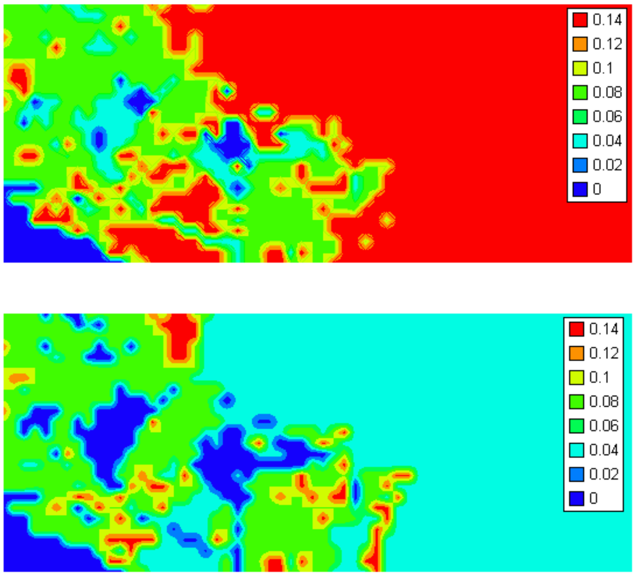

Figure 2.20. Vegetation PAD at 1 m (top) and 10 m (bottom) in O-R modeling domain

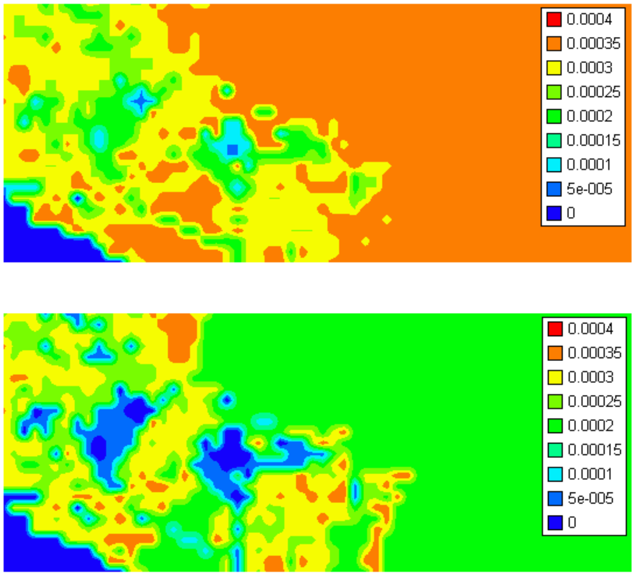

Figure 2.21. Vegetation FAD at 1 m (top) and 10 m (bottom) in O-R modeling domain

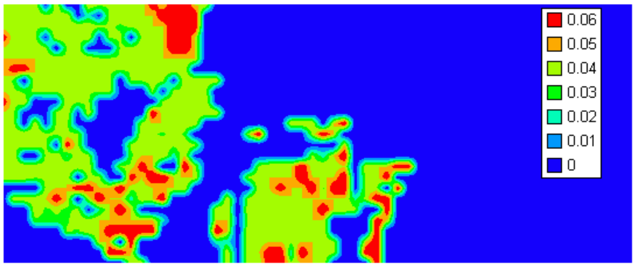

Figure 2.22. Vegetation TAD at 10 m in O-R modeling domain

2.4.2. Development of Surface Perturbation Scenarios (Heat-Island Control)

Since this section's discussion is related to surface characterization and surface properties, it is useful to introduce the basis for developing surface perturbation (UHI control) scenarios. The development of such scenarios was already discussed in detail in the Phase 1 final report. Surface perturbation scenarios evaluated in Phase 2 with the meso-urban meteorological and fine-resolution photochemical models include (1) albedo increase, and (2) canopy cover increase scenarios. Because of the difference in model formulation and input parameters (compared to Phase 1) and UCP scheme, it is not possible to directly compare the perturbation scenarios across both phases of the study. However, the fine-resolution UHI control scenarios developed in Phase 2 generally correspond to the higher end of such feasible modifications. In others words, the scenarios developed and discussed in this report represent some of the *larger* *reasonable* increases in surface albedo and canopy cover. The largest *reasonable* modifications are relatively large but still doable and practical, as opposed to largest *theoretical* increases, which are even larger but the feasibility of easily implementing them would be questionable. Therefore, the two scenarios of interest in Phase 2 were developed as follows:

- **Increased urban albedo:** generally similar to case20 modeled in Phase 1. This scenario was developed to test a case with some of the higher feasible increases in "per-surface" albedo, after accounting for the effects of weathering, aging, and dirt accumulation. The modifications to per-surface albedo are summarized in Table 2.4. To control glare, it is assumed that for walls and paved surfaces at pedestrian level, whenever the resulting albedo is over 0.35, that the increase is implemented using high-albedo materials that are dark in the visible range (discussed in the Phase 1 report). Such cases are highlighted in bold in the table. In addition, calculations were also modified to increase the effective albedo where deep urban canyons exist. These modifications were necessary because the model currently uses an average canyon orientation and geometry that may not capture the full effects of albedo increases in deep canyons throughout the day. The effective albedo is increased by 0.14.

Table 2.4. Per-surface modification in albedo

	Specification of surface-specific albedo					
	Roof		Wall		Paved	
	$\Delta\alpha$	New α	$\Delta\alpha$	New α	$\Delta\alpha$	New α
Residential	0.45	0.55	0.15	**0.40**	0.22	0.30
Commercial/Services	0.55	0.65	0.15	**0.40**	0.27	0.35
Industrial	0.55	0.65	0.20	**0.45**	0.27	0.35
Transportation/Communication	0.25	0.35	0.10	0.35	0.20	0.28
Industrial and Commercial	0.55	0.65	0.20	**0.45**	0.27	0.35
Mixed urban or Built up	0.45	0.55	0.15	**0.40**	0.22	0.30
Other urban or Built up	0.45	0.55	0.15	**0.40**	0.22	0.30

- **Increased canopy cover:** generally similar to case02 modeled in Phase 1. In this case, vegetative cover was increased only in those urban cells with a minimum of roof cover (0.02 or greater) by an amount equal to 0.20 (see the Phase 1 report for discussion). Because vegetative cover is increased (tree canopy), the exposed roof and pavement area (in areas of overlap with vegetation canopy) are decreased according to the overlap amount (by 0.1 each). This assumes a mature canopy shading the surface of roofs and pavements several years after the initial planting. In this scenario, only canopy cover (area fraction of vegetation and associated PAD/TAD functions) was perturbed. FAD was unchanged because elements of the canopy can shade each other (wind shadow). This is an aspect to further evaluate in detail in future vegetation canopy modeling efforts where, hopefully, more site-specific canopy-increase information will become available.

3.0 Model Applications

3.1. Modeling Domains Selection

In Phase2, fine-resolution grids were added to the coarse-grid configuration of domains used in Phase 1. Figure 3.1 shows the additional uMM5 grids for major urban areas in California. In this report, two regions were modeled with the uMM5 and fine-resolution CAMx: (1) the Sacramento region (which is the main focus of this model application), and (2) the Orange-Riverside (O-R) counties area in Southern California.

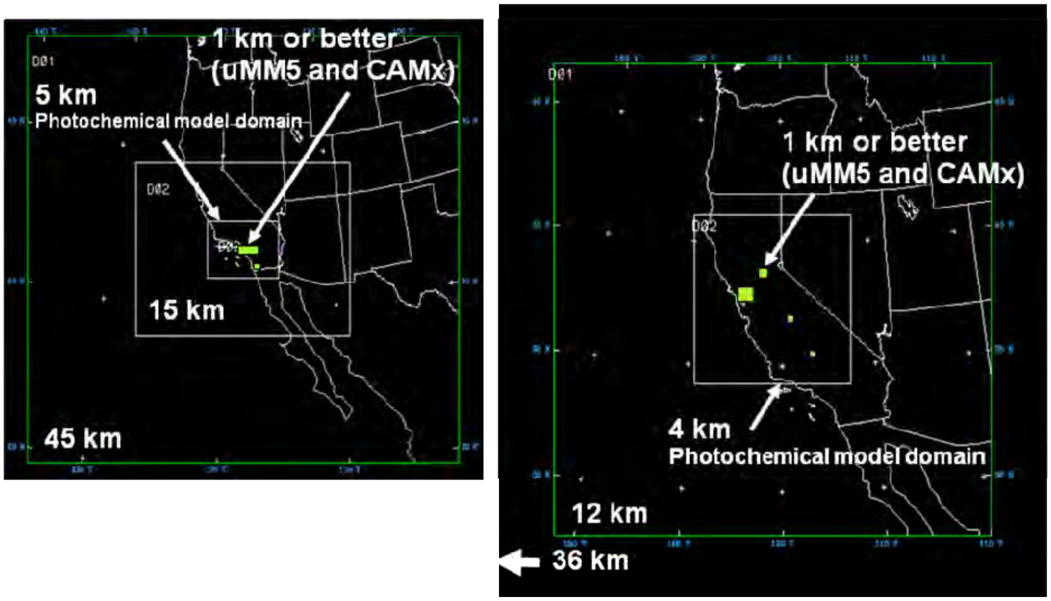

Figure 3.1. Modeling domains for phases 1 and 2 of the study (for Southern California, left, and Central California, right). The black background shows mesoscale meteorological modeling domains. The "mesoscale" photochemical modeling grids of Phase 1 (as also used by regulatory agencies) is shown as 5 km and 4 km grids, respectively. Green rectangles show meso-urban (uMM5) and fine-resolution CAMx modeling grids added in Phase 2.

For the Sacramento Valley, the fine-resolution domain was selected to encompass the entire region, including the city of Davis in the western portion (the horizontal dimensions of this domain are 64 × 64 km). The surface modifications inside this grid represent the impact of UHI control in the entire area. Unlike in Phase 1 modeling, upwind modifications were assumed non-existent in this case, i.e., the San Francisco Bay Area and other regions surrounding Sacramento were not affected by local surface modifications. Therefore, the simulations in Phase 2 were designed to test the effects of scenarios where only local modifications in urban Sacramento were carried out. The focus on Sacramento in Phase 2 was partly due to some local interest, for example, by regulatory agencies, in considering UHI control strategies.

For the Los Angeles-area simulations, the uMM5 domain was chosen to cut across the Orange-Riverside (O-R) counties line. The western part of the domain contains the cities of Santa Ana, Irvine, Tustin, Newport Beach, El Toro, Mission Viejo, and Laguna Hills. The eastern half of the domain is essentially barren. The domain was selected to capture the local peak ozone concentrations just east of the Santa Ana Mountains (SAM) range and south of the Corona area. The horizontal dimensions of this domain are 25 × 60 km (thus about one-third the size of the Sacramento domain). Unlike the Sacramento domain, which is flat and topographically uniform (Figure 3.2a), the peak concentrations in O-R domain typically occur outside of the western basin (that is, east of SAM) (Figure 3.2b). However, the peak concentrations in the eastern O-R domain result from transport from several areas in the Los Angeles basin and not only from the western part of the domain itself. One purpose of selecting this domain was to also test the effects of limited-area surface modifications in the western basin on the peak east of the SAM. In a way, this may be a worst-case UHI-control scenario (where one would expect small or no impacts, or even negative effects, on the downwind peak from surface perturbations).

Figure 3.2 shows the topography of these two fine-resolution domains. The Sacramento domain is essentially flat, except for mildly sloping terrain near the northeastern part. The O-R domain is effectively divided into two "basins" by means of the Santa Ana mountains reaching a maximum elevation of about 1300 m above mean sea level (AMSL). This topographical barrier and basin definition has an implication on the air-quality impacts of upwind surface modifications (as will be discussed in the Results section).

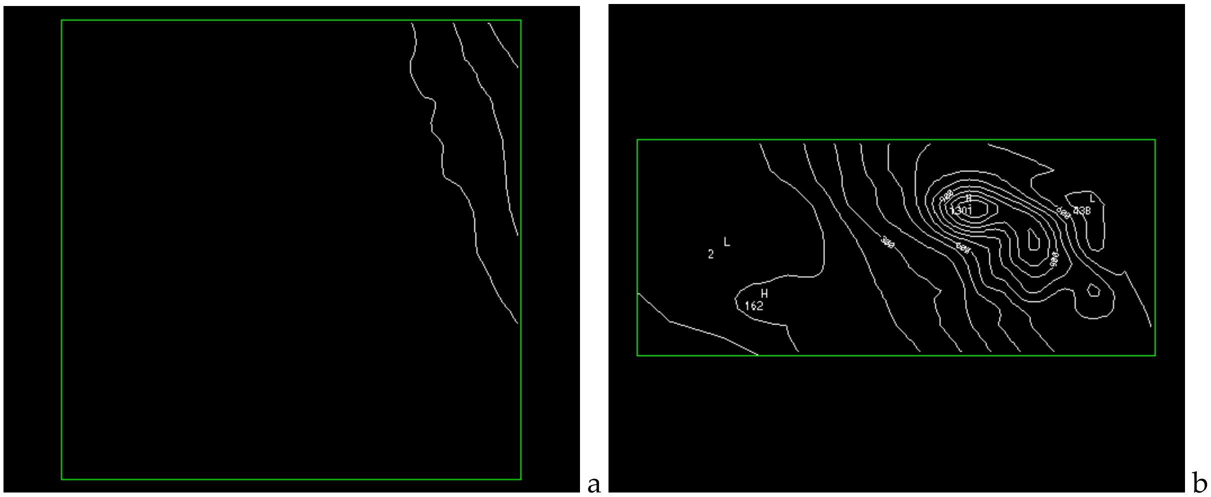

Figure 3.2. Terrain elevation (m AMSL) a: for the Sacramento uMM5 domain, and b: for the O-R uMM5 domain.

In summary, Table 3.1 provides overall information on meteorological model domain configurations, as well as a number of options used in the Phase 2 modeling.

Table 3.1. Summary of model domain configurations and options for MM5 and uMM5

Domain: CCOS / Sacramento	Resolution (km)	Dimensions (i,j,k)	Nest	LULC	LSM	Forcing	Analysis nudging (V,T,q)	Microphysics / Cooling	PBL	Cumulus
1	12	187,187,28	2-way	24	NOAH	NNRP + ADP	Domain	RRTM / Simple ice	MRF	Grell
2	4	187,187,28	2-way	38 modified	NOAH	NNRP + ADP	Above BL	RRTM / Simple ice	MRF	None
3 (UCP)	1	26,61,48	1-way	Morphology and model-specific LULC	SM2 soil model	Boundary conditions from 2nd domain	None	RRTM / Simple ice	Gayno Seaman	None

Domain: SCOS /O-R counties	Resolution (km)	Dimensions (i,j,k)	Nest	LULC	LSM	Forcing	Analysis nudging (V,T,q)	Microphysics / Cooling	PBL	Cumulus
1	45	68,80,28	2-way	24	NOAH	NNRP + ADP	Domain	RRTM / Simple ice	MRF	Grell
2	15	82,118,28	2-way	24	NOAH	NNRP + ADP	Above BL	RRTM / Simple ice	MRF	Grell
3	5	82,118,28	2-way	38 modified	NOAH	NNRP + ADP	Above BL	RRTM / Simple ice	MRF	None
4 (UCP)	1	65,65,48	1-way	Morphology and model-specific LULC	SM2 soil model	Boundary conditions from 3rd domain	None	RRTM / Simple ice	Gayno Seaman	None

In the vertical direction, the coarse (MM5) domains structure is based on the following (29) full σ levels:

1.0, 0.9975, 0.995, 0.988, 0.98, 0.97, 0.95, 0.93, 0.90, 0.87, 0.84, 0.80, 0.75, 0.70, 0.65, 0.60, 0.55, 0.50, 0.45, 0.40, 0.35, 0.30, 0.25, 0.20, 0.15, 0.10, 0.05, 0.025, and 0.0 with a model top at 100.

For the 1 km UCP (uMM5) grid, the following 49 full σ levels were used:

1.0000, 0.9995, 0.9990, 0.9985, 0.9980, 0.9974, 0.9968, 0.9960, 0.9952, 0.9940, 0.9925, 0.9905, 0.9880, 0.9850, 0.9800, 0.9700, 0.9600, 0.9450, 0.9300, 0.9100, 0.8900, 0.8650, 0.8400, 0.8100, 0.7800, 0.7500, 0.7100, 0.6800, 0.6450, 0.6100, 0.5700, 0.5300, 0.4900, 0.4500, 0.4100, 0.3700, 0.3300, 0.2900, 0.2500, 0.2100, 0.1750, 0.1450, 0.1150, 0.0900, 0.0650, 0.0450, 0.0250, 0.0100, and 0.0000.

For Phase 2, the photochemical model (CAMx) was configured with two domains each for Sacramento and O-R regions. These domains are slightly smaller than the corresponding meteorological grids. For the CCOS/Sacramento domains, the grid dimensions for the coarse (4 km) and fine (1 km) domains were 185 ×185 and 58 × 58, respectively. For the SCOS/O-R domains, the coarse (5 km) and fine (1 km) dimensions were 116 × 80 and 22 × 57, respectively. In the vertical direction, the photochemical model was configured with 16 levels. Other model options were discussed in the Phase 1 report.

Figure 3.3 depicts the three models' vertical levels interface. The MM5 and uMM5 domains in this study extend to roughly 15 km AGL (as implied by the upward-pointing arrows), whereas the CAMx domain extends to about 6.8 km. The levels (height in m AGL) at the right end of the figure show the interface heights, and the red lines indicate roughly the highest levels in the urban canopy layer in the Sacramento and O-R domains (roughly corresponding to the tallest buildings in each domain). As discussed earlier, the uMM5 has more vertical levels than either of the other models, and thus interfaces at levels 5, 8, 12, etc., while the other two models interface at levels 1, 2, 3, etc. In future modeling efforts, it may be desirable to further modify the CAMx vertical structure so that there is meshing (finer resolution) in the vertical, but this was not done at this stage because it is not a recommended practice, due to mass inconsistency concerns (Environ 2003).

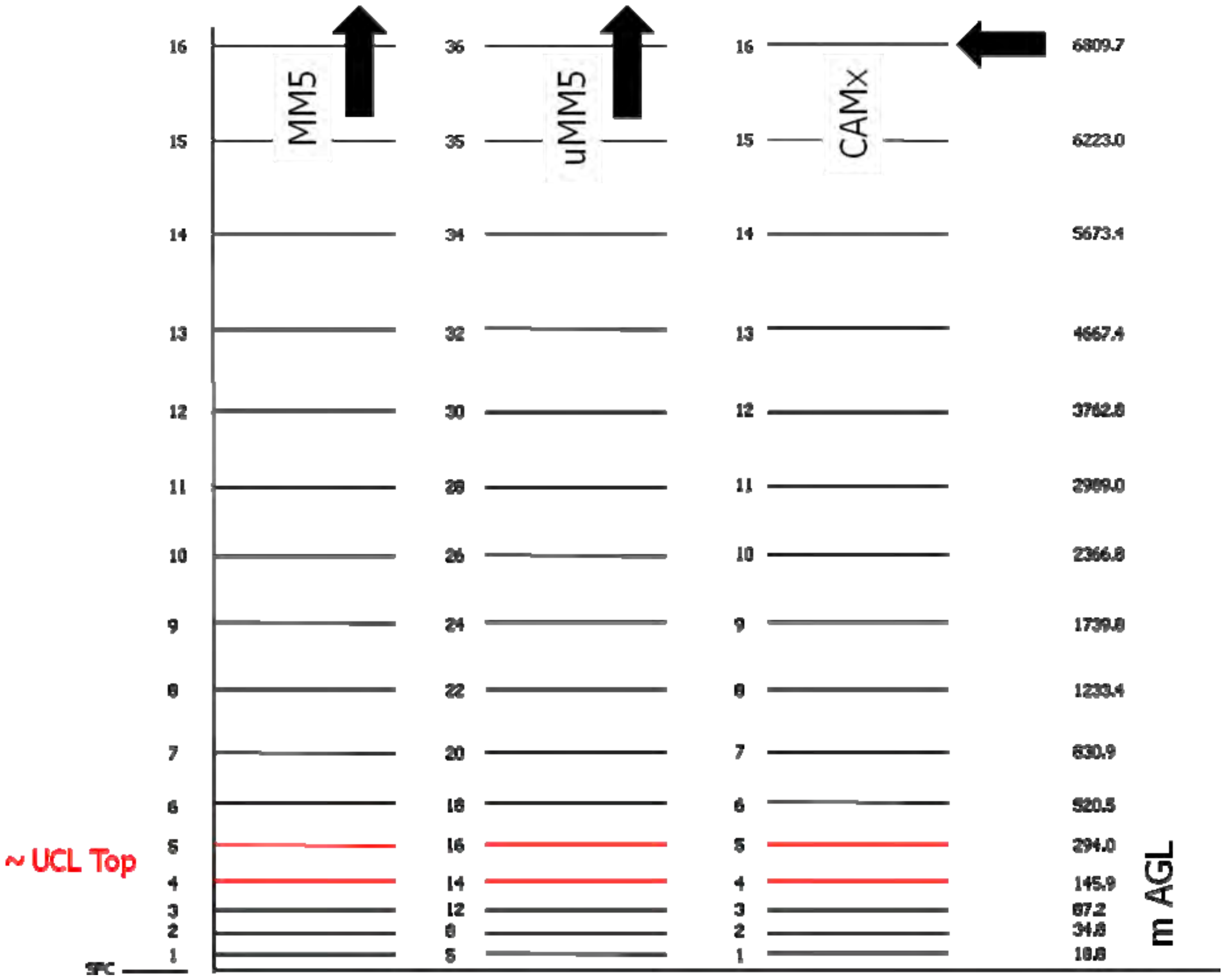

Figure 3.3. Vertical level interfacing among MM5, uMM5, and CAMx models as configured for this application (for both Sacramento and O-R domains)

3.2. Episode Selection

The episodes selected for analysis in both phases of this study are August 3–7, 1997, for Southern California and July 29–August 4, 2000, for Central California. Both episodes represent some of the worst-case conditions for ozone air quality in California. The Southern California episode resulted in the Los Angeles Basin's second highest annual maximum observed ozone concentration of 187 ppb in the Riverside-Rubidoux area. The episode occurred during typical ozone-conducive conditions, e.g., the presence of a high-pressure system, stagnation, small pressure gradients across the basin, high air temperatures, large solar radiation input (actinic flux), and capping inversions (inhibited mixing). Wind transport during the episode was moderate and onshore flow was generally weak as a result of the above conditions. Beginning August 6 of that episode, a coastal eddy developed and continued into August 7. This provided a mechanism for southerly transport of pollutants to the north and northwest of the Basin, as well as into the Santa-Clarita and Antelope Valley regions, where near-peak concentrations were also observed on August 6.

Peak inland temperatures in Southern California during that episode were frequently higher than 38°C and the highest temperature of 45°C in the Los Angeles Basin was observed in Riverside on August 5. The mesoscale temperature, wind, and pressure gradients were relatively consistent from the August 3 through 6, but changed later because of the eddy development on August 7. The peak observed ozone concentrations in the basin are summarized in Table 3.2.

Table 3.2. Observed peak ozone in the Southern California domain

Date in 1997	Observed peak	General location of observed peak
August 4	140 ppb	Central San Bernardino Mountains
August 5	187 ppb	Rubidoux
August 6	170 ppb	Central San Bernardino Mountains
August 7	150 ppb	Central San Bernardino Mountains

The Central California episode, especially on the primary day considered here (July31), was also characterized by strong inversions, as evidenced by a high 500-mb geopotential height and high 850-mb temperatures typical of subsidence motion. It was typical of the conditions conducive to ozone build-up, e.g., Pacific high-pressure system and its extension over California preventing cyclonic systems from passing though the area. As mentioned above, the result is typically a stagnant air mass that is poorly mixed. In all days of the episode, high ozone was observed in Livermore and transport from the San Francisco Bay Area was strong; some days to the southeast (San Joaquin Valley) and other days to the northeast (Sacramento). Flow through the Bay Area affected regions in Fresno and Bakersfield, but had no direct impact on Sacramento on July 31. The flow arriving at Sacramento on that day passed further north of the Bay Area. On August 1, however, the flow went directly through the Bay Area and thus the higher ozone in Sacramento. The peak observed ozone concentrations in various areas of Central California are summarized in Table 3.3.

Table 3.3. Observed peak ozone in the Central California domain

Date in 2000	Observed peak	General location of observed peak
July 31	126 ppb	Livermore
August 1	133 ppb	Sacramento
August 2	151 ppb	San Joaquin (Edison)

4.0 Meteorological and Air Quality Modeling Results

The discussion in this section is only for results from the fine-resolution uMM5 meteorological grids and the corresponding fine-resolution CAMx grids. The coarse-grid results (both meteorological and photochemical) were discussed in detail in the Phase 1 report and will not be repeated here. As in Phase 1, the discussion is related to air temperature and its change in response to surface modifications, because the focus of the study is on urban heat islands. In terms of air quality, the focus is on ozone.

The discussion begins with the Sacramento area. The Orange-Riverside area (O-R) was added to get further insight into potential impacts of modifications in small areas within a larger urban metropolis and to shed some light onto the potential negative impacts on ozone that were identified in Phase 1 (the so-called "threshold effect"). While the simulations of the Sacramento region were designed to test the potential impacts of changes in surface properties in an integral urban region, the O-R simulations were designed to test the potential impacts of limited-area modifications.

4.1. Sacramento uMM5 Grid

4.1.1. Base Case

Heat Island

Figure 4.1 (a–y) shows the base-case simulated air-temperature and wind-vector fields at 10 m AGL for the Sacramento domain. It shows those fields at three-hour intervals starting at 0000 LST on July 31 (the 56th hour of forecast) and ending 72 hours later, at 0000 LST on August 3, 2000 (the 128th hour of forecast). The actual simulations are longer, starting at 1700 LST on July 28 and ending at 1500 LST on August 3, but in this discussion, the focus is only on July 31, August 1, and August 2.

Figure (a), at 0000 LST July 31, depicts a night-time urban heat island (UHI) from earlier in the evening. The UHI, 2°C–3°C in magnitude, is displaced to the north-central part of the domain by the southerly flow. This pattern remains through 0300 LST (b) with essentially unchanged winds at a maximum of 5 ms^{-1} predominantly from the south. At 0600 LST, the flow pattern changes, now with both southerly and northerly components creating cyclonic flow southwest of and including the downtown Sacramento area (the downtown area is shown roughly with the inscribed black square). The UHI is also relatively unchanged, at about 2°C.

By 0900 LST 9 (d), the flow has changed to northerly throughout the domain, and the UHI has disappeared. The urban area is now cooler than surrounding areas (especially near the upwind ones to the north). This is likely due to the effects of street canyons and building shadowing and thermal mass effects that delay the early-morning heating of urban areas. At 1200 LST(e), the domain-wide temperature at 10 m AGL is in the range of 33°C to 38°C, with northwesterly winds and no UHI. The area to the north and west of Sacramento is still about 1°C warmer than the urban area, mainly due to the effects discussed above. By 1500 LST (f), most of the domain is at about 37°C, while the first signs of a UHI appear over the urban area immediately surrounding downtown Sacramento and to the northeast of it. At this hour, the UHI is only

1°C—that is, the urban area is now warmer than its surroundings, which is the opposite of 1200 LST, when it was about 1°C cooler then upwind areas.

The UHI intensifies further by 1800 LST (g), reaching 2°C or more relative to upwind areas to the north and northwest. While the flow is still mainly northwesterly, some stronger westerly component also develops. The UHI at this hour is spatially larger, covering areas around downtown, to the southeast, east, and northeast. It becomes better defined by 2100 LST (h) with a magnitude of up to 6°C relative to upwind areas to the southwest. The UHI covers an area significantly larger than at earlier times, and because of its intensity, flow convergence develops around downtown Sacramento with a cyclonic flow pattern.

At 0000 LST August 1 (i), a well-defined UHI is seen over the urban areas, stretching generally from the southwest to the northeast. The peak of this UHI is displaced with the wind to slightly south of downtown Sacramento. At that location, the UHI is 5°C relative to the upwind areas. There also is a strong convergence and cyclonic flow features around downtown Sacramento and the UHI area in general (UHI circulation). By 0300LST (j), the UHI pattern is still generally similar to that at 0000 LST, albeit at smaller magnitudes (now about 3°C) and more diffuse (less defined as earlier). A similar pattern is seen at 0600LST (k) with a slightly weaker UHI and convergence around the urban area.

At 0900 LST (l), the UHI disappears and by 1200 LST (m), the urban area is again cooler than the surrounding regions by about 1°C. The flow is mainly from the west and northwest. At 1500 LST (n), the urban area, for example, near downtown and to its southeast (downwind), begins to create a UHI (which at this hour is 1°C) and the diurnal cycle repeats itself. Thus by 1800 LST (o), the UHI is again spatially significant and at about 4°C relative to upwind areas to the southwest and the west and the UHI is advected to the eastern portion of the domain by 2100 LST (p) with a magnitude of about 4°C. At 0000 LST on August 2 (q) the UHI is well defined again (spatially) and is advected downwind to the northeastern portion of the domain and with a magnitude of 3°C relative to the upwind area that is southwest of downtown.

At 0300 LST on August 2, the UHI is displaced downwind to the north (with southerly flow) and is more diffuse (less well-defined than at 0000 LST) and with a magnitude of 2°C–3°C (r). A similar pattern exists at 0600 LST (s). The UHI disappears at 0900 LST(t) and the area is a cool island again through 1200 LST (u) by up to 2°C cooler than surrounds and a small UHI develops at 1500 LST (v) exactly at downtown Sacramento (at a magnitude of 1°C). The cycle continues through 0000 LST on August 3 (figure y) with a well defined UHI advected downwind and at a magnitude of 3°C relative to downtown and other upwind area.

Therefore, to attempt to summarize the UHI pattern, the simulations generally produce a UHI that starts small (~1°C) at 1500 LST, grows to about 2°C–4°C by 1800 LST, peaks around 2100 LST (at up to ~6°C), then begins to shrink so that it is at 2°C–3°C (up to ~5°C) by 0000 LST, and continues to get smaller so that between 0900 and 1200 LST, there is no UHI at first and then the urban area becomes ~1°C–2°C cooler than the surrounds. Finally at around 1500 LST, the UHI develops again (~1°C) and the cycle is repeated diurnally through the episode.

The meso-urban simulations capture details that are generally not possible to see in mesoscale or coarser simulations, e.g., cool islands during the pre-noon hours and heat islands during the afternoon and through the night. The simulations suggest a relatively stronger nighttime than daytime UHI in the Sacramento region for the episodic and surface conditions simulated in this phase of the study. The UHI cycles with a peak around 0000 LST in general and the daytime UHI is on the order of 2°C and occurs later during the day. The simulations also clearly show the downwind displacement (advection) of the heat island.

The meso-urban simulations also capture the fine-resolution divergence/convergence features of the flow that was not detectable in Phase 1 mesoscale modeling at 4 km resolution (CCOS domain and episode). Some of the convergence and cyclonic flow occurrences were discussed above. The model also captures the slower wind speeds over urban areas (due to drag and roughness) at various times of the episode. The simulations show that the urban-area winds can be 2–3 ms^{-1} slower compared to upwind or surrounding areas during the early morning hours, e.g., 0600 LST (c and k), 0900 LST (t), and later during the day, 1800 LST (w).

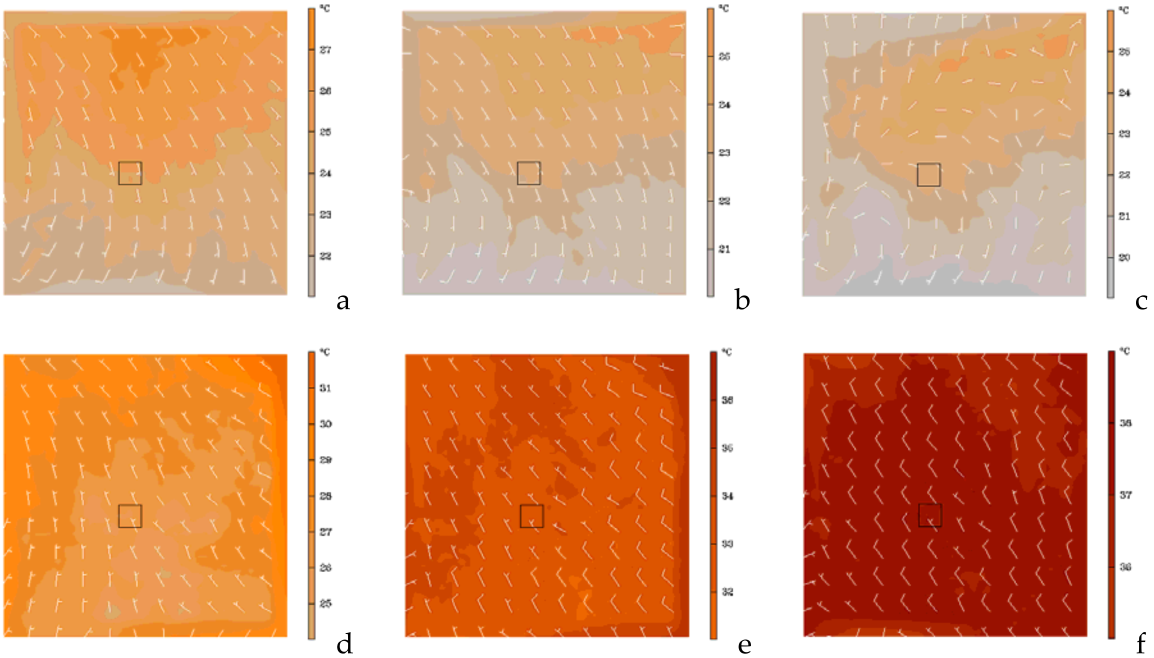

Figure 4.1. Simulated base-case air temperature and wind vector fields for the Sacramento uMM5 domain

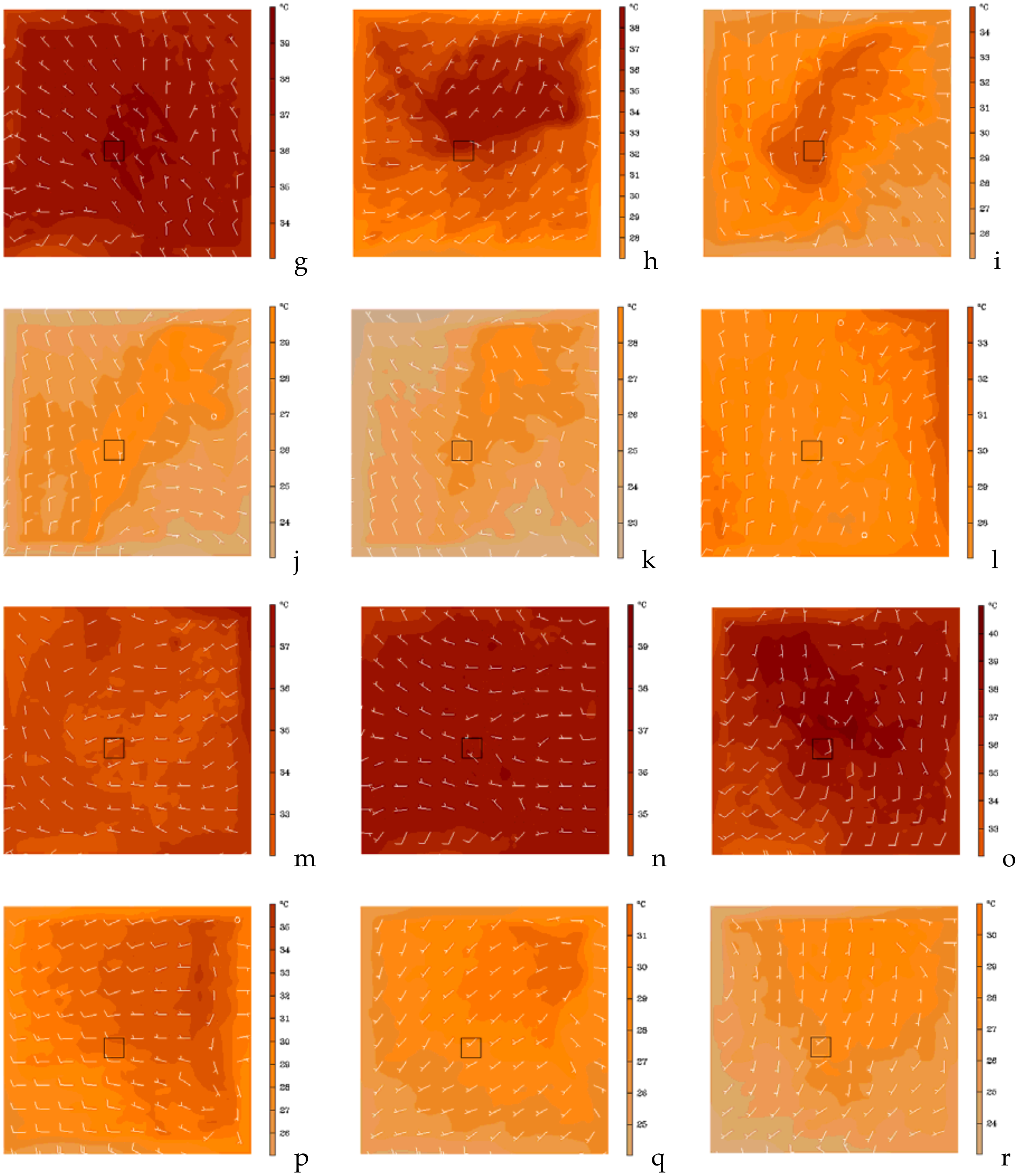

Figure 4.1. (continued)

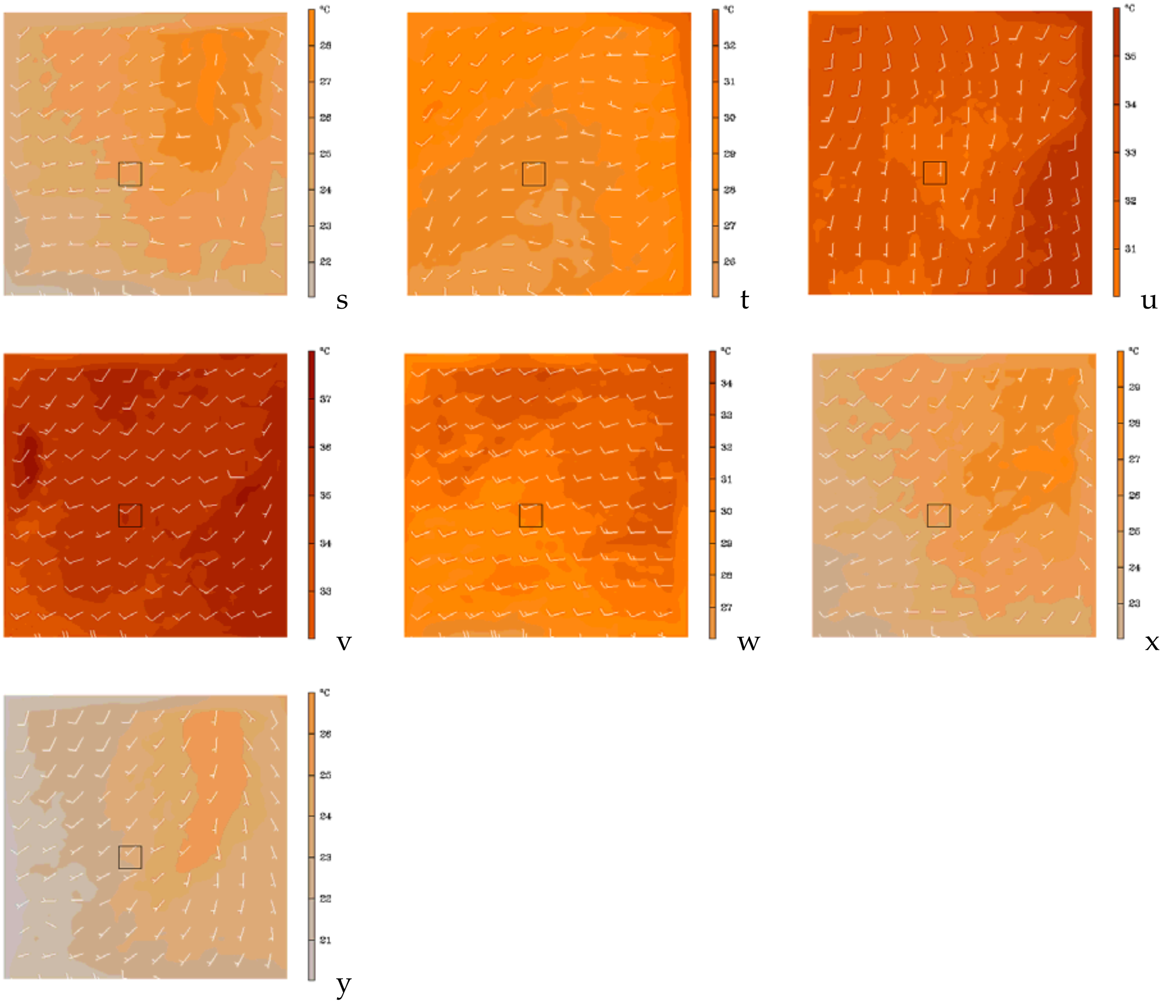

Figure 4.1. (continued)

In Figures 4.2 and 4.3, two arbitrary locations were analyzed for air temperature differences. The locations represent a mixed residential-commercial land-use (RC) at grid location (39,30) and a residential area (R) at grid location (21,29). Figure 4.2 shows the diurnal temperature swing at both locations reaching up to 40°C on July 31 and August 1. In addition, Figure 4.3 shows difference in air temperature between these two locations. The residential-commercial area is generally warmer than the residential area most of the time. It is warmer by about 2°C, with a few time intervals up to 4°C. It can also be cooler at certain times, e.g., earlier during the daytime, by up to 1°C, for the reasons discussed above (shadowing and thermal mass).

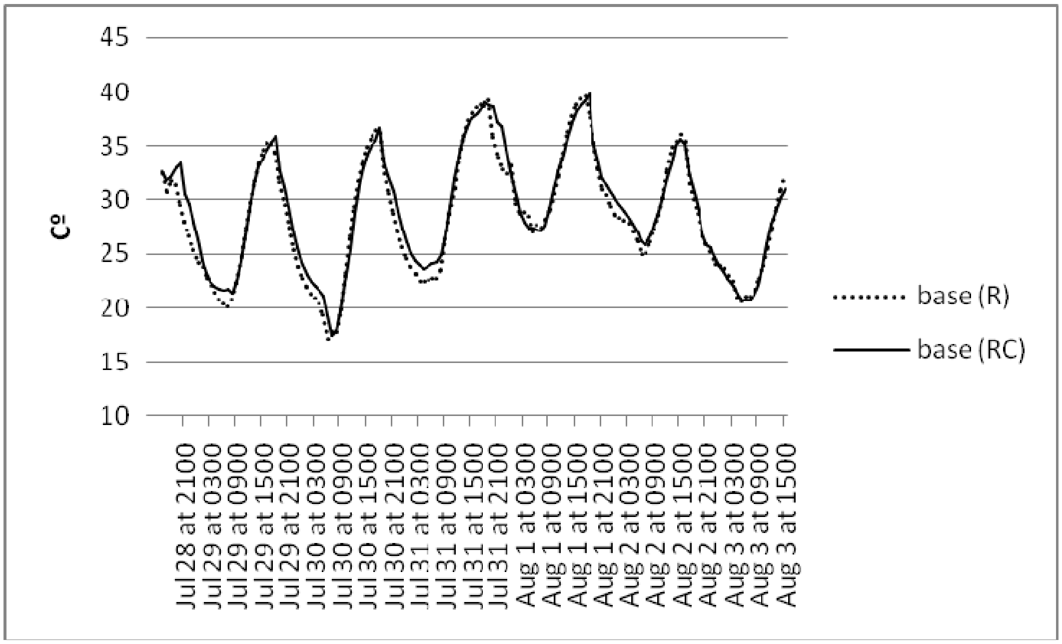

Figure 4.2. Simulated air temperature at a residential-commercial area and a residential area in Sacramento

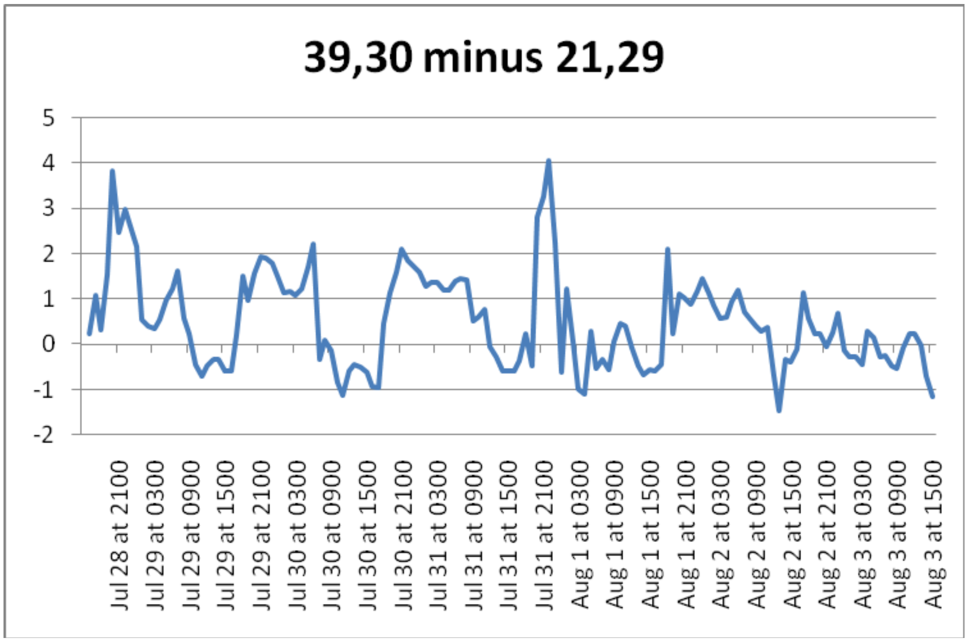

Figure 4.3. Simulated air temeparture differnce (in the base-case scenario) between a residential area and a residential-commercial area in Sacramento

In addition to evaluating the wind and temperature fields throughout the domain, and at certain locations as examples (as above), the model's ability in simulating the fine-resolution vertical profiles of meteorological fields, e.g., in the UCL, was also evaluated, as discussed in the next example. For the following discussion, a number of parameters of interest are plotted as a function of height at a selected hour, e.g., 1400 LST August 1, an hour-of-day of typically high temperatures (unstable conditions) and ozone. (Of course, any other period could have been selected as well—this is just an example). In this discussion, building or vegetation canopy FAD (as appropriate) is used as a surrogate to buildings or vegetation density and their distributions in the vertical inside the canopy layer.

In Figures 4.4 to 4.7, data are plotted for a number of vertical levels up to each grid cell's UCL top. In these examples, the UCL top is at 109 m in grid 28, 28; 19 m in grid 39,30; and 35 m in grid 59,60. In the figures, TKE production terms are plotted as positive, whereas dissipation terms are negative. The first two grid cells have mostly buildings and some vegetation, whereas the last is a vegetation canopy grid cell with forest cover near the Auburn area, northeast of the uMM5 domain. Each figure shows the cell's FAD profile (in m^2m^{-3} scaled by 30 to fit the figure's scale), wind speed (ms^{-1} scaled by 1/100 to fit the figure), and several TKE budget components. The latter include the buoyancy and shear production terms and dissipation and accelerated cascade terms. All are in units of m^2s^{-3} (note that there are a number of other budget terms not shown and that can be more dominant and explain the behavior of the profiles depicted in these figures). Where profiles are not easily distinguishable, details (close-ups) are provided under each figure. As discussed in Dupont et al. (2004), there are no independent ways to verify such result, because TKE component measurements in the urban UCL are very scarce. Thus here, they are merely discussed with some justification as to their profiles.

Generally, the model shows that the vertical profile of shear production follows the FAD profile, whether for buildings or canopy cover. As can be seen in the "Shear" sub-figures, shear production of TKE generally peaks at or higher than the elevation where a significant decrease in FAD exists ("critical FAD elevation"). It is also seen that the vegetation canopy produces relatively larger shear, presumably because of its denser structure *above* ground, causing FAD to actually increase away from the ground up until the critical FAD level, after which it decreases (for buildings, on the other hand, FAD is constant from the ground up to the critical level). Generally, in all locations, shear production is very small near the ground and increases through the canopy to peak at or above the critical FAD elevation. This is a reasonable and expected behavior as explained by Leclerc et al. (1990) and Dupont et al. (2004).

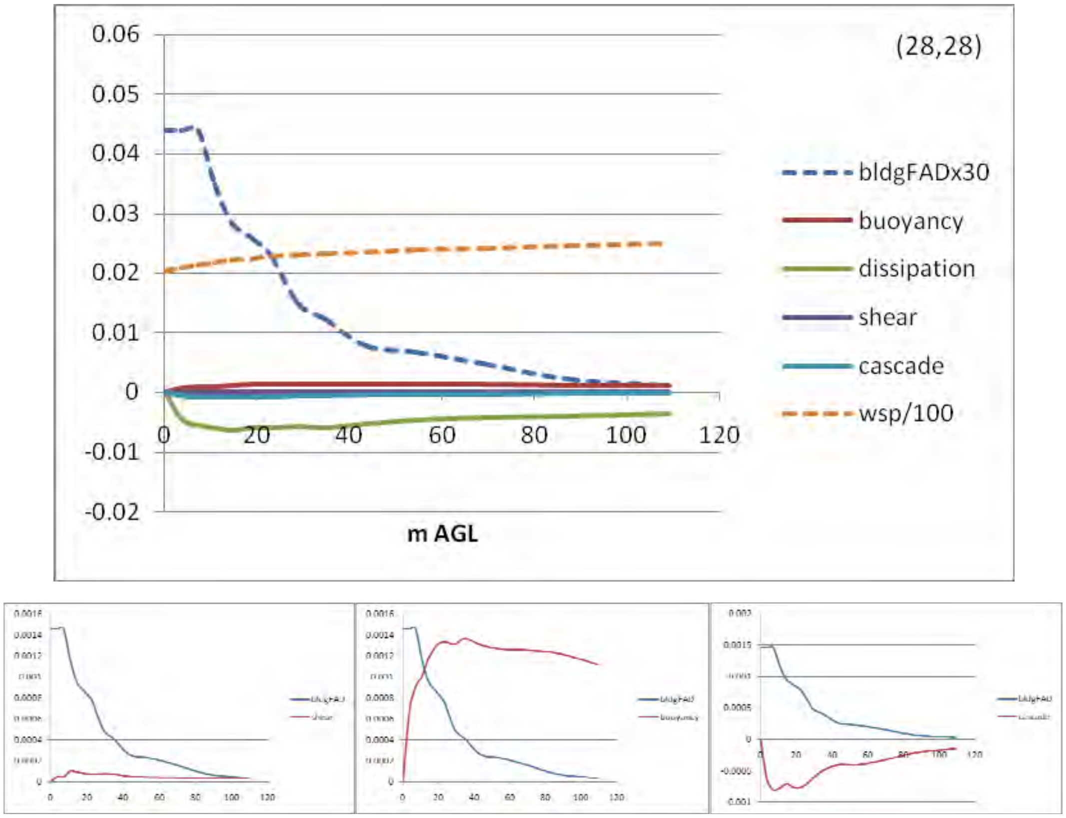

Shear Buoyancy Cascade

Figure 4.4. TKE budget components for location 28,28 in the Sacramento modeling domain (1400 LST, unstable). TKE terms units: m^2s^{-3}

Buoyancy production of TKE also generally follows the behavior discussed above. At this hour (1400 LST) the atmosphere is unstable and thus buoyancy is an active producer of TKE. Buoyancy increases significantly from the surface up to the critical FAD level and then remains roughly constant throughout the rest of the UCL. The area with taller buildings produces relatively smaller buoyancy, likely because of cooler air near the surface (compared to other areas), whereas relatively more open areas (residential) or solid-top canopy (forest) are heated more efficiently and thus produce relatively larger buoyancies.

Finally, the accelerated cascade term also shows that this component of TKE dissipation mechanism also follows the FAD vertical distribution. While buoyancy is sustained above the critical FAD level, the accelerated cascade dissipation of TKE decreases with height as FAD decreases.

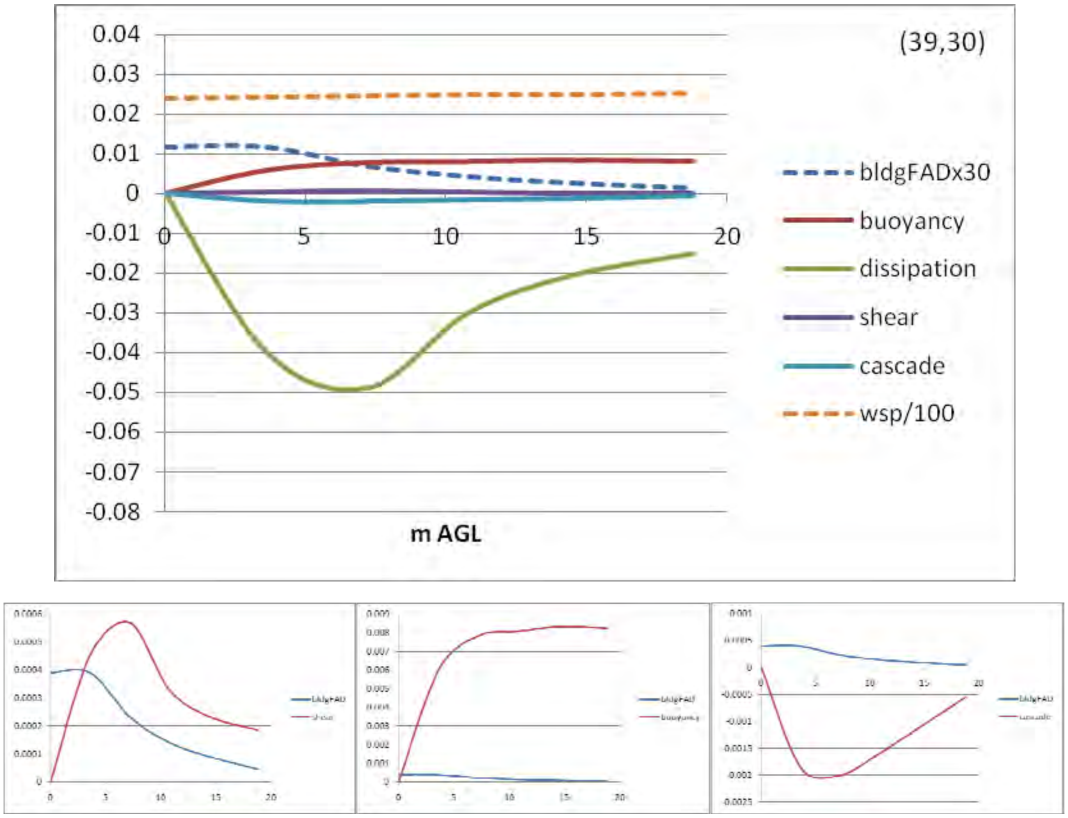

Shear Buoyancy Cascade

Figure 4.5. TKE budget components for location 39,30 in the Sacramento modeling domain (1400 LST, unstable). TKE terms units: m^2s^{-3}

For the above three locations, the base-case sensible and latent heat fluxes and air temperatures are shown in Figure 4.7. Of interest is the near-surface temperaure difference from one location to another. For example, the area with vegetation canopy cover (59,60) is about 2°C cooler than the other areas (35.5°C versus about 37.5°C) and its vertical profile shows a change at about 10 m within the canopy. In terms of heat fluxes, the figures show that the high-rise area (28,28) has negative sensible heat flux near the surface to up to about 25 m AGL within the canopy, suggesting the effects of shadowing and canyon geometry (this is also the cause of the smaller buoyancy production in this area, mentioned above). Above 25 m, sensible heat flux is positive, suggesting larger heating in the upper layers of the UCL. The latent heat flux component is very small (there is only a small amount near the surface) and nearly constant with height since the area is devoid of water or wet vegetation/moist surfaces. The residential area and forest (39,30 and 59,60) have positive fluxes throughout the UCL. As expected, the sensible component is smaller than in the high rise area, but the latent component is larger due to presence of vegetation canopies. In the forested region, the sensible component is smallest and the latent largest, relative to other locations. The Bowen ratio for these three locations are, respectively, very large ($\beta > 20$), $\beta \sim 3.5$, and $\beta \sim 1.3$. These are (in general magnitude) consitent with observed values in such land-cover and land-use situations (Oke 1978).

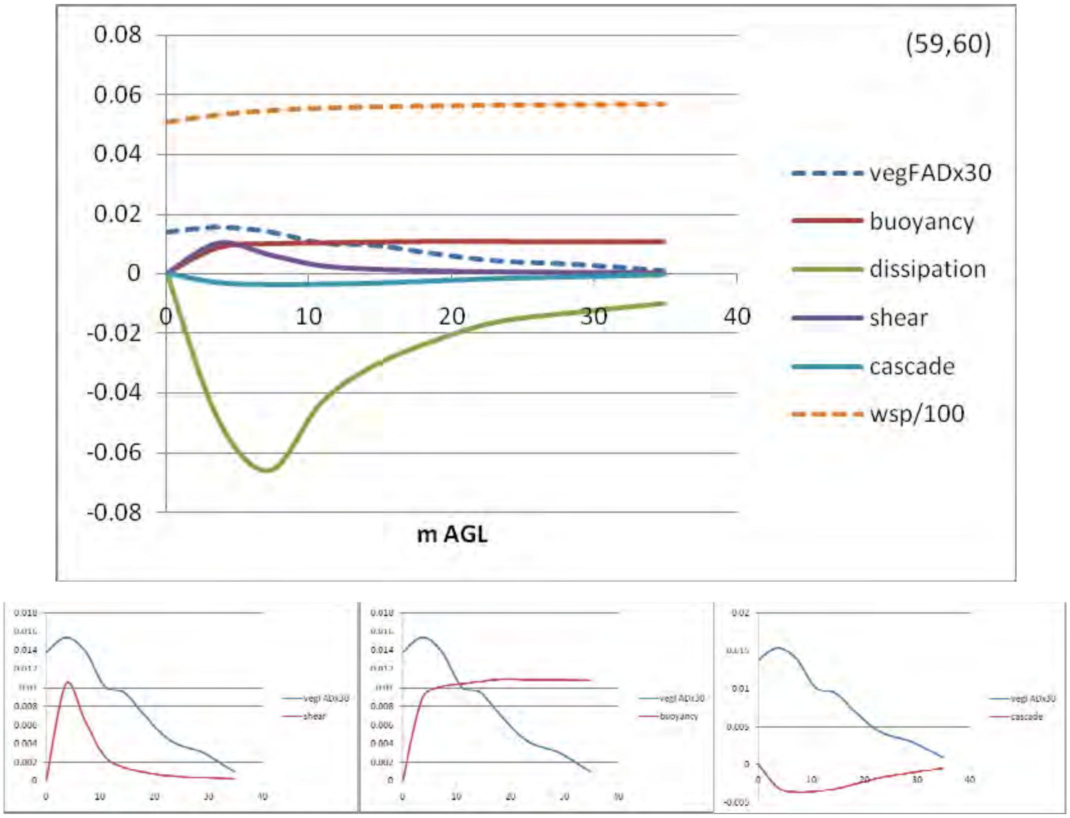

Shear Buoyancy Cascade

Figure 4.6. TKE budget components for location 59,60 in the Sacramento modeling domain (1400 LST, unstable). TKE terms units: m^2s^{-3}

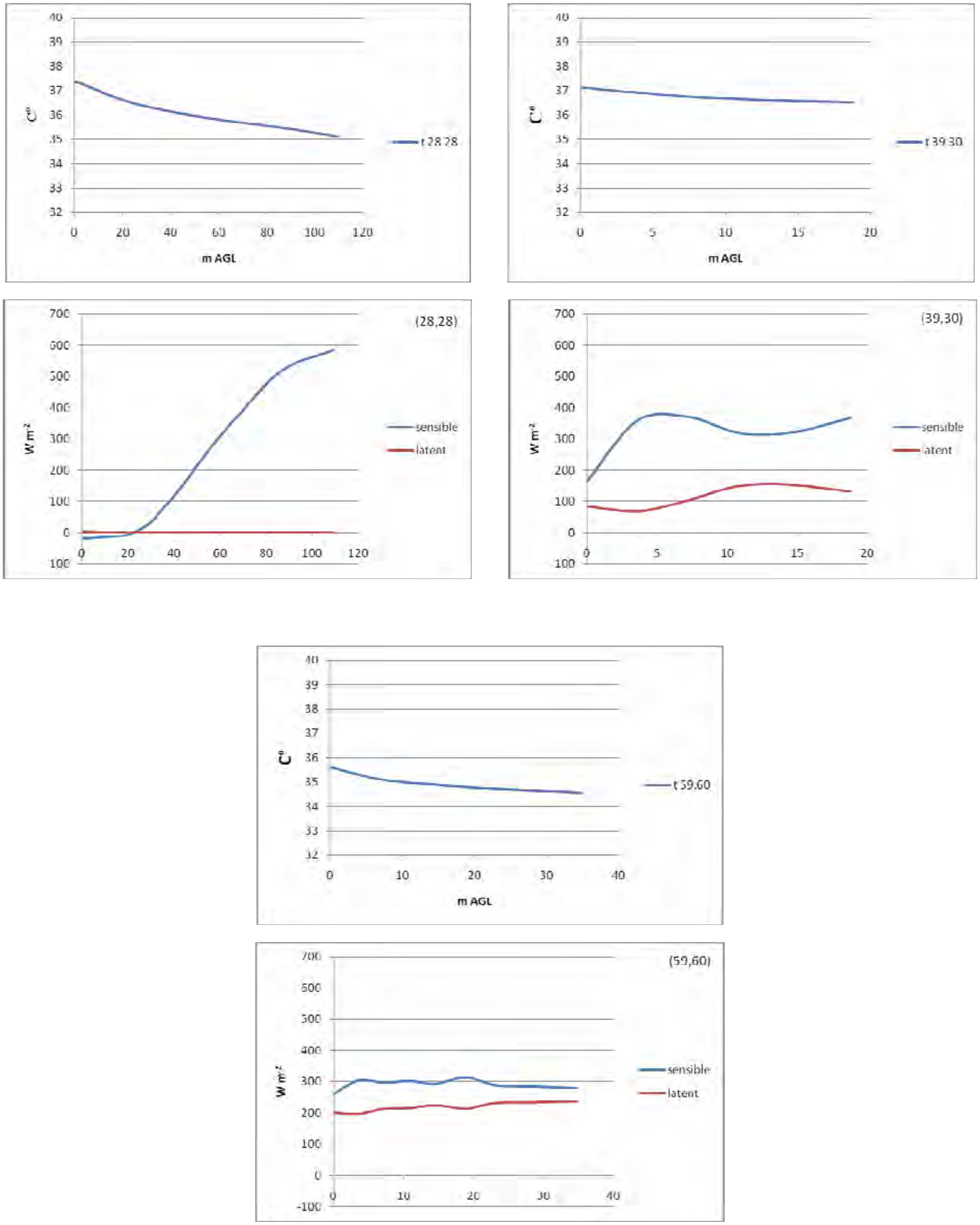

Figure 4.7. Sensible and latent heat fluxes (W m^{-2}) and air temperature (C°) at given locations in the Sacramento uMM5 domain (1400 LST, unstable)

Photochemistry / Air Quality

Figure 4.8 shows the simulated peak ozone concentration fields for July 31 through August 2, 2000 (at the hour of each day's peak). The domain shown here is the 1 km CAMx grid corresponding to the fine-resolution uMM5 modeling grid for the Sacramento area discussed above. The peak concentrations are consistently downwind, advected by the dominant flow to the southeast on July 31, to the east on August 1, and to the northeast on August 2. The 1 km domain's peaks are respectively 96, 117, and 101 ppb on those three days. The local peaks simulated with this modeling configuration (uMM5) are more accurate (for this specific domain) than those obtained from the coarse simulations of Phase 1. The downwind displacement and location of peak concentrations is also consistent with observations and other modeling efforts for this area (e.g., Fujita et al. 2003 and Stockwell et al. 2004).

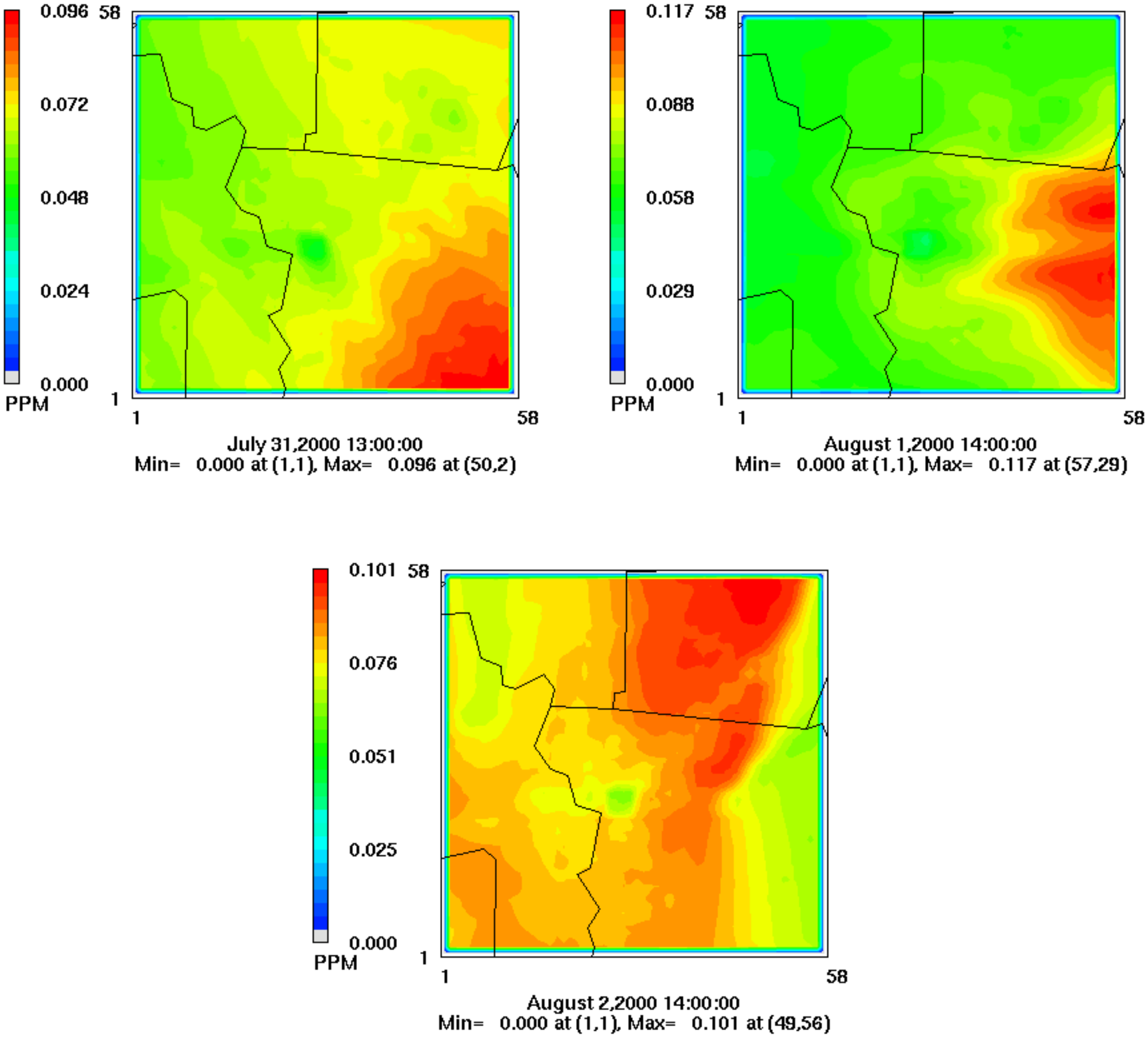

Figure 4.8. Simulated daily peak ozone in the Sacramento 1 km CAMx domain (at the hour of each day's peak)

Figure 4.9 is mostly a duplicate of the above figure but with added information to show a comparison between the simulated and observed concentrations at the appropriate monitor (peak) for each day (July 31 through August 2) and to identify monitors of interest in this and following analysis. On July 31 and August 1, the monitor of interest is SLU (Sloughhouse), whereas on August 2, it is ROC (Rocklin). The accuracy of the *unpaired* peak is satisfactory (ranging from 0.83 to 0.96), thus meeting the U.S. EPA's recommended benchmarks. Even the *paired* peak accuracy meets those benchmarks, ranging from 0.81 through 0.88. Table 4.1 provides some additional statistics related to the *unpaired-in-time* but *paired-in-space* peak accuracy for other monitor locations of interest as well. Detailed model performance statistics for the coarser grids were discussed in Phase 1 report.

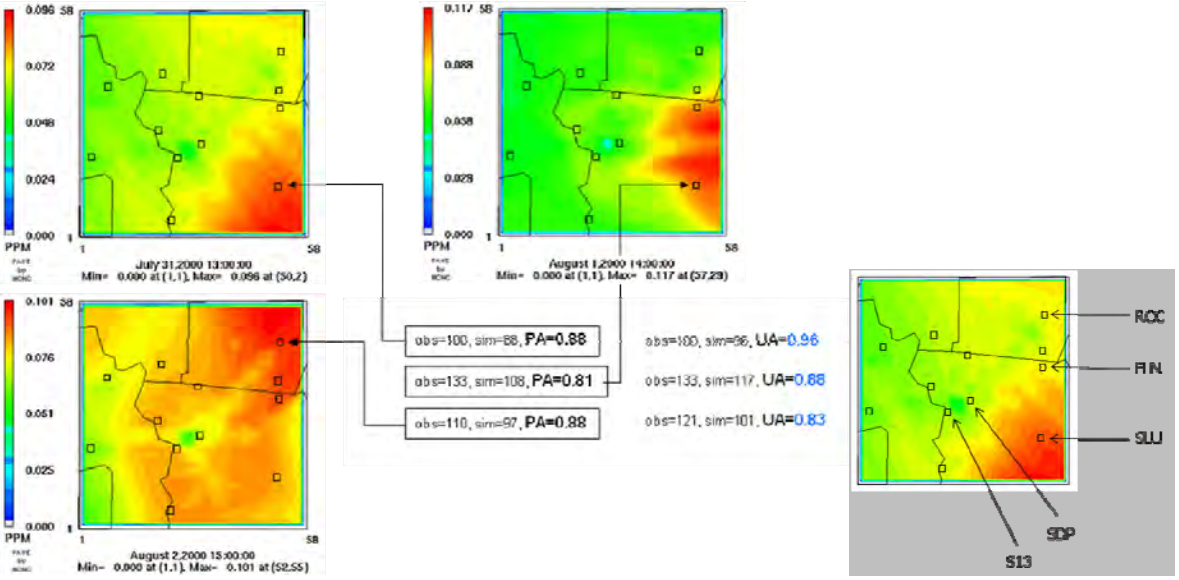

Figure 4.9. Simulated daily peak ozone in the Sacramento 1 km CAMx domain with unpaired (UA) and paired (PA) peak accuracy benchmarks

Table 4.1. Some aspects of simulated peak ozone performance (unpaired-in-time but paired-in-space peak accuracy for monitor locations of interest). Refer to Figure 4.9 for the geographical locations of these monitors. Obs and sim in ppb.

monitor	7/31			8/1			8/2		
	Obs	sim	accuracy	obs	Sim	accuracy	obs	sim	accuracy
SLU	100	88	0.88	133	108	0.81	103	87	0.84
FLN	no data	72	--	no data	112	--	111	92	0.83
ROC	78	71	0.91	103	96	0.93	110	97	0.88
S13	85	63	0.74	96	76	0.79	80	81	1.01
SDP	81	70	0.86	115	80	0.70	102	86	0.84

This brief evaluation of the modeled ozone peak concentrations fields suggests that while the model captures reasonably well the downwind higher concentrations, its performance is relatively poorer in capturing the observed concentrations near and immediately downwind of the downtown area (the mid-domain region) where it underestimates the local peaks. Other, more extensive metrics and detailed statistical evaluation of meteorological and photochemical model performance were presented in Phase 1 final report.

Figures 4.10 and 4.11 depict the simulated base-case ozone concentrations as time series at selected monitors of interest in the uMM5-corresponding 1 km CAMx grid. Monitor locations FLN, ROC, SLU (Folsom-Natoma, Rocklin, and Sloughhouse) are downwind of the major urbanized area (all three are closer to the domain's eastern boundary), whereas monitors S13 and SDP (Sacramento T Street and Sacramento Del Paso Manor) are at mid-domain locations (see again Figure 4.9). As discussed above, the model does capture reasonably well the peak concentrations' downwind displacement and, as a result, higher ozone concentrations at FLN, ROC, and SLU compared to those at S13 and SDP, which is reflected again in the figures below. During the three days of interest here, the simulated peak concentrations in the downwind group reach 112 ppb (1300 PST August 1 at FLN) and 86 ppb in the mid-domain group (1300 PST August 2 at SDP). On all days, the simulated peaks occur between 1200 and 1600 LST.

These simulated ozone-concentration fields will also serve as a basis for compring the effectiveness of UHI control (surface modification) scenarios at these locations, as discussed in the following sections.

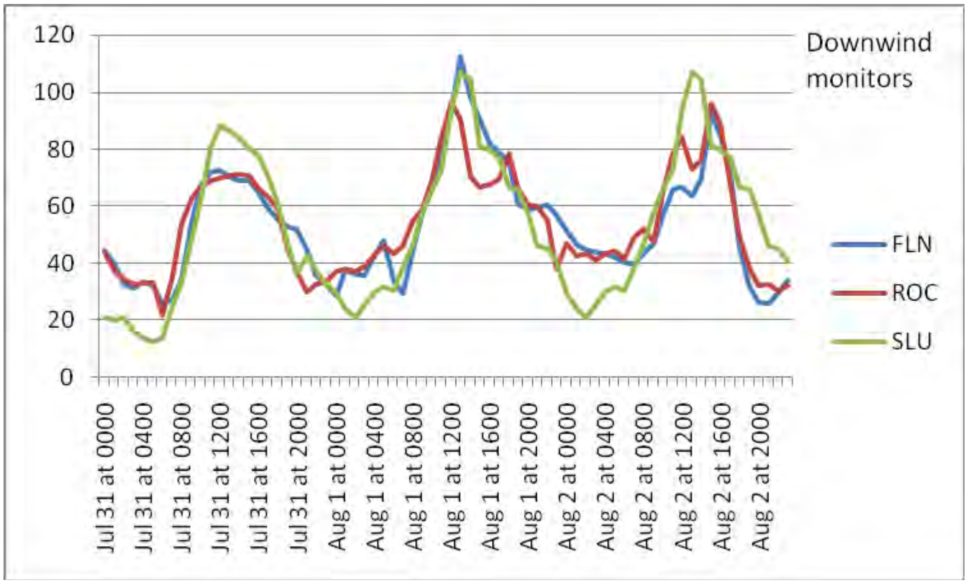

Figure 4.10. Simulated base-case ozone concentrations at downwind monitors in the Sacramento 1 km domain

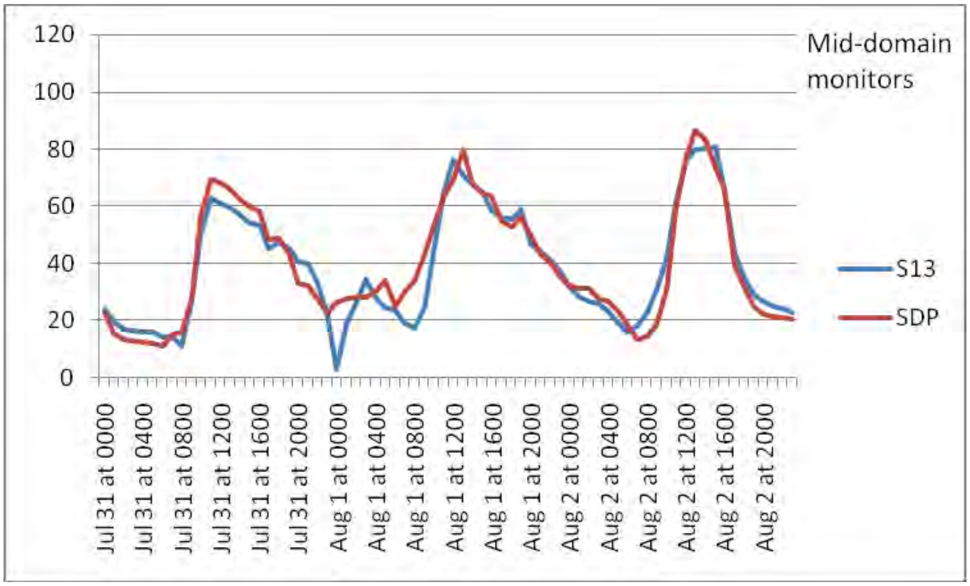

Figure 4.11. Simulated base-case ozone concentrations (ppb) at mid-domain monitors in the Sacramento 1 km domain

4.1.2. Control Scenarios

Meteorology

For this discussion, Figure 4.12 a–l shows two-dimensional cross sections of the temperature-change fields at six-hour intervals starting 0000 LST July 31 (the 56th hour of the forecast) through 1800 LST August 02 (the 122nd hour of forecast). These changes result from the increased-albedo scenario. Superimposed on temperature change is the base-case wind vector field. This figure is followed by Figure 4.13 m–x showing the same sequence of information but for surface temperature change at the corresponding hours. Then, Figure 4.14 1–6 shows the air- and coincident surface temperature-change fields at those hours when the largest changes in *air* temperature occur on each of the three days of interest in this discussion.

The simulations indicate that during nighttime hours, surface modifications via increased urban albedo do not affect air temperature. This can be seen for example at 0000 and 0600 LST on July 31 (Figures a and b). Beginning after sunrise, the temperature difference (cooling effect) appears. Thus by 1200 LST on that day (c), there is a temperature reduction of up to 1.5°C–2°C southeast of downtown Sacramento (in general the temperature difference is advected with the mean wind, in this case to the southeast). The temperature difference becomes larger through 1400–1600 LST (not shown) and begins to taper off so that by 1800 LST (d), there is only a small temperature difference relative to the base case (by up to 1°C at this hour, but affecting a much smaller area). At night, the temperature reduction is nonexistent, as seen at 0000 and 0300 LST (August 1) in figures e and f. This cycle repeats itself on the following days (August 1 and 2), with the large decreases during the day, e.g., at 1200 LST on August 1, where the cooling reaches up to 1.5°C–2°C (g) and 1200 LST on August 2 when the cooling reaches up to 2°C–2.5°C (k) and small or nonexistent reductions at night. In all cases, the “cooler” air is advected downwind (e.g., to the east on August 1 and the north on August 2) and thus can also affect areas outside of the modified regions (e.g., beyond areas where surface albedo was increased).

In Figure 4.13 m through x, the same diurnal cycle is seen for *surface* temperature. Again the pattern consists of small or no effects at night but large decreases in temperature during the daytime. Of course, the main difference (compared to changes in air temperature) is the spatial distribution of the cooler areas (which follow very closely the areas being modified) and the actual magnitude of the decrease in temperature, which is larger than that of air temperature. For the time intervals shown in figures m–x, it can be seen that the largest decrease in surface temperature reaches up to 7°C, 10°C, and 8°C on July 31, August 1, and August 2, respectively (figures o, s, and w). There is also some warming in areas of the domain, for example in Figures 4.12 h and l and 4.13 w and x. However, the areas affected by increased temperatures are not as large or extensive as those affected by reduced temperatures.

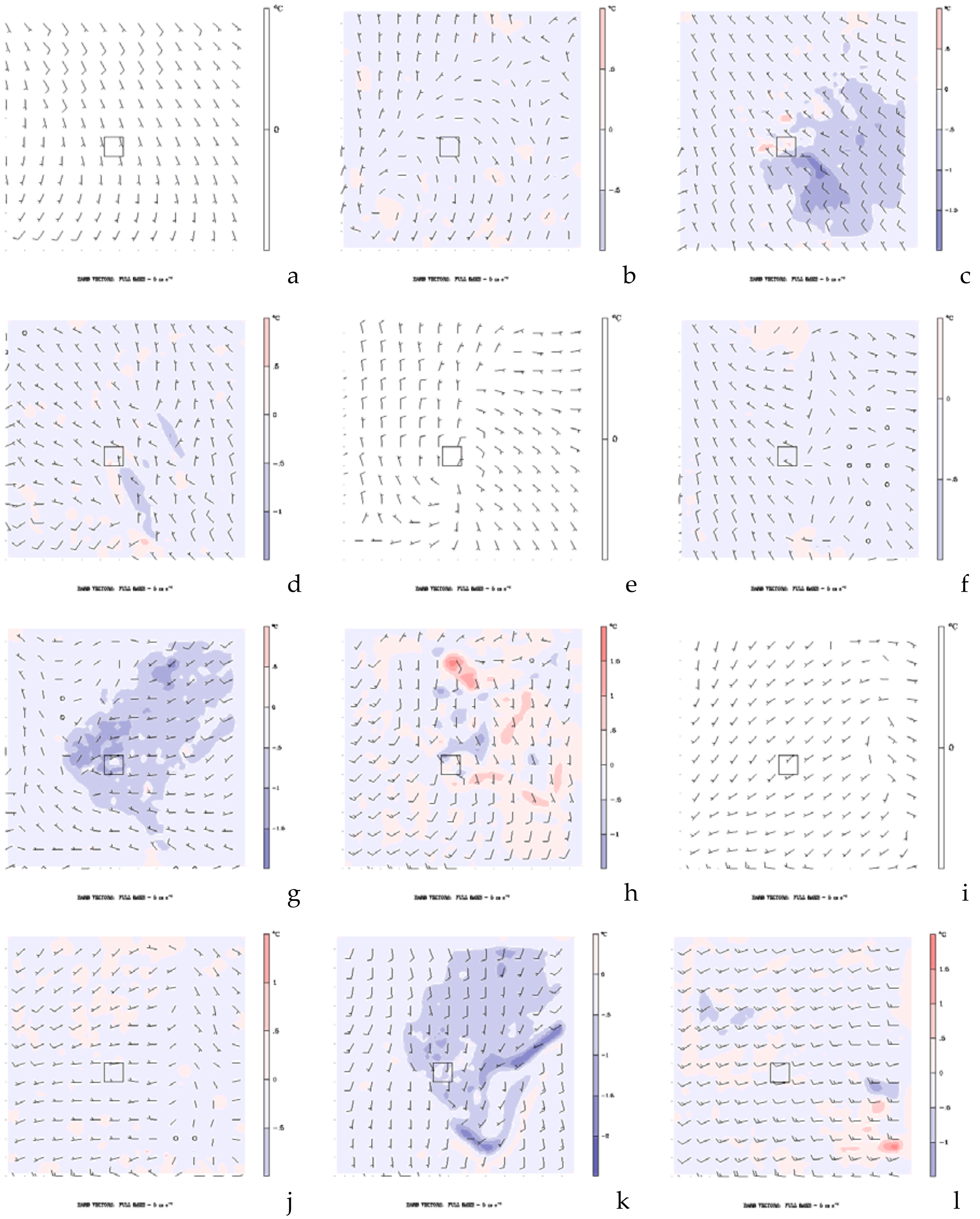

Figure 4.12. Change in air temperature at six-hour intervals, resulting from increased urban albedo

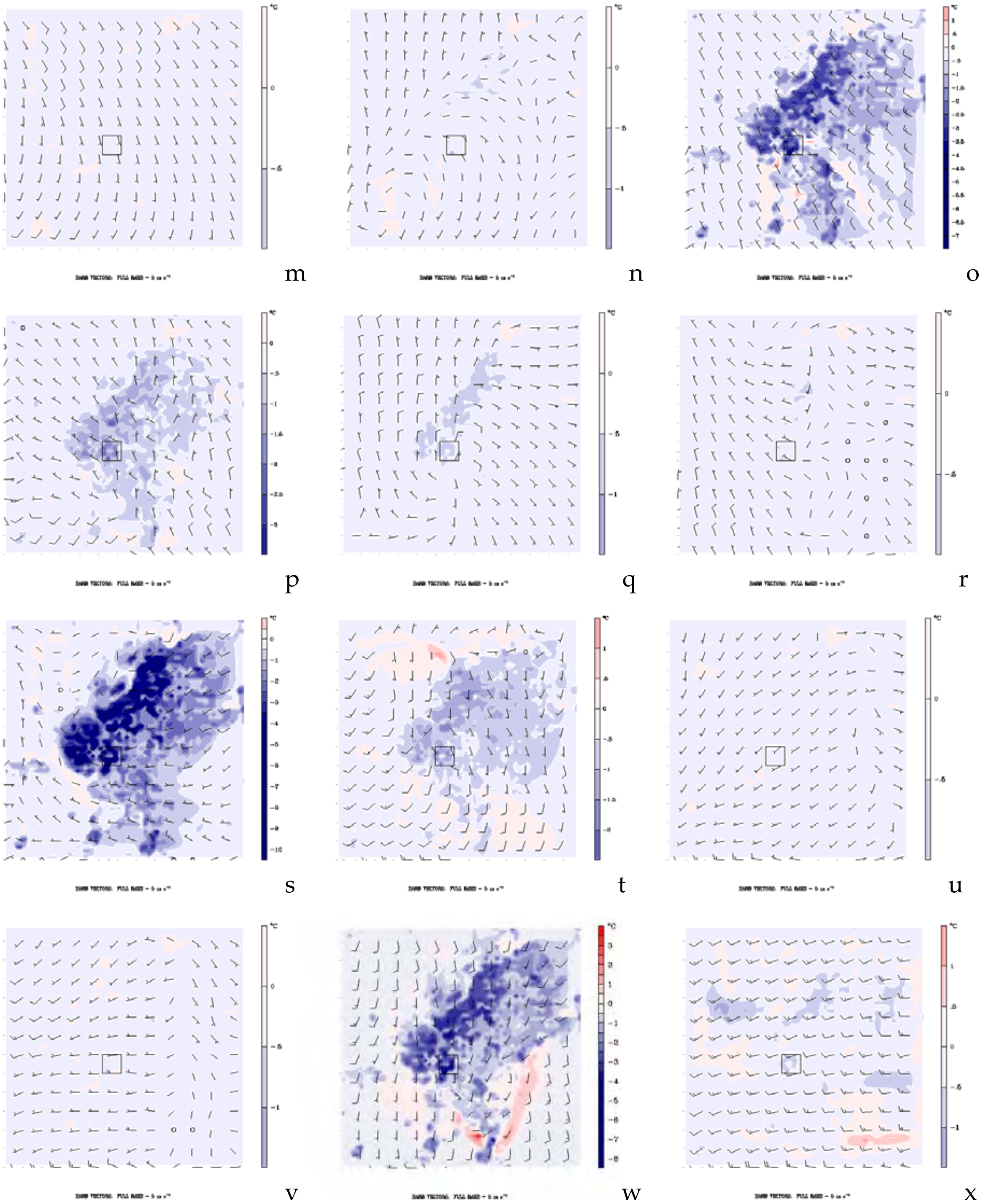

Figure 4.13. Change in near-surface temperature at six-hour intervals, resulting from increased urban albedo

Next, in Figure 4.14, 1–6, the changes in air and surface temperature fields are given at the hour when the largest reductions of the day in *air* temperature are achieved (for each of the three days of interest). Air temperature can be reduced (in the increased-albedo scenario) by up to 2.5°C at 1100 LST July 31, 2°C at 1200 LST August 1, and 3°C at 1300 LST August 2 (Figures 4.14, 1,3, and 5 respectively). In terms of corresponding (time-coincident) surface temperature changes, the high-albedo scenario can cause reductions of up to 7°C at 1100 LST July 31, 10°C at 1200 LST August 1, and 7°C at 1300 LST August 2 (Figures 4.14, 2, 4, and 6 respectively).

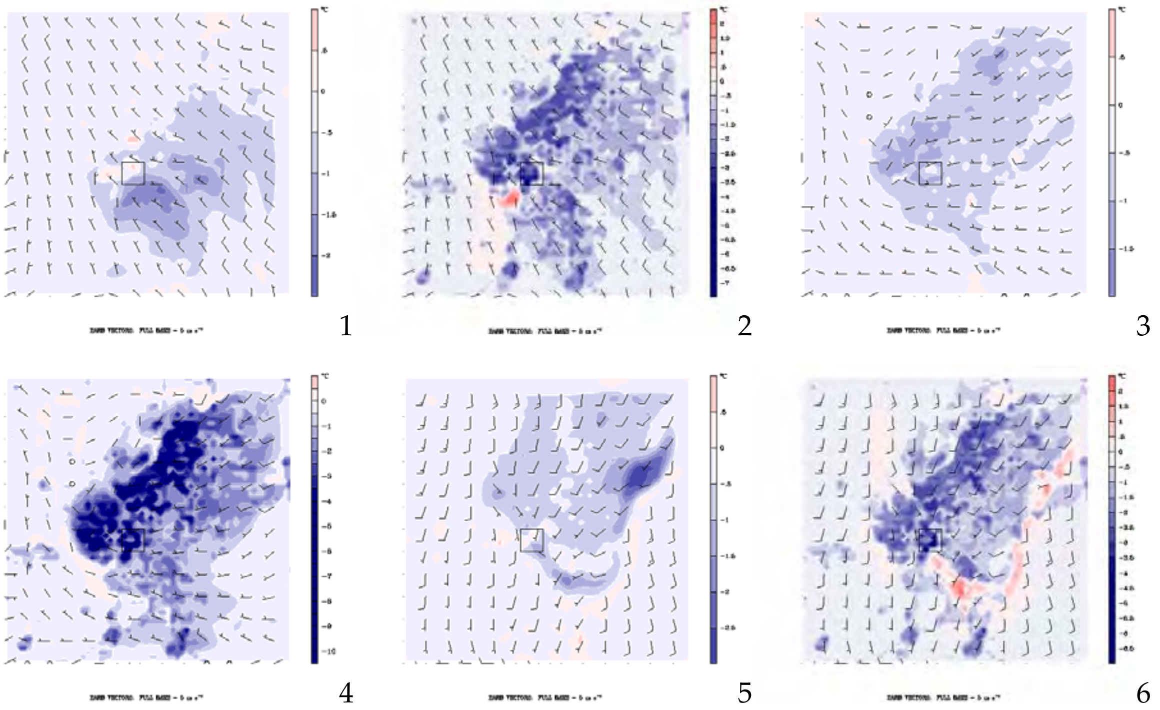

Figure 4.14. Change in air and coincident surface temperatures at the hours of largest decrease in *air* temperature on each day (increased urban albedo scenario)

The increase in canopy cover has generally the same effect but at lower magnitude on air and surface temperatures than the high-albedo scenario. These effects are summarized in Figures 4.15, a–l, for air temperature, and Figure 4.16, m–x, for surface temperature. Figures 4.17, 1–6, then show the largest decreases in *air* temperature (and coincident surface temperature) on each day of interest. In summary, and without repeating much of the foregoing discussion above for the high-albedo scenario, some of the larger reductions in air temperature resulting from increased canopy cover are 1.5°C, 1°C, and 1°C at 1200 LST July 31, August 1, and August 2, respectively (Figures 4.15 c, g, and l). The corresponding reductions in surface temperature at 1200 LST on these days are 5°C, 6.5°C, and 6°C, respectively (Figures 4.16 o, s, and w). The largest reductions in *air* temperature on these days reach up to 1.5°C, 1.5°C, and 2.5°C respectively at 1100 LST July 31, 1300 LST August 1, and 1300 August 2 (Figures 4.17 1, 3, and 5). The corresponding (time-coincident) reductions in surface temperature are 4°C at 1100 LST July 31, 5.5°C at 1300 LST August 1, and 4°C at 1300 LST August 2 (Figures 4.17 2, 4, and 6).

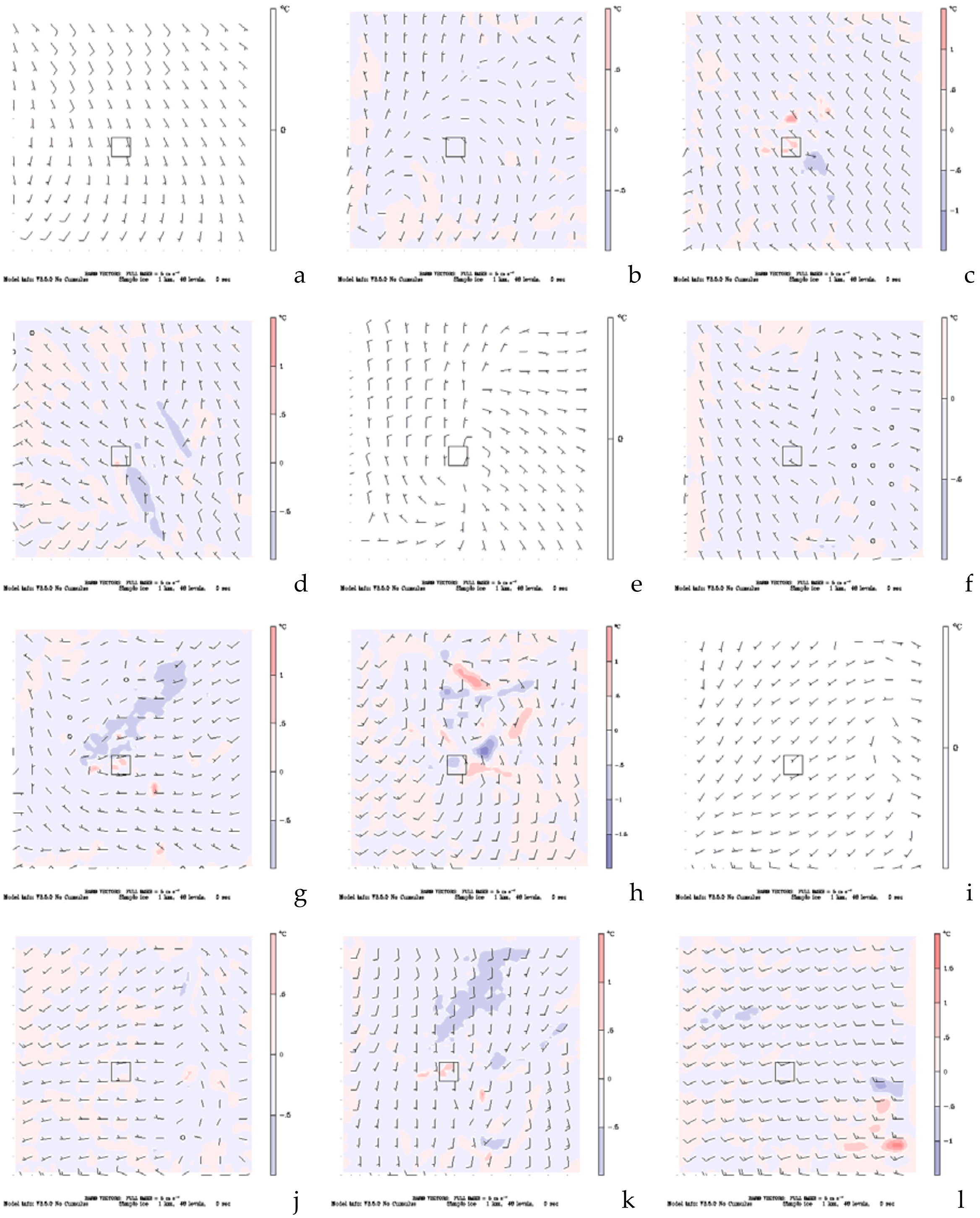

Figure 4.15. Change in air temperature at six-hour intervals, resulting from increased canopy cover

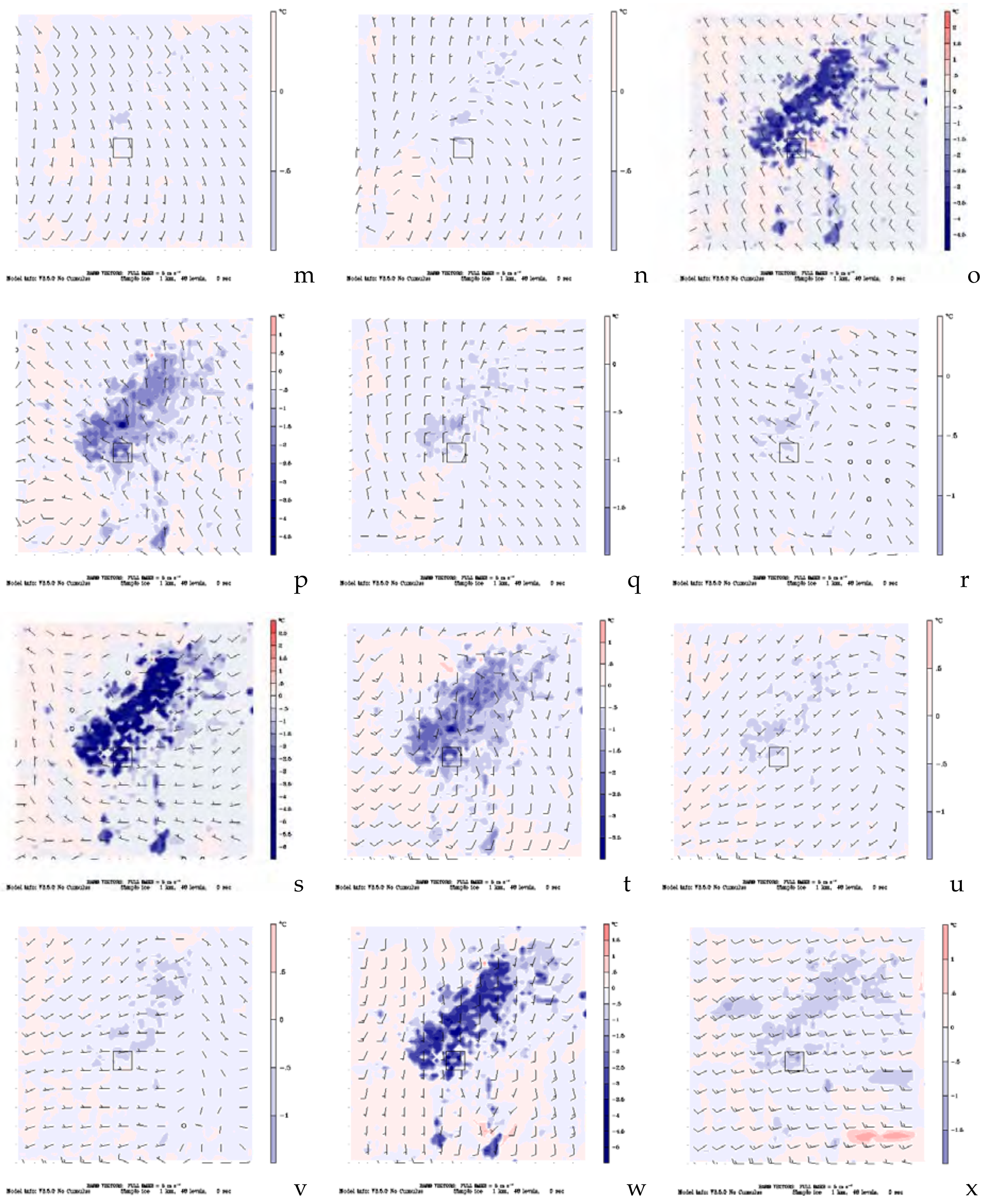

Figure 4.16. Change in near-surface temperature at six-hour intervals resulting from increased canopy cover

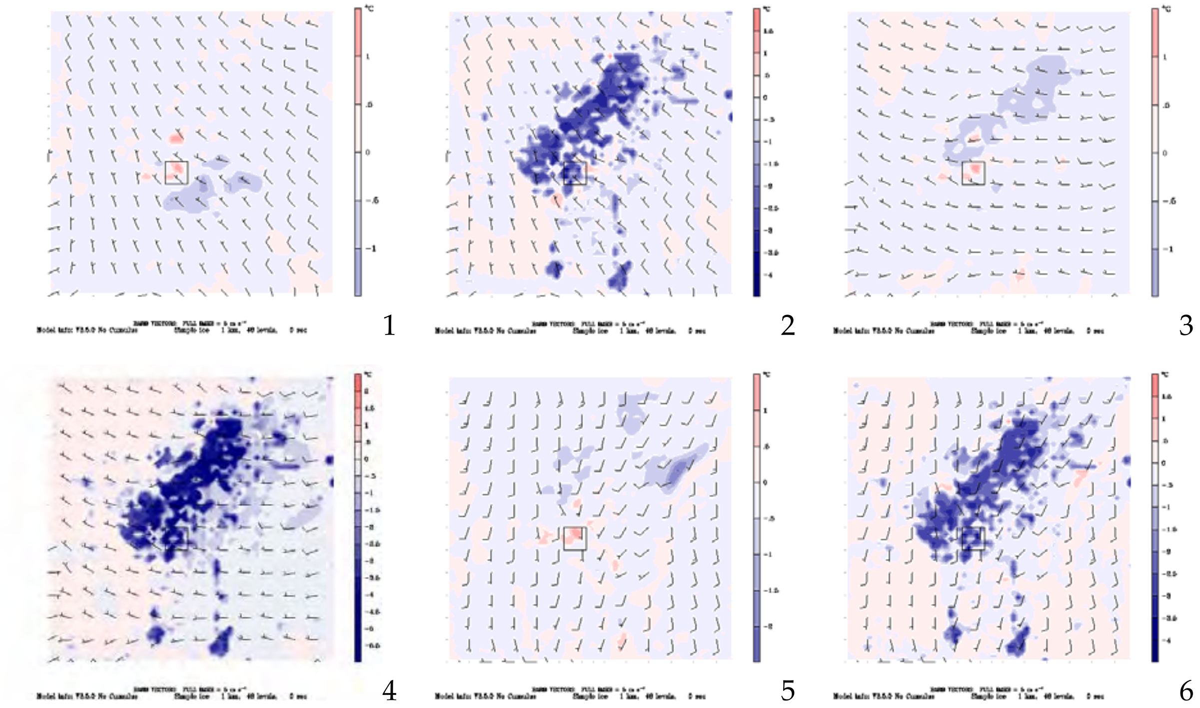

Figure 4.17 (1–6) Change in air and coincident surface temperatures at the hours of largest decrease in *air* temperature on each day (increased canopy cover scenario)

Figure 4.18 shows one example snapshot of surface temperature change (as a result of increased albedo) side-by-side with building PAD function at 1 m AGL. The purpose is to show the almost exact correspondence between surface temperature change and areas affected by albedo increase (which, in this case, is proportional to building PAD). The example shown here is for 1000 LST July 30, but the time stamp is unimportant as changes in temperature follow the surface modification pattern at all times. Initially, this was one of several simple initial tests to ensure correct model functioning, but is included here as an example, since it is interesting to compare the two fields side by side.

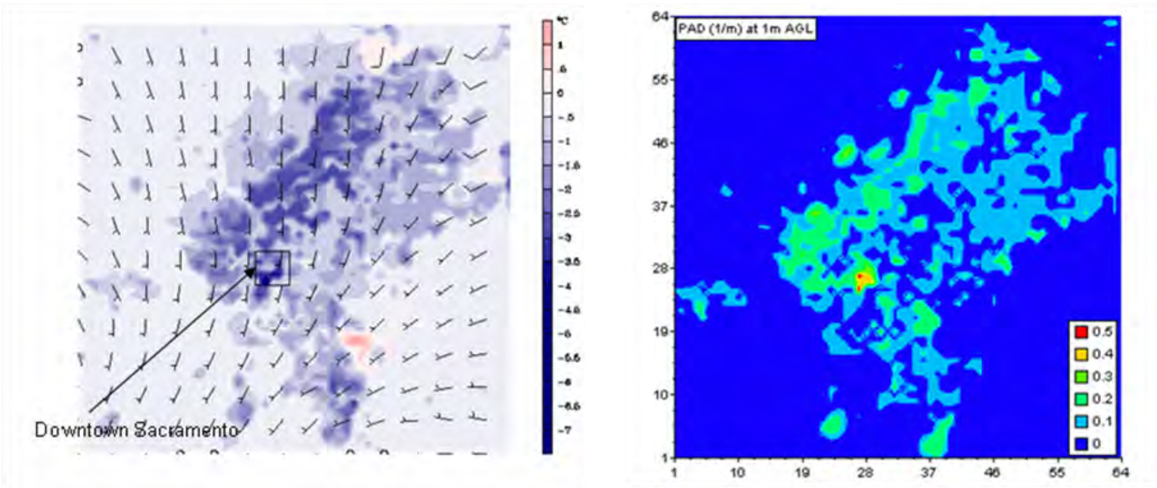

Figure 4.18. Change in surface temperature (left) compared to building PAD function at 1 m AGL (right)

Finally, and to conclude this section, a time series (Figure 4.19 a,b) of temperature change at two locations in the Sacramento uMM5 domain is given for example (these are arbitrarily selected and do not represent locations of maximum temperature change). Location 21,29 is residential, whereas 39,30 is a residential-commercial area. Although the magnitude of temperature and its intensity across the days of the episode are different, both locations exhibit the patterns discussed earlier. That is, temperature decrease occurs through the day and is minimal or nonexistent at night. Figure 4.19 also shows the relative efficacy of increased canopy cover versus increased urban albedo at these two locations.

a

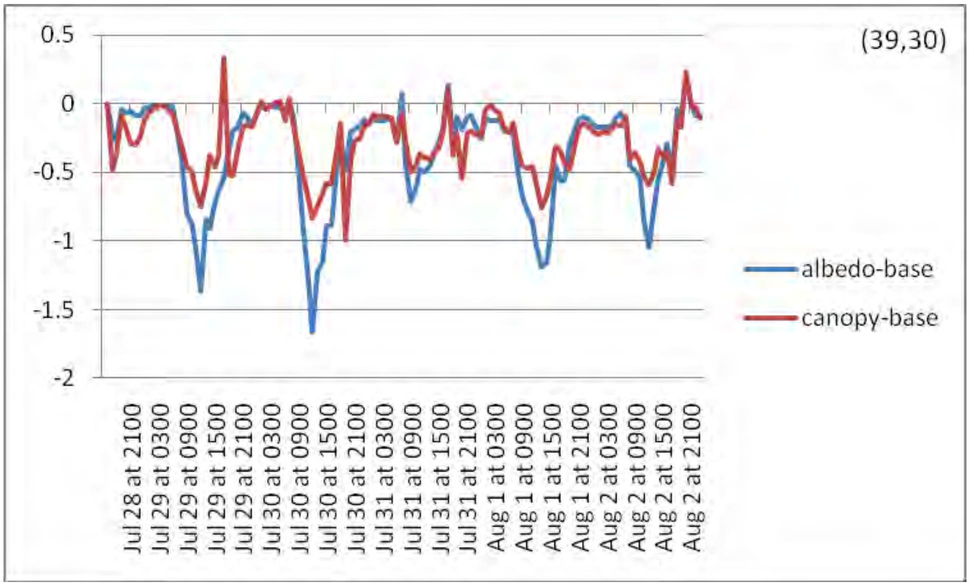

b

Figure 4.19. Time series of air temperature change at two locations in the Sacramento uMM5 domain resulting from increased albedo (blue) and canopy cover (red).

Photochemistry / Air Quality

This section presents the potential impacts of increased urban albedo and canopy cover on a number of ozone air quality-related metrics. The focus here is on the area-average changes as well as some 1- and 8-hour peak concentration statistics. To begin, Figures 4.20–4.22 show the regional impacts (within the 1 km CAMx grid) on ozone at the peak hours (times of simulated daily peak concentration) on each of the three days of interest for the Sacramento domain. In each figure, the top part shows the effects of the high-albedo scenario and the bottom part shows that of increased canopy cover. A small inset at the top-right of each figure shows the corresponding base-case peak ozone at the corresponding hour.

The simulations suggest that, at 1300 LST on July 31, concentrations can be decreased by up to 16 ppb (just east of Downtown Sacramento) in the high-albedo scenario and by up to 15 ppb in that same area in the increased canopy cover scenario. There are also large reductions in ozone further downwind in both scenarios as high as 15–17 ppb; for example there is a reduction of 17 ppb in the southeastern corner of the domain in the increased canopy cover scenario. However, it is the larger area affected by decreased concentrations that is more interesting, for example, in this case, the domain's southeast quadrant. Spatially averaged decreases in concentrations over that area reach up to 5–6 ppb at this hour (in both canopy cover and albedo scenarios). The reductions affect the area with the highest base-case concentrations (compare to the top right inset in the figure) and thus are useful in offsetting the higher ozone in the domain. Note that there are no increased concentrations as a result of surface perturbations.

A generally similar pattern is seen on the next day (August 1). On that day, the peak hour is at 1400 LST and, as depicted in Figure 4.21, the concentrations decrease by up to 26 ppb (in a very small area in the eastern part of the domain) in the high-albedo scenario and by up to 19 ppb in that same area in the increased canopy scenario. The area with decreased concentrations corresponds to that of the high base-case ozone in mid-east portion of the domain (see the inset at top right of figure). In this day and hour, however, some negative impacts also occur upwind of the areas that experience decreased concentrations. The increases can reach up to 9 ppb in the increased albedo scenario and up to 5 ppb in the increased canopy cover scenario. But, the area affected by increased ozone is much smaller than that affected by decreased concentrations, as seen in Figure 4.21.

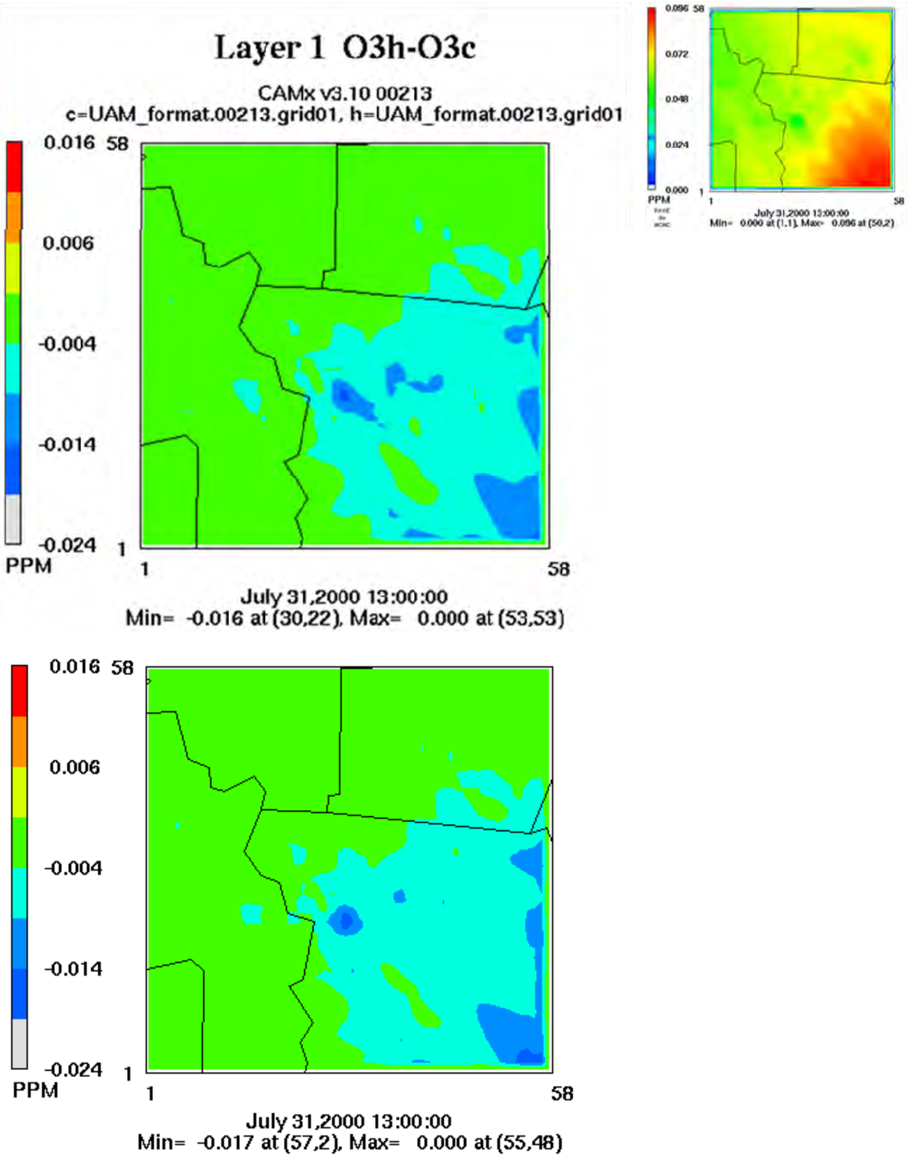

Figure 4.20. Changes in O_3 at time of base-case peak in the Sacramento 1 km domain. Top: Increased urban albedo scenario; Bottom: Increased canopy cover scenario. Top-right: Base-case ozone concentration (peak) at this hour.

The averaged decreases in concentrations in the large impact area reach up to 14 ppb in the high-albedo scenario at this hour and up to 10 ppb in the increased canopy cover scenario. Thus again, the impacts of surface modifications is useful in mitigating the higher ozone.

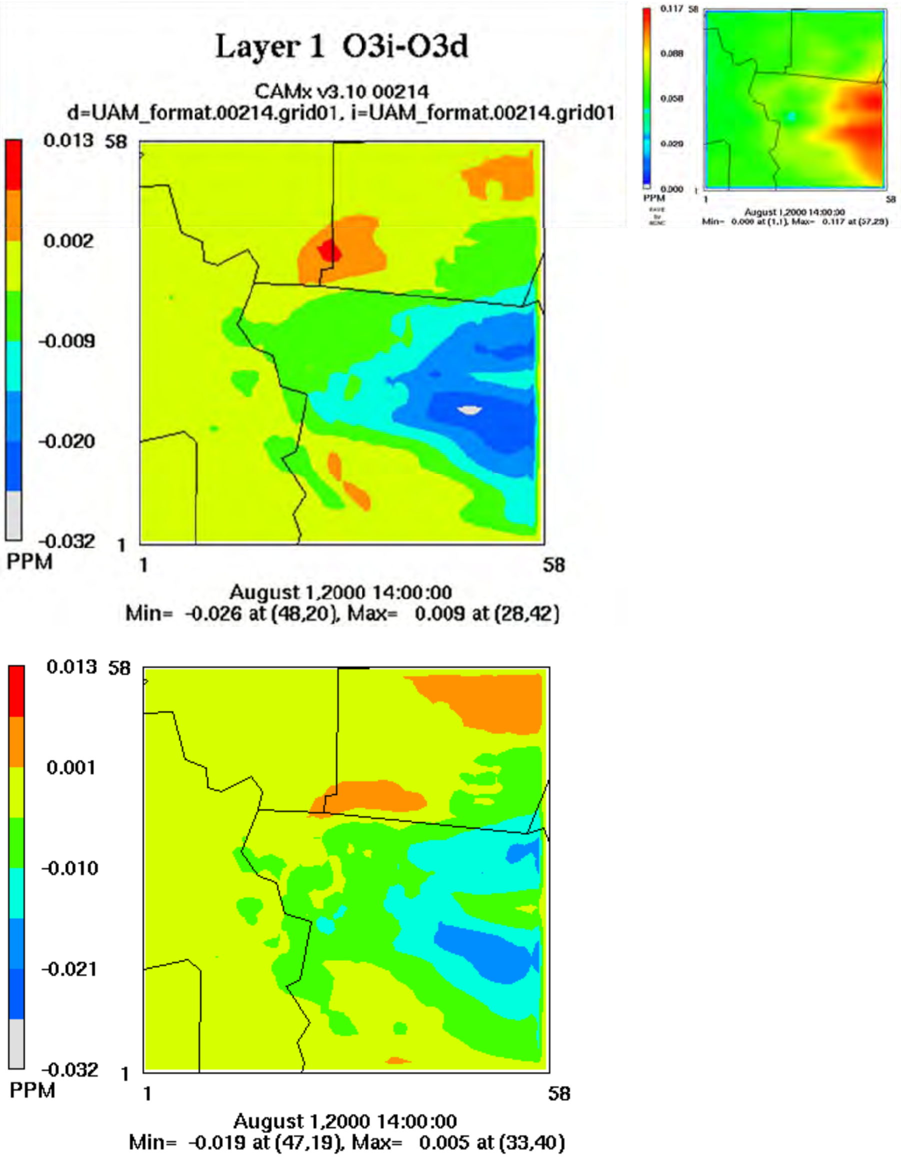

Figure 4.21. Changes in O_3 at time of base-case peak in the Sacramento 1 km domain. Top: Increased urban albedo scenario; Bottom: Increased canopy cover scenario. Top-right: Base-case ozone concentration (peak) at this hour.

Figure 4.22 shows the changes in ozone on August 2 where the peak hour is at 1500 LST. In the high-albedo scenario, the largest decrease at this hour is 17 ppb in a very small (almost negligible) area to the east of Downtown Sacramento. In the increased-canopy scenario, the largest decrease at this hour is 18 ppb at the same location. But both of these areas (affected by the largest decreases in concentrations) are very small, less than three square kilometers (km^2). Therefore, it is more interesting, as before, to examine the decrease in concentrations affecting the larger area in the domain (in this case, running roughly from downtown Sacramento to the northeastern portion of the domain). At this hour (1500 LST) the area-averaged decrease in concentrations in both the high-albedo and increased-canopy cover scenarios is 11 ppb (shown as a dark blue area in the figure). There are also very small areas of increased concentrations at this hour. These reach up to 11 ppb in the high-albedo scenario and up to 3 ppb in the increased canopy scenario.

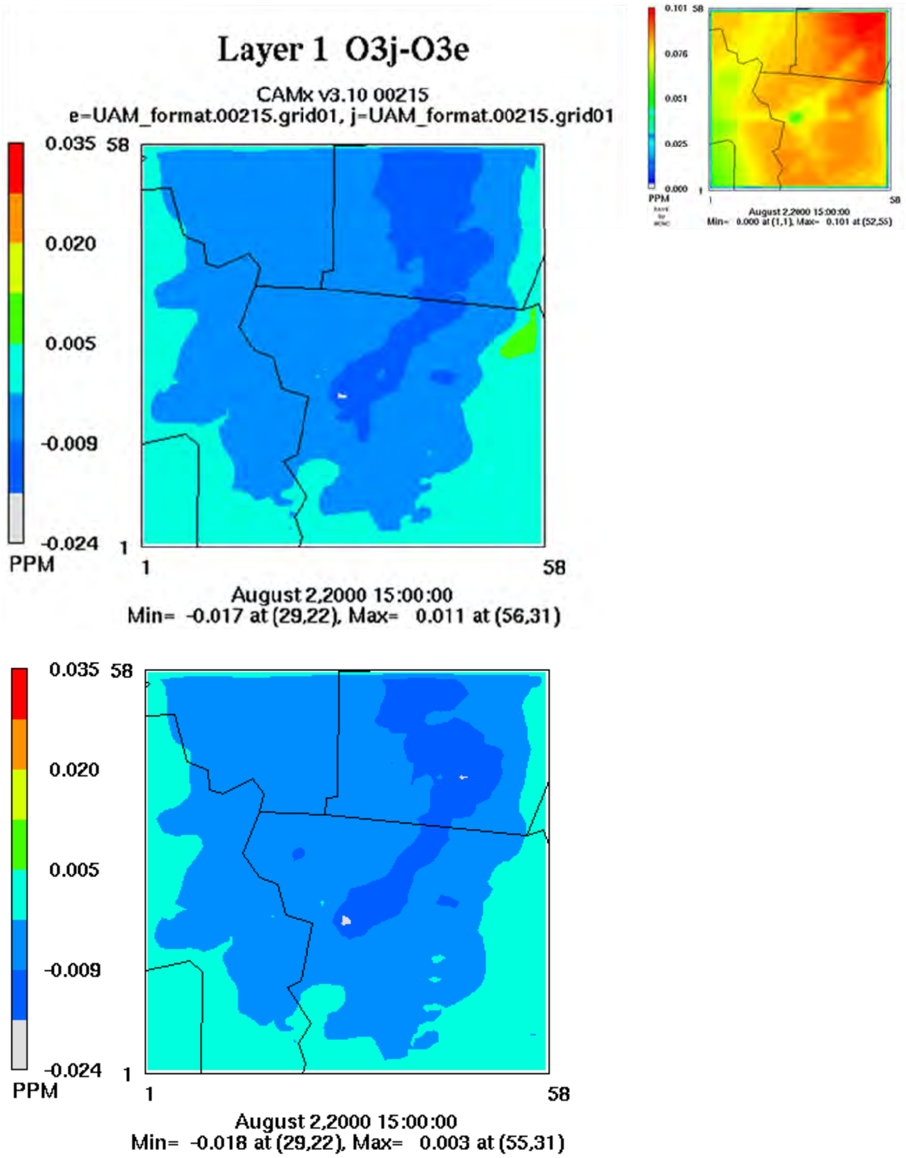

Figure 4.22. Changes in O_3 at time of base-case peak in the Sacramento 1 km domain. Top: Increased urban albedo scenario; Bottom: Increased canopy cover scenario. Top-right: Base-case ozone concentration (peak) at this hour.

To further probe the all-time daily maximum decreases and increases in ozone, Figure 4.23 shows the corresponding times of occurrence for the high albedo scenario. (The increased-canopy scenario is not shown, since the changes are smaller and less extreme than those of increased albedo). The analysis, in summary, shows that while such large increases or decreases can occur, they are typically limited in space and time (e.g., occurring during a single hour interval and at three or fewer grid cells) and that the more general effects identified in the simulations (and discussed above) represent the main signal. Even though they are not representative of the general effect, the large changes in ozone are discussed to show the model's sensitivity to changes in temperature, mixing height, wind field, and related parameters. Note that many of these extreme changes in concentrations do not occur within the critical part of the day. In most cases, they occur either earlier in the morning or later in the evening. Also noticeable, e.g., in Figure 4.23**,** is that while the decreased concentrations affect relatively large areas, the increases in ozone typically affect much smaller areas. In the figure, the scale and color scheme were changed to highlight only those areas with the largest ozone changes. As a result, the graphics in this figure do not correspond to those of the figures above.

Thus, in general, the simulations suggest that surface modification scenarios, as simulated by the uMM5 1 km CAMx, can decrease ozone concentrations by large amounts (e.g., 20s or even 30s of ppb) but that such extreme decreases are limited to small areas (a few km^2). The large reductions are captured by the model because of the fine-resolution simulation capabilities not available relative to coarser and more convectional simulations, such as, those conducted in Phase 1. When such reductions are averaged back to coarse-grid model resolution, they become more comparable to the coarse-grid-predicted changes in concentrations resulting from UHI control, such as those obtained in Phase 1. Therefore, the fine-resolution simulations present a useful tool in "zooming into" the coarse-grid simulated fields to detect and capture the fine-resolution details that may be important for fine-resolution analysis and planning purposes.

Back to the more representative changes in ozone, Figure 4.24, a–e, shows the simulated ozone concentrations as time series at the location (grid cell) of each day's simulated domain-wide peak (July 29 through August 2). These points do not correspond to any monitor location of interest (e.g., those discussed elsewhere in this report), they just correspond to the grid cell where the highest concentration of the day was simulated. Most of these locations are downwind, to the northeast, east, or southeast of the domain, as discussed earlier. In the lower part of each figure, the changes in ozone (ppb) at the corresponding grid cell are given for the high-albedo scenario (red line) and the increased canopy cover scenario (green line).

In general, the modeling suggests that the effects of changes in canopy cover (as assumed in this scenario) are similar to or smaller than those of increased urban albedo. This is seen again in (Figure 4.24a), except for the evening on July 29 at point 41,44. The simulations also show that the general pattern resulting from surface perturbations is a decrease in concentrations during the daytime and sometimes through the evening as well. There can also be periods, e.g., early in the morning (and in one case, in mid-day), when concentrations increase as a result of UHI control. However, in all cases, there is a decrease in concentrations at the time of the peak, which is the desired effect.

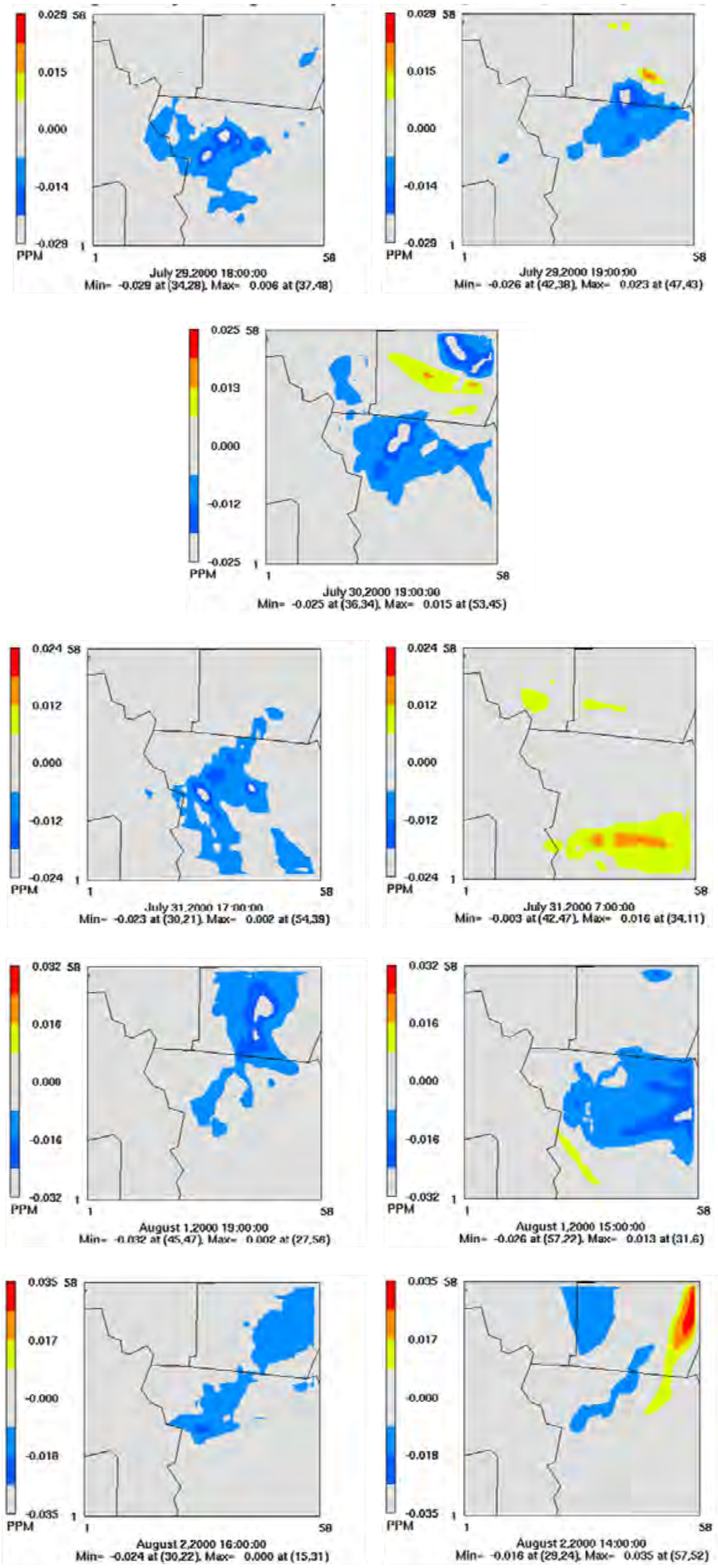

Figure 4.23. Changes in ozone concentration at times of largest decrease (left) and largest increase (right) for the increased urban albedo scenario. The times of these occurrences are given on each figure.

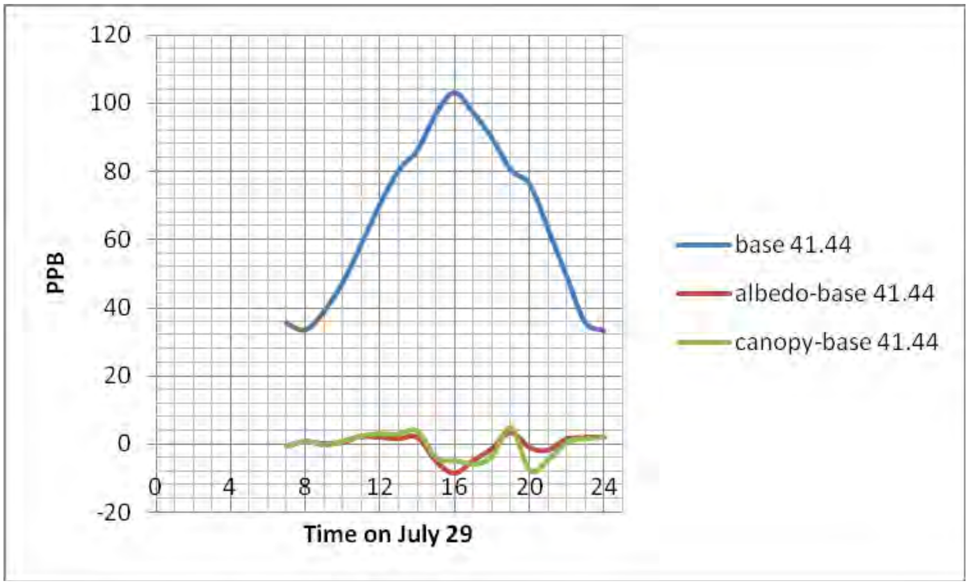

a

29 July: Simulated peak = 103 ppb at 41,44
(bottom of figure: changes in [O3] from UHI control

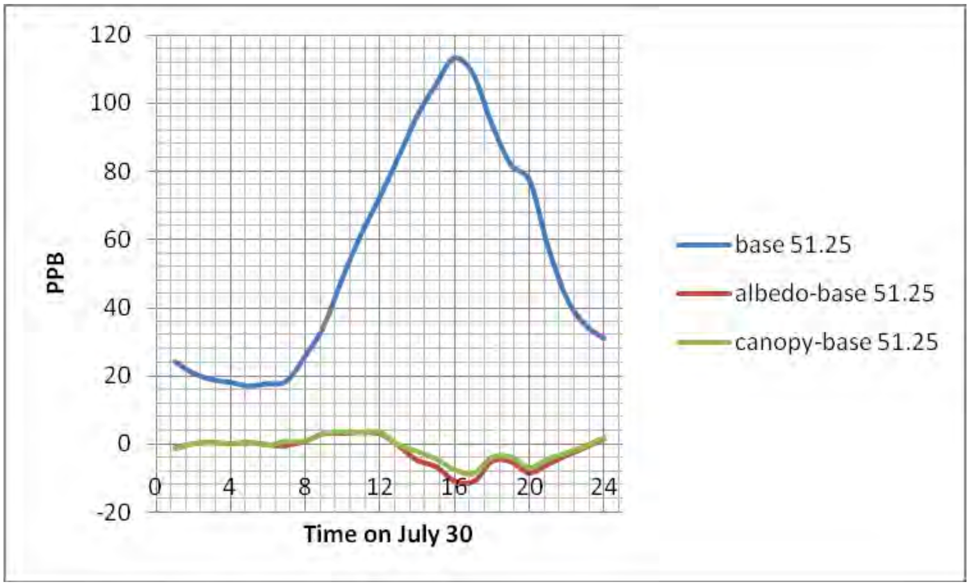

b

30 July: Simulated peak = 113 ppb at 51,25
(bottom of figure: changes in [O3] from UHI control

Figure 4.24 a–e. Simulated ozone concentrations (and changes) time series at locations (grid cell) of each day's simulated domain-wide peak

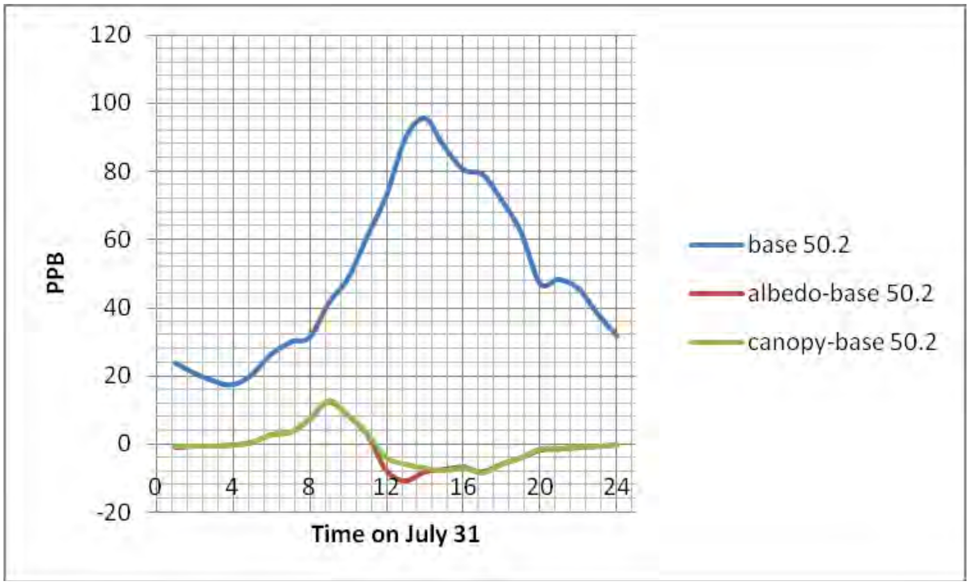

c

31 July: Simulated peak = 96 ppb at 50,2
(bottom of figure: changes in [O3] from UHI control

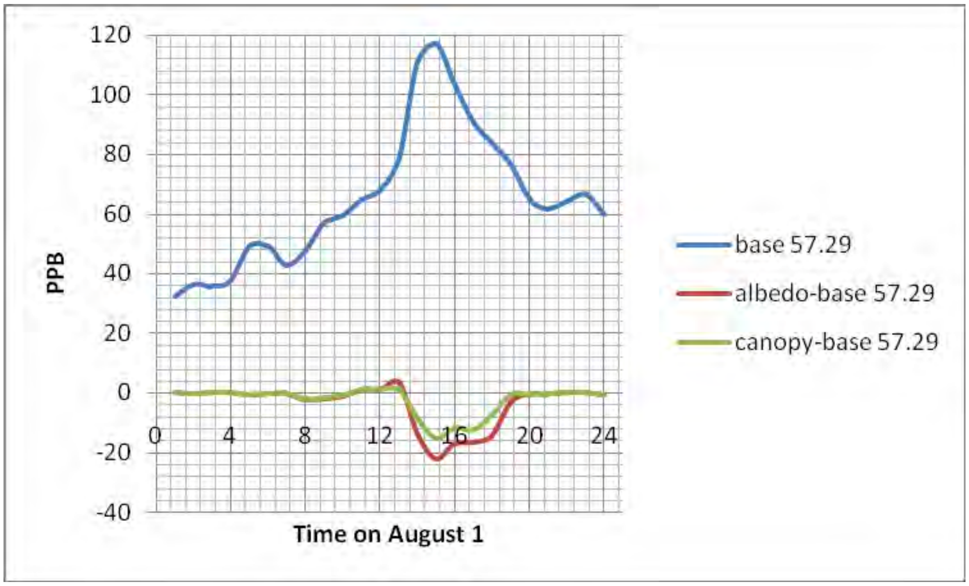

d

1 August: Simulated peak = 117 ppb at 57,29
(bottom of figure: changes in [O3] from UHI control

Figure 4.24 (continued)

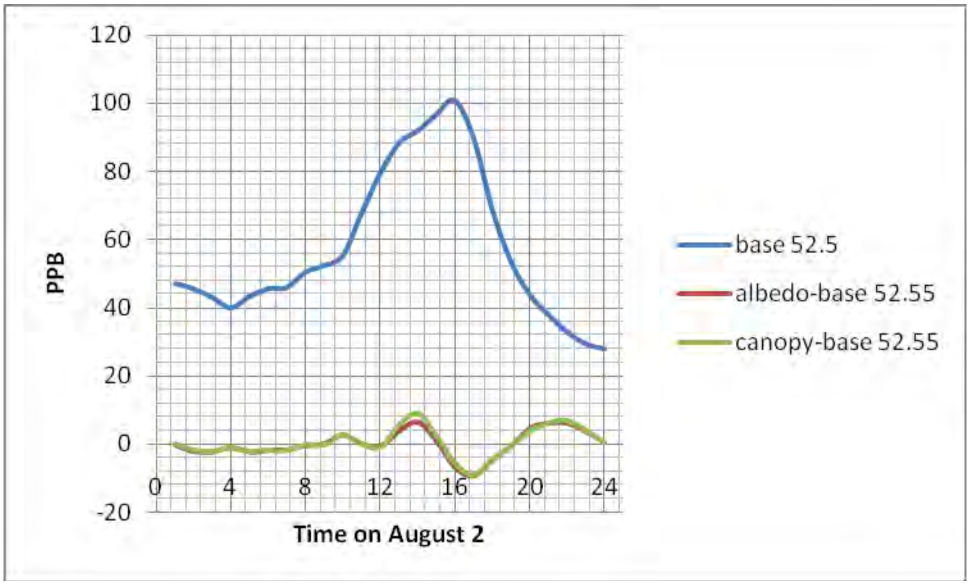

e

2 August: Simulated peak = 101 ppb at 52,5
(bottom of figure: changes in [O3] from UHI control

Figure 4.24 (continued)

Table 4.2 summarizes the changes in ozone concentrations at the locations of the simulated daily peaks. Results indicate that increased urban albedo is relatively more efficient in improving air quality than increased canopy cover. At the times and locations of the simulated daily peaks, albedo increase is 20% to 100% more effective than increased canopy cover (in terms of impacts on the peak concentrations paired in space and time). However, if only pairing in *space* is done, that is, at the peak's location but regardless of the *time*, then both strategies can show similar effectiveness in some cases.

Table 4.2. Summary of ozone changes at locations of simulated daily peaks (i.e., at locations in Figure 4.24)

Base-case peak (simulated)				Δ [O3] (ppb) at location of peak			
		Time of peak (LST)	Location of peak (x,y)	At time of peak		Max Δ [O3] at any time	
	Peak (ppb)			A - B	C - B	A - B	C - B
July 29	103	1600	41,44	-8.7	-4.8	-8.7 (at1600)	-7.8 (at 2000)
July 30	113	1600	51,25	-10.9	-7.4	-11.1 (at 1700)	-8.6 (at 1700)
July 31	96	1400	50,2	-8.1	-6.9	-10.6 (at 1300)	-8.4 (at 1700)
August 1	117	1500	57,29	-22.2	-15.4	-22.2 (at 1500)	-15.4 (at 1500)
August 2	101	1600	52,55	-6.7	-5.6	-9.2 (at 1700)	-9.1 (at 1700)

A: Albedo (high-albedo scenario)
B: Base case
C: Canopy (increased canopy cover scenario)

Further, for downwind monitors at Folsom-Natoma (FLN) and two mid-domain locations, Sacramento T Street (S13) and Del Paso Manor (SDP), Figure 4.25, a–c, shows the affect of UHI control. Interestingly, the effects of increased albedo and increased canopy cover at these locations are relatively more similar than at other locations. The changes in ozone concentrations at these monitors, as a result of surface modifications, are consistent and similar in magnitudes to those discussed earlier.

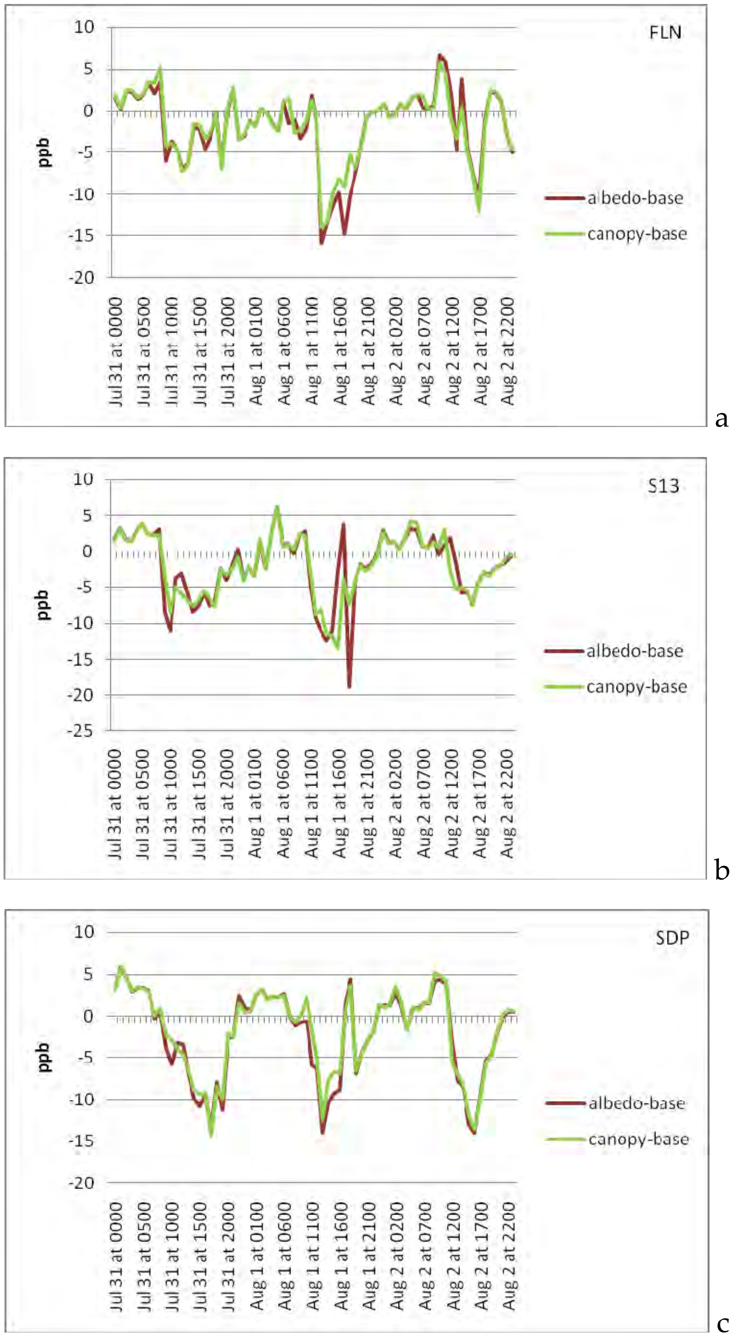

Figure 4.25 (a–c). Change in ozone concentrations (ppb) at monitors of interest for two scenarios: Increased urban albedo (red) and increased canopy cover (green)

Lastly, one way to examine the potential impacts of surface modifications (UHI control) on ozone air quality is to evaluate their impact on the daily maximum 8-hour average. A summary of this analysis, along with the relative reduction factor (RRF) for monitor locations of interest is shown in Figure 4.26. As discussed earlier, monitors FLN, SLU, and ROC are generally downwind, whereas S13 and SDP are closer to mid-domain.

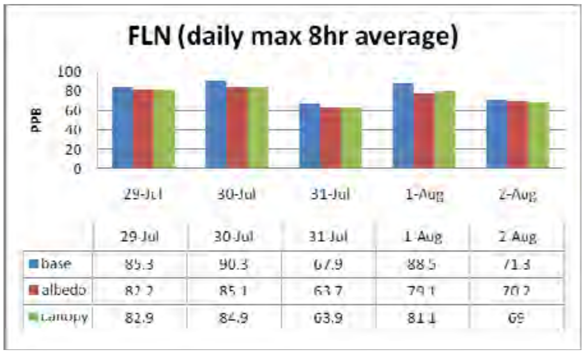
FLN (daily max 8hr average)

	29-Jul	30-Jul	31-Jul	1-Aug	2-Aug
🟦 base	85.3	90.3	67.9	88.5	71.3
🟥 albedo	82.2	85.1	63.7	79.1	70.2
🟩 canopy	82.9	84.9	63.9	81.1	69

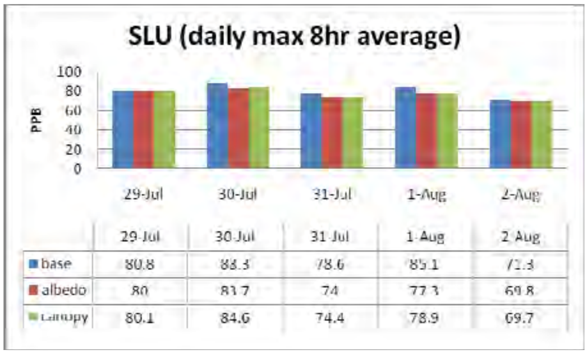
SLU (daily max 8hr average)

	29-Jul	30-Jul	31-Jul	1-Aug	2-Aug
🟦 base	80.8	88.3	78.6	85.1	71.3
🟥 albedo	80	83.7	74	77.3	69.8
🟩 canopy	80.1	84.6	74.4	78.9	69.7

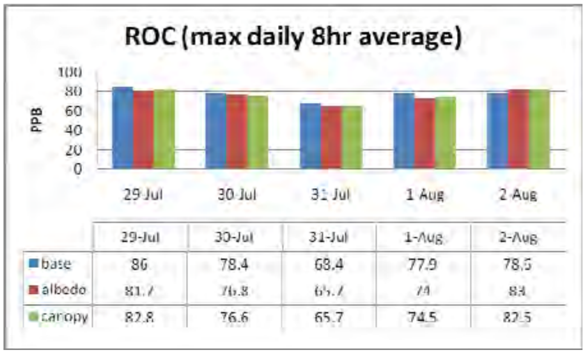
ROC (max daily 8hr average)

	29-Jul	30-Jul	31-Jul	1-Aug	2-Aug
🟦 base	86	78.4	68.4	77.9	78.5
🟥 albedo	81.7	76.8	65.7	74	83
🟩 canopy	82.8	76.6	65.7	74.5	82.5

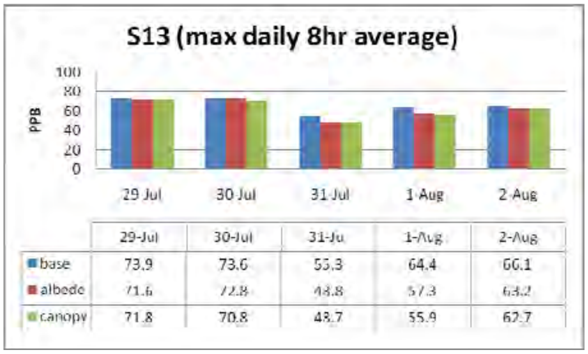
S13 (max daily 8hr average)

	29-Jul	30-Jul	31-Jul	1-Aug	2-Aug
🟦 base	73.9	73.6	55.3	64.4	66.1
🟥 albedo	71.6	72.8	48.8	57.3	63.2
🟩 canopy	71.8	70.8	48.7	55.9	62.7

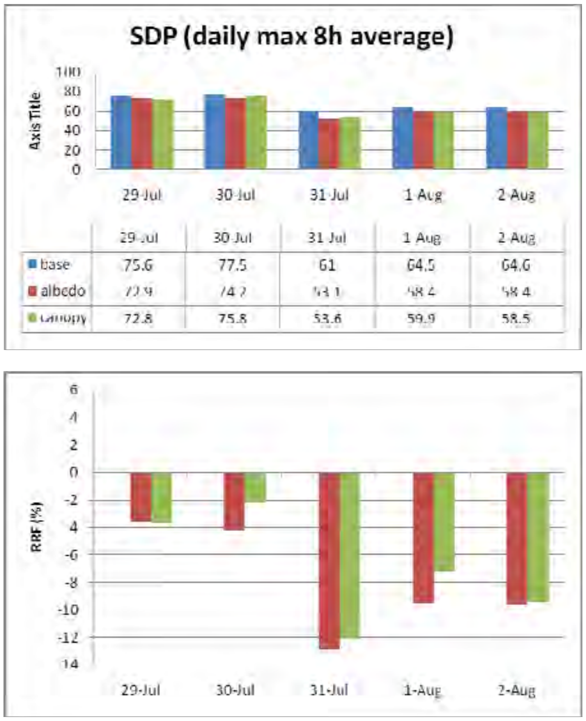

	29-Jul	30-Jul	31-Jul	1-Aug	2-Aug
🟦 base	75.6	77.5	61	64.5	64.6
🟥 albedo	72.9	74.2	53.1	58.4	58.4
🟩 canopy	72.8	75.8	53.6	59.9	58.5

Figure 4.26. Daily maximum 8-hour average ozone (simulated) and potential RRF as a result of increasing surface albedo (red) and canopy cover (green). Blue represents the base-case scenario.

The top portion of each figure depicts the simulated daily maximum 8-hour average (at the given monitor location) for the base case (blue), the scenario with increased albedo (red), and a scenario with increased canopy cover (green) for each of the five days of the episode. The bottom portion of each figure shows the RRF corresponding to these strategies for each day. Here the RRF is plotted as (1-RRF)%.

Except for one instance, on August 2, at ROC (the Rocklin monitor location), the impacts of UHI control at all locations and days represent a decrease in the daily maximum 8-hour average. The RRF analysis shows that the daily maximum 8-hour average can be decreased by anywhere between 4% and 14% across the episode days and monitor locations. The largest impacts are seen on July 31 and August 1 which is important since these are days of high ozone in north Central California, i.e., San Francisco Bay Area and the Sacramento Valley (see Table 3.3). Figure 4.26 also shows that while the effects of increased albedo are generally larger than those of increased canopy cover, there are some cases where increased canopy cover is more effective. This is particularly noticeable at the S13 monitor location, which is close to the downtown area. The simulations also suggest that percentage-wise, the effects of surface perturbations are relatively larger at mid-domain monitors compared to downwind ones. For July 31 and August 1, the downwind monitors (FLN, SLU, ROC) experience reductions of around 5%–10%, whereas mid-domain monitors (S13, SDP) see reductions of 9%–12%.

4.2. Orange-Riverside Grid

The discussion of O-R modeling results in the next few sections follows a pattern similar to that of Sacramento in Section 4.1. However, there are two reasons why the discussion is shorter. First, there is less detail and explanation, because most of the systematic basis for the discussion has already been introduced in the Sacramento sections. Second, the O-R domain was introduced and evaluated as a potentially worst-case scenario, and thus the focus of the discussion is different.

4.2.1. Base Case

Heat Island

Figure 4.27 (a–q) depicts the simulated air temperature and wind fields at the lowest atmospheric layer, for every three hours, starting at 50 hours through the forecast (figure a) through 98 hours of forecast (figure q). The full-modeled episode starts at 0000 LST August 3 and ends 0200 LST August 8 (1997), but the focus of the discussion here is on August 5 and 6.

At 0000 LST on August 5 (a), the temperature field is relatively uniform in the west basin, with a weak gradient between the coastal area (west) and the inland area (east). Temperatures to the east of the Santa Ana Mountains (SAM) are about 3°C higher than in the western domain. The flow is multi-directional, where onshore flow mixes with easterly and northerly flow at about mid domain. A very weak UHI is detectable at this hour, about 1°C in the Santa Ana–Irvine area. This pattern continues through 0300 and 0600 LST (b and c) relatively unchanged except for the lower temperatures over the western, coastal boundary.

At 0900 LST (d), inland areas in the eastern half of the domain warm up faster than the western half due to the cooler onshore flow and the blocking effect of the SAM. The temperature difference is about 3°C–4°C. A small UHI (1°C) is also present in the western half of the domain, mainly near the city of Irvine. Figure e shows the conditions at 1200 LST, when most of the domain is in the range of 34°C–38°C and where the coastal areas are about 6°C, or more, cooler than the far inland areas. Some urban areas are warmer as well; for example, the Garden Grove/Orange and Irvine areas are about 6°C hotter than at Newport Beach. However, it is likely that most of this temperature differential is caused by the warming of the sea breeze and that a smaller fraction is caused by the UHI effect.

A generally similar situation is seen at 1500 LST (f). The cooler area in the eastern part of the domain is at the higher elevations of the SAM. The UHI pattern is similar to that at 1200 LST discussed above. While a large portion of the domain begins to cool down by 1800 LST (g), there are warm areas inland (east of SAM) and in central domain. Urban areas around Garden Grove/Orange to the north and Irvine to the south are within a UHI of 2°C–3°C. The cooling trend continues so that by 2100LST (h) most of the domain is at 24°C–29°C, except for the higher elevations at SAM (inversion), where the temperature is about 2°C higher. A weak (1°C) UHI is also seen at mid domain. The conditions of cooler surface and slightly warmer mountains continue through 0000 and 0300 LST on August 6 and with the same weak UHI in the western half of the domain (i and j).

The pattern then repeats the previous-day's cycle with warming inland (by 0900 LST) and relatively cooler coastal areas (k and l). During this time interval no significant UHI is detected. This is followed by significant warming inland and downwind of the urban area with cooler temperatures at higher altitudes. This pattern can be seen at 1200 and 1500 LST (m and n), during which there also exists a UHI of 2°C–3°C downwind of Irvine. After that, most of the domain cools down (1800, 2100, and 0000LST), as seen in figures o, p, and q, with some warmer spots left over from previous hours in the far inland areas (the eastern boundary of the domain). At about 2100 LST, a weak UHI (1°C–2°C) reappears in the Orange-Irvine areas, thus completing the cycle.

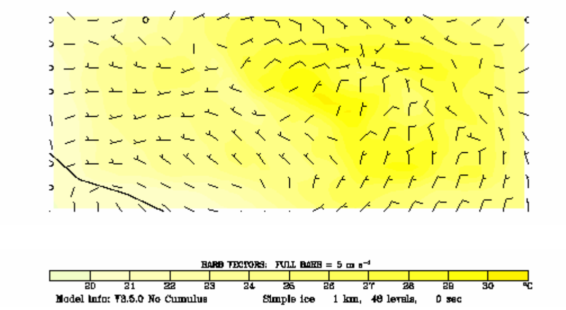

a

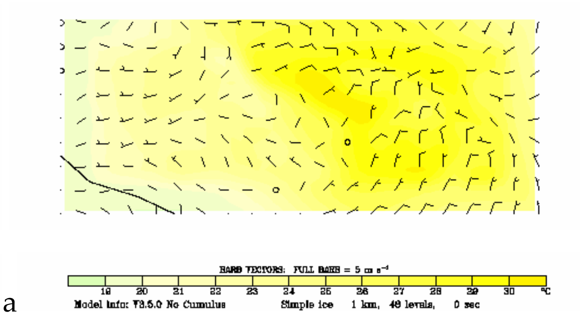

b

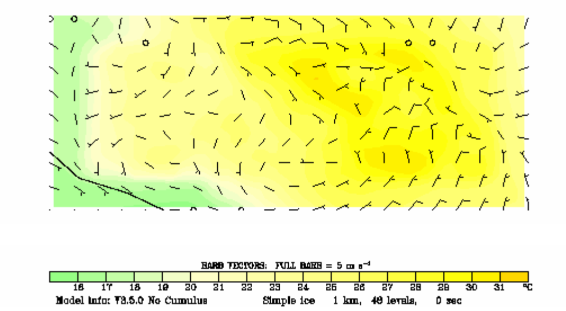

c

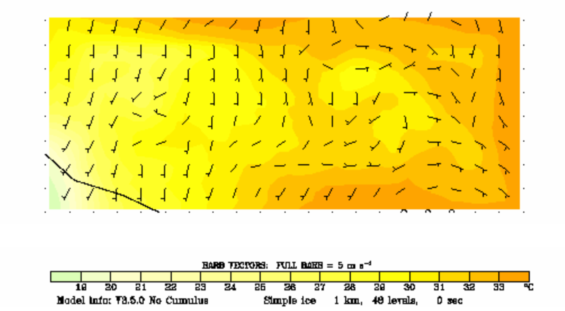

d

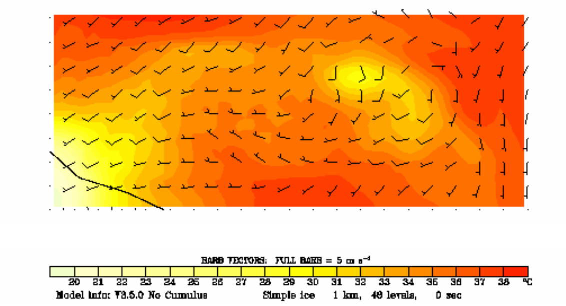

e

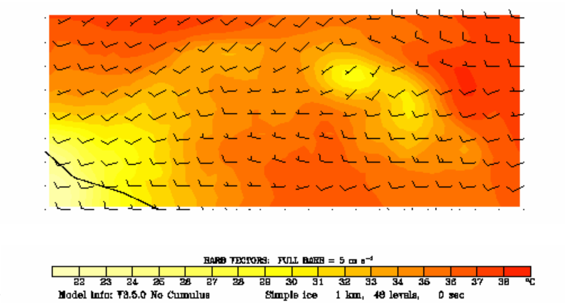

f

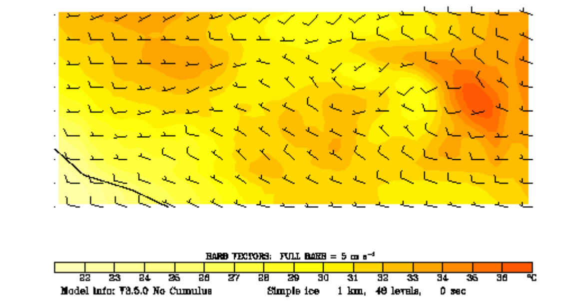
BARB VECTORS: FULL BARB = 5 m s⁻¹
22 23 24 25 26 27 28 29 30 31 32 33 34 35 36 °C
Model Info: V3.5.0 No Cumulus Simple ice 1 km, 40 levels, 0 sec

g

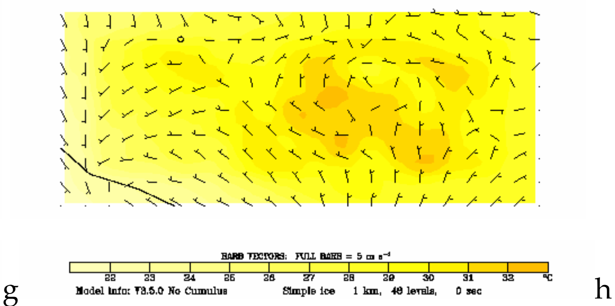
BARB VECTORS: FULL BARB = 5 m s⁻¹
22 23 24 25 26 27 28 29 30 31 32 °C
Model Info: V3.5.0 No Cumulus Simple ice 1 km, 40 levels, 0 sec

h

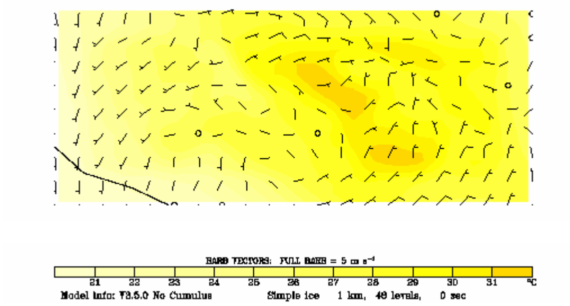
BARB VECTORS: FULL BARB = 5 m s⁻¹
21 22 23 24 25 26 27 28 29 30 31 °C
Model Info: V3.5.0 No Cumulus Simple ice 1 km, 40 levels, 0 sec

i

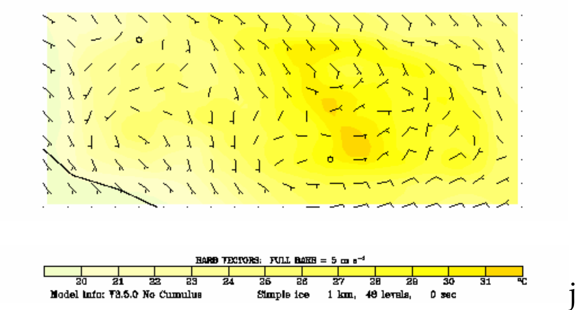
BARB VECTORS: FULL BARB = 5 m s⁻¹
20 21 22 23 24 25 26 27 28 29 30 31 °C
Model Info: V3.5.0 No Cumulus Simple ice 1 km, 40 levels, 0 sec

j

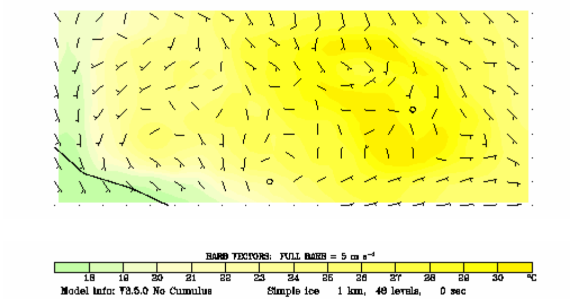
BARB VECTORS: FULL BARB = 5 m s⁻¹
18 19 20 21 22 23 24 25 26 27 28 29 30 °C
Model Info: V3.5.0 No Cumulus Simple ice 1 km, 40 levels, 0 sec

k

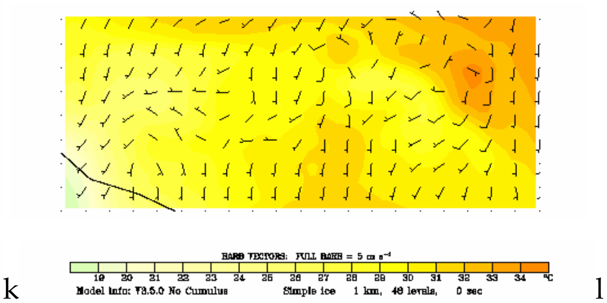
BARB VECTORS: FULL BARB = 5 m s⁻¹
19 20 21 22 23 24 25 26 27 28 29 30 31 32 33 34 °C
Model Info: V3.5.0 No Cumulus Simple ice 1 km, 40 levels, 0 sec

l

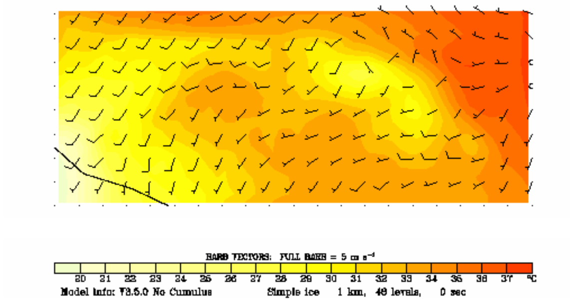
BARB VECTORS: FULL BARB = 5 m s⁻¹
20 21 22 23 24 25 26 27 28 29 30 31 32 33 34 35 36 37 °C
Model Info: V3.5.0 No Cumulus Simple ice 1 km, 40 levels, 0 sec

m

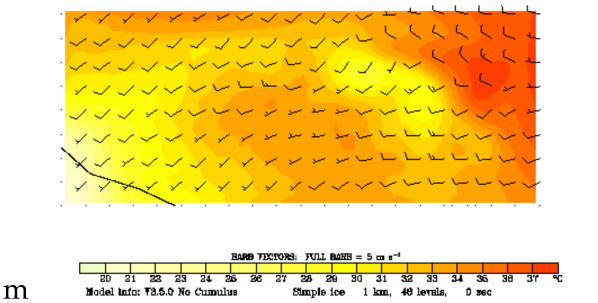
BARB VECTORS: FULL BARB = 5 m s⁻¹
20 21 22 23 24 25 26 27 28 29 30 31 32 33 34 35 36 37 °C
Model Info: V3.5.0 No Cumulus Simple ice 1 km, 40 levels, 0 sec

n

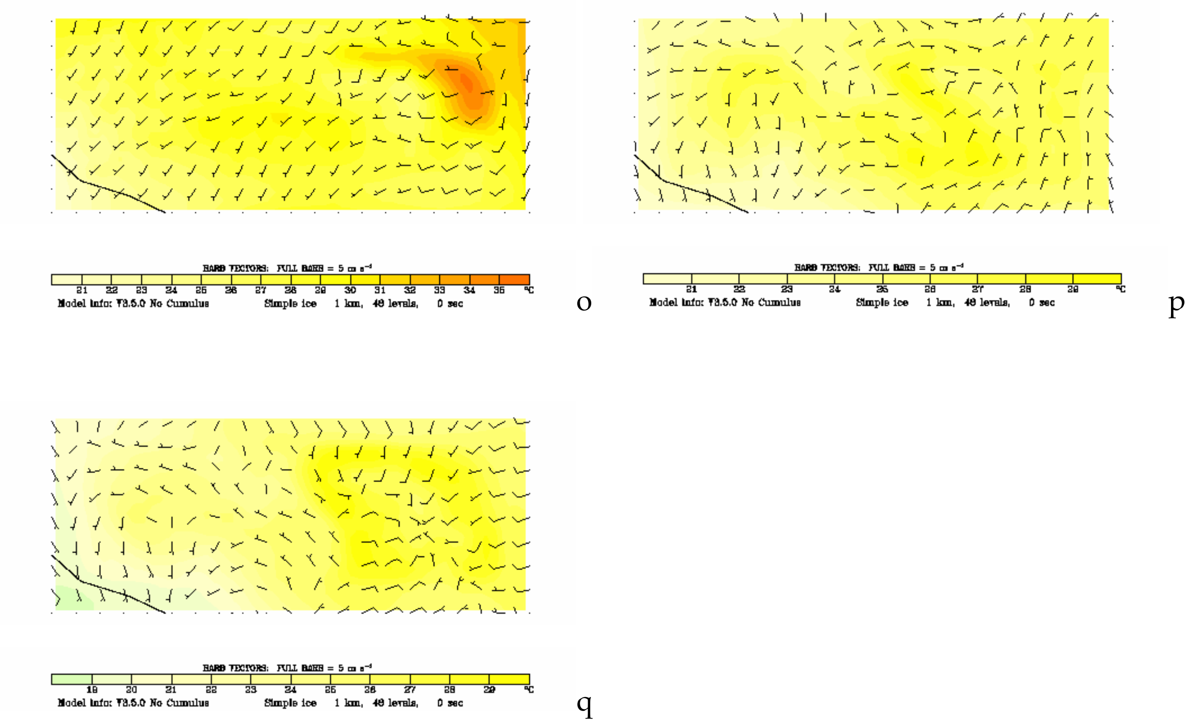

Figure 4.27. Simulated base-case air temperature and wind vector fields for the O-R uMM5 domain

As an example from further analysis of this area, temperature time series at two arbitrary locations are shown below, but first, Figure 4.28 shows the two regions. Location 12,11 is an area with high-rise office buildings and significant amount of paved surfaces (parking lots) but also surrounded by abundant vegetation cover (e.g., parks and golf courses), whereas location 15,20 is a mixed residential-commercial area with lower vegetative cover.

Figure 4.28. Aerial characterization of locations 12,11 (left) and 15,20 (right) in the O-R uMM5 domain

The time series in Figure 4.29a shows simulated air temperature at these two locations for August 3 through 7. Air temperature at location 15,20 reaches a maximum of 35.8°C on August 5 at 1300 LST, whereas the second location (12,11) reaches a maximum of 31.8°C at 1200 LST on that day. Both locations show simulated air temperature peaking on the main days of the episode (August 5 and 6). Figure 4.29b shows the difference in air temperature between these two locations. The effect of land cover (the higher vegetative cover at 12,11) is noticeable, as that area is consistently cooler than location 15,20. The temperature difference reaches up to 4°C at times and the vegetated area is generally cooler during daytime hours. At night the temperature difference is small. Another possible contributing factor to this difference is that location 15,20 is a few kilometers further inland than 12,11 and so its temperature may be higher as a result. But the distance is not large enough to explain all of the temperature difference, so most of the effect can be attributed to land-cover impact.

The model is capable of capturing the cooling effect of urban parks and golf courses at sub-kilometer scale, which is an improvement over the Phase 1 modeling (e.g., at 5 km in this case). It also shows, from a planning perspective, that such small urban parks (smaller than 0.5 km) can have a significant and detectable effect, and therefore should be accounted for both in modeling and in land-use planning.

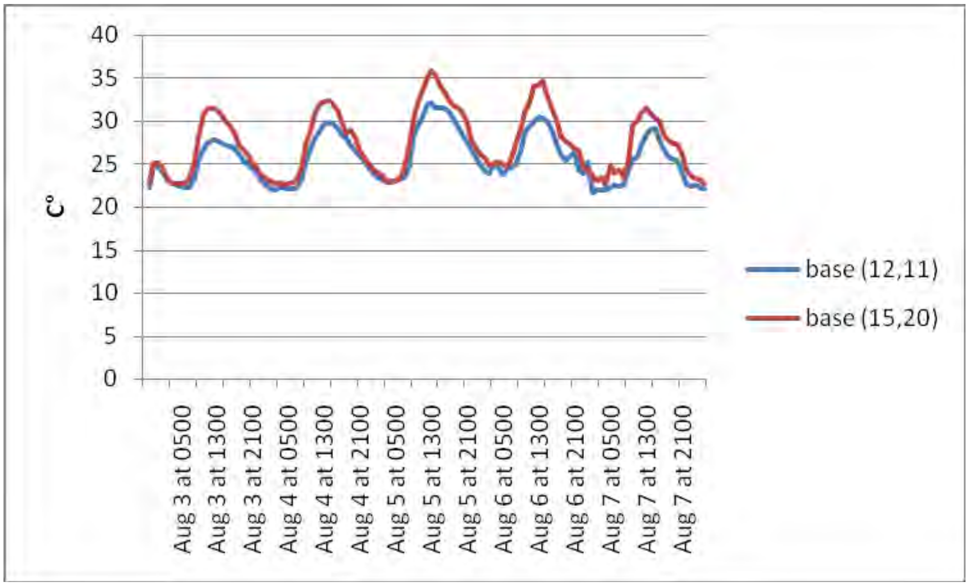

a

Figure 4.29. a: Simulated air temperature at two locations (12,11 and 15, 20) in the O-R domain

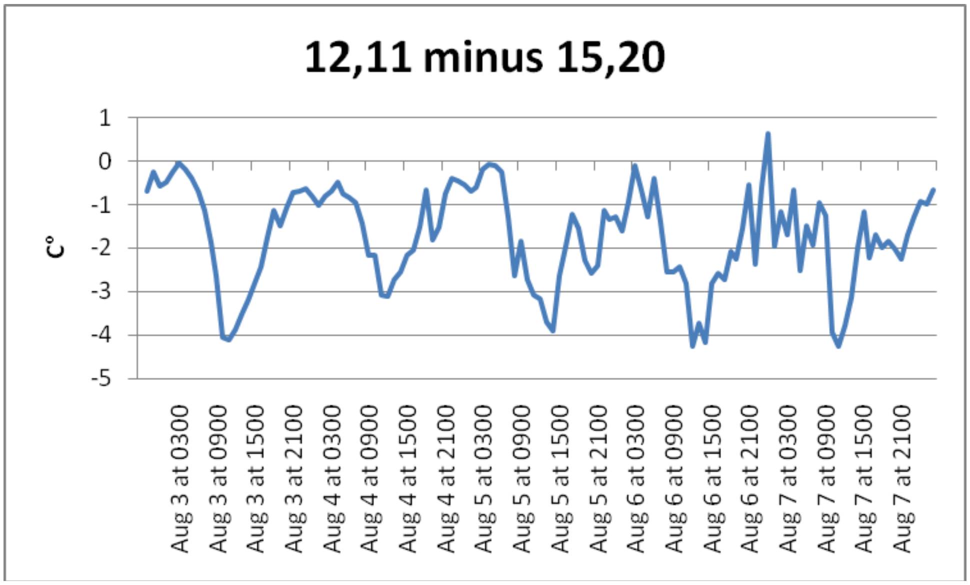

Figure 4.29. b: Air temperature difference between the two locations.

Following this brief temperature analysis, some vertical profiles of TKE budget terms are shown, as was discussed in the heat island part of Section 4.1.1 for Sacramento. The same time-of-day is selected, in this case, 1400 LST August 6 as an example (since this is a time of typically highest temperatures and unstable atmosphere). Nearly all aspects of the heat island discussion in Section 4.1.1 for Sacramento apply here. Of course, the magnitudes and changes involved are different, but the profiles and their response to FAD changes are generally similar. In Figures 4.30 and 4.31, the profiles are plotted for up to each grid cell's UCL top, which is at about 149 m in grid 12,11 and at 11 m in grid 15,20. As discussed above, these two locations have various land covers and functions. As with the Sacramento example, the local building frontal area density function, bldgFAD (m^2m^{-3} scaled by 30 to fit the figure), is shown as a descriptor of the roughness elements present in the cells. Wind speed (wsp,ms^{-1} scaled by 1/100 to fit the figure) and several TKE budget terms are shown (m^2s^{-3}). Close-up details are provided where profiles are too close together.

The results show that vertical profiles of shear production of TKE generally follow the FAD profiles and peak at or higher than the critical FAD elevation. Shear production is very small near the ground, increasing upward through the canopy until the peak level. The same profile is seen for buoyancy and accelerated cascade terms. The cascade term decreases rapidly above the critical FAD elevation, whereas buoyancy production decreases more slowly (at this time of unstable atmospheric conditions).

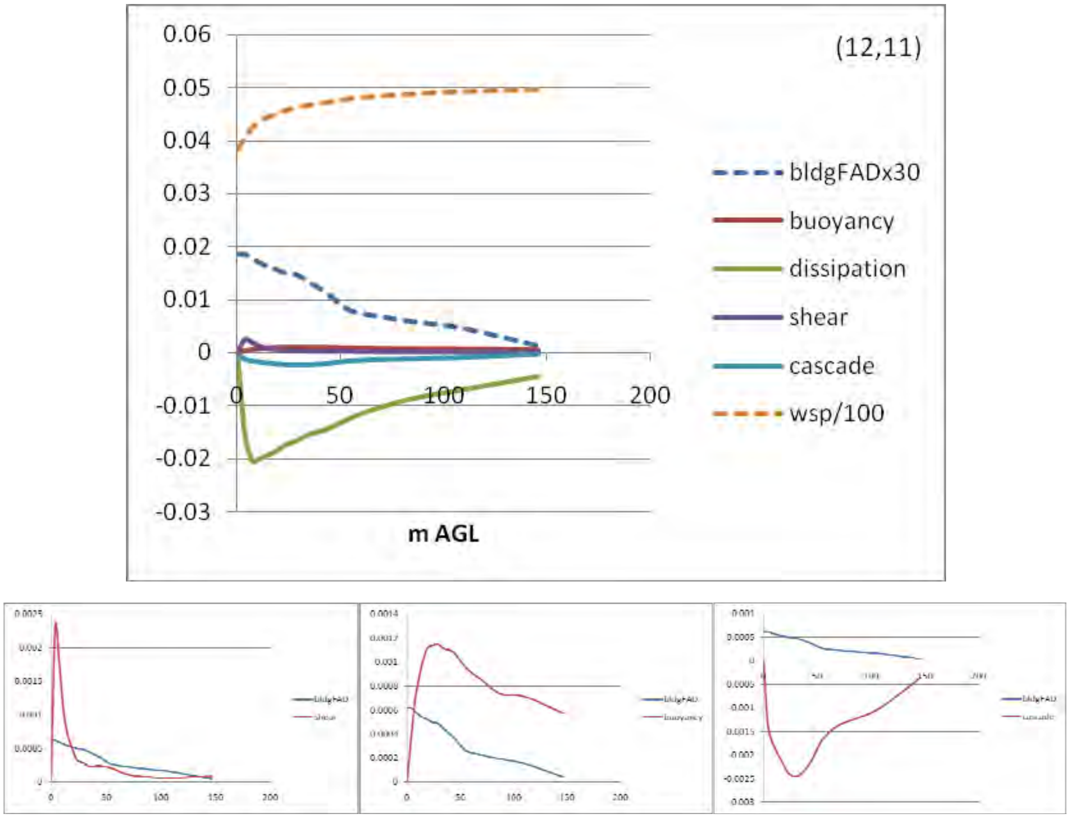

Shear Buoyancy Cascade

Figure 4.30. Selected TKE budget terms for location 12,11 in the O-R modeling domain

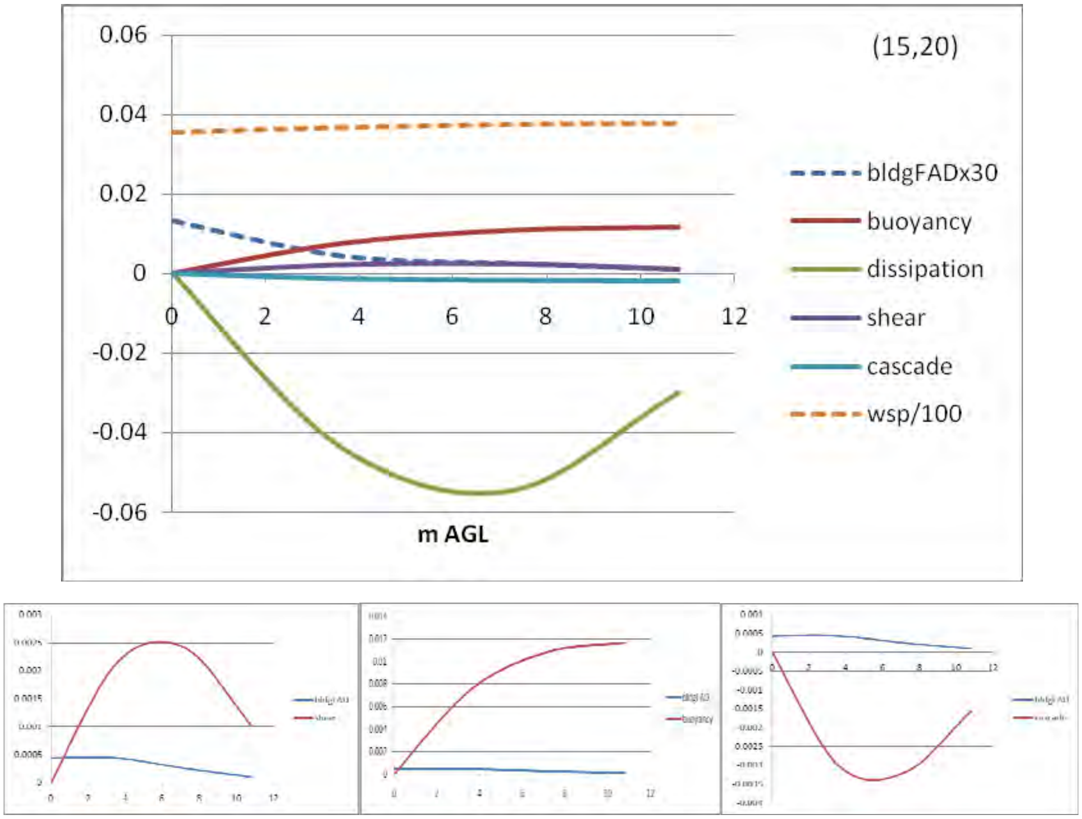

Shear Buoyancy Cascade

Figure 4.31. Selected TKE budget components for location 15,20 in the O-R modeling domain

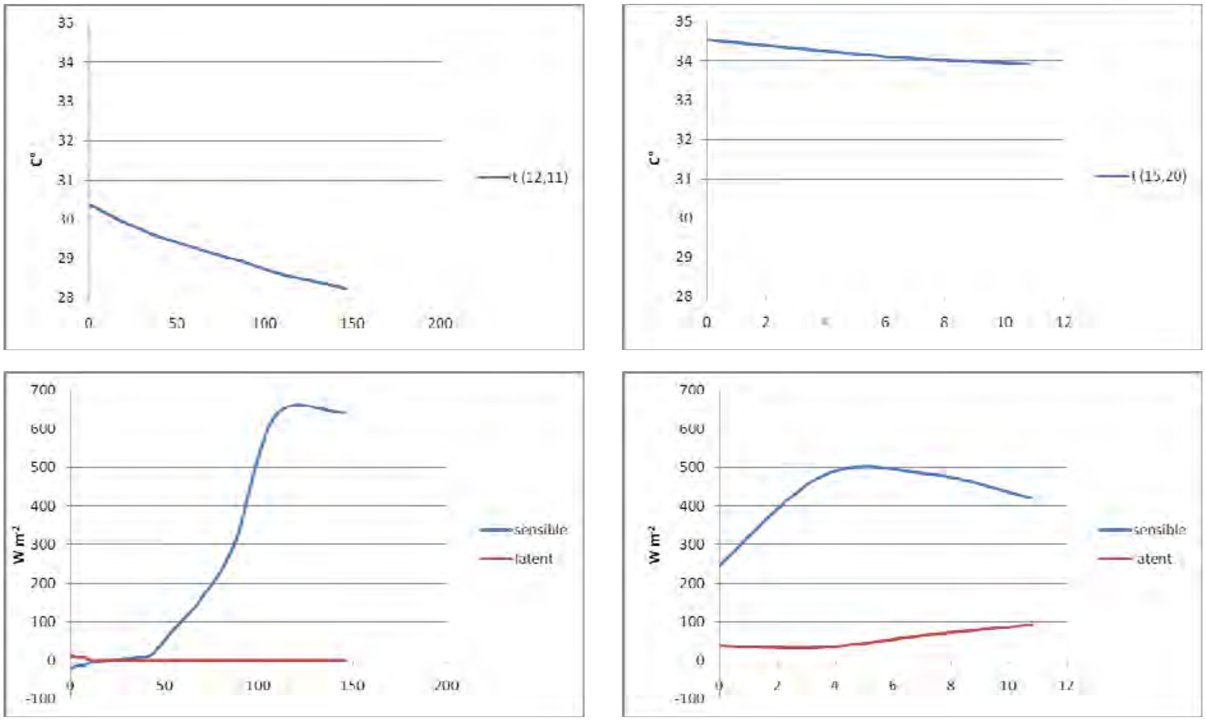

Figure 4.32. Sensible and latent heat fluxes and air temperature at given locations in the O-R uMM5 domain

Figure 4.32 shows the corresponding vertical profiles of air temperature, sensible, and latent heat fluxes at locations 12,11 and 15,20 discussed above. Temperature is about 30.5°C at 3 m AGL (decreasing to 28°C at 149 m AGL) in the high-rise/vegetated area and about 34°C in the residential-commercial area (this difference was discussed earlier). Heat flux profiles show that at location 12,11 there is negative sensible and positive latent heat fluxes near the surface (both contributing to cooling), whereas sensible heat flux is postive all the way at location 15,20; thus the warmer environment.

Photochemistry / Air Quality

Figures 4.33 and 4.34 show the simulated ozone concentration field at the times of the simulated daily peak on August 5 (at 1400 LST) and August 6 (at 1200 LST), respectively. The domain shown here is the O-R 1 km CAMx grid corresponding to the fine-resolution uMM5 modeling grid for this area. The peak concentrations are downwind of the coastal area, in the mountain range and eastern basin as expected, but some higher concentrations on August 5 are also seen at the western boundary of the domain. This high ozone enters the domain from the northwest, i.e., from the Los Angeles area. The simulated peak on August 5 is 113 ppb, and on August 6 it is 97 ppb. The lower concentrations in the western basin reach up to 50–80 ppb on both days (at the given times of the peak). The peaks shown in Figures 4.33 and 4.34 are local peaks in the 1 km grid, not the domain-wide peaks occurring in the coarse grid outside of this domain.

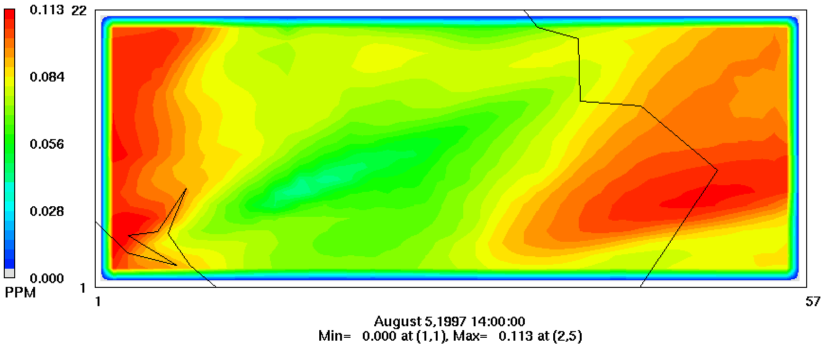

Figure 4.33. Simulated ozone concentration field at the time of the simulated peak on August 5

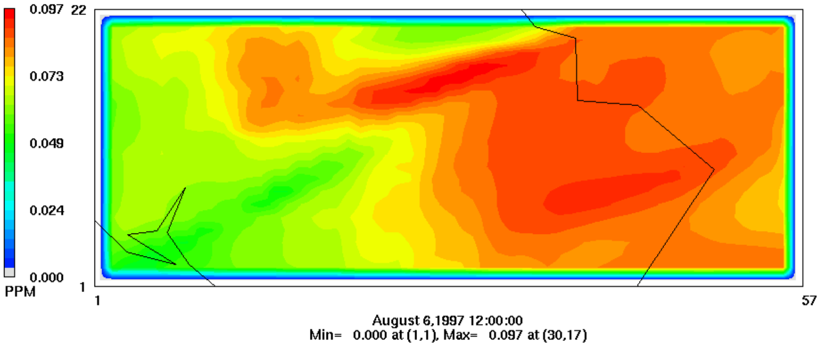

Figure 4.34. Simulated ozone concentration field at the time of the simulated peak on August 6

Figure 4.35 shows the simulated ozone concentrations for the base case as time series at four locations. These are El Toro, Tustin, and locations 20,9 and 21,15 (location 20,9 is in Irvine, whereas location 21,15 is in the Tustin area). All these locations are in the western domain (urban area) and not in the peak ozone regions (non-urbanized eastern half of the domain). The simulated concentrations at these locations reach up to 82 ppb on August 5 and 85 ppb on August 6. The figure shows lower concentrations at Irvine (20,9) compared to the slightly more inland areas of Tustin and El Toro.

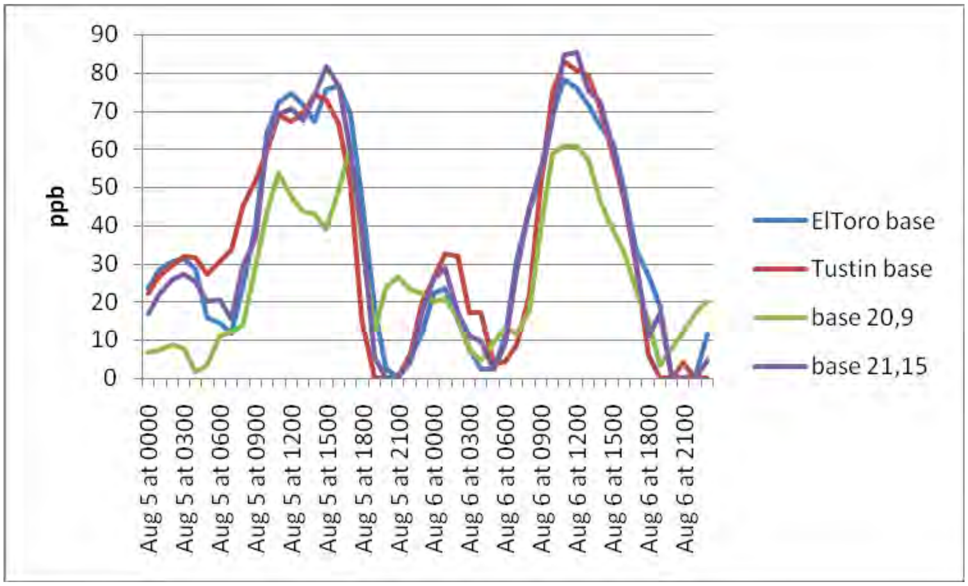

Figure 4.35. Time-series of simulated ozone concentrations for the base case at four locations in the O-R domain

4.2.2. Control Scenarios

Meteorology

For this discussion, Figure 4.36 a–h presents two-dimensional cross sections of the temperature-change field at six-hour intervals starting 0000 LST August 5 (the 50th hour of the forecast) through 1800 LST August 6 (the 92nd hour of forecast) for the high-albedo scenario. Superimposed on temperature change is the base-case wind vector field. This figure is followed by Figure 4.37 i–p showing the same sequence but for change in surface temperature at the corresponding hours. Figure 4.38 1–4 shows the air- and surface temperature-change fields at those hours when the largest changes in *air* temperature occur (for scenario of increased albedo) on each of the two days of interest in this discussion.

Similarly to the Sacramento results, the O-R simulations show that during nighttime hours, increased surface albedo has minimal or no impact on air temperature. This can be seen for example at 0000 and 0600 LST on August 5 (a and b). After sunrise, the temperature difference (cooling effect) appears. Thus, by 1200 LST on that day (c), there is a temperature reduction of up to 2.5°C in the western basin (in the areas of Orange, Santa Ana, and Tustin). The temperature difference becomes larger through 1400–1600 LST (not shown) and begins to taper off so that by 1800 LST (d), there is only a small temperature difference relative to the base case (i.e., by up to 1°C–1.5°C at this hour, but affecting a smaller area in the western basin). At night, the temperature reduction is nonexistent, as seen at 0000 and 0300 LST August 6 (e and f). This diurnal cycle repeats itself with decreases in temperature during the day, e.g., at 1200 LST on August 6, when the cooling reaches up to 1.5°C–2°C (g) and small or nonexistent reductions at night (h). In all cases, the "cooler" air is advected downwind to the east, in general, and thus can also affect areas outside of the modified regions (e.g., beyond areas where surface albedo was increased). In this case, some cooler air can be advected to mid-domain and even to the eastern domain beyond the Santa Ana Mountains range.

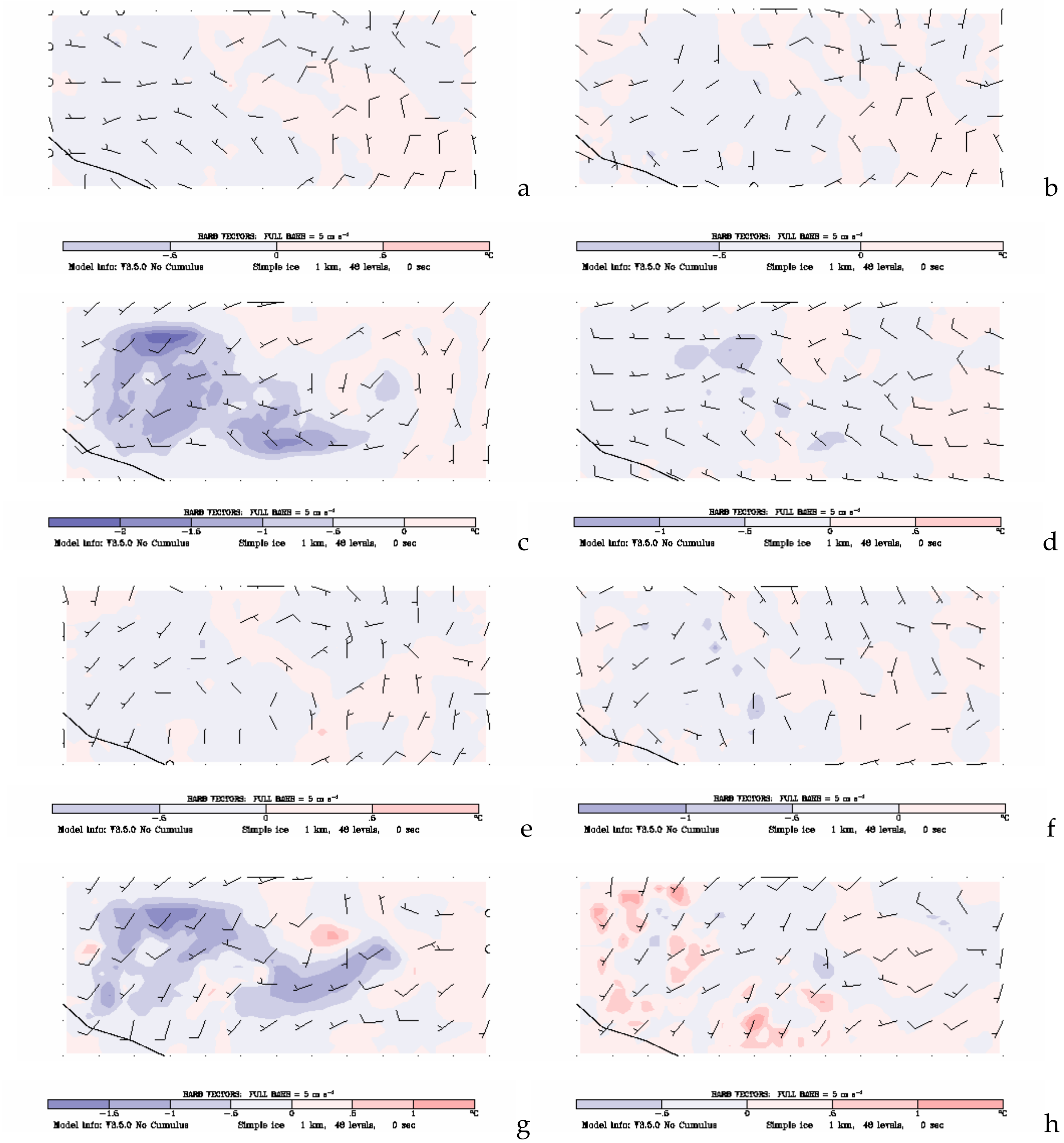

Figure 4.36. Change in air temperature at six-hour intervals (increased albedo scenario)

In Figure 4.37 i–p, the corresponding changes in *surface* temperature are depicted. Again, the pattern consists of small or no effects at night but large decreases in temperature during the daytime. As discussed earlier in the Sacramento example, the main difference here (compared to changes in air temperature) is the spatial distribution of the cooler areas (which follows very closely the areas of increased albedo) and the actual magnitude of the temperature decrease. At the time intervals shown in the figures, the largest decrease in surface temperature can reach up to 6.5°C and 7°C on August 5 and 6, respectively, at 1200 LST on each day (k and o). In some cases, there is also warming in parts of the domain, however, those areas are not as large or extensive as those affected by the cooling effect (k and o).

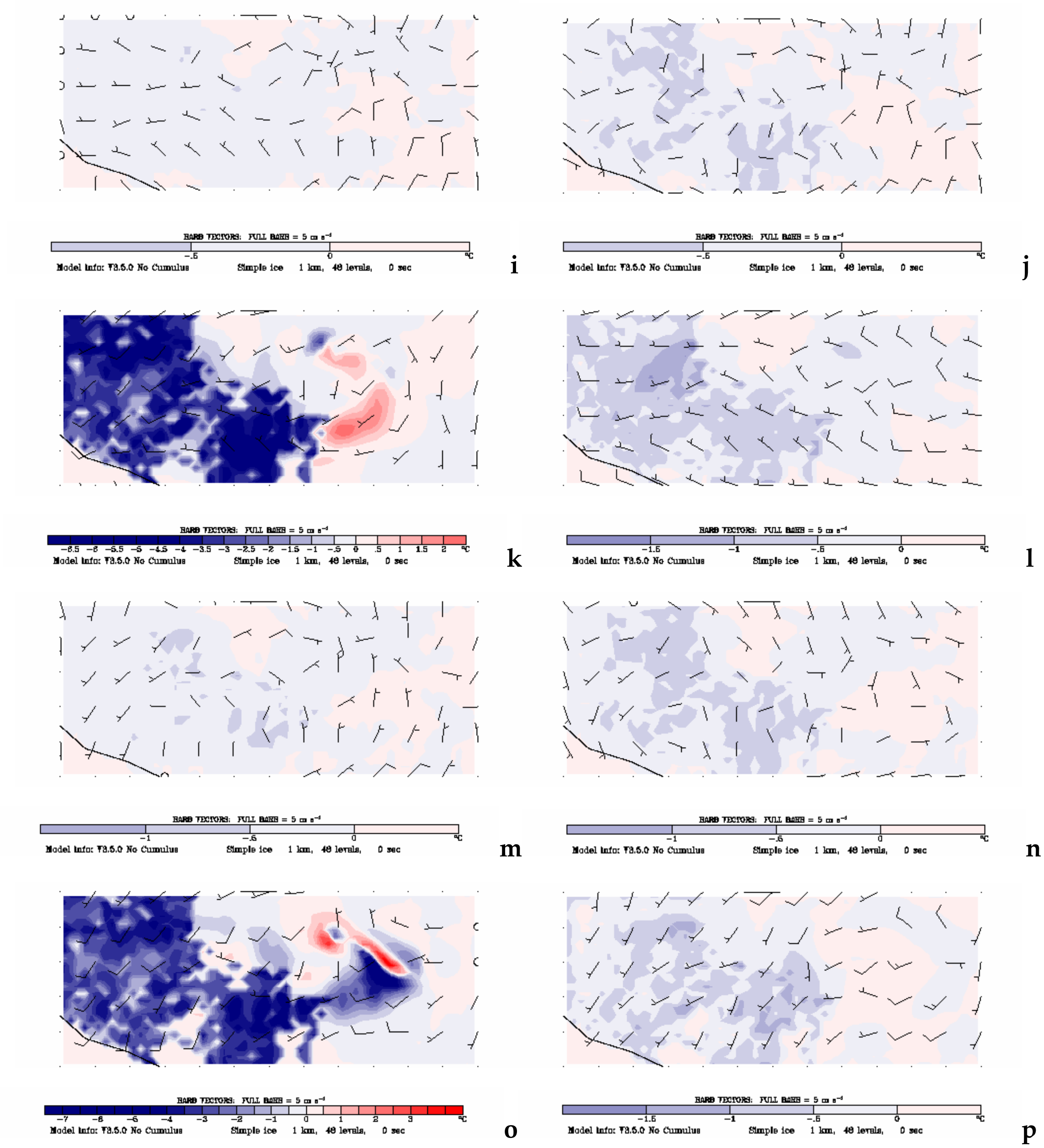

Figure 4.37. Change in surface temperature at six-hour intervals (increased albedo scenario)

Finally, in Figure 4.38 (1–4) the changes in air and coincident surface temperature fields are given for the hour when the largest *air*-temperature reductions of the day are achieved (for each of the two days of interest). Air temperature can be reduced (in the increased-albedo scenario) by up to 2.5°C–3°C at 1500 LST August 5 and 2°C–2.5°C at 1100 LST August 6 (1 and 3). In terms of time-coincident surface temperature change, the high-albedo scenario can cause reductions of up to 5°C at 1500 LST August 5 and 6°C at 1100 LST August 6 (2 and 4).

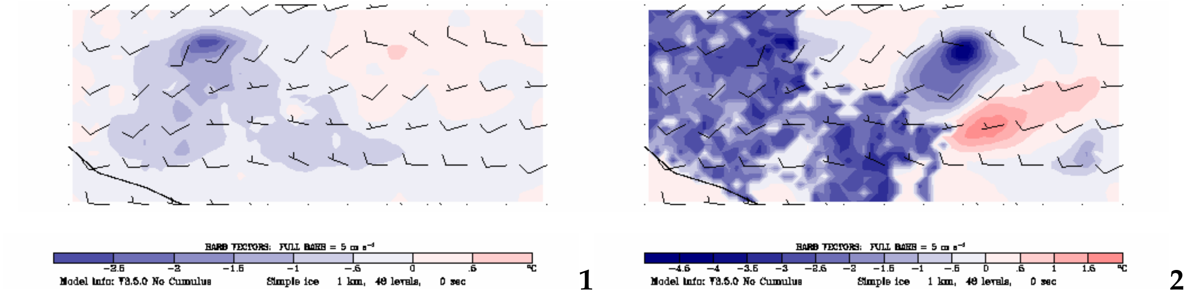

1500 LST August 5 1500 LST August 5

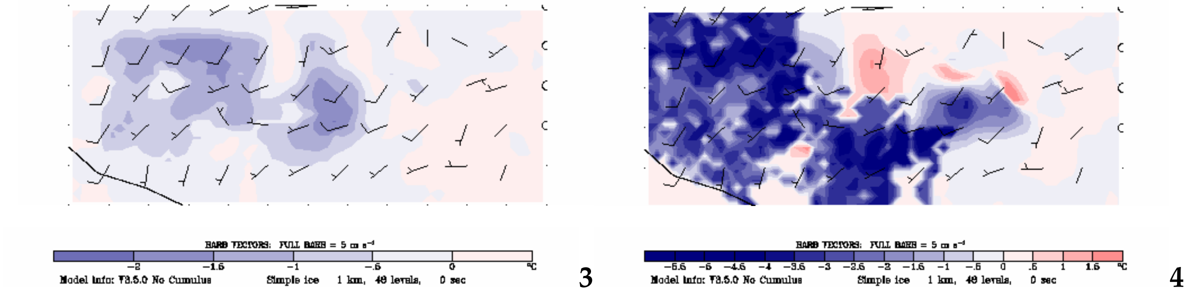

1100 LST August 6 1100 LST August 6

Figure 4.38. Change in temperature at times of largest decrease in *air* temperature (as denoted for each figure) for the scenario of increased albedo

Figure 4.39 shows one snapshot of surface temperature change (as a result of increased albedo), e.g., at 1100 LST August 6, side-by-side with building PAD function at 1 m AGL. The correspondence between surface temperature change and areas affected by albedo increase (which is proportional to building PAD) is obvious.

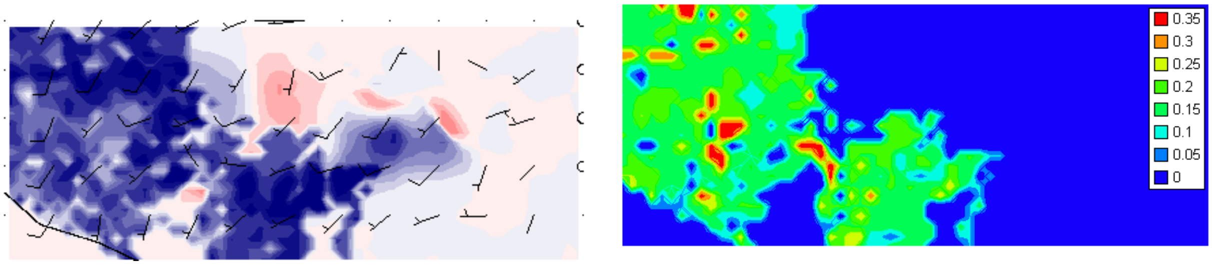

Figure 4.39. Change in surface temperature (left) compared side-by-side to building PAD at 1 m AGL (right)

The increase in canopy cover has the same general impact on temperature but at relatively lower magnitudes than the high-albedo scenario. These effects are summarized in Figures 4.40 a–h for air temperature and 4.41 i–p for surface temperature. Figure 4.42 1–4 shows the largest decreases in air temperature on each day. In summary, some of the larger reductions in air temperature resulting from increased canopy cover are 1.5°C and 1°C at 1200 LST on August 5 and 6, respectively (Figure 4.40 c and g). The corresponding reductions in surface temperature at 1200 LST on these days are 6°C and 5°C, respectively, (Figure 4.41 k and o). In terms of the largest reductions in air temperature on these days, they are 3°C and 1.5°C, respectively, at 1500 LST August 5 and 1400 August 6 (Figure 4.42 1 and 3). The coincident reductions in surface temperature are 4°C at 1500 LST August 5 and 4.5°C 1400 LST on August 6 (Figure 4.42 2 and4).

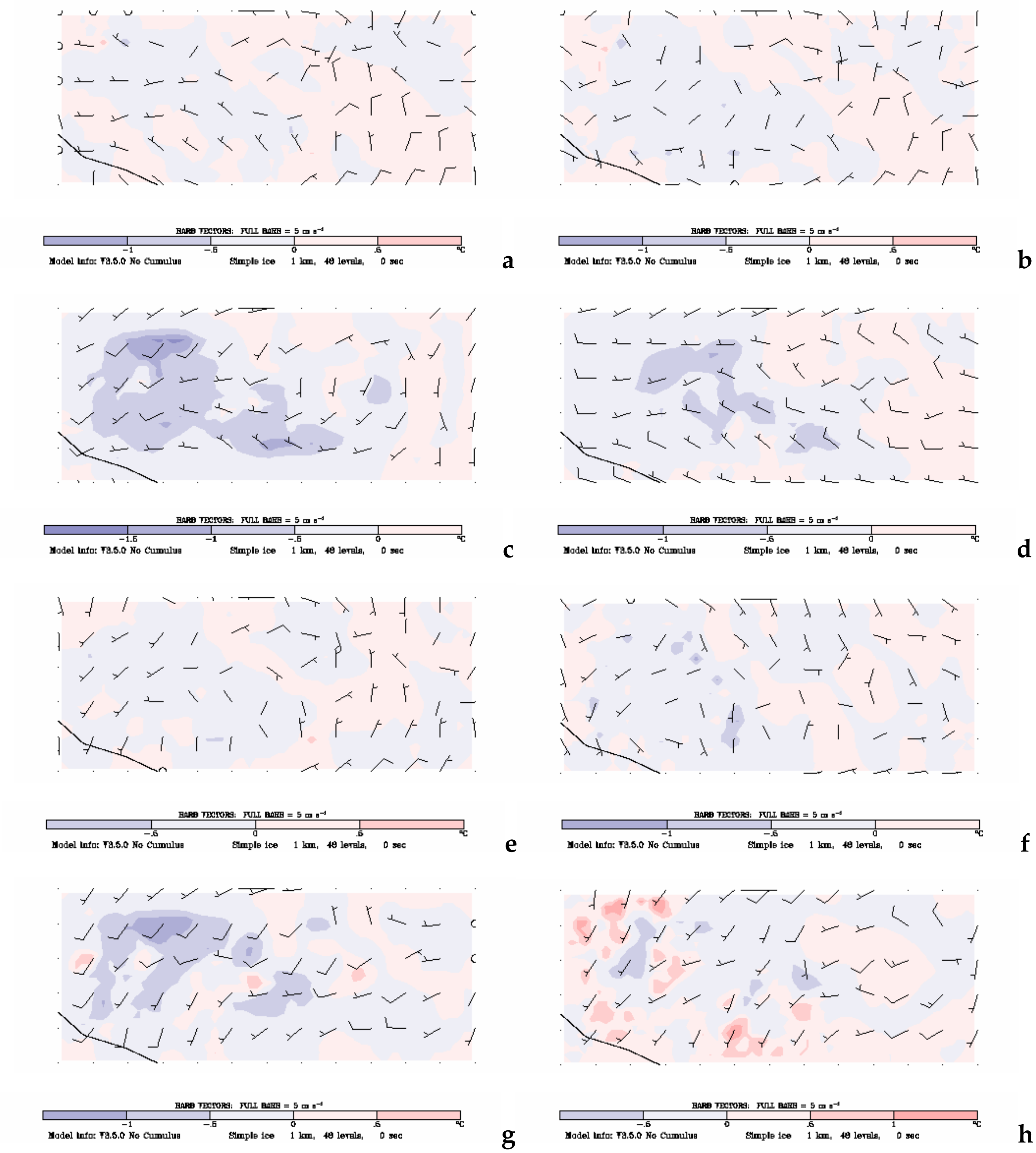

Figure 4.40. Change in air temperature at six-hour intervals (increased canopy scenario)

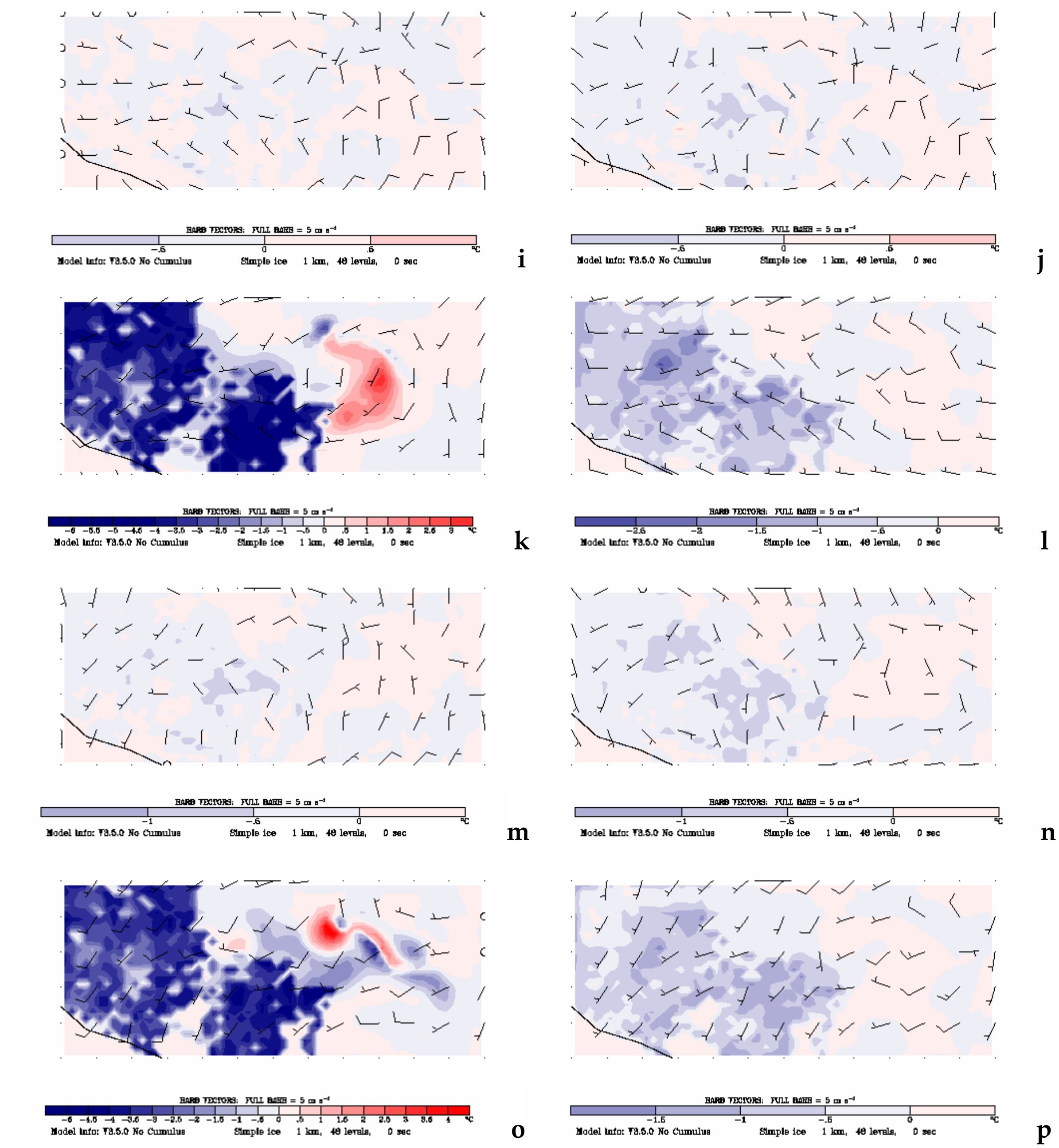

Figure 4.41. Change in near-surface temperature at six-hour intervals (increased canopy scenario)

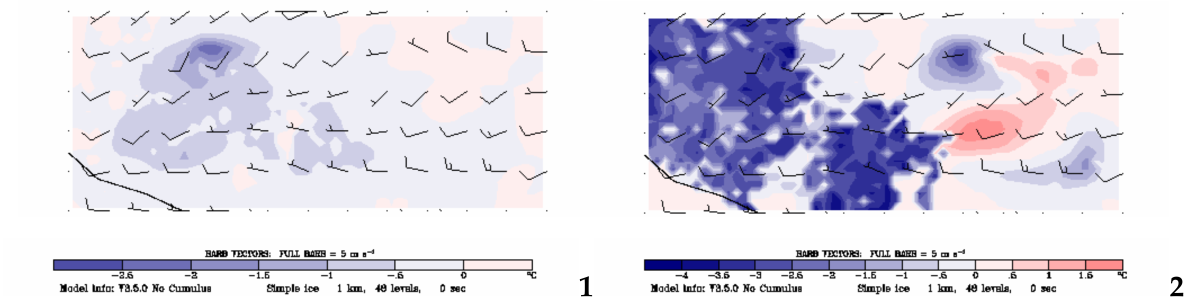

1500 LST August 5 **1500 LST August 5**

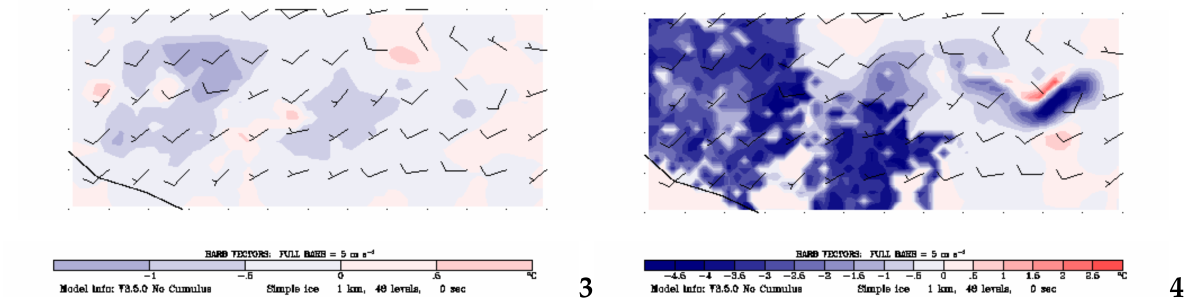

1400 LST August 6 **1400 LST August 6**

Figure 4.42. Change in temperature at times of largest decrease (times identified on figures) for scenario of increased canopy cover

To conclude this section, temperature change time series at two example locations are shown in Figures 4.43 and 4.44 for both high-albedo and increased-canopy scenarios (locations 12,11 and 15,20 as defined earlier). The impacts of surface perturbations on air temperature are clear at these locations and follow the day-night patterns discussed earlier, although at different magnitudes. At location 12,11 the maximum cooling, in the high-albedo scenario, is on the order of 1°C, whereas at 15,20 it reaches 1.75°C. The increase in surface albedo is slightly more effective in reducing air temperature than the scenario of increased canopy cover. The latter causes maximum reductions of 0.75°C at location 12,11 and 1.2°C at location 15,20. The reason why reductions are larger at location 15,20 than at 12,11 is because location 15,20 has relatively larger surface areas available for modification, both in terms of albedo and canopy cover (see Figure 4.28).

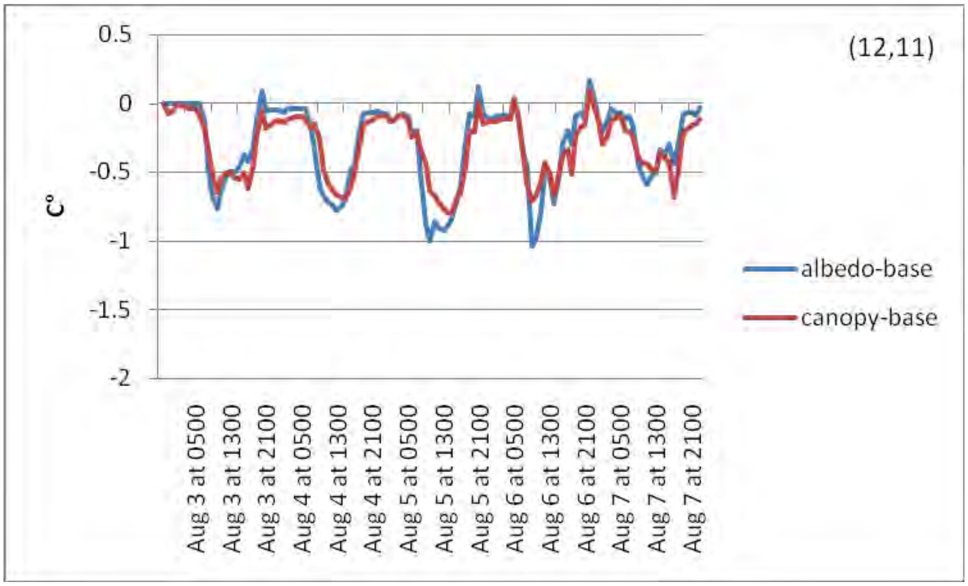

Figure 4.43. Time series of changes in air temperature at location 12,11 for scenarios of increased urban albedo and canopy cover

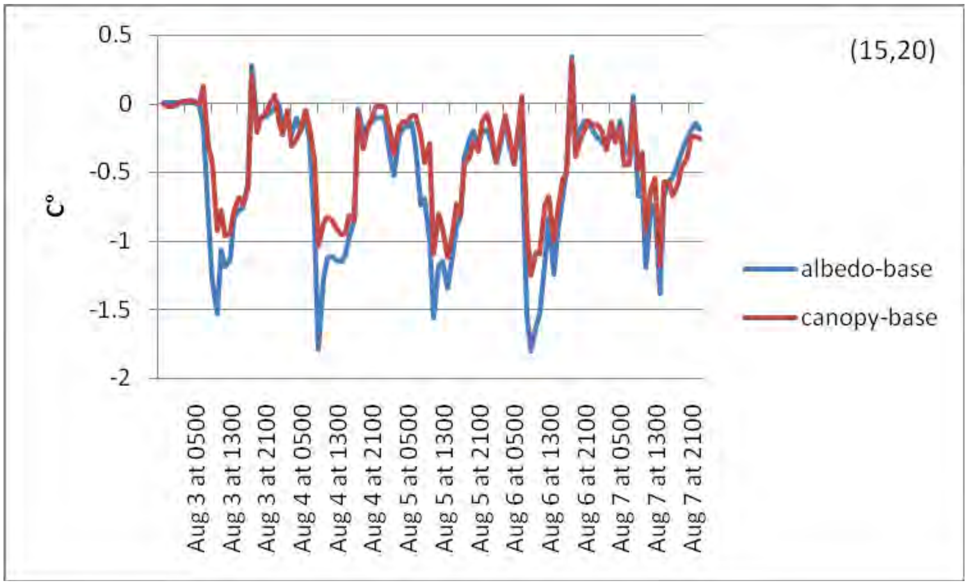

Figure 4.44. Time series of changes in air temperature at location 15,20 for scenarios of increased urban albedo and canopy cover

Photochemistry/Air Quality

Following the same discussion structure used for Sacramento, the changes in ozone concentrations, simulated for O-R at 0300 and 1500 LST on August 5 and 6, are shown in Figures 4.45 and 4.46. Figure 4.45 a–d shows the ozone difference fields for the high-albedo scenario, whereas Figure 4.46 e–h shows the differences corresponding to the increased canopy scenario.

Unlike in the Sacramento simulations, the signal in O-R is relatively noisy. At certain times, there does appear to be both increases and decreases in concentrations of the same order of magnitude. There is a clearer signal at night (small decreases in concentrations) than during the day, when both larger decreases and increases can occur. However, the larger decreases in daytime concentrations tend to occur in the western basin, whereas the larger increases tend to occur in the eastern basin, beyond the Santa Ana Mountain range. Thus, while temperature decrease can be significant in the O-R simulations, as discussed above, the corresponding air-quality impacts are not clearly proportionate. This may relate to the threshold effect identified in Phase 1, when high levels of albedo and/or canopy cover increases are assumed.

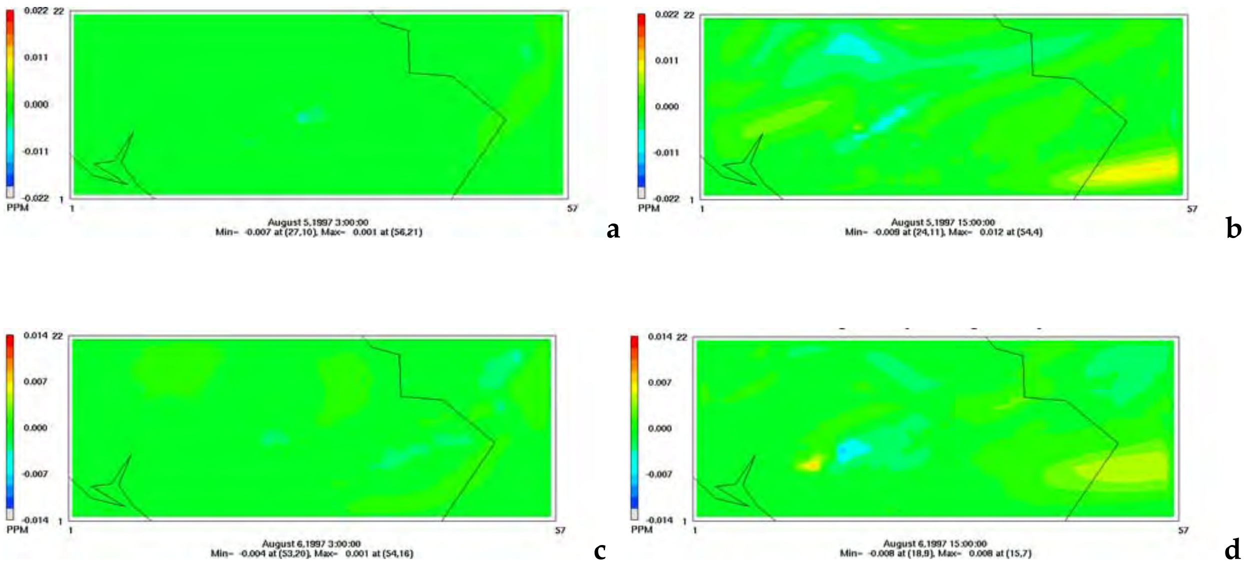

Figure 4.45 a–d. Simulated ozone difference fields for the increased albedo scenario in O-R domain

Because it is difficult to clearly identify the change in ozone concentrations in these figures and at these hours, an additional set of figures (Figure 4.47) was generated to examine a number of daytime hours in a little more detail (0900 through 1700 LST on August 6) for changes due to the high-albedo scenario. The scale was modified so that only the upper bounds of changes in concentrations (stronger positive and negative signals) are captured (changes within the ±3.5 ppb range are not depicted in the figures). The figures show in general that the *dominant* changes in the western basin are decreases in concentrations, whereas the *dominant* changes in the eastern basin (beyond the mountains range) are increases in concentrations.

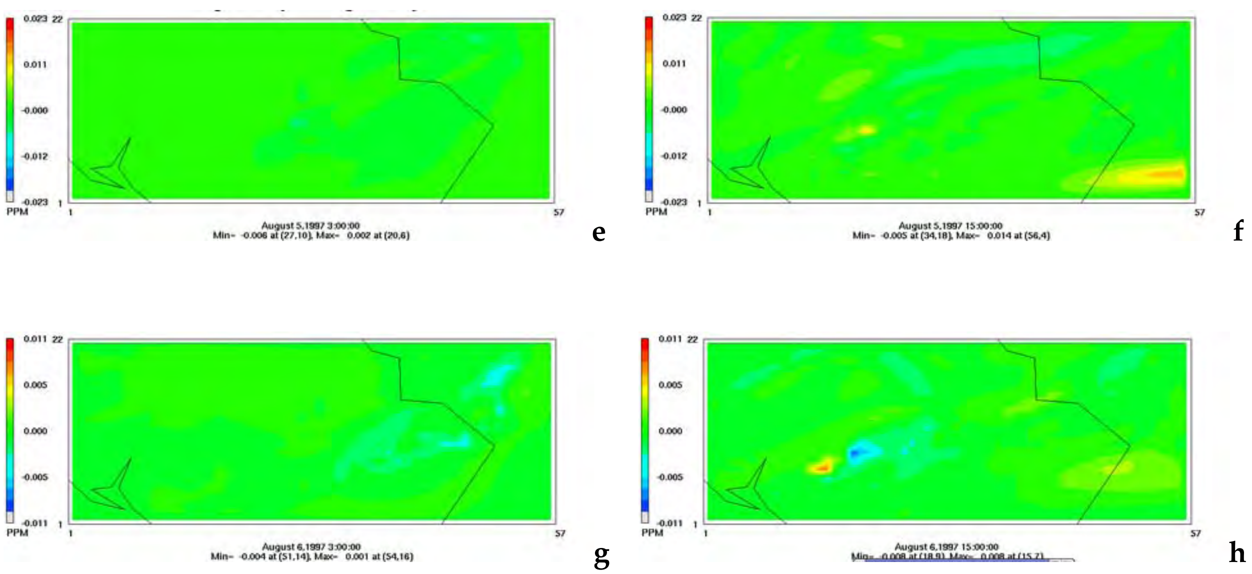

Figure 4.46 e–h. Simulated ozone difference fields for the increased canopy cover scenario in the O-R domain

The simulations suggest that the effects of limited-area UHI control, such as in this hypothetical situation, can produce local improvements in air quality but negative impacts further downwind, such as in a different air basin. There are several explanations for this, one of which (as identified in Phase 1) is the possible existence of a threshold beyond which any further surface modifications will tend to produce smaller *net* benefits in air quality. This is a result of changes in mixing, boundary-layer height, wind speed (flushing of pollutants), and their interaction with the basin's topography—in this case, the blocking effect of the mountain range in the eastern part of the domain.

To explain the effects of changes in wind and mixing on ozone in the O-R domain, Figure 4.48 shows the change in the westerly component (u) of the flow, as a result of increased surface albedo, for the same hours shown in Figure 4.45 (and Figure 4.46). Superimposed on the change in west-to-east velocity component is the base-case wind vector field at the corresponding hour. The purpose of these figures is to show that the west-to-east flow and the sea breeze are weakened in UHI control scenarios and that this effect can contribute to increased downwind concentrations and peaks near and beyond the Santa Ana Mountain range. The simulations show that the flow is essentially unchanged at night and through early morning hours but that the westerly flow is slowed during daytime throughout much of the domain, particularly in the western basin. Thus, the flow does not retain enough momentum (following surface modifications) to go over the mountains and help flush the local high ozone in that area. As a result, the downwind basin sees some elevated concentrations because of UHI control in the western basin. This situation can shed some light on one aspect of the "threshold" effect identified in Phase 1 and suggests that for UHI control to be effective, the larger basin (not only a small portion of it) needs to be modified.

The discussion above also reinforces the notion that while UHI control scenarios can be equally effective locally, they usually have different larger regional implications, depending on an area’s topography, coastal or inland location, emission profiles, level of possible modifications (available area for modification), and so forth.

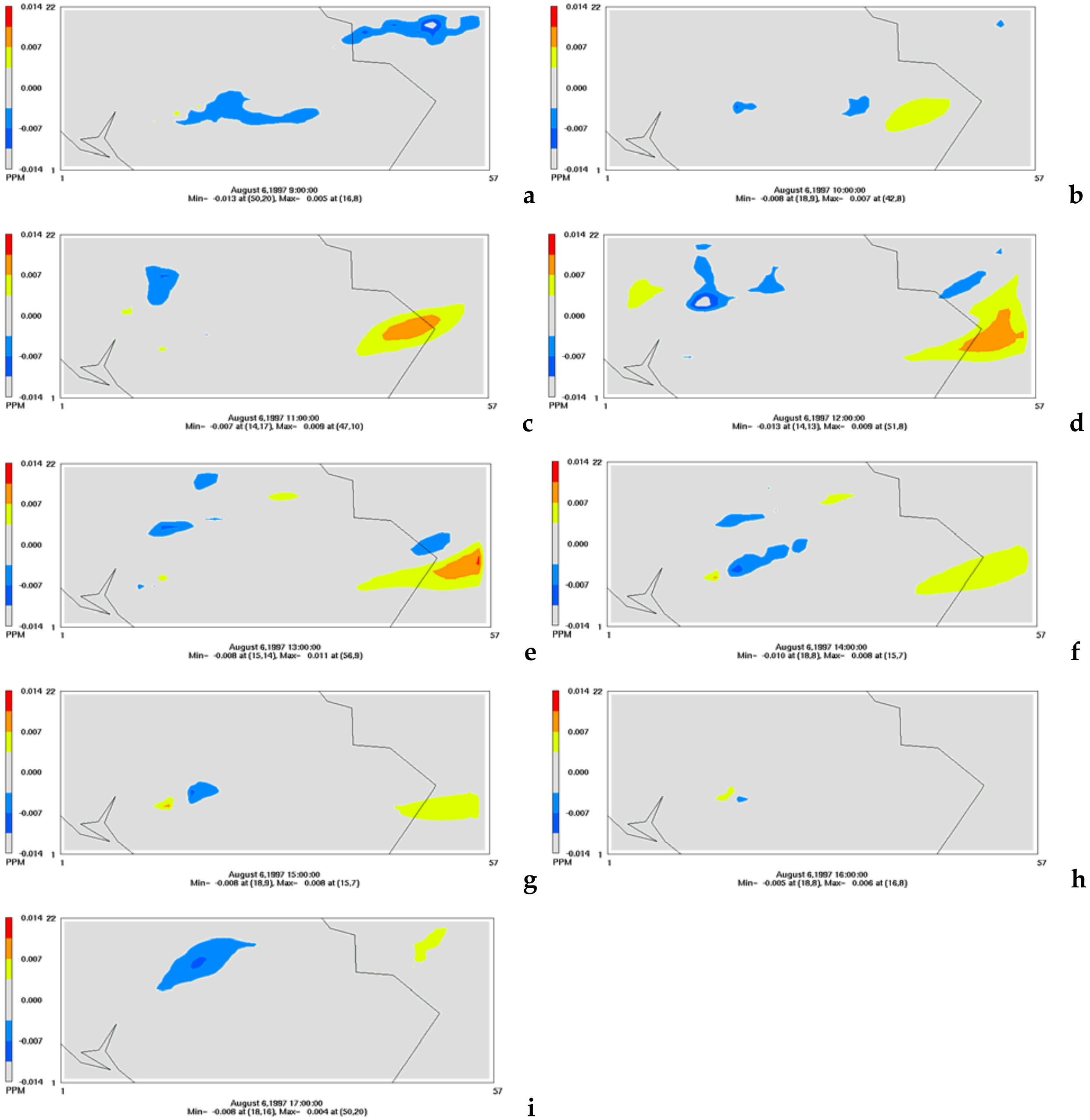

Figure 4.47 a–i. Simulated ozone difference fields for the increased albedo scenario for hours 0900–1700 LST on August 6 in the O-R domain

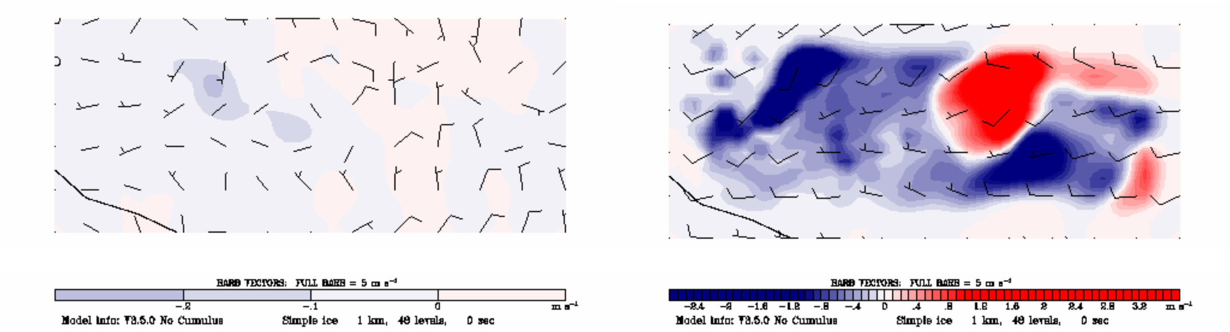

0300 LST August 5 and 1500 LST August 5

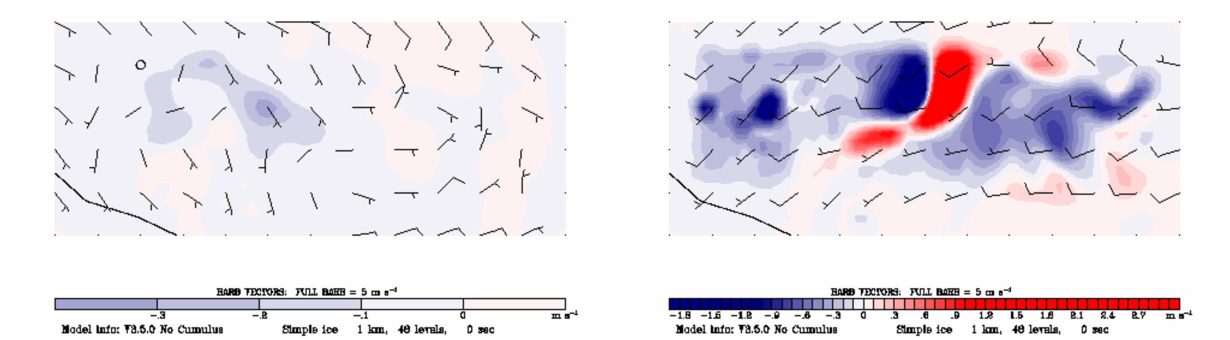

0300 LST August 6 and 1500 LST August 6

Figure 4.48. Changes in u (x-component) of wind velocity overlaid over base-case wind vector field at four different hours in the O-R domain for the increased albedo scenario

Figure 4.49 depicts time series of ozone concentration changes at locations 20,9 (Irvine area) and 21,15 (Tustin area), identified earlier, for the scenarios of increased urban albedo and canopy cover. The time series are for August 5 and 6. Over the span of these two days of interest, both strategies are equally effective generally but with some differences in the timing of largest impacts. As with previous cases, the decreases in ozone tend to occur mostly during the daytime, whereas some increases in concentrations occur earlier in the evening and early morning hours. At location 20,9 (Irvine) the largest concentration decreases are between 6 and 10 ppb and the largest increases between 4 and 7 ppb. At location 21,15 (Tustin) the largest decreases range from 3 to 6 ppb whereas the largest increases reach up to 4 ppb. The simulations also suggest a relatively larger impact on ozone in the Irvine area (20,9) than in the slightly more inland location of Tustin (21,15).

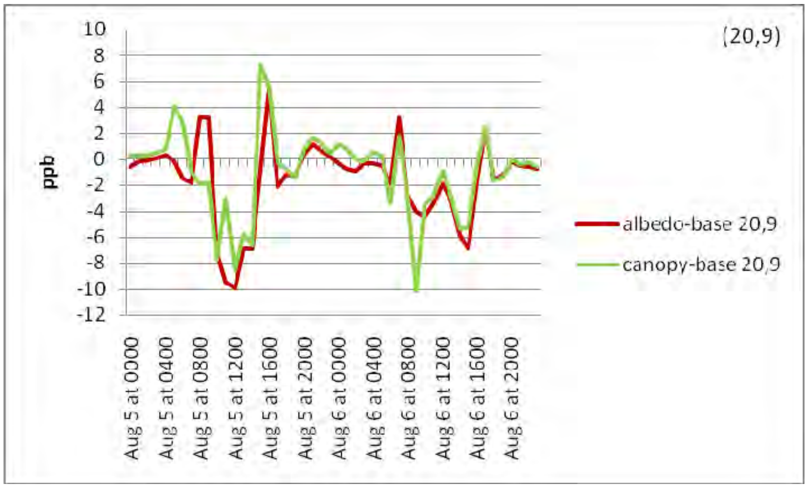

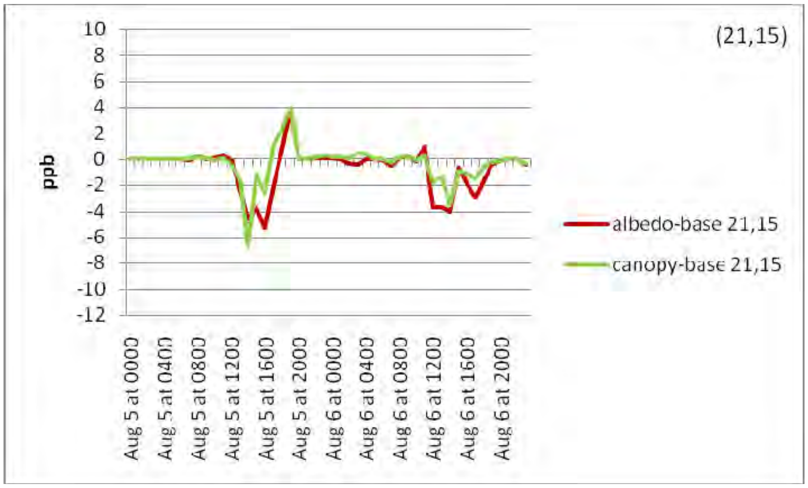

Figure 4.49. Changes in ozone concentrations at location 20,9 (Irvine; top) and 21,15 (Tustin; bottom) for scenarios of increased albedo and canopy cover in the O-R modeling domain

Finally, the potential impacts of surface perturbations on ozone air quality in O-R are evaluated by analyzing their impacts on the daily maximum 8-hour average. Figure 4.50 shows a summary of this analysis, along with RRF, at two locations of interest. The top portion of each figure shows the simulated daily maximum 8-hour average (at the given location) for the base case (blue), the scenario with increased albedo (red), and a scenario with increased canopy cover (green) for each of the five days of the episode. The bottom portion of each figure shows the RRF corresponding to these strategies for each day. Here the RRF is plotted as (1-RRF)%.

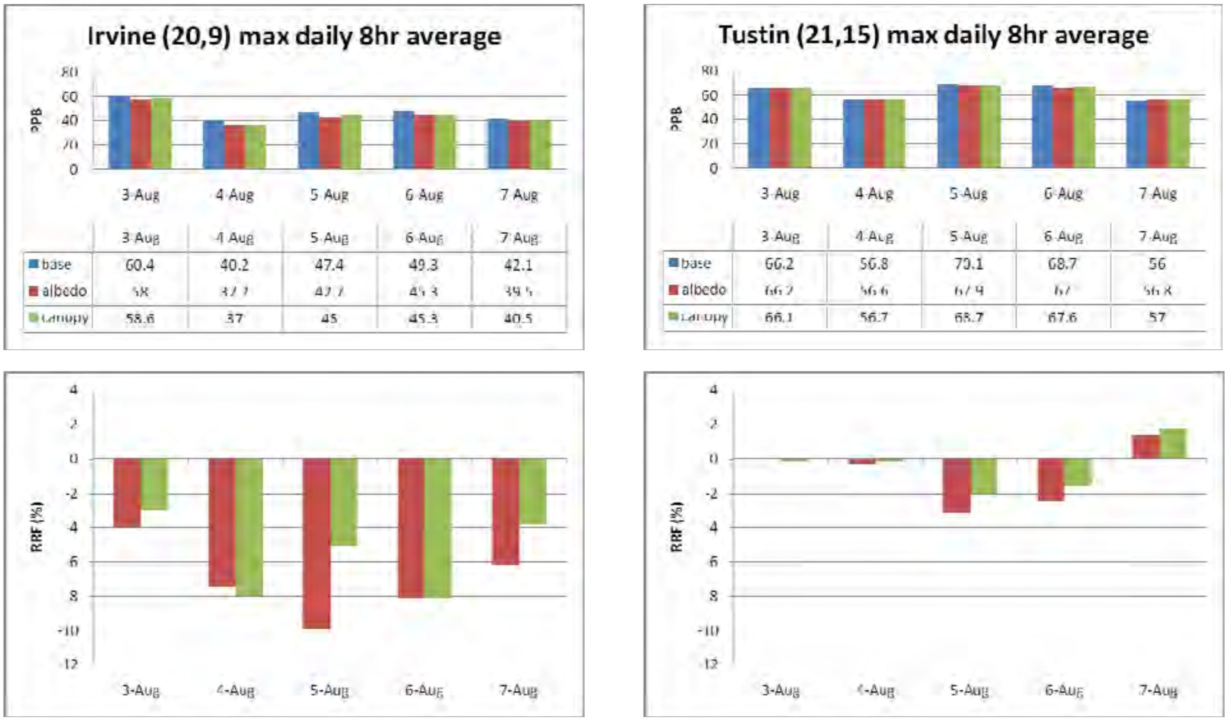

Figure 4.50. Daily maximum 8-hour average ozone (simulated) and potential RRF as a result of increasing surface albedo (red) and canopy cover (green) at two locations in the O-R modeling domain

Except for one instance at Tustin (August 7), the UHI control at both locations and all other days resulted in a decrease in the daily maximum 8-hour average. The RRF analysis shows that the daily maximum 8-hour average can be decreased between 3% and 10% across the episode days in Irvine and between 0% and 3% in the Tustin area. The largest impacts are seen on the main days of the episode (August 5 and 6) at both locations. Thus, as with Sacramento, the surface perturbations are locally useful in offsetting the higher ozone.

5.0 Summary and Conclusion

A fine-resolution, meso-urban meteorological model was updated, improved, and used in driving fine-resolution photochemical simulations. Corresponding data and model-specific input parameters were developed in this study. The combined fine-resolution meteorological-photochemical modeling system was then applied to the Sacramento Valley and an area in Los Angeles (Orange-Riverside counties, O-R). This application is the first time *these* types of models were used in studying the effects of surface perturbations on meteorology and air quality in California.

The development and use of fine-resolution meso-urban meteorological models is important because such tools and corresponding fine-resolution data can be useful not only in enabling more accurate photochemical air-quality modeling but also in developing fine-resolution four-dimensional emission inventories that should ultimately help improve the modeling of other strategies as well. These modeling capabilities are also useful for planning and implementation purposes, because they allow for site-specific evaluation of meteorological and air-quality impacts on a neighborhood basis or city-block scale.

From this perspective, the *primary* objective of Phase 2 of the study was two-fold: (1) to develop, update, and improve a meso-urban fine-resolution meteorological model, and (2) to develop the corresponding fine-resolution region- and model-specific input data. A *secondary* objective was to apply the new meteorological-photochemical modeling system and data to one region in California and demonstrate the models' effectiveness in diagnosing the potential effects of surface modifications (UHI control) on meteorology and air quality. Both objectives were met during this study's second phase.

An alternate, low-cost methodology was devised to develop the three-dimensional fine-resolution morphological input needed by the meso-urban model. The methodology relies in part on using Google Earth Pro imagery and three-dimensional urban models. A number of parameters were developed at 1-m vertical resolution and for several wind approach directions through the top of the canopy layer in each grid cell. Once these parameters were developed in a gridded fashion for a domain of interest, they were then correlated to a region-specific land-use and land-cover classification scheme so as to extrapolate the data to areas for which no three-dimensional morphological information exists. Using a combination of several methods and data sources, the morphology and land use and land cover data were fully characterized for both the Sacramento and O-R modeling domains.

For each domain, a base-case meteorological-photochemical scenario was developed. This was then followed by the simulation of two perturbation cases. One is a high-albedo increase scenario and the other involves increased canopy cover. The fine-resolution meteorological simulations were forced by downscaled meteorological fields from a 4 km domain in Sacramento and a 5 km domain in O-R. The coarse-grid photochemical simulations were forced by coarse-grid (4 and 5 km) meteorological fields, whereas the fine-resolution photochemical simulations (1 km) were forced by fine-resolution meteorological fields (from the meso-urban model) and fine-resolution emissions input developed from interpolating the coarse-grid emission inventories to the 1 km domain.

5.1. Sacramento

In the base-case scenario of the Sacramento domain, the simulations produce a general diurnal profile where about a 1°C heat island effect is seen around 1500 LST, and grows to the peak of about 6°C at 2100 LST. By 0900 LST the next day, the heat island effect has completely faded. At about 1500 LST, the UHI reappears (~1°C) and the cycle is repeated diurnally through the episode. Of course, the magnitudes differ from day to day, but the above is a representative range.

The meso-urban simulations also capture fine-resolution flow divergence/convergence features that were not detectable in Phase 1 mesoscale modeling. For example, the model clearly captures the nighttime convergence associated with heat island circulation (such as the flow convergence near the Downtown Sacramento area). The model also produces slower winds over urban areas (due to drag and roughness) at various times of the episode and produces divergence of the flow at the upwind edge of the urban area. The simulations show that the urban-area winds can be 2–3 ms^{-1} slower compared to upwind or surrounding areas during the early morning hours.

This research evaluated the meso-urban model's ability to simulate the fine-resolution vertical profiles of meteorological fields, e.g., in the UCL. The simulations show that the vertical profiles of TKE budget terms (such as shear, buoyancy, and dissipation) generally follow the vertical density profiles, e.g., frontal-area density function (FAD), of buildings and/or vegetation canopies. The model also captures the impacts of land-cover differences on air temperature. For example, the simulated Bowen ratios are $\beta > 20$, $\beta \sim 3.5$, and $\beta \sim 1.3$, respectively, for high-rise, residential, and forested areas in Sacramento. These ratios are generally comparable with observed values for such land covers.

The base-case photochemical simulations of the 1 km domain produce peak concentrations that are consistently downwind of the downtown area; the high ozone is advected to the southeast on July 31, to the east on August 1, and to the northeast on August 2. The 1 km domain's simulated peaks are respectively 96, 117, and 101 ppb on those three days and are relatively more accurate than those obtained from the coarse simulations of Phase 1 for *this* domain.

The effects of surface modifications were evaluated for three days of interest in Sacramento. The meso-urban model indicates that *air* temperature can be reduced (in the increased-albedo scenario) by up to 2.5°C at 1100 LST July 31, 2°C at 1200 LST August 1, and 3°C at 1300 LST August 2. The increase in canopy cover has generally the same directionality of impact on air and surface temperatures but at relatively lower magnitudes than the high-albedo scenario. The largest reductions in air temperature in this scenario reach up to 1.5°C, 1.5°C, and 2.5°C, respectively, at 1100 LST July 31, 1300 LST August 1, and 1300 LST August 2.

In terms of air quality impacts, the Sacramento simulations suggest that during the episode days of interest, concentrations can be decreased by up to 16–26 ppb in the high-albedo scenario and by up to 15–19 ppb in the increased canopy scenario (some larger changes also occur, e.g., up to 30s of ppb). The latter occur in small areas in the domains, typically 1–2 km^2 and are not representative of the general effects. Such large reductions are captured by the model because of the fine resolution simulations (1 km) relative to the coarser mesoscale modeling (4 km) conducted in Phase 1 of this project.

However, the more interesting aspect is the impact of UHI control on lowering the concentrations over larger areas in the domain, which is likely the more representative effect. Spatially averaged concentrations decrease by 5–14 ppb in the high-albedo scenario and 5–10 ppb in the increased canopy scenario. Negative impacts can also occur, but they are confined to a short period of time and small areas. In general, the modeling suggests that the effects of changes in canopy cover (as assumed in this scenario) are similar to or smaller than those of increased urban albedo.

Analysis of the 8-hour average ozone shows that except for one instance at a downwind monitor location, where there is an increase, the impacts of UHI control at all locations and days are a decrease in the daily maximum. The RRF analysis shows that the daily maximum 8-hour average can be decreased by anywhere between 4% and 14% across the episode days with the largest impacts seen on July 31 and August 1 (main days of episode). While the effects of increased albedo are generally larger than those of increased canopy cover, the opposite can occur in some cases. This is particularly noticeable at monitor locations closer to the downtown area (mid-domain).

5.2. Orange-Riverside (O-R)

The simulations of this domain suggest a general pattern whereby a weak UHI (~1°C) exists at 0000 LST in the Santa Ana–Irvine area. This pattern continues through 0300 and 0600 LST relatively unchanged except for the lower absolute temperatures over the western, coastal areas. At 0900 LST, a small UHI (~1°C) remains in the western half of the domain near the city of Irvine. From 1200 through 1800 LST, a UHI in the Garden Grove/Orange and Irvine areas increases to 2°C–3°C. By 2100 LST a 1°C–2°C UHI is seen at mid-domain, and these conditions continue through 0000 LST. The cycle is repeated the next day with a generally similar pattern.

Of relevance to heat island control, the model is capable of capturing the cooling effects of urban parks at sub-kilometer scale. For example, the temperature difference between two urban areas in O-R western domain (one high-rise area surrounded by extensive green cover and the other a residential area with lower vegetation cover) reaches up to 4°C at times, with the vegetated area being cooler during daytime hours. The model also has improved capability for simulating the fine-resolution vertical profiles of meteorological fields of interest (e.g., TKE budget components, temperature, heat fluxes, and so on).

The base-case photochemical simulation of O-R domain shows that the peak concentrations occur downwind, in the Santa Ana Mountain range and eastern basin, but that some higher concentrations on August 5 also enter the domain from the northwest, i.e., from the Los Angeles area. The simulations produce peaks of 113 ppb on August 5 and 97 ppb on August 6. High concentrations are found in the eastern domain, across the Orange-Riverside border, and just east of the Santa Ana Mountains, in non-urban areas.

Scenarios of surface perturbations, similar to the ones evaluated for Sacramento, were applied to the O-R domain. The simulations again show that during nighttime hours, surface modifications have minimal or no impact on air temperature. After sunrise, the temperature difference (cooling effect) appears. The largest air-temperature reductions in the increased-albedo scenario reach up to 3°C at 1500 LST August 5 and 2.5°C at 1100 LST August 6. The increase in canopy cover has the same general effect on air and surface temperatures. The largest reductions in air temperature in this scenario reach up to 3°C and 1.5°C, respectively, at 1500 LST August 5 and 1400 LST August 6.

The ozone air-quality response to UHI control in O-R differs from that in Sacramento in that it is somewhat "noisy." This is because of the assumed limited-area modifications, changes in the wind field (weaker west-to-east flow in this coastal region), and the blocking effect of the Santa Ana Mountains. There does appear to be both increases and decreases in concentrations that can be on the same order of magnitude, although at different times and locations. The larger decreases in daytime concentrations tend to occur in the western basin (e.g., Orange, Tustin, Irvine, and Mission Viejo), whereas the larger increases tend to occur in the eastern basin, beyond the mountain range, in non-urban areas.

As a result of factors discussed above, the simulations show that limited-area UHI control, such as in this situation in the O-R domain, can produce *local* improvements in air quality but also negative impacts further downwind in a different air basin. The *local* changes in concentrations (i.e., in the modified urban areas of the western basin) follow the more typical patterns seen elsewhere, such as in Sacramento. In the Irvine area, for example, the largest concentration decreases are between 6 and 10 ppb during daytime and the largest increases between 4 and 7 ppb (earlier in the morning or later in the evening). In the Tustin area, the largest daytime decreases range from 3 to 6 ppb, whereas the largest increases reach up to 4 ppb at evening or in the night hours.

In terms of the 8-hour average ozone, the simulations suggest a dominant decrease in concentrations. The RRF analysis shows that the daily maximum 8-hour average can be decreased by between 3% and 10% across the episode days in Irvine and up to 3% in the Tustin area. The largest impacts are seen on the main days of the episode (August 5 and 6) at both locations.

5.3. Comparisons to Phase 1

The modeling effort in Phase 2 was based on a new-generation meso-urban meteorological model, corresponding fine-resolution photochemical simulations, different meteorological-photochemical model configurations, updated urban canopy parameterizations, and new, region-specific data. Thus, the modeling is fundamentally different from that in Phase 1. The resulting simulated meteorological and ozone fields complement those from Phase 1, but some important differences exist. While they are listed here in general terms, such differences are important in improving the site-specificity of the simulated fields and rendering the models more suitable for use in evaluations of implementation scenarios, planning, and regulatory aspects of UHI control strategies.

Compared to the mesoscale modeling results of Phase 1, the Phase-2 models capture more details (i.e., fine-resolution features), both meteorological and photochemical, because of the new model formulation (meteorology) and finer resolutions (meteorology and photochemistry). For example, the simulations produce morning cool islands in inland urban areas (which were undetected in the coarse-grid simulations from Phase 1) and nighttime heat islands. Cool islands occur because urban geometry, shadowing effects, and thermal mass cause a delay in the morning warming of the canopy layer in the urbanized areas relative to more open rural and suburban ones. The model also produces a well-defined heat island later during daytime. In addition, the improved models can capture: (1) the flow's divergence/convergence in and around urban areas more realistically, (2) convergence due to the heat-island circulation (these, too, were not easily detectable in Phase 1), and (3) the slower wind over urbanized areas due to roughness and drag.

The downwind displacement of the UHI is captured in more detail and so is the ozone concentration field, e.g., downwind transport. The local peaks in the Sacramento fine-resolution modeling domain are more accurate (closer to observations) than in Phase 1 modeling, and model performance is thus relatively improved.

The changes in temperature and in ozone, as a result of surface perturbations from UHI control, are larger relative to those obtained in Phase 1 and are suggestive of more efficient local impacts from UHI control scenarios at smaller scales (finer resolutions). The decreases in air temperature, in Sacramento for example, reach up to 3°C at certain times compared to as much as 1.5°C in Phase 1. The effects on ozone are also larger, in the 10–20 ppb reduction range, area-wide, with some more extreme local changes (up to 30s of ppb) compared to Phase 1. While the latter changes are limited in space (1–3 km^2) and are short-lived (one hour), they are captured in Phase 2 results because of the finer resolutions of the models and corresponding data. However, results from both phases are generally in agreement if the difference in resolution is accounted for (averaging the fine-resolution model results). Because of these new and added capabilities, it is recommended that regulatory agencies evaluate these new-generation models for potential use in supplementing their conventional mesoscale modeling systems.

5.4. Issues, Caveats, and Recommendations

Conclusions from both phases of the study show that heat-island control can have significant energy, meteorology, and ozone air-quality impacts. As a result, surface-modification strategies should be considered as an additional means to complement conventional emission control venues in helping California reach and/or maintain attainment status for ozone. The main drawback in evaluating potential impacts of heat-island control, presently, is that the large-scale effects (both positive and negative) currently can be demonstrated solely through numerical modeling. The use of models in this case, as with any other strategy, carries an inherent risk that should be acknowledged. Namely, there is risk in beginning to implement this strategy for the *sole purpose of improving air quality* (the energy benefits of this strategy have already been established). Thus, there may be pitfalls that regulators need to carefully consider when beginning related planning, evaluation, and implementation processes.

Some of the issues that need to be addressed in the near future are summarized in the following pointers:

- Both phases of this study were single-episodic modeling application and impact-evaluation efforts. As discussed elsewhere in the project reports, it is important that the potential impacts of UHI control be evaluated over seasonal time spans and a large number of episodic conditions that, in combination, will capture a range of climatologies and synoptic conditions in California. This would provide a more realistic assessment of the long-term and average impacts of UHI control than with a single episode.
- While the Sacramento fine-resolution domain in Phase 2 was selected in an implementation-realistic manner (e.g., encompassing an entire urban area) the O-R domain was selected for evaluating the effects of limited-area modifications. Therefore, results from the O-R simulations may not be useful in *generalization*. Future *fine-resolution* modeling efforts should evaluate the entire Los Angeles basin (as was done in Phase 1)
- The assumed levels of albedo and canopy cover increases in Phase 2 were the *largest reasonable* levels for such modifications. These assumptions were made to evaluate the larger potential impacts on meteorology and ozone air quality from UHI control. In the near future, site-*specific implementation-type* modeling should be done, whereby more realistic and block-by-block or neighborhood-scale surface modification scenarios are developed and evaluated. These would be based on urban planning information, urban development blueprints, and existing market conditions in various parts of the airsheds. In Phase 2, the modeling system was developed with this type of application in mind and the capability now exists for using the system in evaluating the impacts of detailed planning and development schemes.
- Unlike in Phase 1, where changes in biogenic emissions were accounted for (to reflect changing meteorology), Phase 2 modeling focused only on the meteorological perturbations resulting from UHI control scenarios. This assumption was made because the modeled domains were relatively small and no significant impacts from changes in biogenic emissions were to be expected (especially since they are mostly downwind). Another reason for this approach was to isolate the air-quality effects of meteorological changes only. However, changes in emissions, especially biogenics, will need to be reconsidered again in future *fine-resolution* modeling if the modeling domains were to be increased in size so as to include larger areas with significant vegetative cover (e.g., crops, forests).
- Next modeling effort of UHI control should also evaluate scenarios based on future-year emission inventories that account for (1) increased urbanization as a result of current trends, and (2) full implementation of projected and committed emission controls per regional and local SIP. Related to this issue, it is also useful to evaluate the potential impacts of UHI control strategies under California scenarios of climate change.

- Additional morphological characterization work for California will need to be completed. This study developed detailed morphology and urban data for two domains (commensurate with available resources) but other areas should be characterized in detail in the future as well. These include, in particular, the greater Los Angeles Basin and the greater San Francisco Bay Area.
- Develop and use more accurate morphology extrapolation methodologies to characterize those areas devoid of three-dimensional morphological information. In Phase 2, a preliminary extrapolation scheme was developed based on detailed LULC characterization of the Sacramento and O-R domains. However, a more rigorous approach is needed to capture more region- and site-specific morphological features.

6.0 References

Betts, A. K., and M. J. Miller. 1986. “A new convective adjustment scheme. Part II: Single column tests using GATE wave, BOMEX, ATEX, and Arctic air mass data sets.” Quarterly Journal of the Royal Meteorological Society 112: 693–709.

Burian, S. J., W. S. Han, S. P. Velugubantla, and S. R. K. Maddula. 2003. “Development of gridded fields of urban canopy parameters for Models-3/CMAQ/MM5.” Department of Civil and Environmental Engineering, University of Utah.

Burk, S. D., and W. T. Thompson. 1989. “A vertically nested regional numerical prediction model with second order closure physics.” Monthly Weather Review 117: 2305–2324.

Cardelino, C. A., and W. L. Chameides. 1990. “Natural hydrocarbons, urbanization, and urban ozone.” Journal of Geophysical Research 95 (D9): 13971–13979. August.

Chang, J.S., Brost, R.A., Isaksen, I.S.A., Madronich, S., Middleton, P., Stockwell, W.R., and Walcek, C.J. 1987. “A three-dimensional eulerian acid deposition model: physical concepts and formulation, Journal of Geophysical Research, 92 (D12): 14681-14700

Chen, F., M. Tewari, and J. Ching. 2007. “Effects of high-resolution building and urban data sets on the WRF/urban coupled model simulations for the Houston-Galveston areas.” Presented at the American Meteorological Society, 7th Symposium on the Urban Environment, September 10–13, San Diego, California.

Chen, F. and Dudhia, J. 2000. “Couling and advanced land surface-hydrology model with the Penn State NCAR MM5 modeling system. Part I: Implementation and sensitivity”. Monthly Weather Review, 129: 569-585.

Ching, J. 2007. “National urban database and access portal tools (NUDAPT), a project overview.” Presented at the American Meteorological Society, 7th Symposium on the Urban Environment, September 10–13, San Diego, California.

Dudhia, J. 1993. “A non-hydrostatic version of the Penn State/NCAR mesoscale model: Validation tests and simulation of an Atlantic cyclone and cold front.” Monthly Weather Review 121: 1493–1513.

Dupont, S., T. Otte, and J. Ching. 2004. “Simulation of meteorological fields within and above urban and rural canopies with a mesoscale model (MM5).” Boundary-Layer Meteorology 113: 111–158.

Environ Corp. 2003. “Comprehensive Air Quality Model with Extensions Version 4.” Environ Corp. Air Sciences. 2003.

Fujita, E., Koracin, D., Freeman, D., Keislar, R.E., Podnar, D., McCord, T.E., Campbell, D.E., and Stockwell, W.R. 2003. “SIP planning service for the Sacramento Ozone non-attainment area – Volume 1: Data analysis and episode selection for SIP modeling”, Final report prepared for the Sacramento Metropolitan AQMD, by Desert Research Institute, Reno, Nevada.

Gabersek, S., and H. Taha. 1996. ”Impacts of surface characteristics changes on urban heat island intensity.” ICB 96, 14th International Congress of Biometeorology. September 1–8, 1996. Ljubljana, Slovenia.

Grimmond, C. S. B., and T. R. Oke. 1999. ”Heat storage in urban areas: Local-scale observations and evaluation of a simple model.” Journal of Applied Meteorology 38(7): 922–940.

Grell, G. A., Y. H. Kuo, and R. Pasch. 1991. “Semi prognostic test of cumulus parameterization schemes in the middle latitudes.” Monthly Weather Review 119: 5–31.

Grell, G. A., J. Dudhia, and D. R. Stauffer. 1994. “A description of the fifth generation PSU/NCAR mesoscale modeling system (MM5).” Technical Note NCAR/TN—379+STR, NCAR.

Hogo, H., and M. W. Gery. 1988. “User’s guide for executing OZIPM4 with CBM-IV or optional mechanisms.” EPA report 600/8-88/-82, US EPA, RTP, North Carolina.

Hong, S. H., and H. L. Pan. 1996. “Nonlocal boundary layer vertical diffusion in a medium-range forecast model.” Monthly Weather Review 124: 2322–2339.

Hsie, E. Y., and R. A. Anthes. 1984. “Simulations of frontogenesis in a moist atmosphere using alternative parameterizations of condensation and precipitation.” Journal of Atmospheric Science 41: 2701–2716.

Jones, K., L. Militana, and J. Martini. 1989. “Ozone trend analysis for selected urban areas in the continental U.S.” Presented at the 82nd annual meeting and exhibition of the A&WMA, Anaheim, California. June 1989. A&WMA. Pittsburgh, Pennsylvania.

Kain, J. S., and J. M. Fritsch. 1993. “Convective parameterization for mesoscale models: The Kain-Fritsch scheme.” In The Representation of Cumulus Convection in Numerical Models. Meteorological Monograms, K. A. Emmanuel and D. J. Raymond, eds. No. 46, 165–170, American Meteorological Society.

Leclerc, M. Y., K. C. Beissner, R. H. Shaw, G. D. Hartog, and H. H. Neumann. 1990. “The influence of atmospheric stability on the budgets of the Reynolds stress and turbulent kinetic energy within and above a deciduous forest.” Journal of Applied Meteorology 29: 916–933.

Martilli, A., A. Clappier, and M. Rotach. 2002. “An urban surface exchange parameterization for mesoscale models.” Boundary-Layer Meteorology 104: 261–304.

Macdonald, R.W., Griffiths, R.F., and Hall, D.J. 1998. “An improved method for estimation of surface roughness of obstacle arrays.” Atmospheric Environment, 32, 1857–1864.

Morris, R., M. Gery, M. Liu, G. Moore, C. Daly, and S. Greenfield. 1989. “Sensitivity of a regional oxidant model to variations in climate parameters.” In The potential effects of global climate changes on the United States, Appendix F: Air Quality. U.S. EPA, Washington D.C.

Noilhan, J., and S. Planton. 1989. “A simple parameterization of the land surface processes for meteorological models.” *Monthly Weather Review* 117: 536–549.

Oke, T. R. 1978. *Boundary-Layer Climates.* London: Methuen & Co. Ltd.

Otte, T. L., A. Lacser, S. Dupont, and J. Ching. 2004. “Implementation of an urban canopy parameterization in a mesoscale meteorological model.” *Journal of Applied Meteorology* 43: 1648–1665.

Pan, H. L., and L. Mahrt. 1987. “Interaction between soil hydrology and boundary-layer development.” Boundary Layer Meteorology 38: 185–202.

Reisner, J., Rasmussen, J.M., Bruintjes, R.T., 1998. “Explicit forecasting of supercooled liquid water in winter storms using the MM5 mesoscale model”. Quarterly Journal of the Royal Meteorological Society 124, 1071-1107.

Sailor, D. 1993. Role of surface characteristics in urban meteorology and air quality. Ph.D. dissertation. University of California, Berkeley.

Schultz, P. 1995. “An explicit cloud physics parameterization for operational numerical weather prediction”. Monthly Weather Review, 123, 3331-3343.

Seaman, N. L. et al. 1997. “The use of the San Joaquin Valley meteorological model in preparation of a field program in the South Coast Air Basin and surrounding regions of Southern California.” Volume II: Numerical modeling studies for the development and application of a guidance technique to support the design of the 1997 Southern California Ozone Study field program. Prepared for the California Air Resources Board, Department of Meteorology, Pennsylvania State University. University Park, Pennsylvania.

Seaman, N. L., and D. R. Stauffer. 1996. “SARMAP meteorological model final report.” Prepared for the San Joaquin Valleywide Air Pollution Study Agency, Department of Meteorology, Pennsylvania State University, University Park, Pennsylvania.

Smith, J. B., and D. A. Tirpak. (eds.). 1989. “The potential effects of global climate change on the United States.” Report to Congress, U.S. EPA, EPA-230-05-89-050, Washington D.C. 409 pp.

Stauffer, D. R., and N. L. Seaman. 1990. “Use of four-dimensional data assimilation in a limited area mesoscale model. Part I: Experiments with synoptic-scale data.” *Monthly Weather Review* 118: 1250–1277.

Stockwell, W. R., E. M. Fujita, I. Shumyatsky, D. Freeman, D. E. Campbell, D. Koracin, D. Podnar, and T. McCord. 2004. “State implementation plan (SIP) planning service for the Sacramento ozone non-attainment area.” Vol. 3: SIP Modeling Final Report. Prepared for the Sacramento Metropolitan Air Quality Management District by the Desert Research Institute, Reno, Nevada.

Taha, H. 1996. ″Modeling the Impacts of Increased Urban Vegetation on the Ozone Air Quality in the South Coast Air Basin.″ *Atmospheric Environment* 30(20): 3423–3430.

Taha, H. 1997a. "Urban climates and heat islands: Albedo, evapotranspiration, and anthropogenic heat." *Energy and Buildings* 27(1007): 99–103.

Taha, H. 1997b. ″Modeling the Impacts of Large-Scale Albedo Changes on Ozone Air Quality in the South Coast Air Basin.″ *Atmospheric Environment* 31(11): 1667–1676.

Taha, H. 1999: ″Modifying a Mesoscale Meteorological Model to Better Incorporate Urban Heat Storage: A Bulk-Parameterization Approach.″ *Journal of Applied Meteorology* 38(4): 466–473.

Taha, H., and R. Bornstein. 1999. ″Urbanization of meteorological models: Implications on simulated heat islands and air quality." Invited Paper, International Congress of Biometeorology and International Conference on Urban Climatology (ICB-ICUC) Conference, 8–12 November 1999, Sydney Australia.

Taha, H., S. Konopacki, and S. Gabersek. 1999. ″Impacts of large-scale surface modifications on meteorological conditions and energy use: A 10-region modeling study.″ *Theoretical and Applied Climatology* 62(3-4): 175–185.

Taha, H., S. C. Chang, and H. Akbari. 2000. *Meteorological and air-quality impacts of heat island mitigation in three U.S. cities.* LBNL Report No. 44222. April.

Taha, H. 2003a. "Mesoscale meteorological and air quality modeling of heat island reduction strategies (HIRS)." Technical Note, Lawrence Berkeley National Laboratory, Berkeley, California (April 2003) 53 pp. Available from H. Taha, Altostratus Inc.

Taha, H. 2003b. "Multi-regional modeling assessment of the potential meteorological impacts of heat island reduction." Technical Note, Lawrence Berkeley National Laboratory, Berkeley, California. April 2003. 46 pp. Available from H. Taha, Altostratus Inc.

Taha, H. 2003c. "Potential meteorological and air-quality implications of heat-island reduction strategies in the Houston-Galveston TX region." Technical Note. Lawrence Berkeley National Laboratory, Berkeley, California. 143 pp. Available from H. Taha, Altostratus Inc.

Taha, Haider. 2005. *Urban Surface Modification as a Potential Ozone Air-quality Improvement Strategy in California – Phase One: Initial Mesoscale Modeling.* Altostratus Inc. for the California Energy Commission, PIER Energy-Related Environmental Research. CEC-500-2005-128.

Taha, H. 2007. "Mesoscale and meso-urban modeling of heat islands and control: Evaluation of potential ozone air-quality impacts in California (Formerly 2.1)." Presented at the American Meteorological Society, 7th Symposium on the Urban Environment, September 10–13. San Diego, California.

Tao, W. K., and J. Simpson. 1993. "Goddard cumulus ensemble model. Part I: Model description." Terrestrial, Atmospheric, and Oceanic Science 4: 35–72.

Tesche, T. W., D. E. McNally, C. A. Emery, and E. Tai. 2001. "Evaluation of the MM5 model over the Midwestern U.S. for three 8-hour oxidant episodes." Prepared for the Kansas City Ozone Technical Workgroup. Alpine Geophysics LLC and Environ Corp.

Wakim, P. G. 1989. "Temperature adjusted ozone trends for Houston, New York, and Washington D.C. 1981–1987." Presented at the 82nd annual meeting and exhibition of the A&WMA, Anaheim, California, June 1989. A&WMA, Pittsburgh, Pennsylvania.

Yarwood, G., R. E. Morris, M. A. Yocke, H. Hogo, and T. Chico. 1996. "Development of a methodology for source apportionment of ozone concentration estimates from a photochemical grid model." 89th AWMA Annual Meeting, Nashville, Tennessee. June 1996.

Zhang, D. L., and Anthes, R. A. 1982. "A high resolution model of the planetary boundary layer – Sensitivity tests and comparisons with SESAME 79 data." Journal of Applied Meteorology 21: 1594–1609.

7.0 Acronyms

AGL	Above ground level
AMSL	Above mean sea level
CCOS	Central California Ozone Study
CO_2	Carbon dioxide
FAD	Frontal area density function
FDDA	Four-dimensional data assimilation
GDAS	Global data assimilation system
H2W	Height-to-width ratio
HVAC	heating ventilating and air conditioning
LST	Local standard time
LULC	Land use and land cover
MM5	PSU/NCAR fifth-generation mesoscale meteorological model
MRF	Medium range forecast
NCAR	National Center for Atmospheric Research
NCEP	National Centers for Environmental Prediction
NNRP	NCEP/NCAR Reanalysis Project
NO	Nitric oxide
NO_X	Nitrogen oxides
NSBD	National Statistics Building Database
O-R	Orange-Riverside counties (Southern California)
OSAT	Ozone source apportionment technology
PA	Process analysis
PAD	Plan area density function
PAN	peroxyacetyl nitrate
PBL	Planetary boundary layer
ppb	Parts per billion
PST	Pacific standard time

PSU	Pennsylvania State University
RADM	Regional Acid Deposition Model
RRF	Relative reduction factor
SAM	Santa Ana Mountains
SCOS	Southern California Ozone Study
SIP	State Implementation Plan
SVF	Sky-view factor
TAD	Top area density function
TKE	Turbulent kinetic energy
TUV	NCAR's Tropospheric Ultraviolet & Visible Radiation model
UBL	Urban boundary layer
UCL	Urban canopy layer
UCP	Urban canopy parameterizations (or parameters)
UHI	Urban heat island
uMM5	Urbanized MM5 (H. Taha, Altostratus version)
USGS	United States Geological Survey
UV	Ultraviolet
VOC	Volatile organic compounds
W2P	Wall-to-plan area ratio

8.0 Symbols (unless defined otherwise in text)

α	albedo
β	Bowen ratio
C	Concentration
D	Drag coefficient
D	Displacement height
E	Turbulent kinetic energy
e	Vertical entrainment rate
ε	Emissivity or TKE dissipation term
H	Sensible heat flux
h	Layer-interface height
η	Soil moisture content
K	Diffusivity
k	von Karman constant (or vertical index)
θ	Potential temperature
Q_f	Anthropogenic heat flux
S	Sink/Source term
T	Temperature
u	x-component of wind velocity
v	y-component of wind velocity
V	Wind vector
z	height
Zi	Mixing / boundary layer height
Zo	Roughness length

Appendices

Appendix A

This appendix provides samples aerial snapshots of the land use and land cover (LULC) classes identified in Table 2.3 of the main report. These classes were used in the characterization of urban and non-urban areas for UCP extrapolation purposes. See the discussion in the report.

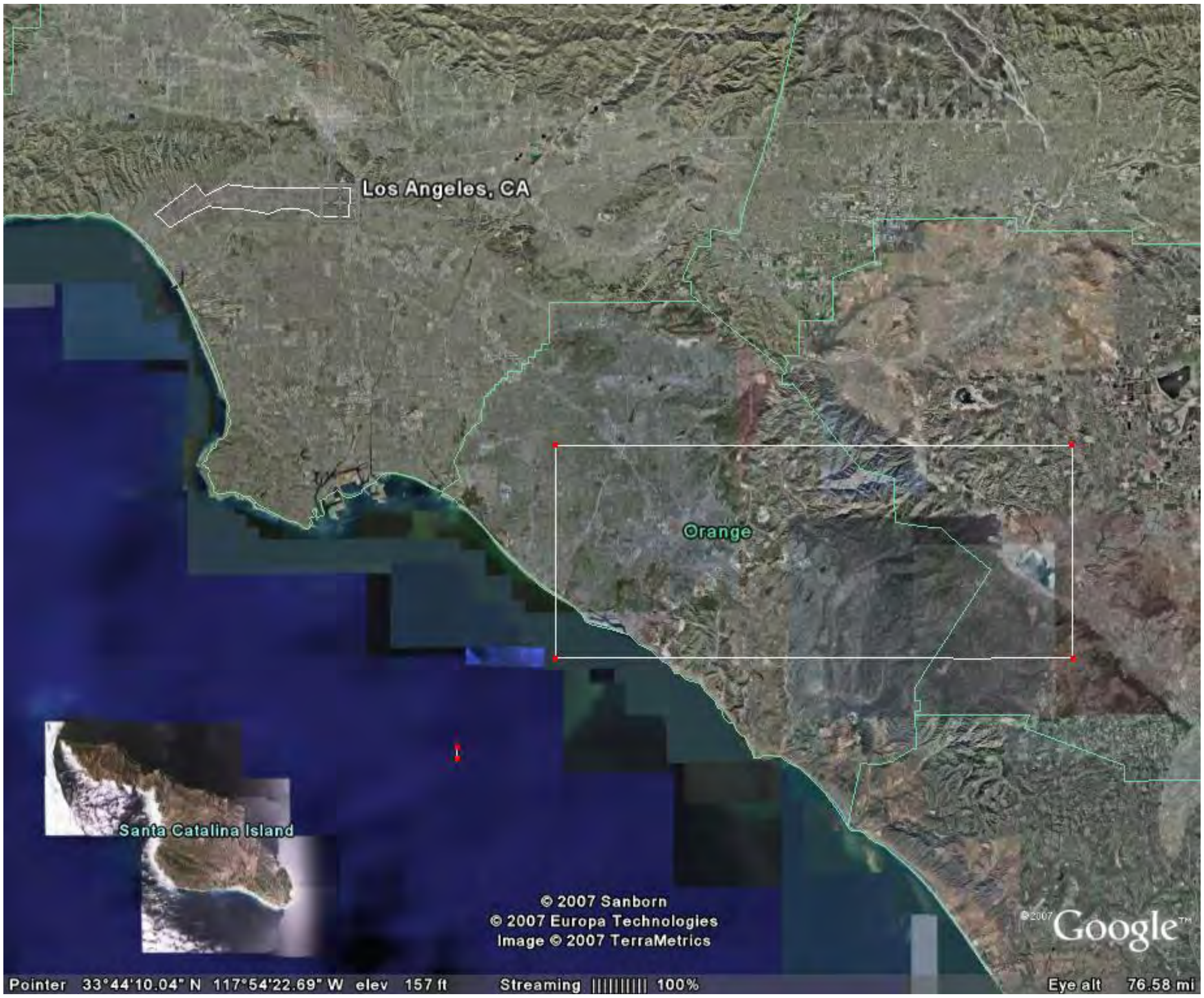

Figure A-1. Los Angeles region and the Orange-Riverside (O-R) uMM5 and fine-resolution CAMx modeling domain

Figure A-2. LULC 11111 example: Single-family, detached, high-density residential

Figure A-3. LULC 11121 example: Single-family, attached, high-density residential

Figure A-4. LULC 11122 example: Multi-family, attached, high-density residential

Figure A-5. LULC 11211 example: Single-family, detached, low-density residential

Figure A-6. LULC 11221 example: Single-family, attached, low-density residential

Figure A-7. LULC 115 example: Mixed residential (e.g., high/low density, attached/detached)

Figure A-8. LULC 116 example: High-density residential mixed with mobile-home parks

Figure A-9. LULC 121 example: Low-rise commercial/offices and/or malls

Figure A-10. LULC 122 example: High-rise commercial and offices

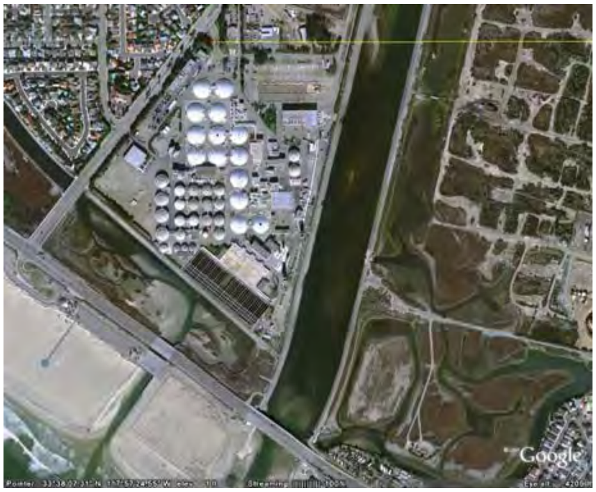

Figure A-11. LULC 13 example: Industrial

Figure A-12. LULC 14 example: Transportation and utility / airports / highways

Figure A-13. LULC 15 example: Mixed commercial and industrial

Figure A-14. LULC 161 example: Mixed residential and commercial

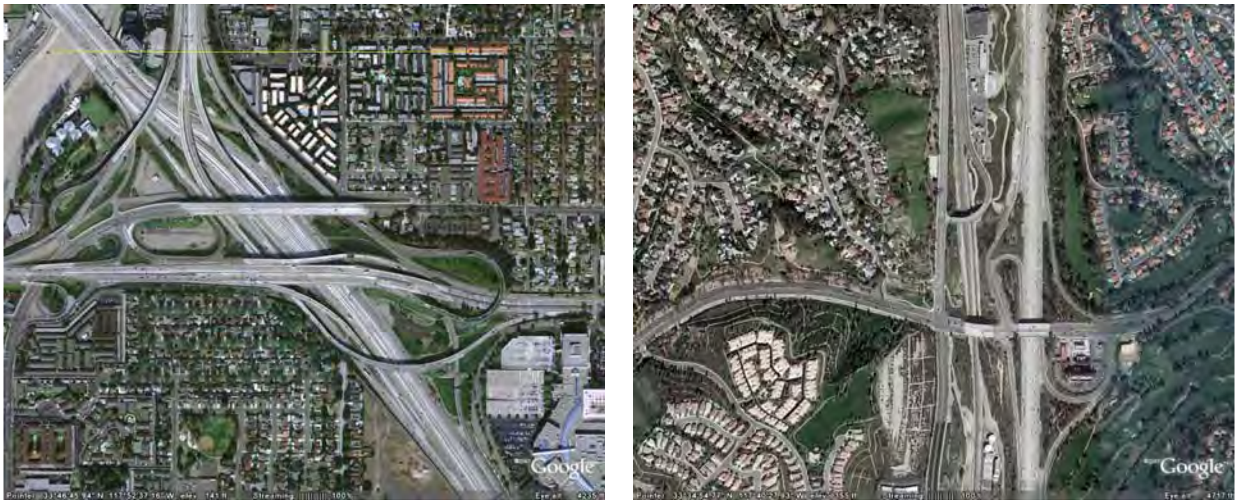

Figure A-15. LULC 162 example: Mixed residential and transportation/highways

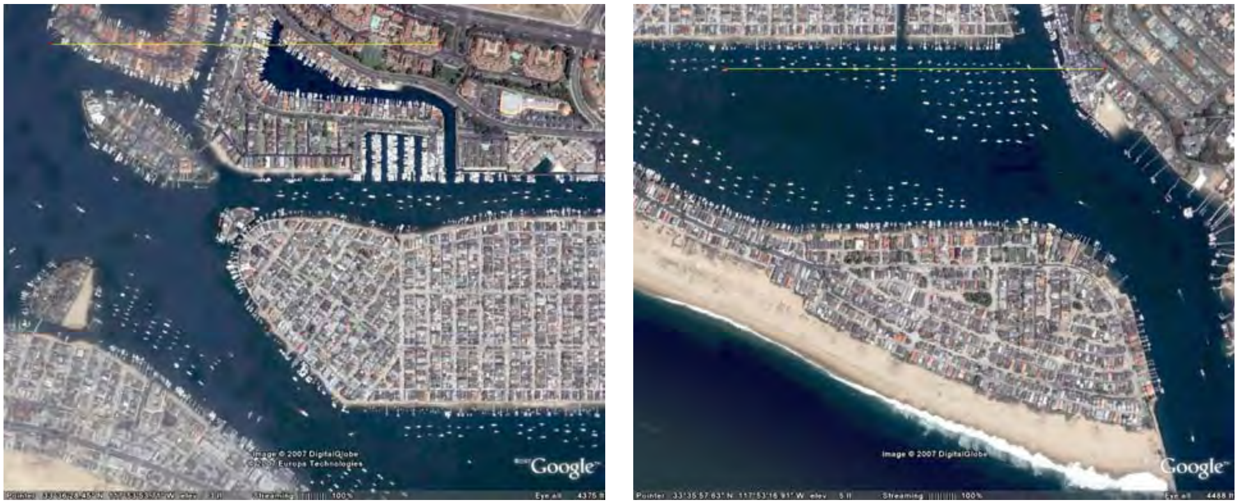

Figure A-16. LULC 164 example: Mixed residential and recreation

Figure A-17. LULC 166 example: Mixed residential and educational

Figure A-18. LULC 19 example: Services

Figure A-19. LULC 22 example: Academic / educational

Figure A-20. LULC 31 example: Open areas / green / golf courses / vineyards

Appendix B

This appendix list selected examples from a larger database of various three-dimensional morphological (UCP) parameters. It provides a comparison of selected UCP between Los Angeles and a number of other U.S. urban regions. In these figures, Los Angeles data is shown in bold red. The data is based on Burian et al. (2003).

Legend for following figures →

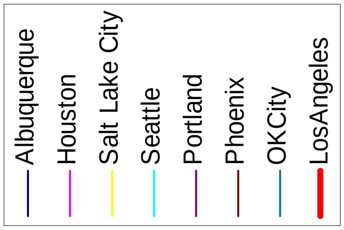

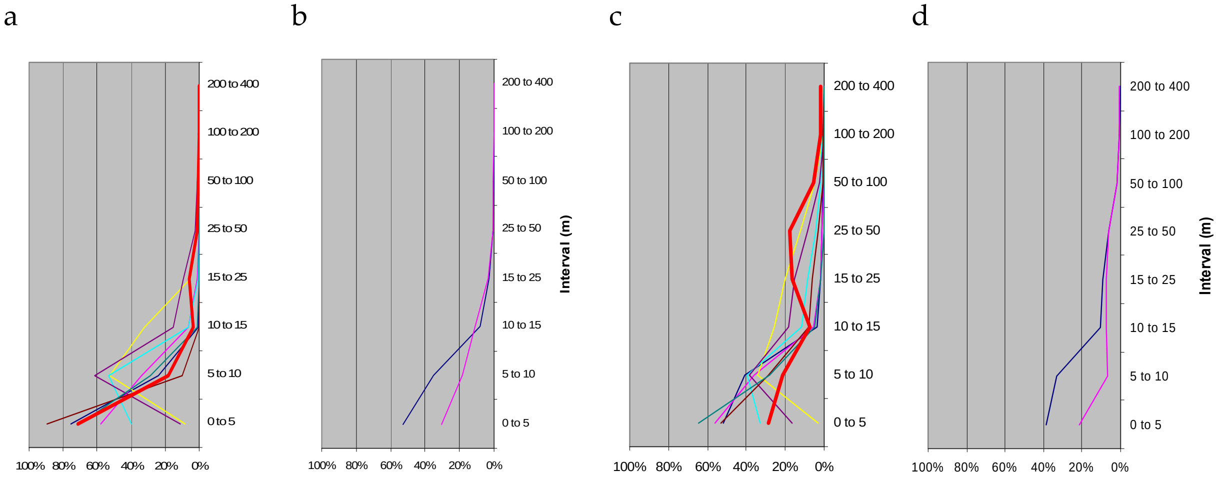

Figure B.1. Left to right: (a) Building height, residential: Actual height, (b) Building height, residential: Mean (blue) and standard deviation (red), (c) Building height, Commercial and Services: Actual height, and (d) Mean (blue) and standard deviation (red)

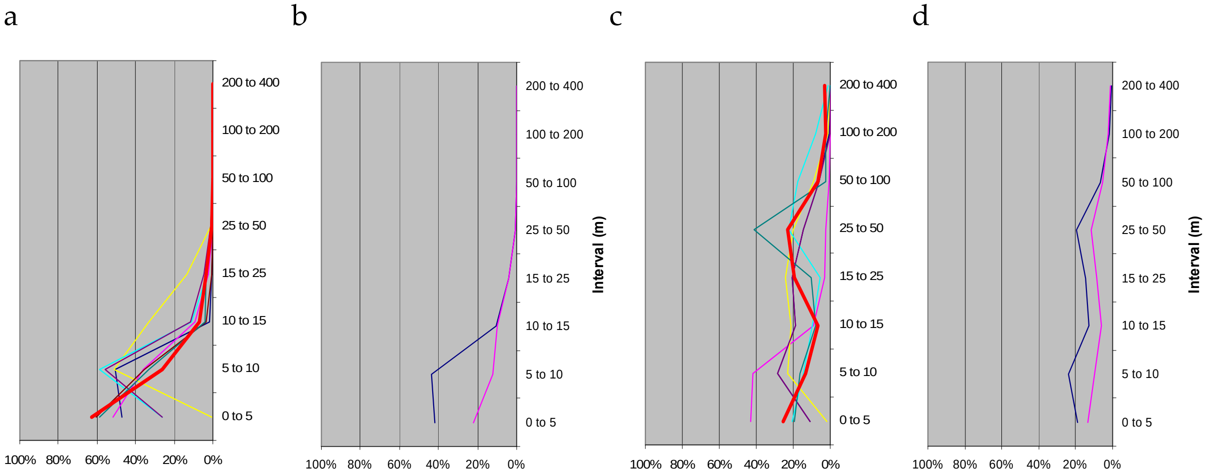

Figure B.2. Left to right: (a) Building height, Industrial: Actual height, (b) Mean (blue) and standard deviation (red), (c) Building height, Urban high-rise: Actual height, and (d) Mean (blue) and standard deviation (red)

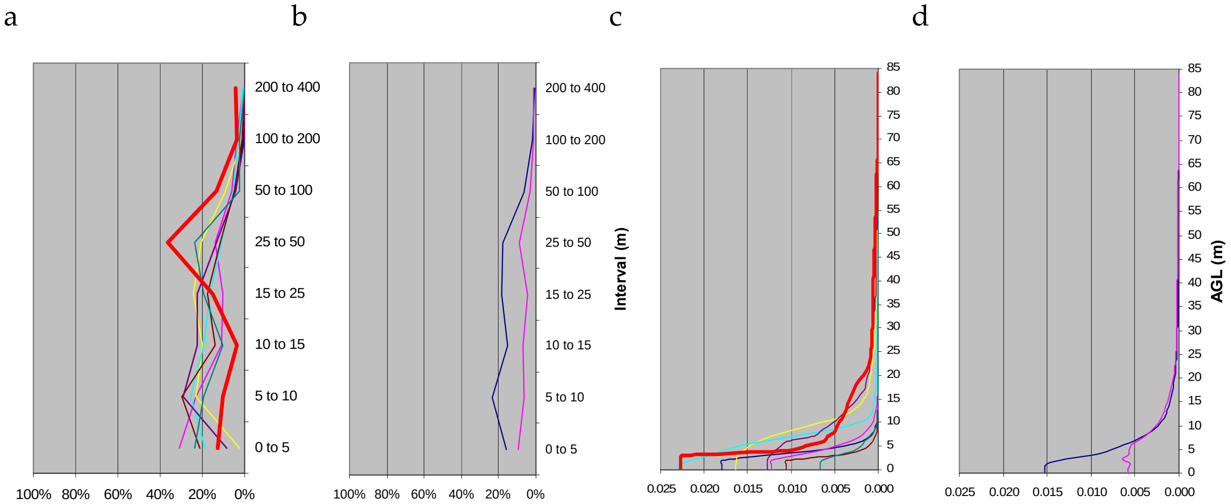

Figure B.3. Left to right: (a) Building height, Downtown core: Actual height, (b) Mean (blue) and standard deviation (red), (c) FAD, General residential FAD, and (d) Mean (blue) and standard deviation (red)

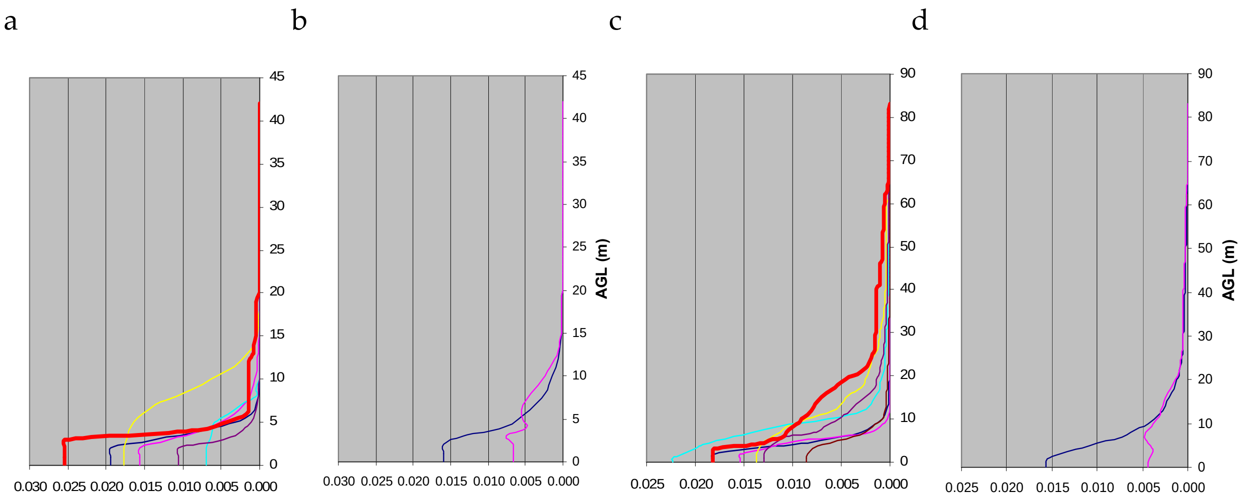

Figure B.4. Left to right: (a) FAD, High-density single-family residential, (b) Mean (blue) and standard deviation (red), (c) FAD, High-density single-family residential, and (d) Mean (blue) and standard deviation (red)

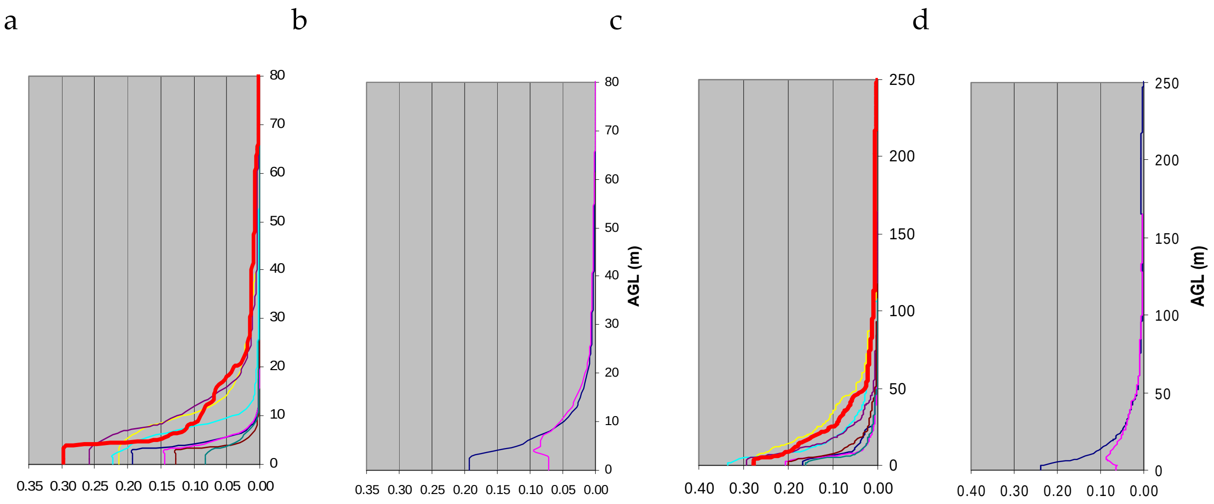

Figure B.5. Left to right: (a) PAD, Residential, (b) Mean (blue) and standard deviation (red), (c) PAD, Commercial and Services, and (d) Mean (blue) and standard deviation (red)

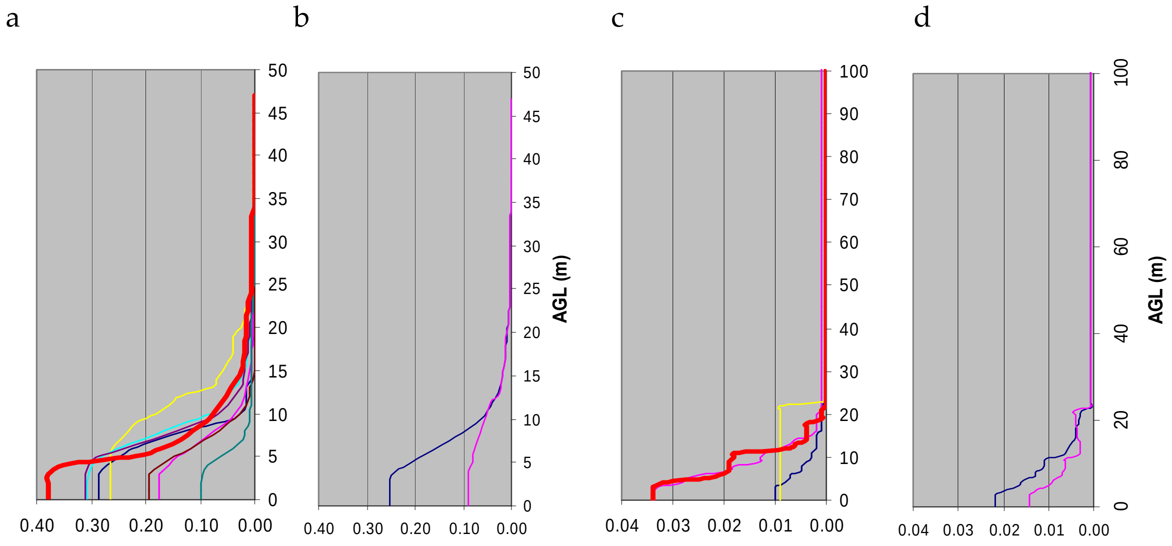

Figure B.6. Left to right: (a) PAD, Industrial, (b) Mean (blue) and standard deviation (red), (c) PAD, Transportation / Utility, and (d) Mean (blue) and standard deviation (red)

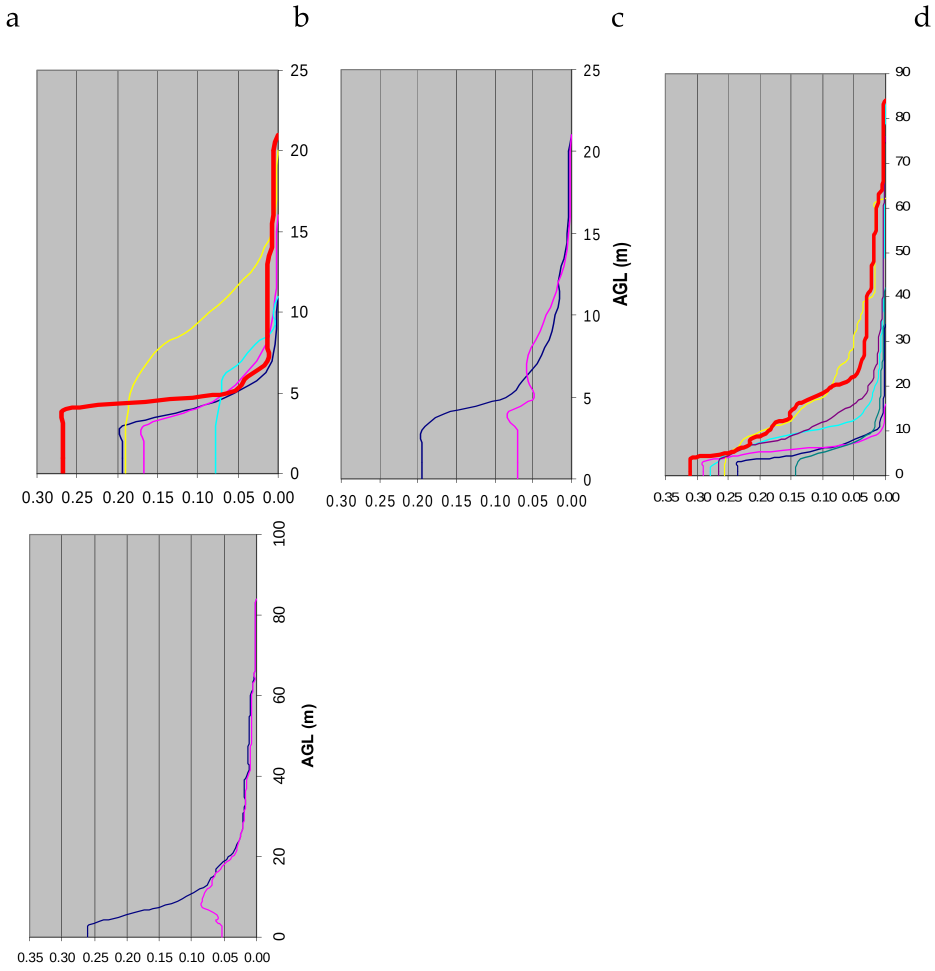

Figure B.7. Left to right: (a) PAD, High-density residential, (b) Mean (blue) and standard deviation (red), (c) PAD, Multi-family residential, and (d) Mean (blue) and standard deviation (red)

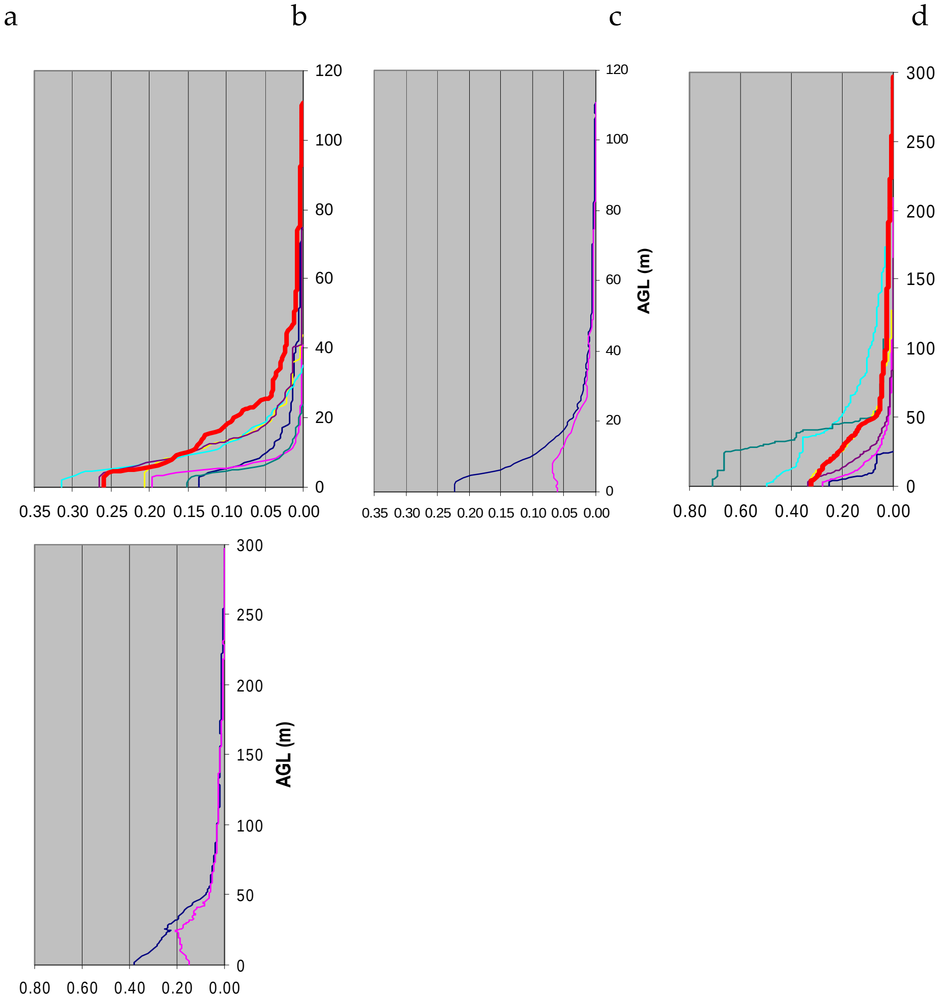

Figure B.8. Left to right: (a) PAD, Non-high-rise commercial, (b) Mean (blue) and standard deviation (red), (c) PAD, High-rise commercial, and (d) Mean (blue) and standard deviation (red)

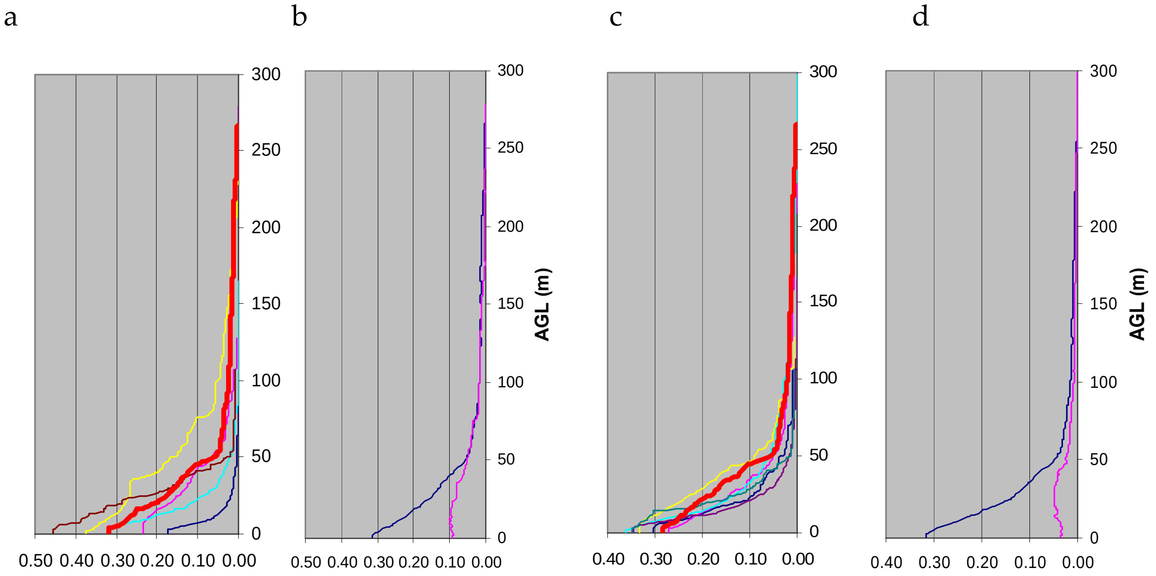

Figure B.9. Left to right: (a) PAD, Urban high-rise, (b) Mean (blue) and standard deviation (red), (c) PAD, Downtown core, and (d) Mean (blue) and standard deviation (red)